Understanding the formation and evolution of asteroids through analysis of carbonaceous chondrites



Helena Bates

Trinity College

University of Oxford

A thesis submitted for the degree of

Doctor of Philosophy

September 2020

Abstract

The transport and evolution of volatiles (e.g. water, organics) during the formation of the inner terrestrial planets of our Solar System is relatively poorly constrained. A number of dynamical mechanisms have been proposed that transport volatile rich material from the outer Solar System (i.e. from beyond the snow-line, currently 5 AU), and primitive, volatile-rich asteroids may provide clues as to these processes. Observations demonstrate that these asteroids have similar infrared spectra to CI, CM and CY carbonaceous chondrite meteorites. Thus, by studying the composition and alteration histories of these families of meteorites it can potentially provide insights into the physical processes that occurred or are occurring on these asteroids.

In this thesis I link trends in the spectra of both aqueously altered and aqueously and thermally altered CI, CM and CY chondrites with meteorite mineralogy. I demonstrate how these trends may be applied to remote asteroid spectra to examine their surface mineralogy and processing history. I describe how trends in the near- (NIR) and mid-infrared (MIR) spectra of aqueously altered meteorites can reflect the phyllosilicate composition and therefore degree of aqueous alteration. I also report that trends in aqueously and thermally altered meteorite NIR and MIR spectra reflect a combination of phyllosilicate and olivine compositions and abundances. Furthermore, I describe and assess differences between the MIR reflectance spectra typically collected in laborato-

ries, and emissivity spectra acquired under asteroid environmental conditions that more accurately replicate the spectral flux received when observing a remote airless body. I then use the spectra collected to aid in the interpretation of spectra of a range of potentially volatile-rich objects including NEOs visited by Hayabusa2 and OSIRIS-REx, main-belt asteroids and Jupiter Trojans. The spectra will also be a valuable aid in analysis of future remote telescopic observations of and spacecraft missions to small bodies.

For Grandi and Judy

Contents

List of figures vi

List of tables xi

Acknowledgements xiii

1 Introduction 1

1.1 Formation of the Solar System 1

1.1.1 Nebula Hypothesis 1

1.1.2 Planetesimals, planetary embryos and planets 2

1.1.3 Orbital migration 5

1.2 Asteroids 8

1.2.1 Asteroid populations 9

1.2.2 Missions to volatile-rich asteroids 14

1.3 Meteorites 17

1.3.1 Chondrite meteorites 17

1.3.2 Aqueously altered carbonaceous chondrites 20

1.3.3 Aqueously and thermally altered carbonaceous chondrites . . . 26

1.4 Linking meteorites and asteroids: Spectroscopy 29

1.4.1 Visible and near-infrared (VNIR) 29

1.4.2 Mid-infrared (MIR) 31

1.4.3 Volatile-rich asteroids and meteorites . . . 33
1.5 Aims and objectives . . . 36

2 Methodology 40
2.1 Samples . . . 40
2.1.1 Characteristics of CM and CI chondrite samples . . . 41
2.1.2 Characteristics of CM, CM-an and CY chondrite samples . . . 48
2.1.3 Other aqueously and thermally altered carbonaceous chondrites 51
2.2 X-ray diffraction . . . 53
2.2.1 High resolution X-ray diffraction . . . 54
2.2.2 Position-sensitive detector X-ray diffraction . . . 55
2.3 Spectroscopy . . . 60
2.3.1 Reflectance spectroscopy . . . 63
2.3.1.1 Sample packing . . . 65
2.3.1.2 Standard spectra . . . 67
2.3.2 Emission spectroscopy . . . 69

3 Linking the reflectance spectroscopy and mineralogy of highly aqueously altered CM and CI carbonaceous chondrites 72
3.1 Introduction . . . 72
3.2 Experimental . . . 73
3.3 Results . . . 74
3.3.1 Modal mineralogy of ALH 83100, ALH 83102, LEW 85311, LEW 90500 and LON 94101 . . . 74
3.3.2 NIR . . . 76
3.3.3 MIR . . . 81

3.4 Discussion . . . 85
3.4.1 NIR spectral relationships to mineralogy . . . 85
3.4.2 MIR spectral relationships to mineralogy . . . 94
3.4.3 Spectral parameters for mineral identification . . . 101
3.5 Conclusions . . . 102

4 Linking the reflectance spectroscopy and mineralogy of aqueously and thermally altered CM and CY carbonaceous chondrites 104
4.1 Introduction . . . 104
4.2 Experimental . . . 105
4.3 Results . . . 106
4.3.1 X-ray diffraction . . . 106
4.3.2 Reflectance spectra . . . 116
4.4 Discussion . . . 126
4.4.1 Mineralogy of thermally altered CM and CY chondrites . . . 126
4.4.2 Potential CY chondrites . . . 128
4.4.3 A 881655 and WIS 91600 . . . 129
4.4.4 NIR spectral relationships to mineralogy . . . 131
4.4.5 MIR spectral relationships to mineralogy . . . 134
4.4.6 Spectral parameters for determining thermal alteration . . . 142
4.5 Conclusions . . . 143

5 The emissivity spectra of heated CM and CY carbonaceous chondrites 145
5.1 Introduction . . . 145
5.2 Experimental . . . 145
5.3 Results . . . 146

5.3.1 Ambient and SAE MIR spectral features in aqueously altered CM chondrites . . . 146
5.3.2 Ambient and SAE MIR spectral features in aqueously and thermally altered CM chondrites . . . 150
5.3.3 Ambient and SAE MIR spectral features in aqueously and thermally altered CM-anomalous chondrites . . . 153
5.3.4 Ambient and SAE MIR spectral features in aqueously and thermally altered CY chondrites . . . 153
5.3.5 Comparing reflectance and emissivity spectra . . . 157
5.4 Discussion . . . 159
5.4.1 Comparing reflectance and emissivity spectra in the MIR . . . 159
5.4.2 Aqueous alteration in MIR emissivity spectra . . . 163
5.4.3 Thermal alteration in MIR emissivity spectra . . . 166
5.4.4 Spectral parameters in emissivity spectra for identifying aqueous and thermal alteration . . . 173
5.5 Conclusions . . . 174

6 Comparing laboratory data to remote observations 175
6.1 Introduction . . . 175
6.2 Bennu . . . 176
6.2.1 3200 Phaethon . . . 179
6.3 Ryugu . . . 180
6.4 Ceres . . . 184
6.5 Jupiter Trojans . . . 188
6.6 Main belt volatile-rich asteroids . . . 193
6.6.1 MIR: 121 Hermione, 130 Elektra . . . 200

6.7 Conclusions 204

7 Conclusions and future work 206

7.1 Introduction 206

7.2 Spectral relationships with aqueous alteration 206

7.3 Spectral relationships with aqueous and thermal alteration 209

7.4 Future work 212

Bibliography 215

Appendix

A PSD-XRD beam flux 241

B PSD-XRD standards 242

C Thermogravimetric analysis 243

C.1 Experimental 243

C.2 Results 243

C.2.1 Aqueously altered CM and CI chondrites 244

C.2.2 Thermally altered CM, CY and CM-/CY-anomalous chondrites . . 247

List of figures

1.1 *The Grand Tack and Nice models of orbital migration* 6

1.2 *Bus-DeMeo asteroid classifications* 10

1.3 *The taxonomic distribution of asteroid types throughout the Solar System* . 13

1.4 *The current meteorite classification system.* 18

1.5 *The petrologic types for each chondrite group.* 19

1.6 *The oxygen isotopic compositions of the carbonaceous chondrite groups.* . . 21

1.7 *The isotopic composition of inner Solar System bodies, Jupiter family and Oort Cloud comets with carbonaceous chondrites* 22

2.1 *The geometry of the Panalytical X'Pert pro diffractometer* 55

2.2 *The geometry of the PSD-XRD* 57

2.3 *The profile stripping method for determining modal mineralogy* 59

2.4 *The profile stripping method for determining modal mineralogy for a dehydrated sample* 61

2.5 *The Specac Selector diffuse reflectance accessory* 63

2.6 *Effect of packing conditions on reflectance spectra* 66

2.7 *Phyllosilicate standard reflectance spectra* 68

2.8 *CAD model of PASCALE* 70

2.9 *Olivine standard emissivity spectrum* 71

3.1 *PSD-XRD patterns of ALH 83100, ALH 83102, LEW 85311, LEW 90500 and LON 94101* 75
3.2 *NIR spectra between 0.8 - 1.7 µm of the aqueously altered CM and CI chondrites* 78
3.3 *The 3 µm features of the aqueously altered CM chondrites studied* 79
3.4 *The 3 µm feature of the aqueously altered CI chondrites studied* 81
3.5 *MIR spectra for the aqueously altered CM chondrites studied* 83
3.6 *MIR spectra for the aqueously altered CI chondrites* 84
3.7 *The relationship between NIR spectral slope and phyllosilicate and magnetite abundance* 88
3.8 *The relationship between the 3 µm band area and Fe-cronstedtite and magnetite abundance* 92
3.9 *The relationship between the CF and phyllosilicate abundance* 96
3.10 *The relationship between the CF and the 3 µm feature position* 98
3.11 *The relationship between the TF and phyllosilicate abundance and composition* 100

4.1 *PSD-XRD patterns of thermally altered CM chondrites* 108
4.2 *High resolution XRD patterns of thermally altered CM chondrites* 109
4.3 *XRD patterns of thermally altered CY chondrites* 112
4.4 *XRD patterns of anomalous CM chondrites* 114
4.5 *XRD patterns of A 881655 and WIS 91600* 115
4.6 *The 3 µm feature from the thermally altered CM spectra* 117
4.7 *The 3 µm feature from the thermally altered CY spectra* 118
4.8 *The 3 µm feature from the CM-/CY-anomalous spectra* 119
4.9 *The 3 µm feature from the A 881655 and WIS 91600 spectra* 120
4.10 *The thermally altered CM MIR spectra* 121

4.11 *The thermally altered CY MIR spectra* 123
4.12 *The CM-/CY-anomalous MIR spectra* 124
4.13 *The A 881655 and WIS 91600 MIR spectra* 125
4.14 *The relationship between 3 µm feature position and degree of thermal alteration* 132
4.15 *The relationship between the CF position and degree of thermal alteration* . 137
4.16 *The relationship between the TF position and degree of thermal alteration* . 138
4.17 *The relationship between Si-O bending vibration features and degree of thermal alteration* 141

5.1 *The MIR emissivity spectra for the unheated CM chondrites ALH 83100, ALH 83102 and LON 94101* 148
5.2 *The MIR emissivity spectra for the stage II CM chondrites EET 96029 and Y 793321* 151
5.3 *The MIR emissivity spectra for the stage IV CM chondrites PCA 02010 and PCA 02012* 152
5.4 *The MIR emissivity spectra for WIS 91600* 154
5.5 *The MIR emissivity spectra for Y 980115* 155
5.6 *The MIR emissivity spectra for the stage IV CY chondrites* 156
5.7 *The positions of features as observed in the reflectance spectra and the ambient and SAE emissivity spectra* 158
5.8 *The MIR emissivity spectra for the unheated CM2 chondrite Murchison* . . . 164
5.9 *The Si-O bending region, between 16.7 - 50 µm from the unheated CMs emissivity spectra* 167
5.10 *The Si-O bending region, between 16.7 - 50 µm from the unheated CMs emissivity spectra* 168

5.11 *The Si-O bending region, between 16.7 - 50 µm from the aqueously and thermally altered CM, CY and CM-anomalous emissivity spectra* 170

5.12 *The effect of thermal alteration on a Si-O bending feature* 172

6.1 *The spectra of ALH 83100 and WIS 91600 collected for fine-particulate samples and coarse-particulate/solid samples.* 179

6.2 *Emissivity spectra resampled using the MARA filter parameters* 183

6.3 *The 3 µm feature of 1 Ceres compared to the spectra of aqueously altered CM and CI chondrites* 185

6.4 *Remote emissivity spectra of comet nuclei and Jupiter Trojan asteroids and emissivity and reflectance spectra of stage IV CY chondrites.* 190

6.5 *The 3 µm feature of asteroids that show 'sharp' 3 µm features, compared to the 3 µm feature observed in aqueously altered CM chondrites* 198

6.6 *The Mg-serpentine abundance against total phyllosilicate abundance for main belt volatile-rich asteroids and for aqueously altered CM samples* . . . 199

6.7 *The relationship between Mg-serpentine/Fe-cronstedtite and semi major axis and asteroid diameter* 201

6.8 *The MIR emissivity spectra of asteroids 121 Hermione and 130 Elektra* . . . 202

7.1 *A summary of the spectral trends and parameters which correlate with degree of aqueous alteration* 207

7.2 *A summary of the spectral trends and parameters which correlate with degree of thermal alteration* 210

APPENDIX

A.1 *PSD-XRD beam flux variation over an experimental run* 241

C.1 *Representative mass loss curves for aqueously altered CM chondrites* 245

C.2 *Mass loss in all samples due to Fe-cronstedtite and Mg-serpentine* 247

C.3 *Representative mass loss curves for aqueously and thermally altered CM chondrites* 249

List of tables

1.1 *Asteroid taxonomies* 9

1.2 *Asteroid and meteorite links* 30

2.1 *Summary of the meteorite samples, sample mass, loan details, and analytical techniques* 42

2.2 *Summary of the classifications and previous analysis of meteorites* 43

3.1 *Mineralogy of the aqueously altered CM and CI chondrites* 77

3.2 *The NIR and MIR parameters determined for the highly aqueously altered CI and CM chondrite samples* 80

4.1 *Modal mineralogy of the CM, CY and CM/CY-anomalous samples* 107

4.2 *The NIR and MIR parameters determined for the aqueously and thermally altered CM, CY and CM-CY-anomalous samples.* 116

5.1 *Positions of features identified in MIR emissivity spectra* 147

6.1 *NIR and MIR parameters calculated for asteroids which are hypothesised to have experienced aqueous alteration.* 196

Appendix

B.1 *Details of the standards used in this project* 242

C.1 *Mass loss in all samples during TGA* 246

Acknowledgements

Go supervisory team, we did it! Kerri - you have made me into a better scientist (and let's be real a better human), with your patience and kindness and unwavering support. You have always encouraged me to be inquisitive and given me the space and confidence to work out what kind of scientist I wanted to be. Sara - it's just been so unbelievable to be able to work with you, your enthusiasm and genuine love for everything meteorite has always reminded me what I am doing and what I've discovered is worth it because it is interesting, and it is exciting. I also want to say that having two female supervisors has been such an inspiration to me, you have both shown me that I have the capability to do anything regardless of my gender, and that means a lot. Neil - you've always been so supportive and have always had my back. It's awesome to see the way your mind works, you can see things and spot things that no one else could, and that's encouraged me to always try and act the same. I will be a proponent of the 'what would Neil do?' school from here on out. Ashley - you took a chance on me as a 2nd year undergrad and have supported me since then. Thank you for all the opportunities, all the time spent explaining things I should probably already know, all the (life) advice, every time you've humoured me by listening to me ramble on about things that have nothing to do with anything.

I must thank STFC for funding this project, but also thanks must go to Zonta International for awarding me the Amelia Earhart fellowship, which enabled me to be in the fortunate position of going to three international conferences in 2019. Thank you also to Trinity college for giving me a graduate scholarship and LPI for the Career Development Award. I am also so grateful for travel support from the Royal Astronomical Society, JAXA and Trinity college.

I received samples from the ANSMET, NIPR, the Russian Academy of Sciences and the NHM. Without these samples this project would not have happened, and I am very grateful.

I want to say thank you to Jens in the labs at the NHM, who took the time to teach me about the XRD machines, and then for always making it easy for me to arrange time and use the instruments. I also want to thank John and Andy in the Oxford labs, who let me use their vacuum oven (even at 7am) and made me special sample cups and the most awesome custom desiccator.

I am very grateful to a number of people who have shared data and advice over the years: Romy Hanna, Andy Rivkin, Audrey Martin, Josh Emery, Bin Yang, Jorn Helbert, Franck Marchis, Zoe Landsman, Lucy Lim and Maria Cristina De Sanctis. With their support I have been able to apply my results to real asteroid data, and think 'big picture', which has been some of the most exciting parts of my project.

I always felt welcome in my Oxford research group, despite most of our interactions being online (even before 2020). I want to say particular thanks to Charlotte, Rowan, Rory, Eloise, Jordan, Burtie, Tris and Katherine (who was kind enough to read and comment on some of this monstrosity – thank you). At the museum I was lucky to have a fantastic support network around me. Eileen and Anna thank you for all your help, and thanks Eileen especially for always having the best cat pics. My museum research group were also amazing: Paul you have always been there for advice and support, or to make me laugh (when I leave I'll tell you my secret for always being able to access papers). Natasha, you deserve all the meteorites you classify to be named after you. Enrica, you've made my time at the museum so much better, thank you.

I was also lucky to have a great group down in the basement of the museum, you guys made coming into work a joy and I'm sure you are all so disappointed that you didn't get to experience me in writing up mode… Joel, Epi, Jack, Ger, Fin, Louise, Lauren, Zach, Sarah,

Sara and Emily (its been a fab 4 years, I am so glad there is someone else going through this with me. Just knowing that is like a little light keeping me going).

I want to thank some things I have termed ‘inanimate’ (I know some of them are actually animate, this is a technicality): Spanish red wine, Secret World, Trails of Cold Steel and Persona 5, the Kpop dancers on my background who give me strength every day, my (multiple) LED keyboards, the Smilodon on my desk and that weird fluffy thing on the back of my desk chair, the alien in the office window, all my stress balls, nail art, BAMF radio, RUDE and Eminem, the podcasts Redhanded, Bloodties, Lets Talk About Sects, Spirits and Heavens Gate (that made for some weird clean lab time), escitalopram, fruit and nut chocolate, olives, South Park, Star Trek, Star Wars, Doug Cook and my shared kindle library with my dad.

Outside of work I wouldn’t be here without Jess, Emma and Rhiannon, you have always been the best and I love you all so much. I also want to say a big thank you to the number one ladies in my life: Hannah, Sabie, Toast and Puddle.

I want to say thank you to my family. My parents have been amazing, they have always been there through thick and thin. I have put them through lots and they have always supported me, looked after me and loved me. I am so lucky and so grateful. And then finally I want to say thank you to Tom, I really did well when I locked you down eh? You are the best person I know and I love you, thank you.

“The asteroid spectrum runs from rocky to metallic. Doesn’t this fit in somewhere?”

“No. It’s like a calico cat. Part this and part that.”

- The Aquila Mission, Doug Cook

Chapter 1: Introduction

1.1 Formation of the Solar System

1.1.1 Nebula Hypothesis

The formation of the Solar System is often explained in the context of a 'nebula hypothesis', where the Sun and planets formed from a cloud of dust and gas called a molecular cloud (Kant, 1755, Laplace, 1796). Our Solar System likely formed in a 'high mass star-forming' region of the interstellar medium (ISM) where there may have been a small number of larger mass stars which went supernova (Hester et al., 2004, Hester and Desch, 2005). Heavier elements produced through nucleosynthesis in these larger stars were released during supernovae and mixed into the surrounding region. This effect produced a mature molecular cloud containing not only H and He but some heavier elements (Hester et al., 2004, Hester and Desch, 2005, Russell, 2007, Apai and Lauretta, 2010). Approximately 4.56 billion years ago, a region of this molecular cloud collapsed, forming a Solar Nebula. This may have been spontaneous or could have resulted from a nearby gravitational perturbation such as a supernova (Schilling, 1999, Hester et al., 2004, Hester and Desch, 2005, Russell, 2007). At the centre of the collapsing Solar Nebula, pressures and temperatures became high enough to trigger nuclear fusion, leading to the birth of the Sun. Gas flowed inwards and contributed to the mass of this early proto-Sun, and because of the conservation of angular momentum material began to flatten into a protoplanetary disk (Russell, 2007).

Within the protoplanetary disk, the first solids to condense were highly refractory minerals including Ca and Al-rich oxides and silicates such as spinel, hibonite, melilite and anorthite (Grossman, 1972, Petaev and Wood, 2005). These minerals were accreted into calcium-aluminium-rich inclusions (CAIs, MacPherson (2014)). CAIs have been dated using uranium and lead isotopes at an average age of ~4567.3 ± 0.16 Ma, which is treated as the time at which the Solar System began (Amelin et al., 2002, 2010, Connelly et al., 2012). Some CAIs have textures indicating they are direct condensates from a gas, whereas others show evidence of crystallising from a melt (Beckett et al., 2009). Also forming at this time were igneous silicate droplets called chondrules that are mainly composed of olivine and low-Ca pyroxene. Chondrules show a much wider range of ages: from 4567.32 ± 0.42 Ma (Connelly et al., 2012, Connolly and Jones, 2016), implying formation of some chondrules overlapped with CAI formation; to younger ages of 4562.49 ± 0.21 Ma (Bollard et al., 2015), indicating some also formed after the first planetesimals had accreted (Connolly and Jones, 2016). Chondrules show textures indicating they were once partially or totally molten, leading to the conclusion that they formed through heating of pre-existing condensed material (e.g. Desch et al., 2005, Russell, 2007). Possible mechanisms for producing the igneous textures observed in CAIs and chondrules include shock waves through the protoplanetary disk (Desch et al., 2005, 2010), jets and outflows ('X-wind') from the young Sun (Shu et al., 1996, 2001); lightning (Desch and Cuzzi, 2000), or impacts between larger solid bodies that would result in melting of surface material (suggested particularly for the chondrules with younger ages) (Sanders, 2017).

1.1.2 Planetesimals, planetary embryos and planets

CAIs, chondrules, metal grains and dust began to coalesce due to van der Waals forces during low-velocity collisions in the protoplanetary disk (Chambers, 2014). The accreting material might have included volatile ices where temperatures were low enough for them to

condense (Lecar et al., 2006). A fine-grained (<5 μm) matrix acted as a glue or cement, binding larger solids together. Models of this initial stage of growth suggest gravitational instabilities in the midplane of the disk, static charges and ices helped bodies to grow into metre sized objects (Poppe et al., 2000, Youdin and Shu, 2002, Russell, 2007). At this stage, bodies grew quickly into > kilometre sized planetesimals due to accumulation of material in a dynamically turbulent protoplanetary disk (Johansen et al., 2007).

Subsequent planetesimal growth would have relied on collisions: either at low velocity resulting in bodies of similar sizes adhering or partially accreting to each other (Leinhardt and Stewart, 2012, for bodies <1 km, velocities of <20 ms^{-1}) or between bodies of different sizes resulting in disruption and re-accumulation of material (Asphaug et al., 2006). At this stage, bodies were large enough to have gravitational attraction, which encouraged planetesimal interaction and collisions in a process called runaway accretion (Ormel et al., 2010, Chambers, 2014). The largest planetesimals grew to between 100- 1000 km in size, at which point they are considered planetary embryos. These embryos continued to grow into Mars-sized bodies (7000 km) in a process called oligarchic growth, whilst the growth of smaller planetesimals slowed before they were accreted into the embryos (Kobuko and Ida, 1998, 2000). In the outer Solar System, there was more material available for accretion, because of lower temperatures allowing the condensation of ices (Inaba et al., 2003, Lodders, 2003, Chambers, 2014). The heliocentric distance at which water ice could condense in the protoplanetary disk is known as the water 'snow-line' (1.8 - 2.7 AU, Lecar et al., 2006). Oligarchic growth therefore produced larger planetary embryos beyond the water snow-line that were able to accrete gas directly from the protoplanetary disk, growing quickly into the gas giant planets before the protoplanetary disk was dispersed.

Planet formation in the disk was likely fast, beginning as early as 0.1 - 0.3 Ma after CAI formation (Kruijer et al., 2014), suggesting the earliest planetesimals were forming concur-

rently with CAIs and chondrules (e.g. Sanders, 2017). Further evidence for this comes from observations by the Atacama Large Millimeter/submillimeter Array (ALMA) of a protoplanetary disk surrounding the star HL Tauri, ~140 light-years from Earth. This star is approximately 0.1 Ma old, and yet the disk has bright rings interspersed with gaps where planetesimals and planetary embryos are appearing to be sweeping up material, implying that formation of the first planetesimals is a rapid process (Brogan et al., 2015).

The final stage of planetary growth came when planetary embryos had accreted half of the solid material in the protoplanetary disk (Kenyon and Bromley, 2006), and the remaining gas and dust in the disk was dispersed (Morbidelli et al., 2012). Protoplanetary disks are estimated to have lifetimes of ~3- 10 Ma (Mamajek et al., 2004, Mordasini et al., 2010, Pascucci and Tachibana, 2010). Removal of the gas and dust in the protoplanetary disk caused the orbits of planetary embryos to become more eccentric and cross with their neighbours' (Morbidelli et al. 2012). The resulting large-scale impacts and disruption eventually led to the largest embryos settling into stable orbits as planets (e.g Goldreich et al., 2004). It is thought that the planets grew to their current sizes 30 - 100 Ma after CAI formation (Kenyon and Bromley, 2006, Morbidelli et al., 2012, Walsh et al., 2012).

One of the outstanding questions arising from this model of Solar System evolution is the origin of inner Solar System water. As Earth and the other terrestrial planets likely formed sunward of the water snow-line they were predicted to have accreted 'dry', as temperatures were too high for volatiles to condense. However, it has been recently suggested that there may have been enough volatiles in the material which Earth and the other terrestrial planets accreted from to account for their water and other volatile budget (Piani et al., 2020). Nevertheless, this explanation does not reproduce the isotopic composition of Earth's water, and it is implied that there must also be a contribution of volatile material from elsewhere in the Solar System (Piani et al., 2020). Historically, water and volatiles were thought to have

been delivered by comets, icy bodies from the outer Solar System which were thrown inwards (Delsemme, 1992). However isotopic compositions of cometary material were found not to match to the water on Earth: for example, the comets have much higher D/H ratios than that of standard mean ocean water (SMOW) (Morbidelli et al., 2002, Alexander, 2017). Alternate models of water delivery suggest asteroids may be responsible (Morbidelli et al., 2000). Asteroids are some of the left over planetesimals from the early Solar System that never accreted into larger planetary embryos. Present day observations of asteroids show a wide range of processing, structures and compositions. Some seem to have experienced minor alteration, however others have differentiated and have a core, mantle and crust. Some asteroids formed outside of the water snow-line and so accreted water ice which altered the original rock. It is these bodies that are hypothesised to have delivered organics, water and other volatiles to the inner Solar System during periods of orbital migration. However, the aqueous and thermal histories of these bodies are not well understood.

1.1.3 Orbital migration

The concept of orbital migration in the early Solar System is based on the theory that planets and other bodies would be unlikely to remain approximately where they formed until the present-day (Lin and Papaloizou, 1986, Armitage, 2007, Walsh et al., 2011, 2012, Kley and Nelson, 2012). There have been two periods of time during which migration of the planets is thought to have occurred: between CAI formation and the dispersion of the protoplanetary disk (Walsh et al., 2011); and approximately 400- 600 Ma after CAI formation (Gomes et al., 2005). These two periods of orbital migration help to describe how planetesimals are mixed throughout or ejected entirely from the Solar System because of planetary migration (Figure 1.1).

The initial period of planetary migration was termed by Walsh et al. (2011) as the Grand Tack scenario, whereby (proto-)Jupiter formed earlier than Saturn, and through interactions

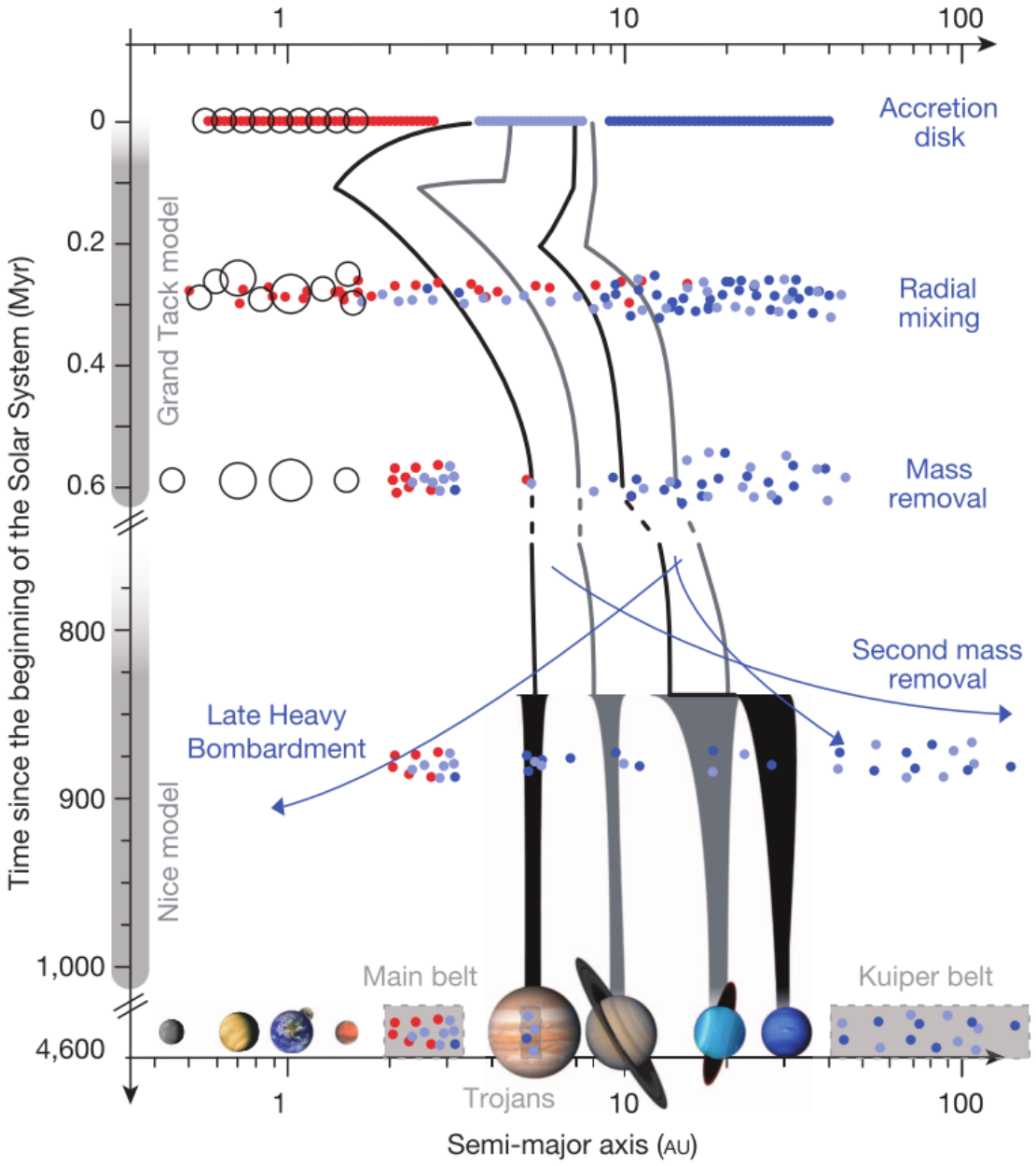


Figure 1.1: *This diagram from DeMeo and Carry (2014) shows the dynamical history of the early Solar System. It shows the forward and backwards migration of Jupiter and Saturn during the Grand Tack model, mixing planetesimals between the inner and outer Solar System. The second period of orbital migration, described by the Nice model, is shown by the movement of outer Solar System planetesimals into the terrestrial planet zone, causing the Late Heavy Bombardment. Blue and red dots signify outer and inner Solar System planetesimals, respectively.*

with the gas in the protoplanetary disk began to migrate sunward (Walsh et al., 2011, 2012, Morbidelli et al., 2015). During this migration, Jupiter would have gravitationally destabilized a region of inner Solar System planetesimals, transferring approximately 10 - 15 % of

the mass of these bodies outwards to beyond 4 AU. Once Saturn grew large enough to interact with Jupiter it also migrated inwards. When Saturn reached a mean-motion resonance of 3:2 with Jupiter (3 orbits of Jupiter around the Sun for every 2 orbits of Saturn), this migration was reversed. Jupiter moved outwards, back through the disk of planetesimals it had scattered back and subsequently migrated further into the region where more volatile-rich planetesimals were formed beyond the snow line (Morbidelli et al., 2015). These interactions would have thrown forward 0.5 % of both the volatile-rich and the originally scattered planetesimals to form an asteroid belt which is between the current orbits of Mars and Jupiter. This would result in a delivery of volatile-rich material into the inner Solar System (Walsh et al., 2011, 2012, O'Brien et al., 2014, Raymond and Morbidelli, 2014, Morbidelli et al., 2015). The outward migration of the giant planets continued until the final removal of the gas in the protoplanetary disk (Morbidelli et al., 2015).

The second period of orbital migration is described by the Nice model, which suggests the exchange of angular momentum between bodies in the Kuiper belt (a large region of planetesimals at a distance of 30 - 50 AU) and the gas giants caused a phase of orbit crossings and scattering of planetesimals (Gomes et al., 2005, Tsiganis et al., 2005, Fassett and Minton, 2013). The model suggests that as Jupiter migrated inwards to its current orbit at 5.2 AU, Saturn, Uranus and Neptune migrated outwards (to their current orbits at 9.5, 19.6 and 30 AU, respectively). These orbital changes scattered planetesimals in the Kuiper belt inwards towards the inner Solar System and outwards until they were ejected. This caused a period of increased activity in the inner Solar System, which has been suggested by the observation of an increase in the impact rate on the moon approximately 3.9 - 4.0 billion years ago (Tsiganis et al., 2005, Fassett and Minton, 2013). This period is called the Late Heavy Bombardment.

1.2 Asteroids

Following these periods of planet building and orbital migration, the architecture of the Solar System would have resembled what is observed today. The current asteroid and Kuiper belts contain leftover planetesimals, and the main asteroid belt population is a mixture of bodies from the inner and outer Solar System, due to periods of planetary migration. The diversity of asteroid types can be observed by looking at the reflected light from different asteroids in the visible (VIS, 0.3 - 0.8 μm) and part of the near-infrared (NIR, 0.8 - 2.5 μm) wavelength ranges. These reflectance spectra can indicate the dominant composition on the surfaces of the observed asteroids and have been used to define taxonomic classifications.

There are several taxonomic classifications in use today: the Tholen (1984) taxonomy is based on the Eight-Color Asteroid Survey (ECAS) data collected over eight filters between 0.337 - 1.041 μm (Zellner et al., 1985); the Bus taxonomy is based on the Small Main-belt Asteroid Spectroscopic Survey (SMASSII) that covers 0.435 - 0.925 μm (Xu et al., 1995, Bus, 1999, Bus and Binzel, 2002b,a); and the Bus-DeMeo taxonomy, which extended the Bus taxonomy up to 2.45 μm (Rayner et al., 2003, DeMeo et al., 2009). All three taxonomies divide asteroids into three major complexes: the S-complex have absorption features near 1.0 and 2.0 μm; the C-complex have flat, mostly featureless spectra; and the X-complex also have relatively featureless spectra but with a slope of increasing reflectance with increasing wavelength (red-sloped). There is an additional 'Other' complex for asteroids whose spectra have distinct characteristics that do not fall into the S-, C- or X-complexes (Tholen, 1984, Bus, 1999, Bus and Binzel, 2002b,a, DeMeo et al., 2009). Each complex is then subdivided into classes. The details of the Bus-DeMeo taxonomy are given in Table 1.1 and Figure 1.2.

Taxonomy	Tholen	Bus	Bus-DeMeo	
Wavelength range (μm)	0.337 - 1.041	0.435 - 0.925	0.435 - 2.450	Bus-DeMeo taxonomy description
S-complex	S	S	S	Absorption features at 1 and 2 μm.
		Sa	Sa	Deep and broad feature at 1 μm.
		Sq	Sq	Wide 1 μm feature, evidence of a feature near 1.3 μm.
		Sr	Sr	Narrow 1 μm feature, and a feature near 2 μm.
		Sk	Sv	Sv: Very narrow 1 μm feature, and a feature near 2 μm.
		Sl		
C-complex	B	B	B	Negatively sloping with a bump near 0.6 μm.
	C	C	C	Neutral slope, slight positive slope after 1.3 μm.
	F	Cb	Cb	Neutral to positive slope after 1.1 μm.
	G	Cg	Cg	Positive slope after 1.3 μm, drop off below 0.6 μm.
		Cgh	Cgh	Similar to Cg but with a 0.7 μm absorption feature
		Ch	Ch	Positive slope after 1.1 μm, 0.7 μm absorption feature.
X-complex	E	X	X	Featureless with medium to high positive slope.
	M	Xc	Xc	Featureless with medium positive slope but with slight concave curve.
	P	Xe	Xe	Similar to Xc but with a absorption feature near 0.55 μm.
		Xk	Xk	Similar to Xc but with a subtle feature between 0.8 - 1.0 μm.
Others	T	T	T	Featureless with medium to high positive slope and slight concave curve.
	D	D	D	Featureless with very high positive slope.
	O	O	O	Rounded and deep bowl shaped 1 μm feature and strong feature at 2 μm.
	R	R	R	Strong features at 1 and 2 μm.
	V	V	V	Strong and narrow feature near 1 μm and strong feature at 2 μm.
	A	A	A	Deep, broad feature at 1 μm followed by strong positive slope. Possible 2 μm feature.
		Q	Q	Strong feature at 1 μm, possible features at 1.3 μm and 2 μm.
		K	K	Wide, angular feature near 1 μm.
		L	L	Steep slope in the visible, followed by concave curve. Possible 2 μm feature.

Table 1.1: *The different asteroid taxonomies developed by Tholen (1984); Bus (1999), Bus and Binzel (2002b,a); and DeMeo et al. (2009). Also included is a description of the spectra in the Bus-DeMeo taxonomy.*

1.2.1 Asteroid populations

The main asteroid belt is concentrated between Mars and Jupiter and is separated into 'inner', 'middle' and 'outer' regions, carved out by the v6 secular resonance with Saturn near 2 AU, and the 3:1 and 5:2 mean-motion resonances with Jupiter near 2.50 and 2.82 AU, respectively (e.g. DeMeo et al., 2015a). There are additional populations of asteroids further inwards and outwards of the orbit of the main asteroid belt, and details of each are summarised below. Asteroids can be arranged into asteroid families, which are groups of bodies thought to be remnants of a collisional event on a larger single parent body.

- *Near-Earth objects (NEOs):* This sparse population of asteroids have perihelia <1.3 AU and short lifespans of a few Ma before impacting the Sun, impacting a terrestrial

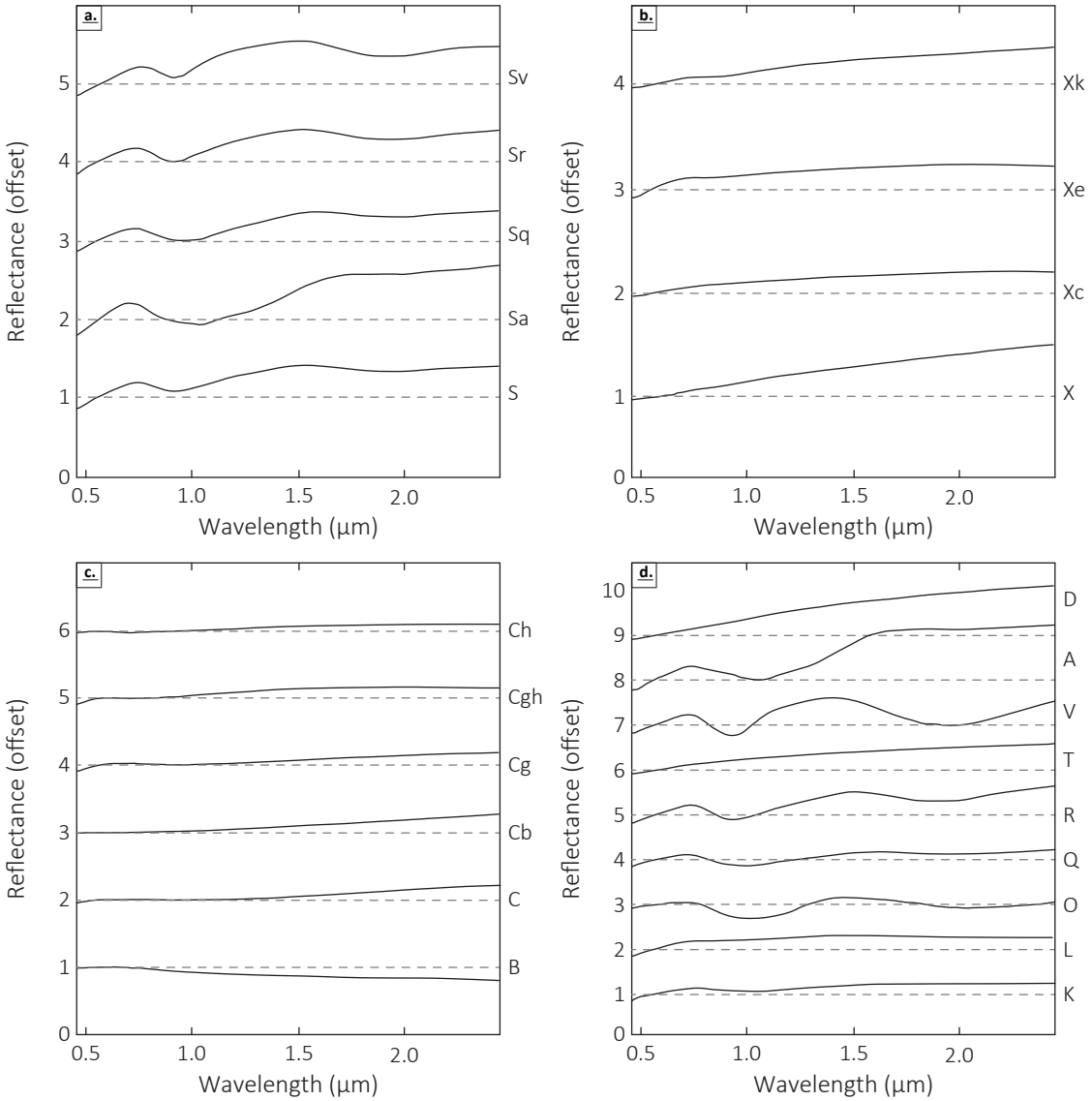


Figure 1.2: *Average spectra from each taxonomic class from the (a) S-complex, (b) X-complex, (c) C-complex and (d) others in the Bus-DeMeo classification. Data for this figure are from the Bus-DeMeo Taxonomy Classification Web tool by Stephen M. Slivan, developed at MIT with the support of the National Science Foundation.*

planet, or being ejected from the Solar System (Morbidelli et al., 2002). All taxonomic classes are found among NEOs, with more than half of the asteroids classified as S-complex, 15 % as C-complex, and 10 % as X-complex (Binzel et al., 2019, Popescu et al., 2019).

- *Hungaria region:* Between 1.8 - 2.0 AU there is a population of asteroids dominated

by E-types (in the Tholen classification). It has been suggested the E-type asteroids in this region are part of a collisional family with 434 Hungaria being the largest member (Warner et al., 2009).

- *Inner main belt:* The inner asteroid belt is located between 2.0 - 2.5 AU, and contains 4 Vesta, a 263 km diameter V-type asteroid (Russell et al. 2012). There are also large numbers of S-complex asteroids and C-complex asteroids, the latter particularly abundant at smaller diameters <20 km (DeMeo et al., 2015a). A few <30 km D-type asteroids have also been observed (DeMeo et al., 2014).

- *Middle main belt:* The middle main asteroid belt is between 2.50 - 2.82 AU. The C-type dwarf planet 1 Ceres and the B-type asteroid 2 Pallas are located in this population and make up 31 % and 7 % of the total mass of the entire asteroid belt, respectively (DeMeo et al., 2015a). The distribution of taxonomic types is similar to the inner asteroid belt, however there are more X-complex asteroids (marked as Tholen P- and M-types in Figure 1.3) in the <100 km diameter asteroid population (DeMeo and Carry, 2014).

- *Outer main belt:* The outer main asteroid belt is between 2.83 and 3.30 AU. The largest asteroid is the C-type 10 Hygeia, and it is the C- and X-complex asteroids that dominate the classification in this region (DeMeo and Carry, 2014, DeMeo et al., 2015a). S-complex asteroids make up a smaller fraction of the total mass, however the outer region of the main belt is the most massive of the three populations, so the absolute mass of S-complex asteroids is still significant (DeMeo and Carry, 2014, DeMeo et al., 2015a).

- *Cybele region:* Between 3.3 - 3.7 AU is a group of asteroids named for their largest member, P/Xc/Xk-type 65 Cybele. This population is dominated by D-type, C- and X-complex asteroids (Gil-Hutton and Licandro, 2010, DeMeo and Carry, 2014, De Prá et al., 2018).

- *Hilda region:* Between approximately 3.7 - 4.5 AU, the Hilda population (named for P-/X-type 153 Hilda) is dominated by D-type, X- and C-complex asteroids (DeMeo and Carry, 2014, De Prá et al., 2018).

- *Jupiter Trojans:* Located in stable Lagrange points in the orbit of Jupiter at 5.2 AU there is a significant population of D-type and X-complex asteroids, with a few C-complex bodies (DeMeo et al., 2015a). There are two 'swarms' of asteroids, leading and trailing Jupiter (Emery et al., 2015).

Figure 1.3 shows the distribution of taxonomic types in the Tholen classification for the different regions, excluding the near-Earth population. The S-complex asteroids are the most common classification in the NEOs, Hungaria region and inner main belt. In contrast, the C- and X-complex asteroids are the most common classifications in the outer main belt, the Cybele and Hilda regions and the Jupiter Trojans. Based on this distribution of taxonomic classes, it is hypothesised that the S-complex asteroids represent inner Solar System planetesimals and C- and X-complex asteroids represent outer Solar System planetesimals and so sample different regions of the protoplanetary disk (DeMeo and Carry, 2014). The presence of some S-complex asteroids in the outer populations and some C- and X-complex asteroids in the inner populations is due to the mixing of planetesimals by periods of orbital migration (section 1.1.3, Walsh et al., 2012). This conclusion is supported by the dominant mineralogy suggested by the visible and near-infrared (VNIR) spectra of the different asteroid classes. For example, the 1 and 2 μm absorption features in S-complex spectra

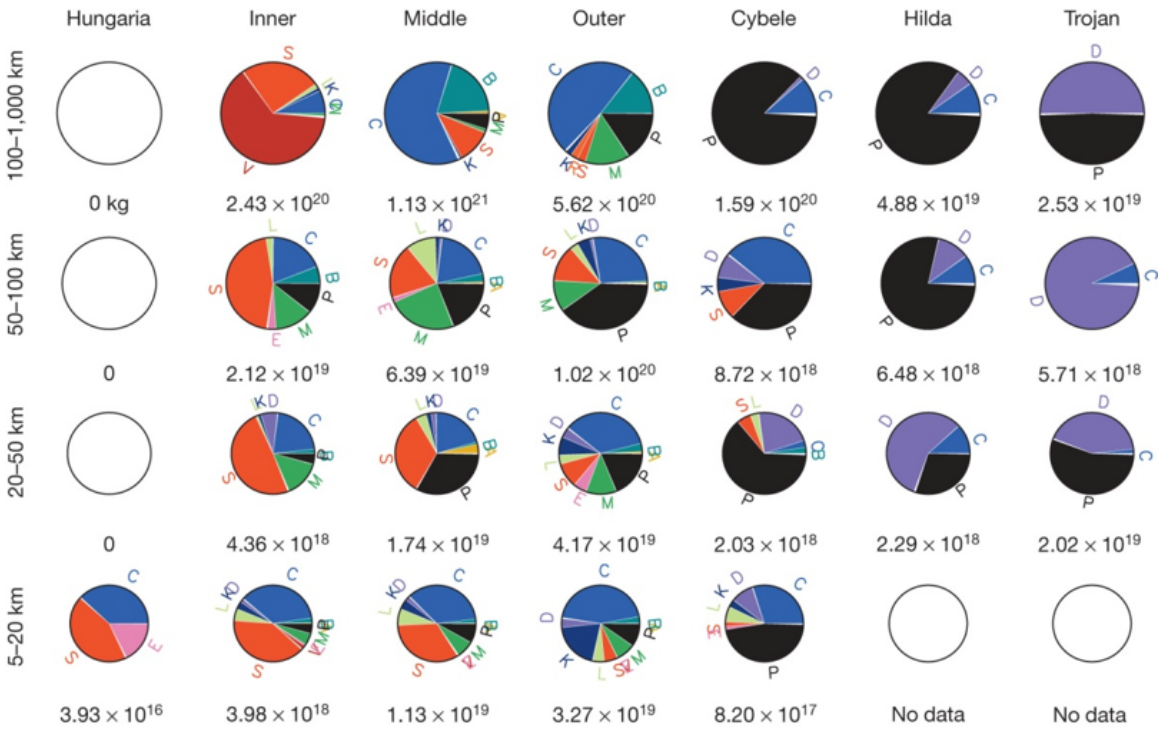


Figure 1.3: *A diagram from DeMeo and Carry (2014) showing the compositional mass distribution throughout the main asteroid belt out to the Trojans. The total mass of the Hilda and Trojan populations are underestimated due to discovery incompleteness. The diagram shows the C-complex, X-complex and D-type asteroids increase in frequency in the outer Solar System populations.*

are consistent with anhydrous silicates such as olivine and pyroxene, implying these bodies accreted dry and within the snow-line (Gaffey et al., 2006). Additionally, the 0.7 µm features seen in Cg- and Cgh-types are probably due to Fe^{2+} to Fe^{3+} charge transfer in Fe-rich hydrated silicates (phyllosilicates, e.g. Vilas and Gaffey, 1989), and the flat, relatively featureless spectra in the C-complex, some X-complex and the T- and D-type asteroids suggest the presence of organics and opaque minerals such as magnetite and sulfide (Cloutis et al., 2011a,b). Phyllosilicates, organics and opaque mineral assemblages can be the result of aqueous alteration, implying these bodies formed outside the snowline, accreting water ice which then melted and reacted with the original rock (Grimm and Mcsween, 1989, Morbidelli et al., 2015).

Investigating the C- and X-complex asteroids, as well as T- and D-type asteroids can there-

fore provide an insight into the processing occurring on and within planetesimals which appear to have been aqueously altered during the early evolution of the Solar System. This is of particular interest because these bodies were scattered into the inner Solar System during periods of orbital migration and may have impacted the early Earth, delivering water, organics and other volatiles (Alexander et al., 2012, Alexander, 2017).

1.2.2 Missions to volatile-rich asteroids

Volatile-rich C- and X-complex asteroids are and have been the focus of several space missions. NASA's Dawn mission was the first to comprehensively investigate a C-type body, orbiting the dwarf planet 1 Ceres in the middle main belt for just over three years (e.g. Russell and Raymond, 2011). The results from Dawn indicated that Ceres is a differentiated body with an average bulk density of 2162 kg/m^3, which implies a significant water content (Konopliv et al., 2018, McCord and Zambon, 2019). The presence of bright patches (faculae) in craters have been associated with subsurface water: they are made of mostly Na_2CO_3, which is consistent with the residue expected from the interaction of fluids with the phyllosilicate mineralogy on the surface of Ceres (Carrozzo et al., 2018).

There are two sample return missions to volatile-rich asteroids. JAXA's Hayabusa2 visited the ~900 m diameter NEO Cg-type asteroid 162173 Ryugu (Tsuda et al., 2013, Tachibana et al., 2014), arriving in June 2018 and leaving in November 2019. Hayabusa2 was equipped with four small rovers: the Mirco-Nano Experimental Robot Vehicle for Asteroid II 1 (MINERVA-II-1) contained Rover-1A (HIBOU) and Rover-1B (OWL), MINERVA-II-2 contained Rover-2 and the Mobile Asteroid Surface Scout (MASCOT). Rover-1A and Rover-1B both successfully delivered detailed images and videos of the surface of Ryugu (Tsuda et al., 2020), and MASCOT was able to collect information about the surface structure, composition, thermal and magnetic properties (Grott et al., 2019). MINERVA-II-2 failed before deployment but was still

able to collect gravitational measurements of Ryugu. Data showed that Ryugu was a rubble-pile asteroid composed of phyllosilicate minerals, however there is some evidence that the surface of Ryugu has experienced some dehydration (Kitazato et al., 2019). Hayabusa2 successfully performed two sample collections from the surface of Ryugu, the first recovered surface material and the second was preceded by the Small Carry-on Impactor (SCI) which excavated a small crater so subsurface material could be collected (Morota et al., 2020). Hayabusa2 returned the sample capsule to Earth on the 6th December 2020. Following collection of the capsule from where it landed in the Woomera region in Northern Australia, ~5.4 g of Ryugu material was found to have been collected and the mission was declared a success.

NASA's Origins, Spectral Interpretation, Resource Identification, Security Regolith Explorer (OSIRIS-REx, Lauretta et al. (2017)) is currently in orbit around the ~500 m diameter NEO B-type asteroid 101955 Bennu. It arrived in December 2018 to find a rubble-pile body covered in boulders and composed of phyllosilicate minerals (DellaGiustina et al., 2019, Hamilton et al., 2019). A rubble-pile asteroid is formed when a parent planetesimal is disrupted during a collisional event, and the resulting material is re-accumulated into a 'rubble-pile' (Walsh, 2018, and references therin). The aqueous alteration which formed the phyllosilicate mineralogy observed on the surface may have happened on the original parent body before disruption and reaccumulation into Bennu (Michel et al., 2020). In October 2020, the OSIRIS-REx spacecraft descended to the surface of the asteroid and collected a sample. Images taken of the collection container show that over 400 g of material was collected, enough that some material was observed to be escaping the container before it was stored in the return capsule. OSIRIS-REx will leave Bennu in March 2021 and return to Earth in September 2023. The returned sample will have geological context following detailed analysis of the sampling site.

Future missions to volatile-rich asteroids include NASA's Lucy mission, which will launch in 2021. It aims to perform a flyby of one main belt asteroid and five Jupiter Trojans (Levison, 2016). These asteroids are classified as C-, D- or P-type asteroids, and Lucy aims to evaluate whether the Trojans are hydrous or so primitive they did not experience aqueous alteration (Tholen, 1984). Another mission of interest is JAXA's Demonstration and Experiment of Space Technology for Interplanetary voYage, Phaethon fLyby and dUst Science (DESTINY+, Arai et al. (2018)) which will perform a flyby of the F/B-type asteroid 3200 Phaethon, which is an active asteroid and is source of the Geminid meteor shower (Jewitt and Li, 2010, Jewitt et al., 2013). DESTINY+ will launch in 2022. Of additional interest the M-/X- type asteroid 16 Psyche will be visited by the NASA mission Psyche, which is scheduled to launch in 2022 (Elkins-Tanton et al., 2014). Finally, JAXA's Martian Moons Exploration (MMX) mission which will be launching in 2024 and aims to return a sample from the largest Martian moon Phobos (Kuramoto et al., 2018), which has been suggested to be a captured D-type asteroid (Murchie et al., 1999, Pajola et al., 2013).

The space missions should tell us about the composition and evolution of several volatile-rich asteroids; however, it is important to link those observations back to the meteorite population we have on Earth. Meteorites are rocky objects which come from extraterrestrial sources, the vast majority of them coming from asteroids. Their compositions are direct results of their alteration histories on their parent bodies, and so they offer an opportunity to investigate asteroids without spacecraft: 'natural sample return'. Tentative links have been made between asteroid types and meteorite groups (which will be expanded on in section 1.4), although this is challenging.

1.3 Meteorites

Meteorites are classified based on their petrology, chemistry and isotopic variations (e.g. Weisberg et al., 2006). The current meteorite classification scheme is shown in Figure 1.4. Broadly they are classified into chondrites and achondrites. Achondrite meteorites are grouped into irons, stony-irons and stones, which originate from bodies which underwent melting and differentiation (ie. they have been significantly processed). Some achondrites can be tied to specific parent bodies: lunar meteorites are from the Moon (e.g. Korotev, 2005); shergottites, nakhlites and chassignites are from Mars (Smith et al. 1984); and howardites, eucrites and diogenites are from the V-type asteroid 4 Vesta (McSween et al., 2013). Primitive achondrites are slightly different in that they represent melted or partially melted material from local heating events but retain a similar chemical composition to chondrites (Weisberg et al., 2006).

1.3.1 Chondrite meteorites

In contrast to achondrites, chondrites come from smaller bodies and have therefore experienced less processing, so are some of the most primitive extraterrestrial material available to study. Their parent bodies are representative of the smaller planetesimals that were the building blocks of the larger planetary embryos and planets, and so studying them gives an insight into the processes and evolution of planet formation. The main components of chondrites are chondrules, CAIs, metal and matrix material (e.g. Hutchison, 2004, Russell, 2007). Chondrites are grouped into ordinary, enstatite, and carbonaceous chondrites, based on their primary characteristics, such as mineralogy, texture, chemical and isotopic compositions. Most chondrites have also experienced some degree of thermal or aqueous alteration and are therefore assigned a petrologic type (Van Schmus and Wood, 1967,

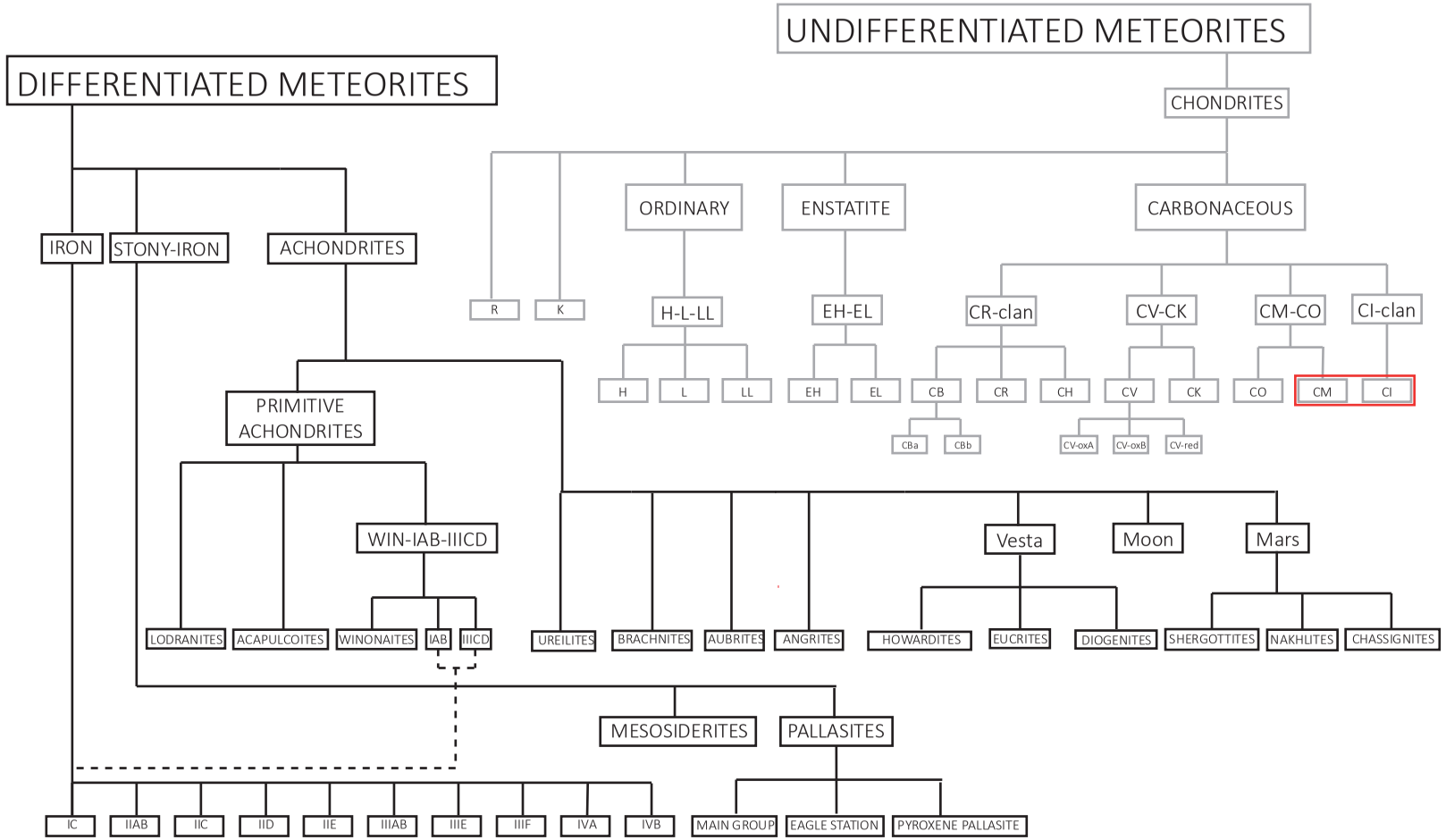


Figure 1.4: *The current meteorite classification system, adapted from Weisberg et al. (2006). The meteorite groups studied are highlighted in red.*

Fig. 1.5,). Petrologic type 3 represents 'pristine' material that has experienced minimal alteration. Types 2 to 1 indicate increasing amounts of aqueous alteration and types 4 to 6 indicate increasing thermal alteration. Most chondrites are breccias (fragments of rock embedded in a matrix) and record impacts. They can therefore be assigned a shock stage (S1 - S6) with increasing shock experienced.

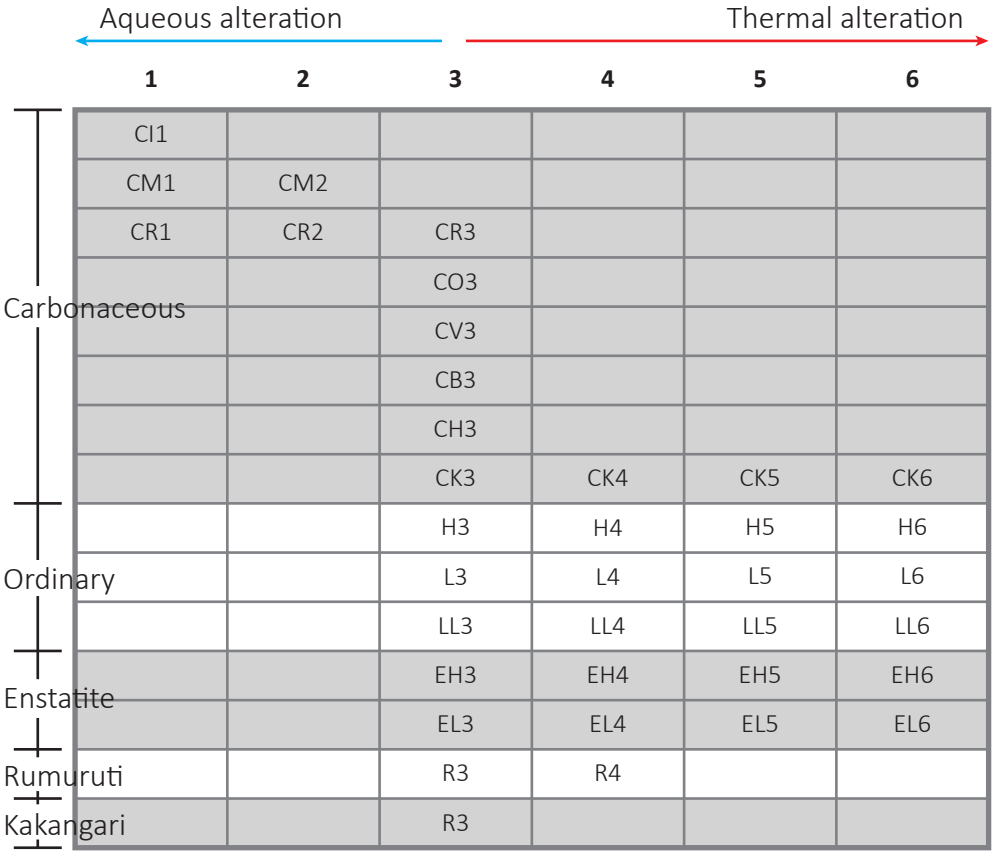


Figure 1.5: *The petrologic types for each chondrite group. Adapted from Weisberg et al. (2006).*

Ordinary chondrites represent > 85 % of all meteorite falls and are subdivided into H, L and LL types, based on the abundance and composition of Fe (Weisberg et al., 2006). They have ~10 - 15 vol% matrix and a high abundance (60 - 80 vol%) of millimetre-sized chondrules (Weisberg et al., 2006). Ordinary chondrites span the petrologic range from type 3 to type 6. Enstatite chondrites formed under very reducing conditions and contain significant enstatite ($MgSiO_3$), and only minor olivine. They are subdivided into EH and EL types, with

EH enstatite chondrites being more reduced than EL (e.g. Sears et al., 1982). They show oxygen isotopic compositions similar to that determined for the Earth-Moon system, and it has been suggested that their parent bodies may be representative of the building blocks of our planet (Javoy, 1995, Javoy et al., 2010). Enstatite chondrites also span the petrologic range from type 3 to type 6. Rumuruti (R) chondrites have similar oxygen isotopic compositions to ordinary chondrites but they have ~50 vol% matrix, are highly oxidised and have negligible metal. Kakangari (K) chondrites have 70 - 77 vol% matrix largely composed of enstatite, and 6 - 9 vol% metal (Hutchison, 2004, Weisberg et al., 2006).

Carbonaceous chondrites are rich in volatile elements and excluding hydrogen, lithium and noble gas abundances, have compositions similar to the solar photosphere (Hutchison, 2004). They are further divided into subgroups which show a wide range of chondrule sizes and compositions, matrix abundances, and petrologic types. Some carbonaceous chondrites have been aqueously altered (CM, CI, CR, Figure 1.5), suggesting they come from volatile-rich asteroids.

1.3.2 Aqueously altered carbonaceous chondrites

Carbonaceous chondrites are subdivided into eight groups based on their water, sulfur and carbon content, isotopic ratios, chondrule and metal composition, chondrule, CAI and matrix abundances and oxygen isotopic composition (Figure 1.6). Of the carbonaceous chondrites, the CK chondrites (named for the type meteorite Karoonda) are thermally altered and have petrologic types 3 to 6. The CO (named for Ornans), CV (Vigarano), CB (Bencubbin) and CH (named due to their high metal abundance) chondrites are all petrologic type 3: they have neither been significantly heated nor aqueously altered. The CI (Ivuna), CM (Mighei) and CR (Renazzo) chondrites have petrologic types of 1 to 3: they have been aqueously altered and are hypothesised to originate from volatile-rich asteroids.

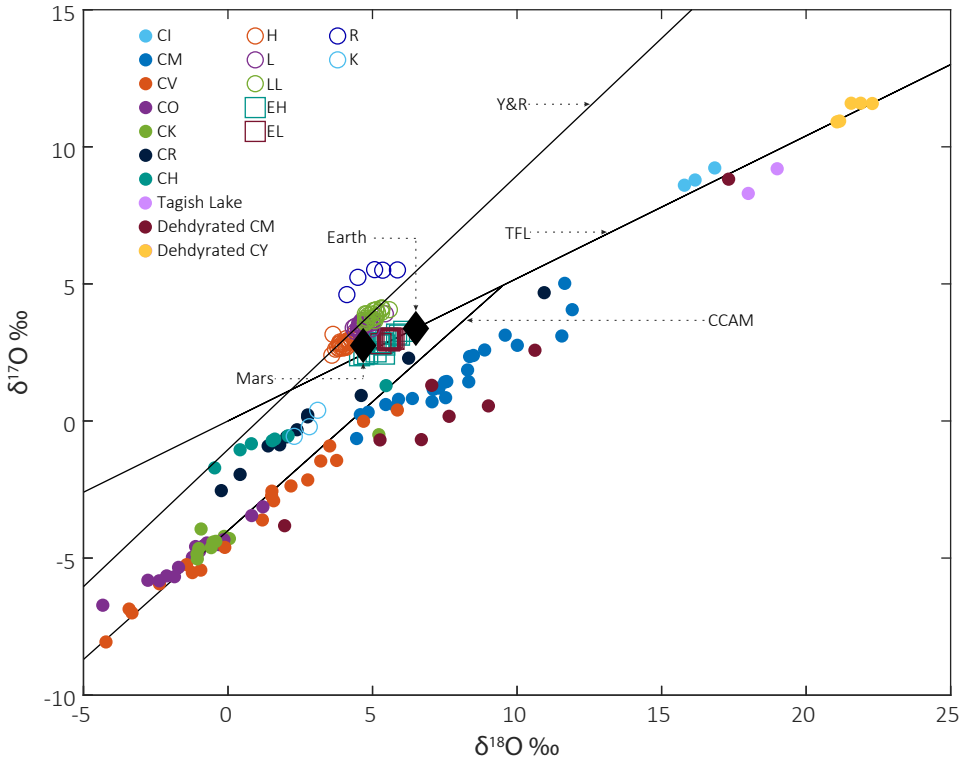


Figure 1.6: *The oxygen isotopic compositions for the ordinary, enstatite and carbonaceous chondrite groups. Also included are values for the C2-ung Tagish Lake, which has affinities to D-type asteroids (section 1.4.3) and dehydrated CM and CY chondrites, which will be discussed further in section 1.3.3. Carbonaceous chondrites plot below the terrestrial fractionation line (TFL) and the CV chondrites define the carbonaceous chondrite anhydrous mixing line (CCAM). Also included is the Young and Russell line (Y&R, Young and Russell, 1998). Data are from Clayton et al. (1984, 1991), Weisberg et al. (1991), Bischoff et al. (1994), Schulze et al. (1994), Weisberg et al. (1996), Clayton and Mayeda (1999), Franchi et al. (1999), Tonui et al. (2014).*

If we assume the aqueously altered meteorites come from the volatile-rich C-complex asteroids, we can use these meteorites to determine whether these asteroids may have had a role in the delivery of organics, water and other volatiles to the early Earth. Figure 1.7 shows the CM and CI chondrites best reproduce the Earth's bulk H and N isotopic composition, implying the parent bodies of these meteorites are more likely to have delivered water to Earth than cometary material. The volatile budget of the Earth can be achieved by addition of 2 - 4 wt% CM/CI-like material to a volatile depleted early Earth (Marty, 2012, Alexander, 2017). The CM and CI chondrites can therefore be used to understand more

about the alteration histories of volatile-rich asteroids which may have had a role in volatile delivery to the terrestrial planets.

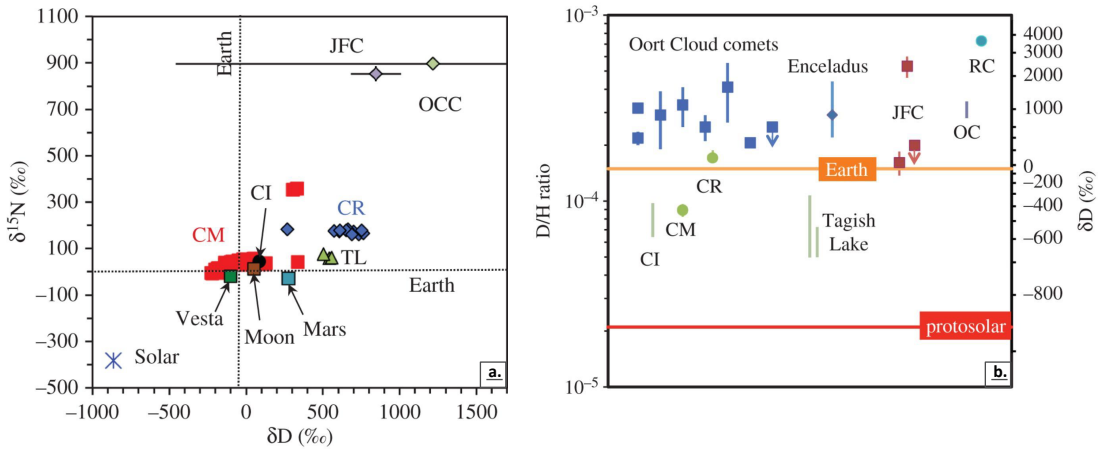


Figure 1.7: *From Alexander (2017), (a) shows a comparison of the bulk H and N isotopic compositions of some inner Solar System bodies with Jupiter family (JFC) and Oort Cloud comets (OCC) and with several carbonaceous chondrite groups. (b) shows the estimated H isotopic compositions of water in chondrites, OCC, JFC and Enceladus (a moon of Saturn), relative to H isotopic composition of water on Earth. Carbonaceous chondrites are intermediate between Earth and protosolar values which is distinct from most cometary values.*

CI CHONDRITES

CI (named for the type specimen Ivuna) carbonaceous chondrites consist of only five meteorite falls (three other Antarctic meteorites, Yamato (Y) 82162, Y 980115 and Y 86029, are classified as CIs in the Meteoritical Bulletin but have recently been suggested to instead be part of a separate group, the CYs, that will be discussed elsewhere), and are all classified as petrologic type 1. CI chondrites have oxygen isotopic compositions of $\delta^{18}O$ ~16 and $\delta^{17}O$ ~9 (Figure 1.6, Clayton and Mayeda (1999)). This heavy oxygen composition likely results from intense aqueous alteration of ^{16}O-rich anhydrous silicates by ^{16}O-poor fluids (Clayton and Mayeda, 1999, Fujiya, 2018). The CI oxygen isotopic composition therefore implies they accreted ^{16}O-poor and then were heavily aqueously altered.

Petrographic observations show CI chondrites are composed almost entirely of matrix. They contain >80 vol% phyllosilicate and lack any obvious chondrules or CAIs (Tomeoka and Buseck, 1988, Zolensky et al., 1993, Endress and Bischoff, 1996, Bullock et al., 2005, Morlok et al., 2006, King et al., 2020). This may be a result of chondrules and CAIs not being accreted into the CI parent body, however partially altered CAIs and fully altered microchondrules have been observed in petrographic studies (Frank et al., 2011, Zolensky and Frank, 2014). The CI chondrite matrix is composed of fine-grained (<1 μm) intergrown Fe-Mg serpentine and saponite phyllosilicates, with carbonates (dolomite and calcite), sulfates (although Gounelle and Zolensky (2001) suggest most sulfates in the CI chondrites are a result of terrestrial contamination), sulfides (including troilite, pyrrhotite and pentlandite), and oxides (magnetite, maghemite and ferrihydrite) (Tomeoka and Buseck, 1988, Tomeoka, 1990, Endress and Bischoff, 1996, Bullock et al., 2005, King et al., 2015a,b, 2020). Organic materials are also found in CI chondrites, including amino acids, aliphatic hydrocarbons and aromatic hydrocarbons. CI chondrites have a carbon content of ~3 wt% (Botta and Bada, 2002, Garvie and Buseck, 2005). The CI mineralogy and composition was obtained through aqueous alteration by melted water ice on the CI parent body asteroid at high water/rock ratios (>5) and temperatures of ~150 ^{o}C (Zolensky et al., 1993, Clayton and Mayeda, 1999, Brearley, 2006). CI chondrites show bulk elemental ratios which match the solar photosphere (disregarding Li and the most volatile elements) and are therefore considered the most primitive meteorite group (e.g. Lodders, 2003, Barrat et al., 2012).

CM CHONDRITES

CM (named for the type specimen Mighei) chondrites are the most abundant carbonaceous chondrite group (currently numbering at 648 in the Meteoritical Bulletin) and cover the petrologic range from type 2 to type 1 (Zolensky et al., 1997, Rubin et al., 2007, Howard

et al., 2009, 2011, 2015, King et al., 2017b). CM chondrites are composed mostly of matrix material (60- 90 vol%); however, they contain partially altered chondrules, chondrule fragments and CAIs which have not been fully aqueously altered (Fuchs et al., 1973, Browning et al., 1996). CM chondrites contain 70- 90 vol% serpentine-group phyllosilicates, which have compositions between the Fe-rich and Mg-rich endmembers depending on the extent of aqueous alteration (Tomeoka and Buseck, 1985, Zolensky et al., 1997, King et al., 2017b). Primary, anhdyrous silicates (olivine and pyroxene), tochilinite (a hydroxysulfide often used as a diagnostic for CM chondrites), carbonates (mainly calcite and dolomite), sulfides (pyrrhotite, troilite and pentlandite), oxides (magnetite) and sulfates are also found in CM chondrites (Brearley, 2006, Howard et al., 2009, 2011, 2015, King et al., 2017b). They have a carbon content of ~2 wt% and contain organic molecules; amino acids, hydrocarbons and carboxylic acids (Botta and Bada, 2002).

CM chondrites were aqueously altered on their parent bodies at temperatures of 0-150 ^{o}C and water rock/ratios of 0.3 - 0.8 (DuFresne and Anders, 1962, Zolensky et al., 1989, 1993, Hutchison, 2004, Brearley, 2006, Vacher et al., 2019, Verdier-Paoletti et al., 2019). CM chondrites show a genetic relationship to the CO (Ornans-type) carbonaceous chondrites, and it has been suggested the two groups are in fact part of the same family and CMs are aqueously altered COs (Clayton and Mayeda, 1999, Greenwood and Franchi, 2004, Greenwood et al., 2014).

Aqueous alteration scales

The petrologic scale developed by Van Schmus and Wood (1967) and shown in Figure 1.5 is relatively coarse. Following observations of more subtle variations of aqueous alteration extent in CI and CM chondrites, several higher resolution classification schemes were developed. Browning et al. (1996) proposed the mineralogic alteration index (MAI) to track

aqueous alteration. The MAI is based on three parameters: the alteration of more Mg-rich anhydrous silicates as aqueous alteration proceeds, making the altering fluids more Mg-rich and resulting in more Mg-rich serpentines being produced; the volume percent of isolated anhydrous silicates in the matrix, which decreases with progressive alteration; and the proportion of altered phases within chondrules, which increases with progressive alteration. However, the MAI has been found to correlate with the year the meteorite fell, thus is suggested to be affected by terrestrial contamination (Benedix and Bland, 2004, Bland et al., 2006). As a result it is not widely used.

Rubin et al. (2007) assigned petrologic types for CM chondrites between unaltered types 3.0 to fully altered types 2.0, based on qualitative petrologic observations such as the formation of phyllosilicates, alteration of chondrules, oxidation of metal, changes in tochilinite mineralogy and changes in carbonate mineralogy; and quantitative measurements such as sulfide and tochilinite-cronstedtite-intergrowth (TCI) compositions. Alexander et al. (2013) developed a scale based on bulk H abundances which can be applied to CI, CM and CR chondrites. They determined that bulk H and C isotopes can be used to establish wt% of H in water and -OH, which indicates the degree of alteration of a meteorite. The degree of alteration determined using H and C isotopes was found to correlate well with petrologic estimation of hydration. The scale varies between the least altered type 3 chondrites and the most altered type 1s.

The phyllosilicate fraction (PSF) petrologic scale from Howard et al. (2009, 2011, 2015) is based on the modal mineralogy and can be used for any meteorite group. They determined a negative correlation between abundances of anhydrous silicates and total phyllosilicate abundance and so used the phyllosilicate fraction to define a new petrologic scale. PSF is calculated as the volume of phyllosilicates divided by the total volume of phyllosilicates and anhydrous silicates. The PSF is converted to a petrologic type on a linear scale where

each subtype represents a 5 vol% increment in total phyllosilicate abundance. Phyllosilicate fractions of <0.05 are defined as type 3.0, and a fraction of >0.95 gives a petrologic type of 1.0.

1.3.3 Aqueously and thermally altered carbonaceous chondrites

In addition to aqueous alteration, several aqueously and thermally altered carbonaceous chondrites have been identified. The discovery of these meteorites indicates that processing of volatile-rich asteroids was not limited to just aqueous or thermal alteration but was a more complex interaction of both. The initial meteorites identified as such were Belgica (B) 7904, Y 793321, Y 86720 and Y 82162 (Skirius et al., 1986, Akai, 1984, 1988, Tomeoka et al., 1989b,a, Ikeda, 1992), and many others have since been identified through petrological, chemical, spectroscopic, isotopic and mineralogical analyses (Akai, 1988, 1992, Tomeoka et al., 1989b,a, Matsuoka et al., 1996, Akai and Tari, 1997, Wang and Lipschutz, 1998, Clayton and Mayeda, 1999, Tonui et al., 2001, 2002, 2003, 2014, Nakamura, 2005, 2006, Nakato et al., 2008, Choe et al., 2010, Ivanova et al., 2010, King et al., 2015a,b, Mahan et al., 2018). Most of these identified meteorites are considered to be dehydrated CM chondrites, based on original textures which have survived thermal alteration and can be identified in petrographic analyses, isotopic and elemental compositions (Nakamura, 2005, Tonui et al., 2014), and comparisons to experimentally heated CM chondrites (Nakato et al. 2008). The available oxygen isotopic ratios of CMs that have been identified as thermally altered are shown in Figure 1.6, which shows they have similar compositions to CM chondrites, but can extend up to the heavier CI chondrites (Clayton and Mayeda, 1999, Nakato et al., 2013). This believed to be due to the preferential loss of light oxygen during thermal alteration (Clayton and Mayeda, 1999). Nakamura (2005) developed a heating scale for aqueous and thermally altered CM and CI carbonaceous chondrites, from stage I to stage IV, using XRD, scanning

electron microscope (SEM) and transmission electron microscope (TEM) analyses of mineralogy and texture. This is described below.

- Stage I (very weakly heated, <300 ^{o}C): No mineralogical changes; phyllosilicates, and tochilinite still identifiable in XRD patterns. In TEM observations, the initial decomposition of some Fe-rich phyllosilicate phases into an amorphous structure is observed (Akai and Tari, 1997, Nakato et al., 2009). All thermally altered samples may contain anhydrous, primary phases which were not aqueously altered. These are identifiable by sharp peaks in XRD indicative of highly crystalline phases.

- Stage II (weakly heated, 300 - 500 ^{o}C): At these temperatures Fe-rich phyllosilicates will have fully decomposed, however some crystalline Mg-rich phyllosilicates may still be present (King et al., 2015a). The phyllosilicates that have decomposed are present as a highly disordered phase which has been observed as patchy and platy crystals uncharacteristic of phyllosilicates in TEM studies (Akai, 1988, Tonui et al., 2014). These phases do not produce coherent diffraction and so are difficult to observe in XRD patterns (Nakamura, 2005). There is no regrowth of any secondary phases. Some troilite and metal might be present, as they are the decomposition products of tochilinite. Pyrrhotite begins to break down between 400 and 600 ^{o}C (Burgess et al., 1991, Nakato et al., 2008).

- Stage III (moderately heated, 500 - 750 ^{o}C): Mg and Fe-rich phyllosilicates are present as a disordered phase, and Fe-rich olivine begins to re-crystallise from this disordered material. The XRD peaks of this secondary olivine are broad, indicating low crystallinity. Pentlandite decomposes at 610 ^{o}C, and so along with pyrrhotite, is largely absent in meteorites heated to mid-stage III. Metal (kamacite and taenite) starts to re-crystallise from decomposed sulfides (Nakato et al., 2008).

- Stage IV (strongly heated, >750 ^{o}C): At these temperatures, samples are almost completely dehydrated, and contain broad, low crystalline secondary olivine and pyroxene, troilite and metal. Some minor disordered phyllosilicate material may still be present.

CY CHONDRITES

B 7904 and Y 86720 were initially described as stage IV thermally altered CI chondrites, and Y 82162 as a stage III CI chondrite (Clayton and Mayeda, 1999, Tomeoka et al., 1989b,a, Tomeoka and Kazushige, 1990). However, Ikeda (1992) reported that these meteorites have mineralogy, textures and elemental compositions intermediate between CM and CI chondrites, which was expanded on by King et al. (2019), who showed their pre-metamorphosed mineralogy was distinct from both CI and CM chondrites. These three chondrites, along with Y 86789 (which is likely paired with Y 86720, Matsuoka et al. (1996)), Y 86029 and Y 980115 are therefore suggested to be part of a separate group from the CI and CM chondrites called the CY chondrites.

The CY chondrites show oxygen isotopic compositions of δ^{17}O ~12 ‰ and δ^{18}O ~22 ‰, which are heavier than those found even in the CI chondrites (Figure 1.6). This is a result of a high degree of aqueous alteration, followed by thermal alteration (Clayton and Mayeda, 1999). All CYs have been thermally altered, with Y 86029, Y 82162 and Y 980115 to 500 - 750 ^{o}C (stage III), and Y 86720, Y 86789 and B 7904 to >750 ^{o}C (stage IV). All show high sulfide abundances (~10 - 30 vol%), suggesting a high availability of sulfur on the CY parent body, and also contain periclase, a magnesium oxide thought to have formed via thermal decomposition of Mg and Fe-rich carbonates (Tonui et al., 2014, King et al., 2019). The CYs are therefore classified as their own meteorite group that is likely from a different parent body than the CM and CI chondrites.

1.4 Linking meteorites and asteroids: Spectroscopy

1.4.1 Visible and near-infrared (VNIR)

Tentative links between asteroid classes and meteorite groups have been made based on comparisons between spectra collected remotely from telescopes or spacecraft and laboratory spectra of meteorites collected over similar wavelength ranges. The associations that have been made are listed in Table 1.2, which shows the meteorite groups that have been suggested for each asteroid type. The contrasting meteorite types for a particular asteroid classification highlight how challenging this exercise can be.

Diagnostic absorption features in the VNIR (approximately 0.4 - 5 μm) region include those near 0.4 μm due to iron oxides (Vilas et al., 1993), near 0.6 and 0.9 μm consistent with a combination of phyllosilicates and iron oxides (Vilas et al., 1994, Vilas, 1994), near 1 and 2 μm due to anhydrous silicates (Gaffey et al., 1993), near 2.3 μm due to Mg-OH in Mg-rich phyllosilicates (Cloutis et al., 2012), and near 3.4 μm due to organic material (Clark et al., 2009). Two of the more commonly identified features, particularly in hydrated asteroids and meteorites, occur near 0.7 and 3 μm. The 0.7 μm charge transfer feature is used in taxonomy and gives an indication of phyllosilicate composition (Vilas and Gaffey, 1989). Near 3 μm, water and hydroxyl have strong absorption features. For the hydroxyl feature the position is sensitive to the cation the -OH is bonded to. The 3 μm feature is correlated with the degree of hydration in meteorites (Rivkin, 2002, Beck et al., 2010, Takir and Emery, 2012). Spectral slope in the VNIR range is also a useful parameter, and in hydrated meteorites has been tied to phyllosilicate abundance. It is also influenced by the presence of opaques (Cloutis et al., 2011a,b, McAdam et al., 2015).

Taxonomy	Tholen	Bus	Bus-DeMeo	
Wavelength range (μm)	0.337 - 1.041	0.435 - 0.925	0.435 - 2.45	Meteorite links
S-complex	S	S	S	H (Gafffey and Gilbert 1998, Bottke et al. 2010), L (Bottke et al. 2005, Nesvorny et al. 2009), LL (Vernazza et al. 2008, Nakamura et al. 2011, Reddy et al. 2014)
		Sa	Sa	
		Sq	Sq	LL (Binzel et al. 2009)
		Sr	Sr	
		Sk		
		Sl		
			Sv	
C-complex	B	B	B	CM, CI thermally altered CM, thermally altered CY (Clark et al. 2010)
	C	C	C	CM, CI (Ostrowski et al. 2011), CH (Burbine et al. 2002)
	F			Thermally altered CY (Hiroi et al. 1993), Ureilite (Jenniskens et al. 2009)
	G			Thermally altered CY (Hiroi et al. 1993)
		Cb	Cb	
		Cg	Cg	
		Cgh	Cgh	CM (Vernazza et al. 2016), CI, CK (Ostrowski et al. 2011)
		Ch	Ch	CM (Fornasier et al. 2014, Vernazza et al. 2016), CK (Ostrowski et al. 2011)
X-complex	E			Aubrites (Cloutis et al. 1990, Clark et al. 2004)
	M			Iron meteorites (Cloutis et al. 1990, Shepard et al. 2015)
	P			
		X	X	
		Xe	Xe	
		Xc	Xc	Aubrites, enstatite chondrites (Vernazza et al. 2009, 2011, Shepherd et al. 2015), CV, CR (Ostrowski et al. 2011)
		Xk	Xk	Mesosiderites (Vernazza et al. 2009), CM (Ostrowski et al. 2011)
Others	T	T	T	
	D	D	D	Olivine rich IDPs (Vernazza et al. 2015), Tagish Lake (Hiroi et al. 2001)
	O	O	O	
	R	R	R	
	V	V	V	HED meteorites (4 Vesta is the HED parent body)
	A	A	A	Pallasite, Brachnite (Sunshine et al. 2007)
		Q	Q	LL (Vernazza et al. 2008, Reddy et al. 2014)
		K	K	CR, CO, CV, CK (Burbine et al. 2001, 2002, Clark et al. 2009)
		L	L	High abundances of CAIs (Sunshine et al. 2008)

Table 1.2: *Links that have been suggested between asteroid and meteorite types.*

CHALLENGES

Observations of asteroids in the 0.3 - 2.5 μm range are used for classifications, however ground-based observations over 2.5 - 2.85 μm are masked by absorption features from water vapour, ozone and carbon dioxide in the terrestrial atmosphere (e.g. Takir and Emery, 2012). This means the 3 μm absorption feature cannot be directly observed in ground-

based observations of hydrated asteroids. Use of the surrounding wavelength ranges can indicate the shape of the 3 µm feature, however this has some error as the centre of the feature cannot be confirmed (Takir and Emery, 2012). Additionally, investigating the 3 µm feature is complicated by a change in the dominant spectral flux received from a remote body, transitioning from reflected light to thermally emitted radiation between 3 - 5 µm (e.g. Rivkin et al., 2005). The amount of thermally emitted radiation and the wavelength at which it becomes apparent is affected by the temperature of the body, which itself is a function of heliocentric distance and physical properties of the asteroid. The spectra need to be processed through a thermal model to reproduce an accurate spectrum (Harris, 1998, Rivkin et al., 2005).

Spectral slope in the VNIR is influenced by grain size, viewing geometry and, especially in the case of observing airless bodies, space weathering. This includes small impacts on the surface by micrometeorites and alteration by the solar wind (Brunetto et al., 2015). Space weathering can change the overall spectral slope and cause shallower absorption features than observed in laboratory spectra (Pieters et al., 2000, Burbine, 2017). A good example of the complications introduced through space weathering are in the comparison of S-complex spectra to ordinary chondrites. There was a spectral mismatch between the most common type of meteorites (ordinary chondrites) and the most common asteroids (S-complex) (Bell et al., 1989). This was resolved by the JAXA mission Hayabusa which found the surface of the S-type asteroid 25143 Itokawa was identical to LL5-6 ordinary chondrites and that space weathering accounted for the differences in spectral slope between remote and laboratory spectra (Nakamura et al., 2011, DeMeo et al., 2015a).

1.4.2 Mid-infrared (MIR)

The mid-infrared (MIR) spectral range (approximately 5 - 50 µm) contains many fundamental diagnostic features compared to the VNIR range, and so has the capability of improving

determinations of composition. Most asteroid observations have been made in the VNIR, however MIR is increasingly used as a comparative tool and there are plans for space-based telescopes which will be able to observe asteroids in the MIR at a higher resolution than has been possible before (Rivkin et al., 2016); for example, the James Webb Space Telescope (Gardner et al., 2006, JWST,), which at the time of writing is due to launch in 2021.

Anhydrous silicate and phyllosilicate minerals show vibrational features throughout the entire MIR range. Between 5 - 7 µm there are Si-O overtone and combination features, between ~10 - 11.8 µm there are vibrational features due to Si-O stretching and between ~16.5 - 50 µm there are features due to Si-O bending (e.g. Salisbury et al., 1991, Hamilton, 2000, 2010, Michalski et al., 2006). The positions of these vibrational features are correlated with the mineral structure and chemistry and features associated with one mineral can overlap with others, sometimes making it challenging to interpret (Hamilton, 2000, 2010). A feature near 6.1 µm due to bending vibrations of H_2O is also important in hydrated asteroids and meteorites, as it can be used to indicate hydration (Salisbury et al., 1991, Lucey et al., 2017).

The Christiansen feature (CF) is a reflectance minimum/emissivity maximum between 7.5 - 9.0 µm and is caused by the real part of the refractive index of a mineral approaching the refractive index of the surrounding medium (Conel, 1969). In complex materials such as meteorites and asteroid surfaces the observed CF is a combination of the CFs of individual minerals, so it can be challenging to identify a single feature diagnostic of mineralogy. Despite this, the shape of the feature becomes sharper with the degree of hydration in CM chondrites as phyllosilicate mineralogy becomes the dominant composition (McAdam et al., 2015). Another important feature is the transparency feature (TF), a reflectance maximum/emissivity minimum between 11 - 13 µm that is caused by volume scattering in fine particulate (<75 µm), optically thin materials (Salisbury, 1993, Cooper, 2002). The TF shifts in

position with changes in the surrounding vibrational features so can be used as a diagnostic feature (Salisbury and Walter, 1989, McAdam et al., 2015).

Challenges

Observations of asteroids in the MIR are complicated by thermal emission being the dominant spectral flux at wavelengths > 5 µm, which is in turn affected by thermal gradients, fine particulates and porosity. As described for the VNIR spectra above 3 µm, when observing remote bodies in the MIR, spectral flux needs to be reduced using a thermal model to produce an emissivity spectrum (e.g. Harris, 1998). Most laboratories collect reflectance spectra, which can be approximated as emissivity using Kirchoff's law (emissivity= 1- reflectance) but only accurately when directional hemispherical reflectance is collected (Salisbury et al., 1991). Biconical and bidirectional reflectance spectra are more often collected. Recently laboratory measurements of meteorites have used environment chambers that can simulate the near-surface conditions of airless bodies in order to mimic the thermal gradient and subsequent MIR thermal emission expected on an asteroid surface (Donaldson Hanna et al., 2012a,b, 2019, 2020). Comparisons between these laboratory emissivity measurements to remote spectra are more accurate but are limited due to the sample mass requirements required to accurately recreate the thermal gradients expected. Reflectance spectroscopy remains a more accessible technique for collecting meteorite MIR spectra and so it is important to understand the differences between the reflectance and emissivity methods.

1.4.3 Volatile-rich asteroids and meteorites

Due to shared characteristics between C-complex and CI and CM VNIR spectra, CI and CM chondrites have been hypothesised to be representative of the surface material of C-complex asteroids (Vilas, 1994, Fornasier et al., 1999, Burbine et al., 2002, Ziffer et al., 2011, Takir et al., 2015). For example, the charge transfer feature observed in the C-complex asteroid

spectra at 0.7 μm has been identified in the VNIR spectra of hydrated CI and CM chondrites (Gaffey, 1976, Cloutis et al., 2011a,b, Takir et al., 2013, McAdam et al., 2015, Beck et al., 2018). The CI and CM chondrites also show flat, relatively featureless slopes consistent with those for C-complex spectra. The hydroxyl absorption feature near 3 μm has been observed in some C-complex spectra (Lebofsky, 1980, Jones et al., 1990, Rivkin, 2002, Takir and Emery, 2012), although observing it from ground-based telescopes is difficult. The Dawn and OSIRIS-REx missions observed unambiguous 3 μm features in the VNIR spectra of Ceres and Bennu, respectively (De Sanctis et al., 2015, 2018, Hamilton et al., 2019). The 3 μm feature is also observed in hydrated CI and CM spectra, and its position, shape and depth are related to the phyllosilicate chemistry in these meteorites (Beck et al., 2010, 2014, Takir et al., 2013). For the Bennu feature, the position of the hydroxyl absorption feature is near 2.74 μm, which when compared to the same feature in CI and CM chondrites, indicates the presence of Mg-rich serpentines and suggests a high degree of aqueous alteration (Hamilton et al., 2019). There is also evidence that despite the effect of the atmosphere, the 3 μm absorption features in ground-based telescopic spectra can be used to evaluate the degree of hydration in C-complex spectra through comparisons with CM chondrites (Takir et al., 2015).

Observations of C-complex asteroids in the MIR generally support these conclusions. C-complex members of the Themis and Veritas family have been compared to MIR spectra of CM2 chondrites (Landsman et al., 2016), and the MIR spectrum of Bennu collected by OSIRIS-REx shows a CF and vibrational features similar to those observed in the spectra of CM1/2 chondrites (Hamilton et al., 2019). Due to the lower abundance of MIR data and its lower signal to noise, comparisons with meteorites in this spectral range are more limited.

Spectroscopic evidence for aqueous and thermal alteration on volatile-rich asteroids

Some C-complex asteroid spectra show similar characteristics to aqueously and thermally altered carbonaceous chondrite spectra. Hiroi et al. (1993) suggested the spectral slope of some Tholen C, B, F and G-type asteroids are similar to VNIR spectra of the CY chondrites Y 82162, Y86720 and B 7904, and to spectra of experimentally heated CM2 Murchison. Furthermore, the 3 µm feature of C-complex asteroids have been used to estimate their surface water content by Rivkin et al. (2003), who found 8 asteroids (of multiple spectral types within the C-complex) that either had anhydrous or dehydrated surfaces. Some additional observations of C- and F-type asteroids show similar spectral slopes in the VNIR to aqueously and thermally altered carbonaceous chondrites (Fornasier et al., 2016). More specific spectral types have been suggested to have dehydrated surfaces: B-type asteroid spectra, which have negative spectral slopes in the VNIR range, were compared to aqueously and thermally altered carbonaceous chondrite spectra by Clark et al. (2010). They found 19 of the 30 asteroids observed appeared to show evidence for dehydration. More recently, it has been suggested that B-type asteroid 3200 Phaethon may have a dehydrated surface, based on the absence of a feature near 3 µm which suggests no hydrated phases are present (Takir et al., 2020). Other specific classes of asteroids within the C-complex also show evidence for dehydration: spectra collected by the Hayabusa2 spacecraft of Cg-type asteroid Ryugu show a 3 µm feature which is most closely matched with the 3 µm feature in spectra of experimentally heated CI and shock heated CM material (Kitazato et al., 2019) leading to conclusions that it experienced both aqueous and thermal alteration (Sugita et al., 2019, Michel et al., 2020).

Not only the C-complex asteroids have spectra which suggest these types of alteration. The D and T-type asteroids have featureless slopes between 0.3 - 2.5 µm. Based on the

higher abundance of these asteroid classes in the outer regions of the asteroid belt (section 1.2.1, Figure 1.3, DeMeo and Carry (2014)) these bodies were hypothesised to have formed outside the snow-line and so may have accreted water ice (DeMeo et al., 2015a, Morbidelli et al., 2015). Hiroi et al. (2001) showed the spectra of D and T-type asteroids are similar to the spectra of the C2-ungrouped Tagish Lake, and so suggested the asteroids are primitive, aqueously altered bodies. Additionally, a tentative 2.3 µm phyllosilicate feature was identified in the spectrum of D-type 617 Patroclus (Emery and Brown, 2003), although this has not been reproduced (e.g. Yang and Jewitt, 2007). However, no hydroxyl absorption feature near 3 µm has been observed in D-type asteroid spectra (Emery and Brown, 2003), and MIR observations of D-type Jupiter Trojans are best matched with amorphous and crystalline silicate minerals (Emery et al., 2006, Vernazza et al., 2015). These asteroids would therefore be interesting to consider in the context of hydration and dehydration on C-complex asteroids.

The C-complex and other 'volatile-rich' asteroids show a variety of hydrated and dehydrated compositions and unravelling the effects of the two alteration processes is necessary to understand how these bodies formed and evolved. To do this we need to identify spectral features and trends in the spectra of aqueously and thermally altered carbonaceous chondrites that can be tied to processing and composition, parameters which can then be evaluated in asteroid spectra.

1.5 Aims and objectives

The overarching aim of this project is to unravel the aqueous and thermal histories of volatile-rich asteroids, by investigating key science questions introduced in this chapter.

- *Question A:* Can relationships between spectra and mineralogy of carbonaceous chondrites be used to infer the mineralogy and alteration history of water-rich asteroids?

Question A can be subdivided. As volatile-rich asteroids may have experienced both hydration and dehydration it will be important to be able to identify the products of these alterations in remote spectra, and also to distinguish the two alteration processes. I will therefore look at both aqueously altered and aqueously and thermally altered meteorites, to identify appropriate relationships between spectra and mineralogy:

- *Question A-1:* Are there spectral trends and parameters that correlate with the mineralogy of highly aqueously altered CM and CI chondrites?

  Objective A-1: To do this I will collect the NIR and MIR reflectance spectra of 13 highly hydrated CM and CI chondrites which have had their mineralogy previously determined. I will also collect MIR spectra for additional five CM chondrites for which I will determine mineralogy. This will enable me to tie features to specific mineralogies present in the meteorite samples. I will identify diagnostic parameters which can be used to estimate the degree of aqueous alteration in meteorite spectra. This will be presented in chapter 3.

- *Question A-2:* Are there spectral trends and parameters that correlate with the mineralogy of aqueously and thermally altered carbonaceous chondrites?

  Objective A-2: To do this I will determine the modal mineralogy for aqueously and thermally altered CM and CY chondrites, and then collect NIR (2.5 - 5 µm) and MIR reflectance spectra. As with the highly hydrated meteorites, features in the spectra can be tied to specific mineralogies in meteorite samples. I will identify diagnostic parameters which can be used to identify the occurrence and degree of thermal alteration in meteorite spectra. This will be presented in chapter 4.

Question B relates to the challenge of comparing laboratory to remote spectra of airless bodies. Remote observations of Solar System airless bodies are affected by thermal gradients, the presence of which have been shown to vary the positions and shapes of features. It is therefore important to evaluate whether laboratory reflectance spectra can be used to interpret remote observations of asteroids:

- *Question B:* Are there spectral trends and parameters in emissivity spectra collected under the appropriate near-surface environmental conditions of volatile-rich asteroids that correlate with mineralogy and alteration history of aqueously and thermally altered carbonaceous chondrites? Can reflectance measurements be a good approximation of emissivity?

  Objective B: I will collect emissivity spectra for aqueously and thermally altered CM and CY chondrites using the same material that modal mineralogy was determined for and reflectance spectra was collected on. I will compare reflectance and emissivity spectra so future reflectance measurements can be more accurately compared to both remote and laboratory emissivity spectra. I will also identify additional parameters associated with hydration and dehydration that are present in emissivity spectra. This will be presented in chapter 5.

Following objectives A and B, I can interpret the spectra of volatile-rich asteroids in order to establish their aqueous and thermal histories:

- *Question C:* Can relationships between the spectra and mineralogy of aqueously and thermally altered carbonaceous chondrites be applied to remote observations of volatile-rich asteroids, in order to characterise their aqueous and thermal histories?

  Objective C: To do this I will compare both NIR and MIR meteorite and asteroid spectra for a number of single asteroids and asteroid populations. I will use the features

and parameters determined in the previous chapters to estimate the asteroid surface composition and discuss what the composition might imply for the formation and evolution of those bodies. I will also show how the meteorite spectra collected in previous chapters might be used in the future to further evaluate asteroid data. This will be presented in chapter 6.

In chapter 2 I will present sample descriptions and methodology and in chapter 7 I will present my conclusions and discuss avenues for future work.

Chapter 2: Methodology

2.1 Samples

During this project a total of 39 meteorites were investigated as part of three studies, which constitute chapters 3, 4, and 5 respectively. Table 2.1 summarises the meteorites investigated, the experimental techniques applied to each one, and the chapters where the samples and techniques are discussed. Also included in Table 2.1 are the mass of each meteorite and whether they were obtained from the Antarctic Search for Meteorites (ANSMET), National Institute for Polar Research (NIPR), Russian Academy of Sciences or Natural History Museum (NHM) collections. For clarification: the term 'sample' in Table 2.1 refers to a particular meteorite chip, and the use of multiple techniques on the same sample means the same chip was used. Details of the three studies are below.

- Reflectance spectra for 18 well-characterised aqueously altered CM2, CM1/2, CM1, and CI1 chondrites were collected. The aim of this investigation was to correlate spectral features and trends with known mineralogy. 13 of these meteorites had their modal mineralogy determined by King et al. (2015a) and King et al. (2017b) and spectra were collected on the same samples. For the 5 remaining meteorites I determined modal mineralogy using position-sensitive detector X-ray diffraction (PSD-XRD) and spectra were again collected on the same samples. The results from this are presented in chapter 3.

- Using the practice established for the CM and CI chondrites, the modal mineralogy and geological history for 21 aqueously altered and thermally metamorphosed CM and CY chondrites were determined using a combination of high-resolution X-ray diffraction and PSD-XRD. Reflectance spectra were then collected for the same samples. Further features and trends associated not only with aqueous alteration, but also with thermal metamorphism were then established. The results from this are presented in chapter 4.

- For 12 of the samples from the previous two studies, I collected emissivity spectra. Trends in emissivity spectra were then related to known mineralogy, and comparisons were made with reflectance spectra of the same powders. The results from this are presented in chapter 5.

Thermogravimetric analysis (TGA) was performed for all samples except Dhofar (Dho) 225 and Dho 735, due to limited available mass. Details of the TGA experiments are provided in the appendix and the data were used to support the mineralogical and spectral observations.

2.1.1 Characteristics of CM and CI chondrite samples

I investigated 16 aqueously altered CM chondrites and 2 CI chondrites covering a range of petrologic types from partially altered type 2s to fully hydrated type 1s. Table 2.2a summarises the previous studies of these meteorites, including their petrologic types in the Rubin, Alexander and PSF scales (chapter 1, Rubin et al., 2007, Alexander et al., 2013, Howard et al., 2015). I investigated samples of the CM1/2 chondrites LaPaz Icefield (LAP) 031166, LAP 031214, McKay Glacier (MCY) 05231, Miller Range (MIL) 090288 and North West Africa (NWA) 8534; the CM1s Grosvenor Mountains (GRO) 95645, LAP 02277, MIL 05137, MIL 07689, Moapa Valley and NWA 4765; and the CIs Orgueil and Ivuna. The modal mineralogy

Meteorite	Sample	Mass (g)	Loan details (request number/research program number)	High resolution XRD	PSD-XRD	Reflectance	Emission	TGA	Chapter
A 881334 (46)	HB1	0.498	NIPR (1673)	x	x	x		x	4
A 881655 (85)	HB1	0.492	NIPR (1673)	x	x	x		x	4
ALH 83100 (306)	HB2	2.240	ANSMET (3499)		x	x	x	x	3 & 5
ALH 83102 (92)	HB2	2.210	ANSMET (3499)		x	x	x	x	3 & 5
B 7904 (63)	HB2	1.788	NIPR (1721)	x	x	x	x	x	4 & 5
Dho 2046	HB1	0.056	CEREGE#20160614	x	x	x		x	4
Dho 225	HB1	0.067	Russian Academy of Science		x	x			4
Dho 735	HB1	0.050	Russian Academy of Science		x	x			4
DOM 03183 (38)	HB1	0.427	ANSMET (3423)	x	x	x		x	4
EET 96010 (31)	HB1	0.254	ANSMET (3423)	x	x	x		x	4
EET 96029 (82)	HB2	2.200	ANSMET (3499)	x	x	x	x	x	4 & 5
GRO 95645 (11)	AK-1	0.110	ANSMET			x		x	3
Ivuna (BM1991, M5)	Ivu-1	0.119	NHM (MIN2013-308 (MET))			x		x	3
LAP 02277 (33)	AK-1	0.300	ANSMET			x		x	3
LAP 031166 (17,5)	AK-1	0.240	ANSMET			x		x	3
LAP 031214 (11)	AK-1	0.280	ANSMET			x		x	3
LEW 85311 (59)	HB1	0.515	ANSMET (3423)	x	x	x		x	3
LEW 90500 (87)	HB1	0.560	ANSMET (3423)	x	x	x		x	3
LON 94101 (113)	HB2	2.200	ANSMET (3499)		x	x	x	x	3 & 5
MCY 05231 (9)	AK-1	0.290	ANSMET			x		x	3
MIL 05137 (6)	AK-1	0.120	ANSMET			x		x	3
MIL 07689 (6)	AK-1	0.270	ANSMET			x		x	3
MIL 07700 (31)	HB1	0.515	ANSMET (3423)	x	x	x		x	4
MIL 090288 (5)	AK-1	0.300	ANSMET			x		x	3
Moapa Valley	AK-1	0.063	ASU (1710)			x		x	3
NWA 4765	AK-1	0.098	ASU (1891_1)			x		x	3
NWA 8534	AK-1	0.481	ASU (1915_14)			x		x	3
Orgueil (BM1985, M148)	Org-1	0.055	NHM (MIN2013-308 (MET))			x		x	3
PCA 02010 (28)	HB2	2.210	ANSMET (3499)	x	x	x	x	x	4 & 5
PCA 02012 (28)	HB2	2.180	ANSMET (3499)	x	x	x	x	x	4 & 5
PCA91084 (20)	HB1	0.546	ANSMET (3423)	x	x	x		x	4
WIS 91600 (76)	HB2	2.200	ANSMET (3499)		x	x	x	x	4 & 5
Y 793321 (53)	HB2	1.722	NIPR (1721)	x	x	x	x	x	4 & 5
Y 793595 (42)	HB1	0.506	NIPR (1673)	x	x	x		x	4
Y 794080 (60)	HB1	0.195	NIPR (1673)	x	x	x		x	4
Y 86029 (52)	HB1	0.181	NIPR (1673)	x	x	x		x	4
Y 86720 (61)	HB1	0.506	NIPR (1673)	x	x	x		x	4
Y 86720 (54)	HB2	1.402	NIPR (1721)		x	x	x	x	4 & 5
Y 86789 (60)	HB1	0.507	NIPR (1673)	x	x	x		x	4
Y 86789 (70)	HB2	1.527	NIPR (1721)		x	x	x	x	4 & 5
Y 980115 (62)	HB2	1.706	NIPR (1721)		x	x	x	x	4 & 5

Table 2.1: *Summary of the meteorite samples, sample mass, loan details, and analytical techniques applied.*

of these samples was reported by King et al. (2017b) for the CMs (AK-1 in table 2.1) and King et al. (2015a) for the CIs (Org-1 and Ivu-1 in Table 2.1), and I used exactly the same powders. The mineralogical characteristics of these samples are summarised below.

The chondrites LAP 031214 and MCY 05231 are classified as CM1/2 chondrites and are dominated by phyllosilicates (~72 vol%). This phyllosilicate is a mix of Mg-rich serpentine

Unheated CM and CIs	Classification	Weathering grade	Rubin	Alexander	PSF	Heating stage (/estimated peak temperature)	XRD[a]	PSD-XRD[b] (modal mineralogy)	VNIR[c]	MIR	Oxygen[e]	Petrography[f]	H,C,N abundances and composition[g]	Trace elements[h]	References **a.**
ALH 83100	CM1/2	Be	2.1	1.1	1.2	Unheated	o	o	o	o	o	o	o	o	[a,b]Howard et al. 2015, [c](Cloutis et al. 2011a, McAdam et al. 2015, Garenne et al. 2016, Beck et al. 2018) [d](McAdam et al. 2015, Beck et al. 2018), [e]Clayton & Mayeda 1999, [f]Zolensky et al. 1997, [g]Alexander et al. 2012, [h]Mahan et al. 2018
ALH 83102	CM2	B/Ce	2.1	1.1	1.2	Unheated	-	-	-	o	-	-	-	-	[d]Salisbury et al. 1991
GRO 95645	CM1	B/Ce	-	-	1.2	Unheated	o	o	-	-	o	-	-	-	[a,b]King et al. 2017, [e]King et al. 2018
LAP 02277	CM1	A	2.1	1.4	1.2	Unheated	o	o	-	-	o	o	o	o	[a,b]King et al. 2017, [c]Takir et al. 2013, [e]King et al. 2018, [f]Rubin et al. 2007, [g]Alexander et al. 2012, [h]Moriarty et al. 2009,
LAP 031166	CM1/2	B	2.1	-	1.2	Unheated	o	o	-	-	o	o	-	-	[a,b]King et al. 2017, [e]King et al. 2018, [f]Lindgren et al. 2015
LAP 031214	CM1/2	B	-	-	1.5	Unheated	o	o	-	-	o	-	-	-	[a,b]King et al. 2017, [e]King et al. 2018
LEW 85311	CM2	Be	2.6-2.7	1.9	1.7	Unheated	o	o	o	o	o	o	o	o	[a,b,e,f]Lee et al. 2019, [c](Hiroi et al. 1997, Garenne et al. 2016, Beck et al. 2018) [d]Beck et al. 2018, [g]Alexander et al. 2013, [h]Xiao & Lipschutz 1992
LEW 90500	CM2	B	2.2	1.6	1.4	Unheated	o	o	-	-	o	o	o	o	[a,b]Howard et al. 2015, [c](Hiroi et al. 1996, Garenne et al. 2016) [e]Clayton & Mayeda 1999, [f]Freidrich et al. 2018, [h]Hua et al. 2002, [g]Alexander et al. 2012
LON 94101	CM2	Be	2.2-2.3	1.8	1.3	Unheated	-	-	o	o	-	o	-	o	[c](Cloutis et al. 2011b, Beck et al. 2018), [d]Beck et al. 2018, [f]Lindgren et al. 2015, [h]Mahan et al. 2018
MCY 05231	CM1/2	B	-	-	1.5	Unheated	o	o	-	-	o	-	-	-	[a,b]King et al. 2017, [e]King et al. 2018
MIL 05137	CM1	Be	-	-	1.1	Unheated	o	o	-	-	o	-	-	-	[a,b]King et al. 2017, [e]King et al. 2018
MIL 07689	CM1	C	-	-	1.1	Unheated	o	o	-	-	o	-	-	-	[a,b]King et al. 2017, [e]King et al. 2018
MIL 090288	CM1/2	Be	-	-	1.2	Unheated	o	o	-	-	o	-	-	-	[a,b]King et al. 2017, [e]King et al. 2018
Moapa Valley	CM1	-	-	-	1.1	Unheated	o	o	-	-	o	o	-	-	[a,b]King et al. 2017, [e]King et al. 2018, [f]Irving et al. 2009
NWA 4765	CM1	Low	-	-	1.2	Unheated	o	o	-	-	o	-	-	-	[a,b]King et al. 2017, [e]King et al. 2018
NWA 8534	CM1/2	Low	-	-	1.2	Unheated	o	o	-	-	o	-	-	-	[a,b]King et al. 2017, [e]King et al. 2018

Table 2.2: *Summary of the petrologic classifications of the (a) aqueously altered CM and CI samples, (b) thermally altered CM and CM-an samples, (c) thermally altered CY samples and(d)CM, CM-an or CY samples which may be thermally altered in the Rubin, Alexander and PSF schemes (chapter 1), weathering grade, heating stage after Nakamura (2005), and previous analysis. 'o' indicates where data is available, '-' indicates there is no data of this type for this meteorite.*

Ivuna	CI1		-	1.1	1.1	Unheated	o	o	o	o	o	o	o	o	[a,b]King et al. 2015, [c](Hiroi et al. 1996, Cloutis et al. 2011b, Takir et al. 2013), [d](Salisbury et al.1991, King et al. 2015), [e]Clayton & Mayeda 1999, [f,g]King et al. 2020, [g]Alexander et al. 2012
Orgueil	CI1		-	1.1	1.1	Unheated	o	o	o	o	o	o	o	o	[a,b]King et al. 2015, [c](Hiroi et al. 1997, Cloutis et al. 2011b, McAdam et al. 2015, Garenne et al. 2016), [d](Salisbury et al.1991, King et al. 2015, McAdam et al. 2015), [e]Clayton & Mayeda 1999, [f]Tomeoka & Buseck 1988, [g]Alexander et al. 2012, [h]Barrat et al. 2012
Heated CM and CM-an chondrites															**b.**
A 881334	CM2	-	-	-	-	II	o	-	o	-	o		-		[a]Nakamura 2005, [c]Hiroi et al. 1997, [e]Clayton & Mayeda 1999
A 881655	CM2	-	-	-	-	III	o	-	o	-	o		-		[a]Nakamura 2005, [c]Hiroi et al. 1997, [e]Clayton & Mayeda 1999
EET 96029	CM2	A/B	2.7	1.6	2	II	o	o	-	-	-	o	o		[a,b,f]Lee et al. 2016, [c]Garenne et al. 2016, [g]Alexander et al. 2012
PCA 02010	CM2	B	-	-	-	III/IV	o	o	o	o	-	-	o	o	[a,b,d]Hanna et al 2020, [c]Garenne et al. 2016, [c,d]Beck et al. 2018, [g]Alexander et al. 2013, [h]Mahan et al. 2018
WIS 91600	CM-an	A/Be	-	1.9	1.4	II	o	o	o	o	o			o	[a,b]Howard et al. 2015, [c](Hiroi et al. 1997, McAdam et al. 2015), [d]McAdam et al. 2015, [e,h]Moriarty et al. 2009,
Y 793321	CM2	-	-	-	-	II	o	-	o	-	o			o	[a]Nakamura 2005, [c]Hiroi et al. 1997, [h]Xiao & Lipschutz 1992
Y 793595	CM2	-	-	-	-	I	o	-	o	-	o		-		[a]Nakamura 2005, [c]Hiroi et al. 1997
Heated CY chondrites															**c.**
B 7904	C2-ung/CY	-	-	-	-	IV	o	o	o		o	o	-	o	[a,b,e,f,h]King et al. 2019, [c]Hiroi et al. 1997
Y 86029	CI1/CY	-	-	-	-	III	o	o			o	o	-	o	[a,b,e,f,h]King et al. 2019
Y 86720	C2-ung/CY	-	-	-	-	IV	o	o	o		o	o	-	o	[a,b,e,f,h]King et al. 2019, [c]Hiroi et al. 1997
Y 86789	C2-ung/CY	-	-	-	-	IV	o	o			o	o	-	o	[a,b,e,f,h]King et al. 2019, [c]Hiroi et al. 1997
Y 980115	CI1/CY	-	-	-	-	III	o	o			o	o	-	o	[a,b,e,f,h]King et al. 2019, [d]King et al. 2015

Table 2.2: *(cont.)*

Heated (?) CM, CM-an or CY chondrites															d.
Dho 2046	CM2-an	-	-	-	-	-	-	-	-	-	o	-	-	-	[e]Bouvier et al. 2017
Dho 225	CM-an	-	-	-	-	600 – 650 °C	o	-	-	-	o	o	-	o	[a,d,e,f,h]Ivanova et al. 2010
Dho 735	CM2	-	-	-	-	600 – 650 °C	o	-	-	-	o	o	-	o	[a,d,e,f,h]Ivanova et al. 2010
DOM 03183	CM2	B	-	1.6	-	-	-	-	o	-	-	-	o		[c]Garenne et al. 2016, [g]Alexander et al. 2012
EET 96010	CM2	B	-	-	-	700 – 900 °C	-	-	-	-	o	o	-	o	[e,h]Moriarty et al. 2009, [f]Tonui et al. 2001
MIL 07700	CM2	A	-	-	-	-	-	-	o	o	-	-	o	o	[c](Takir et al. 2013, Garenne et al. 2016, Beck et al. 2018) [d]Beck et al. 2018, [g]Alexander et al. 2012, [h]Mahan et al. 2018
PCA 91084	CM2	Be	-	1.8	-	-	-	-	o	-	-	-	o	-	[c]Hiroi et al. 1997, [g]Alexander et al. 2012
PCA 02012	CM2	B	-	-	-	'severe'	-	-	o	o	-	o	o	o	[a,f,e]Nakato et al. 2013, [c]Garenne et al. 2016, [c,d]Beck et al. 2018, [g]Alexander et al. 2013, [h]Mahan et al. 2018
Y 794080	CM2	-	-	-	-	-	-	-	o	-	-	-	-	-	[c]Hiroi et al. 1997

Table 2.2: *(cont.)*

and Mg-Fe-rich serpentine, and for consistency with Howard et al. (2015) and King et al. (2017b), from this point I will refer to these polytypes as Mg-serpentine and Fe-cronstedtite. LAP 031214 and MCY 05231 also contain ~19 vol% primary olivine, ~5 vol% pyroxene, ~2 vol% magnetite, ~1 vol% Fe-sulfide (pyrrhotite and pentlandite) and carbonates (calcite) (King et al., 2017b). They both have PSF petrologic types of 1.5, with mineral abundances consistent with those previously determined for CM2 chondrites (Howard et al., 2015). King et al. (2017b) suggested that LAP 031214 and MCY 05231 should be classified as CM2 chondrites and I will refer to them as such throughout this thesis. The other CM1/2 chondrite samples consist of ~86 vol% phyllosilicate (Mg-serpentine and Fe-cronstedtite), ~7 vol% primary olivine, ~2 vol% pyroxene, ~3 vol% magnetite, <2 vol% Fe-sulfide, and minor (<1 vol%) carbonates and gypsum and have PSF petrologic types of 1.2 (King et al., 2017b). The CM1 chondrite samples consist of ~87 vol% phyllosilicate (Mg-serpentine and Fe-cronstedtite), ~6 vol% primary olivine, ~3 vol% magnetite, <4 vol% Fe-sulfide, and minor pyroxene, carbonates, and gypsum. They have PSF petrologic types of 1.1 - 1.2 (King et al., 2017b). The CI1s Orgueil and Ivuna contain ~84 vol% phyllosilicate, ~8 vol% magnetite, and ~6 vol% Fe-sulfide (King et al., 2015a). Ferrihydrite and gypsum are present in the sample of Orgueil at an abundance of 2 vol%, and the Ivuna sample contains 2 vol% carbonate (dolomite) (King et al., 2015a). The phyllosilicates in the CI chondrites differ in composition from phyllosilicates in CM chondrites, being a mixture of Mg-serpentine and Mg-rich smectite (Tomeoka and Buseck, 1988, Tomeoka, 1990, Brearley, 2006).

I also investigated samples of the CM1/2 Alan Hills (ALH) 83100, and the CM2s ALH 83102, Lewis Cliff (LEW) 85311, LEW 90500 and Lonewolf Nunataks (LON) 94101. ALH 83100 and ALH 83102 are part of the ALH 83100 pairing group (Grossman, 1994), having been found in geographical proximity and showing similar physical characteristics and alteration histories (eg. cosmic ray exposure (CRE) age and weathering) (Benoit et al., 1996).

Paired meteorites are assumed to be part of the same meteorite fall. Zolensky et al. (1997) described the petrography of ALH 83100 as a matrix supported assemblage of highly altered chondrules, serpentines, carbonates and sulfides, and its Rubin petrologic type is 2.1 (Rubin et al., 2007), indicating that it's a highly aqueously altered meteorite. This is supported by a high H abundance (giving a petrologic type of 1.1 in the Alexander scale, Alexander et al., 2013), and XRD observations: Howard et al. (2011) reported the modal mineralogy of a sample of ALH 83100 (different to the sample in this study) as 87 vol% phyllosilicate (Mg-serpentine and Fe-cronstedtite), 9 vol% primary olivine, and <2 vol% pyroxene, sulfide, carbonates (calcite), magnetite and Fe metal, and assigned it a PSF petrologic type of 1.2. In addition, reflectance spectra (2.5 - 13.5 µm) for ALH 83100 and ALH 83102 show 3 µm features with depths that correlate to the water content of the meteorites (Salisbury et al., 1991). Both also show spectral signatures around the CF that are consistent with the presence of hydrated minerals, a trait which is supported by recent observations of the same feature for ALH 83100 by Beck et al. (2018).

LEW 85311 is officially classified as a CM2, but has an unusual elemental composition that falls between the CM and CV chondrites (Choe et al., 2010), and an oxygen isotopic composition that sits within the CV-CK-CO field (Clayton and Mayeda, 1999). The presence of unaltered silicate phenocrysts in chondrules and resulting Rubin petrologic type of 2.6 - 2.7 suggest that it has experienced less aqueous alteration than the other CM2 chondrites in this project (Choe et al., 2010, Lee et al., 2019). This is supported by its low H (petrologic type of 1.9 in Alexander et al., 2013) and phyllosilicate abundance (65 vol%, PSF petrologic type of 1.7, Lee et al., 2019).

Petrographic observations of LEW 90500 show abundant matrix phyllosilicates and partially altered chondrules, giving a Rubin petrologic classification of 2.2 (Friedrich et al., 2018, Hanna et al., 2020). Its H abundance suggests a lesser degree of aqueous alteration, giving

a petrologic type of 1.6 (Alexander et al., 2013). The modal mineralogy of a sample of LEW 90500 (again different to the sample in this study) is 69 vol% phyllosilicate (Mg-serpentine and Fe-cronstedtite), 15 vol% primary olivine, 5 vol% pyroxene, 4 vol% gypsum, 3 vol% sulfide, 2 vol% magnetite and minor calcite, giving a PSF petrologic type of 1.4 (Howard et al., 2015). Reflectance spectra (2.5 - 25 μm) from a thin section of LEW 90500 showed features due to both olivine and phyllosilicate, consistent with its bulk mineralogy (Hanna et al., 2020).

Lindgren et al. (2011) and Lee et al. (2013) described LON 94101 as consisting of unaltered and aqueously altered chondrules in a fine-grained matrix composed of phyllosilicates, sulfides and minor calcite, and assigned it as a petrologic type 2.2 - 2.3 in the Rubin scheme. Beck et al. (2018) collected spectra between 0.35 - 28 μm for a powdered sample of LON 94101 and identified features consistent with phyllosilicates.

2.1.2 Characteristics of CM, CM-an and CY chondrite samples

Table 2.2b lists seven meteorites that have been identified as aqueously and thermally altered CM or CM-anomalous chondrites and given a Nakamura (2005) heating stage. Thermal alteration in CM chondrites results in the low H_2O abundances, loss of mobile trace elements and partial or complete dehydration of phyllosilicates into a disordered phase (Nakamura, 2005, Nakato et al., 2008, Tonui et al., 2014). At temperatures >500 ^{o}C, anhydrous phases such as poorly crystalline olivine and pyroxene can recrystallise out of this disordered phase (Nakato et al., 2008, Tonui et al., 2014). Aqueously and thermally altered chondrites are grouped into four stages based on their thermal history (Nakamura, 2005), the characteristics of which are described in section 1.3.4. The seven meteorites in Table 2.2b have heating stages assigned: Yamato (Y) 793595 is a stage I; Asuka (A) 881334, Elephant Moraine (EET) 96029, Wisconsin Range (WIS) 91600 and Y 793321 are stage IIs; A 881655 is a stage III; and Pecora Escarpment (PCA) 02010 is a stage IV.

Transmission electron microscopy (TEM) analyses of the stage I CM Y 793595 confirm some initial decomposition of phyllosilicates has occurred, shown by the presence of small amounts of a disordered serpentine (Nakamura, 2005). However, bulk XRD observations show no apparent dehydration of phyllosilicates, with diffraction peaks associated with Mg-serpentine and Fe-cronstedtite still present (Nakamura, 2005). It is hypothesised that Y 793595 (and other stage I samples) has been heated to <300 ^{o}C, which would result in some initial decomposition but the survival of most phyllosilicates (Nakamura, 2005). The CMs A 881334, EET 96029 and Y 793321 show no diffraction peaks associated with phyllosilicates in XRD patterns, leading to the conclusion that phyllosilicates were dehydrated into a disordered phase during heating to 300 – 500 ^{o}C (stage II, Nakamura, 2005, 2006, Tonui et al., 2001, 2014, Lee et al., 2016). Furthermore, EET 96029 and Y 793321 show petrographic evidence for dehydration such as disordered and defect structures in phyllosilicates, vesicles in carbonate grains due to the release of CO_2 during heating (observed in Y 793321 but not EET 96029), and hexagonal features that resemble desiccation cracks (Akai, 1988, Nakamura, 2006, Tonui et al., 2014, Lee et al., 2016). The mineralogy of a sample of EET 96029 (not the same as the sample in this study) is 65 vol% dehydrated phyllosilicate, 16 vol% pyroxene, 12 vol% primary olivine, 3 vol% magnetite, 2 vol% sulfide and minor calcite, gypsum and metal (Lee et al., 2016).

The stage II CM-an WIS 91600 has unusual characteristics compared to most CM chondrites, including a high magnetite content (~7 vol%, Howard et al., 2015), heavy oxygen composition (Clayton and Mayeda, 1999) and a phyllosilicate composition consistent with the presence of possible smectite phases (more CI-like than CM-like) (Tonui et al., 2014). These smectite phyllosilicates were only partially dehydrated, as observed in TEM observations (Tonui et al., 2014). The bulk mineralogy of a sample of WIS 91600 (not the same

sample as in this study) was determined by Howard et al. (2015) to be 74 vol% phyllosilicate, 15 vol% primary olivine, 7 vol% magnetite, 4 vol% sulfide, and minor pyroxene.

Petrographic observations of A 881655 show CAIs and highly altered chondrules embedded in a fine-grained matrix. Dehydrated serpentines are identified in this matrix, as well as grains of smectite that are still hydrous (Lipschutz et al. 1999). Unlike other dehydrated CM chondrites, it shows abundant magnetite and sulfide within both the matrix and chondrules (Lipschutz et al., 1999, Tonui et al., 2014). Based on the depletion of the thermally mobile element Cd, A 881655 is classified as a stage III (Wang and Lipschutz, 1998, Nakamura, 2005), however it is distinct from the other dehydrated CMs, and its high magnetite abundance suggests an affinity with WIS 91600.

Alexander et al. (2013) reported that the CM2 PCA 02010 had amongst the lowest bulk H, N and C contents of any CM chondrite analysed. It also shows very low mass losses during TGA, indicating it has lost most of its H_2O (Garenne et al., 2014). Petrographic observations indicate an absence of phyllosilicates and instead a matrix dominated by fine-grained Fe-rich olivine and pyroxene, with 'blurred' chondrules and dehydration cracks (Hanna et al., 2020). PCA 02010 shows depletions in volatile elements and an enrichment in heavy Zn isotopes - a trait explained by severe dehydration (Mahan et al., 2018). Its MIR reflectance spectra are similar to that of olivine (Beck et al., 2018, Hanna et al., 2020), and the bulk modal mineralogy of a sample (again not the same sample as in this study) is 75 vol% olivine, 16 vol% pyroxene, 4 vol% sulfide, 3 vol% feldspar, 1 vol% carbonate and minor metal (Hanna et al., 2020). Based on its XRD pattern, PCA 02010 is likely a stage IV CM chondrite.

I also investigated five aqueously and thermally altered CY chondrites (Table 2.2c). King et al. (2019) recently proposed the CYs as a new carbonaceous chondrite group and assigned them heating stages based on the criteria of Nakamura (2005) and Tonui et al. (2014). Petrographic observations of Y 86029 and Y 980115 show abundant matrix, dehydrated phyllosili-

cates that have a mixed serpentine/smectite composition, periclase, magnetite, sulfides and phosphates (Akai, 1990, Ikeda and Yukio, 1991, Tonui et al., 2003, King et al., 2015a, 2019). King et al. (2019) suggested that Y 86029 and Y 980115 are stage III CYs and reported a bulk mineralogy for samples of both of ~70 vol% disordered, dehydrated phyllosilicate, ~19 vol% Fe-sulfide, ~10 vol% secondary olivine, and ~3 vol% metal. B 7904, Y 86720 and Y 86789 are also CY chondrites but were heated to a higher peak temperature and are classified as stage IVs (King et al., 2019). Petrographic observations show dehydrated phyllosilicates, carbonates, phosphates, sulfides and recrystallised olivine, pyroxene and metal. Partially aqueously altered chondrules were observed in B 7904 but chondrules were almost fully replaced by phyllosilicates in Y 86720 and Y 86789 (Tomeoka and Kazushige, 1990, Bischoff and Metzler, 1991, Ikeda, 1992, Tonui et al., 2014). King et al. (2019) determined the bulk mineralogy of the stage IV CYs as 58 - 63 vol% recrystallised, secondary olivine, 0 - 20 vol% primary olivine, 6 - 11 vol% pyroxene, 12 - 29 vol% sulfide and <2 vol% metal. Y 86720 and Y 86789 are paired meteorites (Matsuoka et al., 1996) and in this study I had two samples of each of these (referred to as HB1 and HB2).

2.1.3 Other aqueously and thermally altered carbonaceous chondrites

Table 2.2d lists 10 CM and CM-an chondrites that show evidence for dehydration but have no assigned heating stage in the literature. The key characteristics of these meteorites are summarised in the following paragraphs. For some samples, such as Y 794080 (CM2) which was identified as a potentially dehydrated from the shape and structure of its 3 µm feature (Hiroi et al., 1997), there are limited data available. Similarly, there are few reports for Dho 2046 (CM2-an), but petrographic observations are consistent with CM chondrites: it has chondrules and chondrule fragments, and olivine, sulfide and Fe-metal grains all embedded in a fine-grained, Fe-rich matrix (80 vol%) (Bouvier et al., 2017). However, its oxygen isotopic composition ($\delta^{17}O$ = 7.78 ‰ and $\delta^{18}O$ = 19.93 ‰) is heavier than most other CMs and

instead closer to the CY chondrites (Bouvier et al., 2017), which could suggest the meteorite has been dehydrated, preferentially losing light oxygen isotopes resulting in a heavier bulk composition.

Ivanova et al. (2010) investigated the petrography, mineralogy and bulk chemistry of the CM-an Dho 225 and the CM2 Dho 735. Texturally these meteorites appear similar to CM2 chondrites, however Ivanova et al. (2010) found a lower bulk water content (~1.5 wt%) and a lack of tochilinite and phyllosilicates in the matrices. Furthermore, they identified recrystallised olivine in XRD patterns but saw no diffraction peaks associated with phyllosilicates. This led them to conclude that Dho 225 and Dho 735 were heated to temperatures of 600 - 650 ^{o}C.

EET 96010 was originally classified as a CV3 chondrite (Grossman, 1998), but its major element abundances and magnetic properties are more consistent with CM chondrites (Moriarty et al., 2009, Rochette et al., 2008), leading to a later reclassification as a CM2. EET 96010 shows petrographic evidence for severe heating, such as fusion of chondrules with matrix and high abundances of fine-grained, recrystallised olivine (Tonui et al., 2001) and it is depleted in the most thermally labile elements (Moriarty et al., 2009). Its oxygen isotopes are heavier than typical compositions for CV and CM chondrites and are instead more consistent with the CI chondrites, suggesting a loss of light oxygen during dehydration (Moriarty et al., 2009). EET 96010 is estimated to have been heated to 700 – 900 ^{o}C (Tonui et al., 2001, Moriarty et al., 2009).

Several samples in Table 2.2d were identified as dehydrated due to the abundance and composition of H, C and N by Alexander et al. (2012) and Alexander et al. (2013). For example, mild dehydration of Dominion Range (DOM) 03183 (CM2) is indicated by depletions in H relative to other CM chondrites (Alexander et al., 2013), although transmission MIR spectra, water and volatile element abundances are similar to typical CMs (Beck et al., 2014,

Garenne et al., 2016, Mahan et al., 2018). MIL 07700 (CM2) and PCA 91084 (CM2) also show depletions in H (Alexander et al., 2012). For MIL 07700 metamorphism is supported by the presence of thermally modified insoluble organic matter (IOM) (Quirico et al., 2018), while for PCA 91084 dehydration can be inferred from the shape and reduced strength of its 3 µm feature (Hiroi et al., 1997).

PCA 02012 was identified by Alexander et al. (2013) as having very low bulk H, N and C contents, similar to values obtained for PCA 02010 (stage IV). Petrographic observations show a fine-grained matrix embedded with CAIs and chondrules, and a matrix mineralogy dominated by Fe-rich olivine and pyroxene, with minor sulfide, chromite and metal and an absence of phyllosilicates (Nakato et al., 2013). As with PCA 02010, PCA 02012 shows depletions in volatile elements and an enrichment in heavy Zn isotopes (Mahan et al., 2018). Its MIR reflectance spectra is similar to those of anhydrous silicates (Beck et al., 2018), and it has a low bulk H_2O content (Garenne et al., 2014). PCA 02012 shows additional evidence for dehydration; its oxygen isotopes are heavier than typical CM chondrites (Nakato et al., 2013) and its IOM is substantially altered in both structure and chemistry (Quirico et al., 2018). Nakato et al. (2013) suggested PCA 02012 has experienced temperatures of > 900 ^{o}C.

2.2 X-RAY DIFFRACTION

Powder X-ray diffraction (XRD) is a non-destructive technique that is used to study crystalline and non-crystalline materials. Atoms within a crystal lattice are arranged in planes separated by a distance d, which is generally 0.1 - 10 nm. This distance is similar to X-ray wavelengths, so when X-ray radiation is incident on a crystal, diffraction occurs. The diffracted beam will constructively interfere if conditions defined by Bragg's law: $n\lambda = 2d\sin\theta$ are satisfied, where λ is the wavelength of the incident radiation, d is the spacing of planes in the crystal lattice

and θ is the angle of incidence. In XRD the wavelength of the incident radiation is controlled, so the angle at which constructive interference occurs can be used to work out the distance between crystal planes, which indicate the crystal and therefore mineral structure.

X-ray diffractometers consist of an X-ray source, a sample holder and a detector. A beam of X-rays is usually generated by directing electrons on to a target material (e.g. Cu or Co) to produce characteristic X-ray radiation. This radiation has several components with slightly different wavelengths and intensities, the most common called $K\alpha_1$, $K\alpha_2$ and Kβ, so the X-ray beam is filtered to produce a specific monochromatic wavelength (e.g. Cu $K\alpha_1$ = 1.5418 Å). This monochromatic radiation is directed onto a sample, and the intensity of the diffracted X-rays are recorded. When the geometry of the system satisfies Bragg's law, at the 2θ angle a peak in intensity is observed and recorded. The crystal structure determined from this angle can indicate the mineral present in a sample. In complex materials such as meteorites, a typical diffraction pattern will have intensity peaks from all minerals in the sample. Two powder XRD techniques were used in this project: high resolution XRD for phase identification and PSD-XRD for determining modal mineralogy.

2.2.1 High resolution X-ray diffraction

High resolution XRD was performed on the majority of samples (Table 2.1) to help with mineral phase identification. This was carried out using a Panalytical X'Pert Pro MPD Alpha 1 with a θ:2θ Bragg-Brentano geometry at the Natural History Museum, London (Figure 2.1), where the X-ray tube is fixed in place and the sample holder and detector rotate at θ °/min and 2θ °/min, respectively. These rotation rates ensure the distance between the sample holder and detector stays constant and is equal to the distance between the X-ray source and sample holder, which is important to ensure that the diffracted beam is focussed onto the detector. For my analyses the instrument was set-up to use Co Kα radiation, which does

not cause the iron in the meteorites to fluoresce, resulting in patterns with high signal-to-noise suitable for accurate phase identification. The instrument was calibrated using LaB_6, a cubic phase with diffraction peaks evenly spaced across the 2θ range investigated.

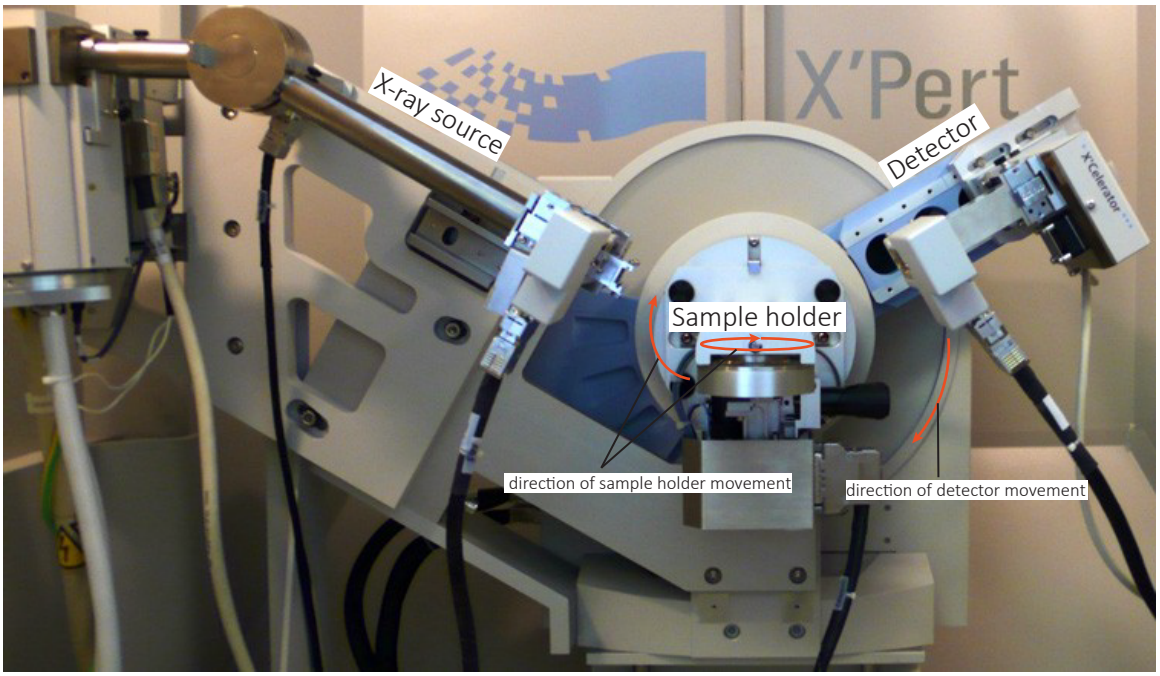


Figure 2.1: *The geometry of the Panalytical X'Pert pro.*

Chips of all HB1 and HB2 samples in Table 2.1 were ground using an agate mortar and pestle into a powder with particle size of <35 µm. Approximately 1 - 2 mg of the powdered sample was mixed with a few drops of acetone and deposited onto a silicon substrate. XRD patterns were collected for 23 hours with a scan range of 5 - 90° 2θ with a step size of 0.212°. For phase identification the high-resolution XRD patterns were compared with standard reference patterns from the International Centre for Diffraction Data Powder Diffraction File (ICDD PDF) 2 2004 database in the WinXPow software.

2.2.2 Position-sensitive detector X-ray diffraction

PSD-XRD has been used previously to determine modal mineralogy for CI, CM, CO, CV, CR, and CY chondrites (Bland et al., 2004, Howard et al., 2009, 2010, 2015, King et al., 2015a,

Alexander et al., 2018). 50 mg was taken from the powdered meteorite sample and as the powder was mixed and homogenised during grinding, this was assumed to be representative of the whole sample. For HB2 samples, which had much larger mass (Table 2.1), two separate aliquots were analysed using PSD-XRD (referred to as HB2-1 and HB2-2). Powders were packed into an aluminium well and the surface flattened using the sharp edge of a spatula in order to increase randomness and minimise the effects of preferential crystal alignment during XRD analysis (Batchelder and Cressey, 1998). Modal mineralogy was obtained using an Enraf-Nonius PDS 120 powder diffractometer with an INEL curved 120^{o} PSD at the Natural History Museum, London, in a static geometry relative to the X-ray beam and sample, which was rotated throughout the analysis (Figure 2.2). The detector is able to collect diffracted X-rays from 0 - 120^{o} simultaneously. Cu Kα_1 radiation was selected using a Ge 111 monochromator and focussed onto the flat top of the sample. Cu radiation was used as it causes fluorescence which contributes to the background of XRD patterns and the level of fluorescence is correlated with the amount of Fe in the sample. For all measurements, the size of the beam was restricted to 0.24 x 2.00 mm using post-monochromator slits. The instrument was calibrated using Ag-Behenate as a standard for low angles, and Si powder for high angles.

Following previous studies of carbonaceous chondrites, PSD-XRD patterns were collected from each sample for 16 hours to achieve good signal-to-noise (Howard et al., 2009, King et al., 2015a, 2017b). PSD-XRD patterns were collected under exactly the same analytical conditions from terrestrial mineral standards sourced from the NHM mineral collection for 30 minutes (Table B.1). Differences in the intensity of the beam were monitored by measuring a polished Fe block at the beginning and end of each measurement day and were found to be <1% over the duration of an experimental run (Figure A.1).

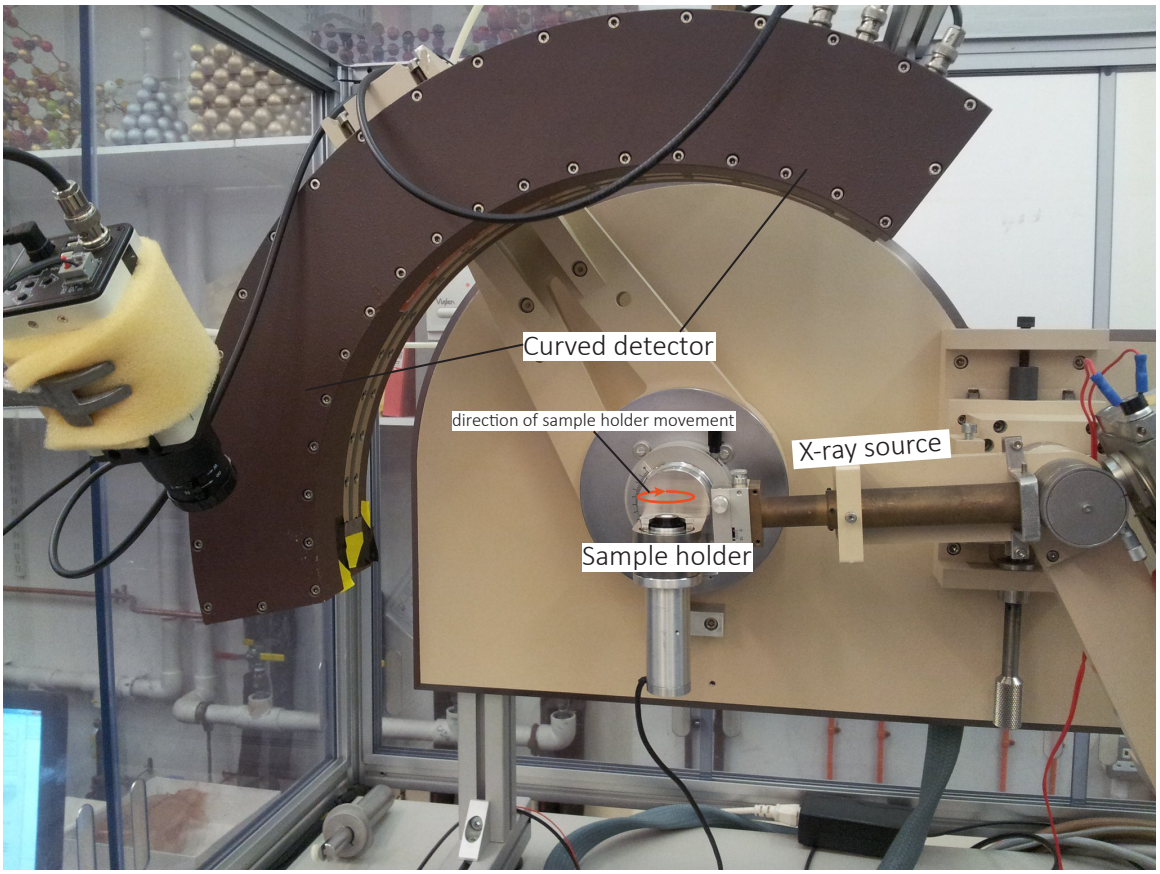


Figure 2.2: *The geometry of the PSD-XRD.*

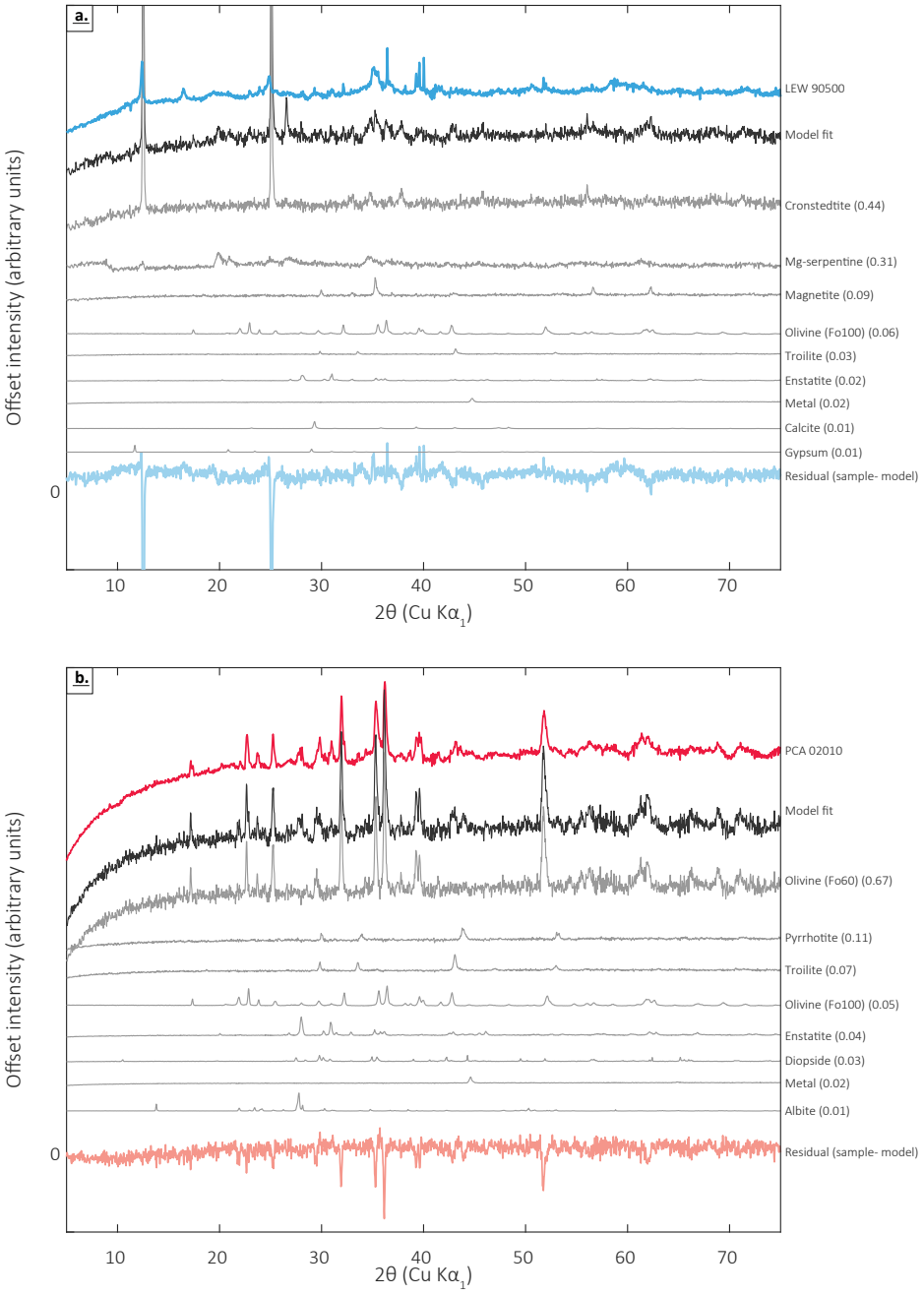
Phase identification was done using results from the high resolution XRD and by comparison with standard reference patterns in the ICDD PDF 2 2004 database using the WinX-Pow software. To determine the modal mineralogy of a sample from its PSD-XRD pattern, a profile-stripping technique was employed (Cressey and Schofield, 1996). The XRD patterns of mineral standards were scaled to the same measurement time as the meteorite patterns (e.g. 30 mins x 32 = 16 hours), and then reduced by a factor so that peaks in the standard were the same intensity as the respective peaks in the meteorite. The mineral standard was then subtracted out of the meteorite pattern to leave a residual pattern. The background fluorescence generated by the Cu radiation was also used to improve the determination of the proportion of Fe-bearing minerals. This was particularly important in the case of fitting Fe-cronstedtite, as during packing of the standard into the sample cup, the mineral is sensi-

tive to preferential alignment of crystals, causing anomalously strong peaks in resulting XRD patterns which cannot be used for phase quantification. Instead the background is used to estimate the Fe-cronstedtite proportion. Figures 2.3a and 2.3b show this method for an aqueously altered CM2 chondrite that contains phyllosilicates, and a thermally altered CM2 sample composed of crystalline anhydrous phases, respectively. Profile-stripping was repeated for all crystalline minerals identified in the sample until the residual was equal to zero intensity and the mineral scale factors used to scale the mineral standards to the meteorite pattern summed to 1. The factors were corrected for relative differences in X-ray absorption (Table B.1) to give the final mineral fraction in volume %.

Following the removal of crystalline phases from the meteorite pattern, if a significant residual remained this was assumed to be due to the disordered phase resulting from dehydration of the phyllosilicates. Figure 2.4 shows the profile stripping method for a sample where this is the case. Figure 2.4a shows that upon removal of crystalline phases the residual background matches well with scaled phyllosilicate standard patterns without the diffraction peaks. This phyllosilicate standard can be subtracted from the residual until it has zero counts. The volume fraction determined from the scaling factors of the phyllosilicate patterns is assumed to represent the volume fraction of the disordered phyllosilicate phase. I cannot rule out the presence of amorphous silicates or poorly crystalline Fe-(oxy)hydroxides and rusts, however the residual patterns were generally in good agreement with the overall shape and intensity of the scaled phyllosilicate patterns (excluding the diffraction peaks).

Previous studies using the profile-stripping method have applied a linear least-squares routine to fit the standard patterns to the meteorite patterns in order to determine detection limits and uncertainties in mineral abundances (Schofield et al., 2002, King et al.,

Figure 2.3: *The profile stripping method for (a) an aqueously altered CM2 (LEW 90500) which contains phyllosilicates and (b) an aqueously and thermally altered CM2 (PCA 02010) which contains only anhydrous phases. The mineral patterns are shown multiplied by 32 and then by the scale factor used to scale the mineral standards to the meteorite pattern. Scale factors are in brackets next to the mineral name.*



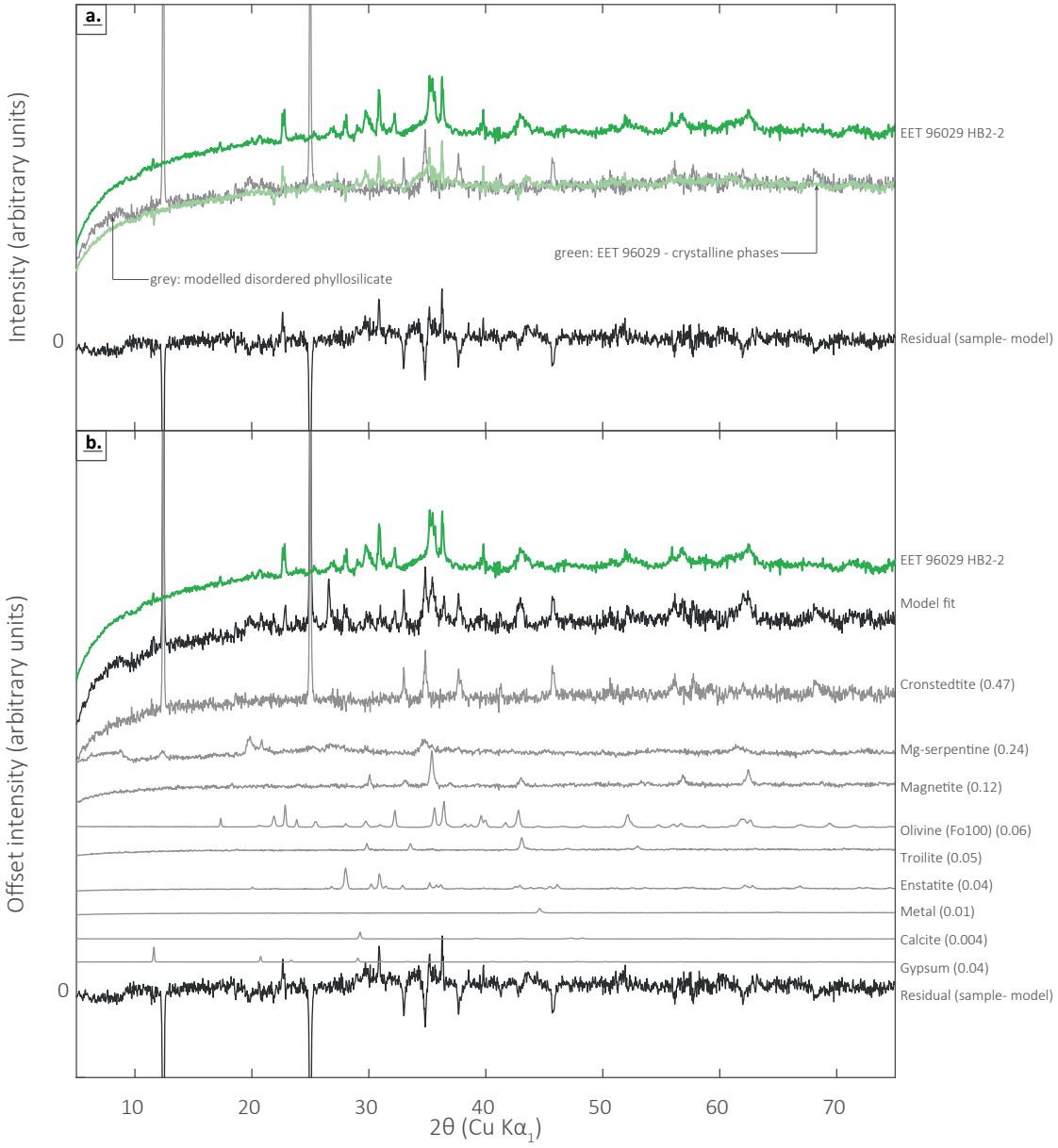
2015a). This process found similar mineral standard factors that were identified using profile-stripping and yielded typical detection limits of ~0.5 - 1 vol% and absolute uncertainties in the modal abundances of 1 - 1.5%.

From the modal mineralogy, a petrologic type based on the PSF was determined (Howard et al., 2015). The PSF expresses the degree of aqueous alteration of CMs as the volume of phyllosilicates divided by the abundance of phyllosilicates plus anhydrous silicates. This then gives a petrologic type, with a phyllosilicate fraction of <0.05 as type 3.0, and >0.95 as type 1.0. For aqueously and thermally metamorphosed samples, King et al. (2018b) showed that a petrologic type could be determined if all disordered phyllosilicate and recrystallised phases were assumed to be hydrated phyllosilicates in the pre-metamorphosed mineralogy.

2.3 Spectroscopy

The visible and infrared wavelengths of light encompass the ~0.4 - ~0.8 µm and ~0.8 - ~1000 µm wavelength ranges, respectively. The infrared is split into the near-infrared (NIR:~0.8 - ~5), mid-infrared (MIR: ~5 - ~50 µm) and far-infrared (FIR: ~50 - ~1000 µm) regions, based on their proximity to the visible spectrum. Spectroscopy makes use of the fact that molecules absorb certain frequencies of light that match the vibrational frequency of the molecule. If atoms or molecules absorb wavelengths within the VIS range, they can undergo electronic transitions, where electrons are excited to a higher energy level. The NIR wavelength range is sensitive to overtone and combination vibrational features within molecules and the MIR is sensitive to fundamental vibrations of molecules. Absorption in the FIR is usually due to rotational vibrations. When multiple wavelengths of light are absorbed by a material, the molecules represented by these absorptions can build a picture of the mineralogy. As discussed in chapter 1, the NIR and MIR are particularly relevant for looking at meteorites

Figure 2.4: *The profile stripping method for EET 96029, which contains disordered phyllosilicate. (a) shows how the background flux of a scaled phyllosilicate pattern (Fe-cronstedtite and Mg-serpentine) can be matched to the background of the meteorite pattern that has all other phases removed, excluding diffraction peaks. Once this phyllosilicate is removed from the meteorite pattern, the residual shows zero counts. (b) shows all individual minerals used in the profile stripping. As with Figure 2.3, mineral patterns are shown multiplied by 32 and then by the scale factor used to scale the mineral standards to the meteorite pattern. Scale factors are in brackets next to the mineral name.*



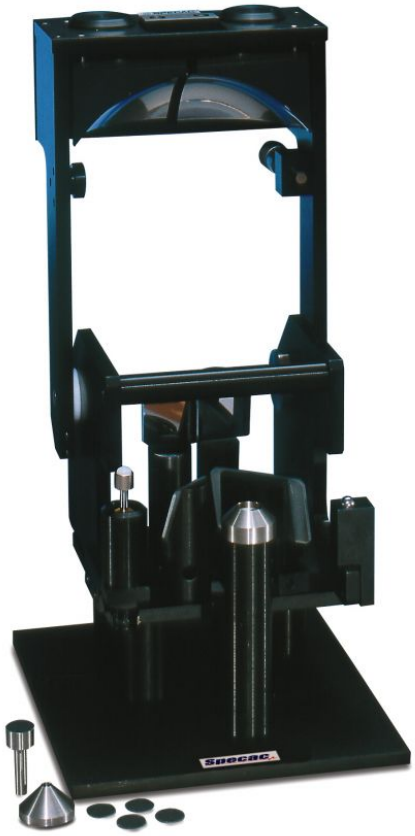
and asteroids as many hydrous and anhydrous rock-forming minerals have features in these ranges.

Fourier transform infrared (FTIR) reflectance spectroscopy is a technique of collecting how much light is absorbed by a material at each wavelength to produce an IR spectrum. An FTIR spectrometer is composed of a source of light, an interferometer, sample compartment and a detector. The source produces a polychromatic beam of infrared radiation that passes through the interferometer to reach the sample. The interferometer consists of a beam splitter and two mirrors (one stationary and one moving), and when the infrared radiation passes through the beam splitter it splits into two beams that are directed to each of the mirrors. These are reflected and are recombined at the beam splitter before being directed at the sample. The distance the two beams travel can vary if the moving mirror is moved closer to or further away from the beam splitter, and the difference in distance the two beams have to travel is referred to as the optical path difference (OPD).

The sample can absorb certain wavelengths of this recombined beam based on its composition and reflect certain wavelengths towards the detector. In the case of rough materials or powdered samples, diffuse reflectance occurs. The beam incident on the sample penetrates the material and can be scattered, absorbed or reflected by a second surface, before leaving the sample. As discussed in chapter 1, in the MIR wavelength range emitted radiation can dominate the spectral flux when observing a remote body. Collecting diffuse reflectance, as opposed to specular reflectance, from samples in the laboratory can more realistically reproduce emissivity (therefore improving comparisons between remote and laboratory measurements), as both are isotropic processes. This diffusely reflected beam is collected by mirrors on a diffuse reflectance selector accessory (Figure 2.5), before being directed towards the detector. The intensity of the reflected beam on the detector after interacting with the sample is controlled by the OPD due to constructive or destructive interference when the beam recombines. The detector records an interferogram, which is a plot of intensity against OPD, and there is a peak when the OPD is 0. This interferogram

is modulated by absorptions due to the sample, and a Fourier transform can be applied to produce an infrared reflectance spectrum.

Figure 2.5: *The Specac Selector diffuse reflectance accessory used to collect the diffusely reflected beams and direct the result towards the spectrometer detector.*



2.3.1 Reflectance spectroscopy

NIR (0.8 - 5 µm) reflectance spectra were collected for the 11 AK-1 CM2, CM1/2 and CM1 samples and the Org-1 and Ivu-1 samples of the CI chondrites. MIR (5 - 50 µm) reflectance spectra were collected for all HB1, HB2, AK-1, Ivu-1 and Org-1 samples. Infrared reflectance spectra were obtained using a Bruker VERTEX 70v FTIR spectrometer in diffuse reflectance geometry with a Specac Selector diffuse reflectance accessory at the Planetary Spectroscopy Facility (PSF) at the University of Oxford. All measurements were obtained under vacuum (~2 hPa) at a spectral resolution of 4 cm^{-1}, and the resulting spectra are the average of

250 scans (chosen so that features with spectral contrast of 2 % were able to be identified from noise (Donaldson Hanna et al., 2019)). A VIS/Q beam splitter and a combination of a Si-diode detector and an Indium Gallium Arsenide (InGaAs) detector were used to measure reflectance between 0.8 - 1.7 µm (12500 - 6000 cm^{-1}). Samples were not heated prior to analysis as this spectral region is unaffected by adsorbed terrestrial water (Gaffey et al., 1993, McAdam et al., 2015). A wide range mid- to far-IR (MIR-FIR) beam splitter and a room temperature deuterated L-alanine doped tryglycine sulfate (RT-DLaTGS) detector were used to measure the reflectance between ~1.7 - 50 µm (6000 - 200 cm^{-1}). For these wavelength ranges, samples were measured after being heated at ~150 ^{o}C for 2.5 hrs, in order to remove the effects of adsorbed water on the resulting spectra (e.g. Takir et al., 2013, Beck et al., 2014). I used two sizes of stainless-steel sample cups, depending on the total mass of the meteorite sample. The sample cups hold 50 mg or 200 mg and the sharp edge of a spatula was used to flatten the top of the sample. Loaded samples were heated in a vacuum oven and then stored in a custom desiccator before spectra were collected. To remove instrument effects, each meteorite spectrum was divided by either the spectrum of a Spectralon (a diffusely reflecting fluoropolymer) (0.8 - 1.7 µm) or diffuse gold calibration target (1.7 - 50 µm) measured using the same experimental parameters and under the same conditions as the samples.

For analysis of the meteorite spectra, several diagnostic parameters were calculated, including spectral slope in the NIR, the position and area of the feature near 3 µm, and the positions of vibrational features, the CF and the TF (chapter 1). Near 15 - 16 µm the beam splitter has a region of low signal-to-noise, so this range is excluded from analysis. For calculation of the NIR spectral slope, spectra were normalised to unity at 0.8 µm and the slope was calculated as the reflectance at ~1.65 µm divided by the reflectance at ~1.05 µm. The point at which reflectance was taken was varied between 1.6 - 1.7 µm and 1.0 -

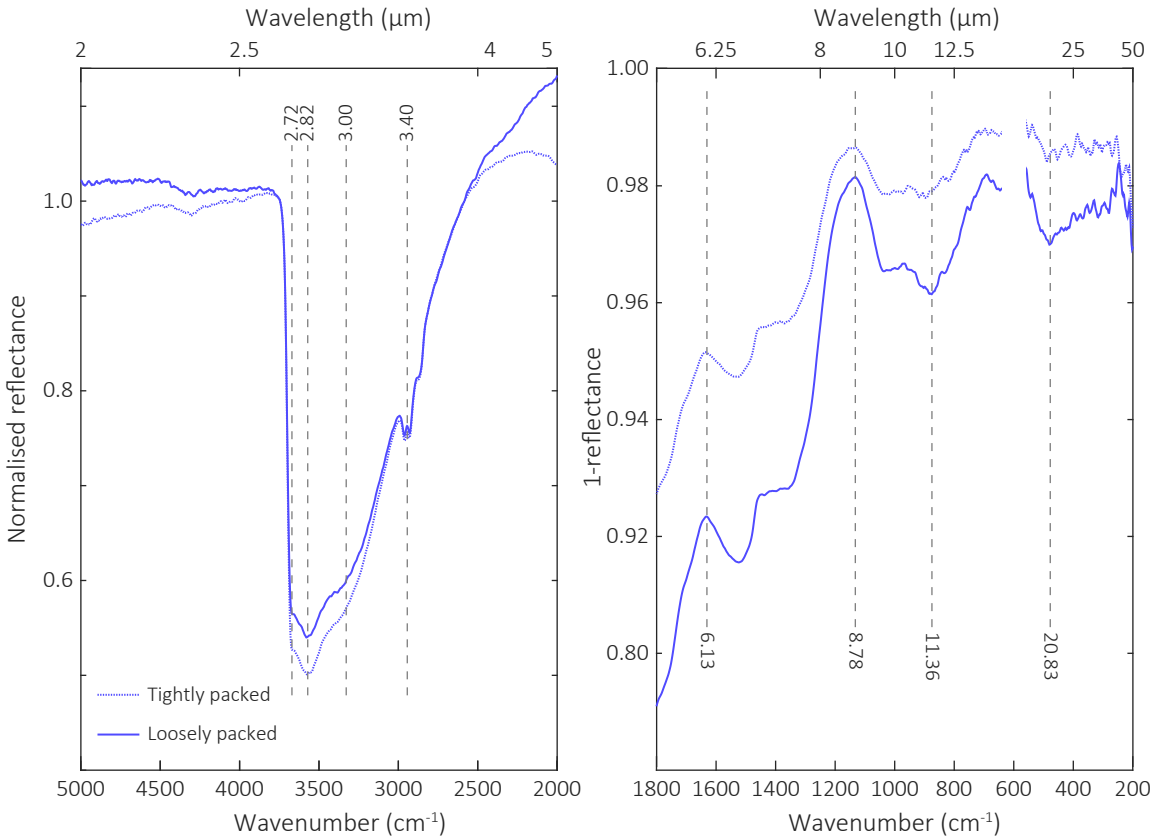
1.1 μm and an average of the spectral slope determined was calculated. These points were chosen to ensure the maximum range without noise or artefacts was used for calculations. The error in the slope was calculated as one standard deviation representing variation from the average.

For analysis of features, the region investigated was isolated and smoothed with a moving average across 10 - 15 wavelength bins, enough to remove noise, but not to the point that the spectral shape of the feature was affected. A wavelength grid was generated across the region with an increment of 2×10^{-4} μm, and at least a 3rd order polynomial was fit across the centre of the feature, which was used to calculate feature position and area (Donaldson Hanna et al., 2012b). Feature position was established to be the point of minimum or maximum reflectance. 3 μm feature area was calculated on normalised spectra by fitting a continuum as a straight line between two points on either side of the feature and calculating the area between the continuum and the continuum removed spectra. The uncertainties are presented as one standard deviation, representing variability from the average of calculated parameters.

2.3.1.1 Sample packing

Spectra are strongly affected by how a sample is prepared and packed, with reductions in spectral contrast and changes in the depth of features (e.g. Salisbury, 1993). In all measurements I attempted to be consistent, however it should be noted that some variations in spectral signature may be a result of minor differences in sample packing. In order to explore the effect of sample packing, the reflectance spectra of one meteorite was measured under two conditions: 'loosely packed' and 'tightly packed'. For both conditions the sample cup was filled fully, however under the tightly packed conditions, the powder was compacted using a spatula. The resulting spectra are shown in Figure 2.6.

Figure 2.6: *Reflectance spectra of the CM2 chondrite Y 793595 under both loosely packed and tightly packed conditions in the (a) NIR and (b) MIR spectral ranges. In the NIR, the spectrum is normalised to a linear continuum between 2.67 – 3.87 µm.*



The mineralogical significance of the spectral parameters identified for these samples will be discussed further in chapter 4, however there are clear differences between the two packing conditions. The band depth of the feature identified at 2.72 µm is qualitatively reduced when the sample was tightly packed, however the area of the whole feature between 2.67 - 3.87 µm calculated for both spectral conditions are within error of each other. Band area of this feature appears to be less affected by packing conditions, and so is a more reliable parameter and will be what I discuss in later chapters. Another key difference is the disappearance of the TF near 11.4 µm under tightly packed conditions. As discussed in chapter 1, the TF is caused by volume scattering in fine particulate, optically thin materials (Salisbury, 1993, Cooper, 2002). Under tightly packed conditions the sample becomes

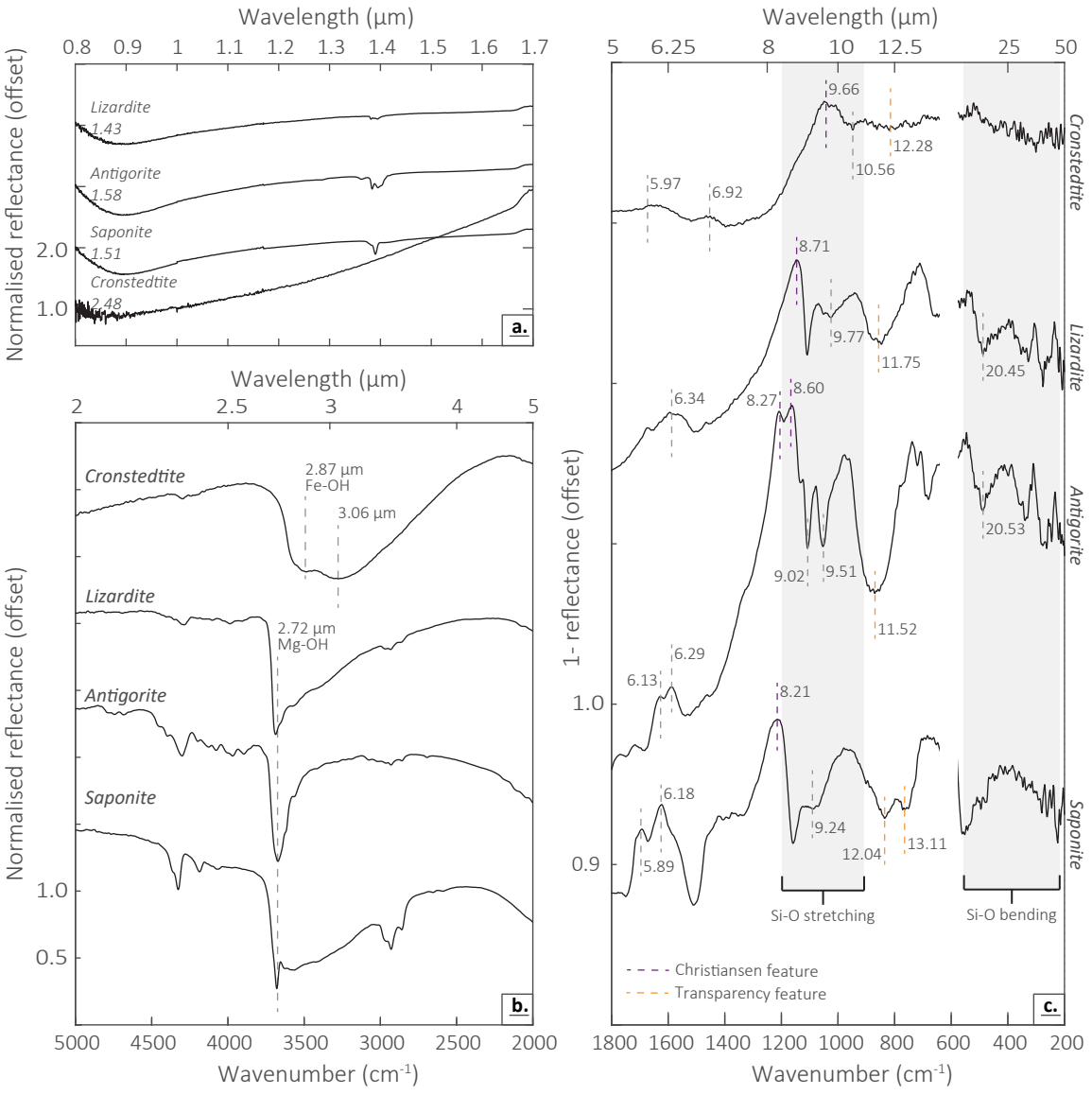
less optically thin and the resulting spectrum looks similar to whole rock and coarse particle spectra that lack TFs. This could prove an issue if packing is not consistent as the position of the TF has been shown to vary with mineralogy, and trends have been identified with its position and aqueous alteration extent (Salisbury et al., 1991, McAdam et al., 2015). Features at longer wavelengths (e.g., the feature at 20.80 µm in Figure 2.6) are also less identifiable under tightly packed conditions, so a lack of feature in this range in other spectra cannot be assumed to be a case of mineralogy but may be a result of packing conditions. In an attempt to alleviate this complication, I tried to be consistent in packing my samples loosely, so the TF and any vibrational features at longer wavelengths can be identified. Other features for both conditions varied in position by less than 0.1 µm across the spectral range, indicating that feature position is likely a reliable spectral parameter as it is not strongly affected by packing.

2.3.1.2 Standard spectra

I collected the NIR and MIR reflectance spectra of several phyllosilicate standards using the methodology described in section 2.4.1 (Figure 2.7). These included the serpentine phyllosilicates lizardite, antigorite and cronstedtite, and the smectite phyllosilicate saponite (Table B.1).

The spectra of the phyllosilicate standards match well with previous measurements of similar minerals across the same wavelength ranges (e.g. Christensen et al., 2000, Bishop et al., 2008, Baldridge et al., 2009, Cloutis et al., 2011a, Takir et al., 2013). The Fe-cronstedtite spectrum shows a rounded feature near 3 µm, with two minima that can be identified at 2.87 µm and 3.06 µm. The 3.06 µm feature in this Fe-cronstedtite spectral measurement was also observed by Takir et al. (2013) in an unheated Fe-cronstedtite spectrum. They suggested this may indicate rust in the sample, as Fe-(oxy)hydroxides are known to have

Figure 2.7: *(a) NIR spectra for the phyllosilicate standards, normalised to unity at 0.8 µm and offset (Saponite + 1, Antigorite + 2, Lizardite + 3). Ratios are calculated as the reflectance at 1.65 µm divided by the reflectance at 1.05 µm and are included in the figure. (b) shows the 3 µm feature for the phyllosilicate standards, normalised to a continuum between 2.67 – 3.87 µm and offset (Antigorite + 1, Lizardite + 2, Cronstedtite + 3). (c) shows the MIR spectra for the phyllosilicate standards. Spectra are plotted as 1 – reflectance and offset (Antigorite + 0.2, Lizardite + 0.3, Cronstedtite + 0.4). Christiansen and transparency features are noted, and the regions of Si-O stretching and bending vibrations are highlighted.*



features near 3.06 µm (Bishop et al., 1993, Pommerol et al., 2009), however XRD patterns of the same standard sample show no other phases present. I therefore assume this is a

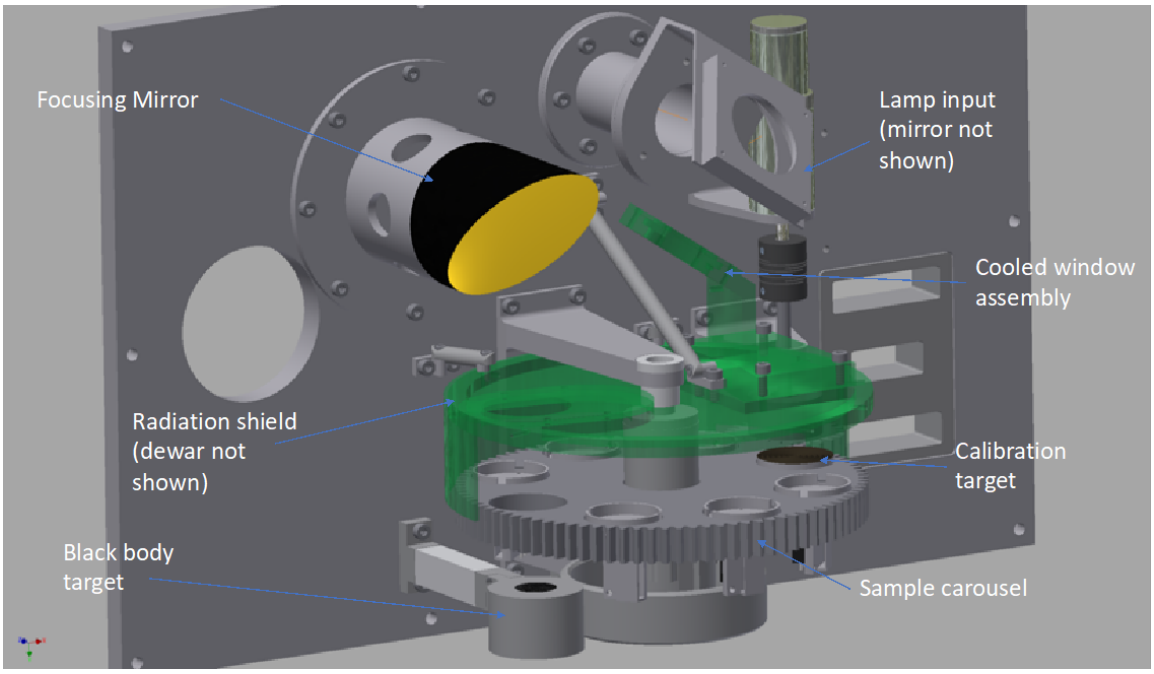
feature caused by the cronstedtite crystal structure.

2.3.2 Emission spectroscopy

Direct comparison of laboratory reflectance spectra to remotely observed bodies is challenging due to the dominance of emitted radiation in the MIR wavelengths. Whilst diffuse reflectance can approximate emissivity, the optimum method involves collecting emissivity spectra under appropriate environmental conditions. This is possible using the Planetary Analogue Surface Chamber for Asteroid and Lunar Environments (PASCALE) at the Planetary Spectroscopy Facility at the University of Oxford (Figure 2.8). The chamber is mounted to the same BRUKER VERTEX 70v spectrometer that reflectance measurements were made in. The chamber has a sample carousel, which includes integrated calibration targets, surrounded by a radiation shield painted with Nextel black paint. This shield is attached to a liquid nitrogen dewar for cooling and has multiple layers of insulation. Samples in the carousel can be heated from below and above using a sample cup heater and a quartz-halogen lamp, respectively. The thermally emitted radiation from the samples is collected using a series of mirrors and directed into the spectrometer, which is held under vacuum, via a CsI window.

Emissivity spectra were collected for the HB2 samples under ambient (Earth-like) and simulated asteroid environment (SAE) conditions. Sample cups are designed to adequately replicate the thermal gradient expected on an airless body and to create an area within the sample cup that has a fairly homogeneous thermal gradient for sampling by the FTIR spectrometer. The sample cups require ~1.4 g of material to be filled fully. The same powders for which XRD and reflectance spectroscopy were collected were used for emissivity spectral analysis. MIR emissivity measurements between 5.5 - 50 µm were collected at a resolution

Figure 2.8: *CAD model of PASCALE sample carousel and calibration targets. The radiation shield is shown in cut-away for clarity.*

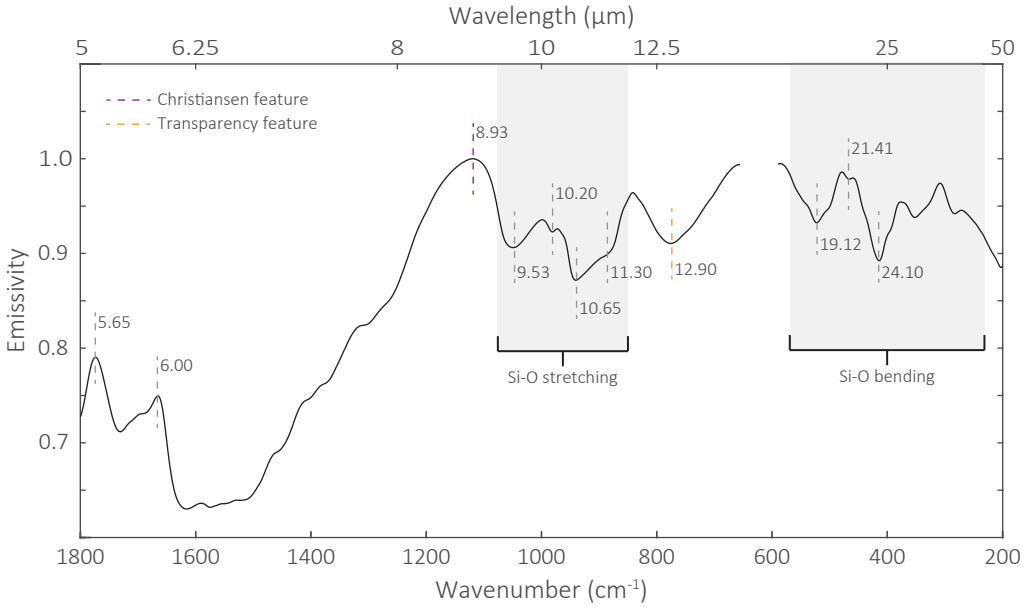


of 4 cm^{-1} using the same wide range beam splitter and a DLaTGS detector as used for reflectance. For each spectrum, three repeat measurements were made, each one including 250 scans.

Under ambient conditions the environment chamber is backfilled with dry nitrogen gas to an atmospheric pressure of ~1000 mbar and maintained at an ambient temperature. Each sample is heated from below to a temperature of ~80 °C. Figure 2.9 shows the emissivity spectrum between 5.5 - 50 µm of San Carlos olivine (~Fo_{91}) collected under ambient environmental conditions in PASCALE. The spectrum matches well with previous emissivity measurements of olivine with a similar Fo composition (Hamilton, 2010, Lane et al., 2011), showing a CF at 8.93 µm and a TF at 12.90 µm.

The near-surface environment of an airless body was simulated by removing atmospheric gases (<10^{-4} mbar), cooling the interior of the chamber to <-150 °C and heating samples from above and below until the maximum brightness temperature of the sample

Figure 2.9: *The emissivity spectrum of San Carlos Olivine.*



was ~75 °C (Donaldson Hanna et al., 2019). This induces a thermal gradient in the upper hundreds of microns of the sample, which is what we would expect on the surface of an airless body such as the OSIRIS-REx target asteroid Bennu near local midday (Hergenrother et al., 2014). Spectra were calibrated using published techniques (Ruff et al., 1997) and measurements of a target painted with Nextel high emissivity black paint at two temperatures (~67 and ~87 °C) which is consistent with previous studies (e.g. Thomas et al., 2012, Donaldson Hanna et al., 2019). For identification of features, the same approach to the reflectance spectra analysis was used. Spectra were compared to standard spectra, features of interest isolated, and their position calculated using the same methodology as described in section 2.3.1.

Chapter 3: Linking the reflectance spectroscopy and mineralogy of highly aqueously altered CM and CI carbonaceous chondrites

3.1 Introduction

This chapter was published as Bates, H. C, King, A. J, Donaldson Hanna, K. L., Bowles, N. E., Russell, S. S, 2020, Linking mineralogy and spectroscopy of hydrated CM and CI carbonaceous chondrites in preparation for primitive asteroid sample return, Meteoritics and Planetary Science, 55, 77 - 101, doi:10.1111/maps.13411. The mineralogy and spectra of the meteorites ALH 83100, ALH 83102, LEW 85311, LEW 90500 and LON 94101 were not included in the published study.

One of the key science questions introduced in chapter 1 was whether there are spectral trends and parameters that correlate with mineralogy of highly aqueously altered CM and CI chondrites (question A-1). Highly aqueously altered CM and CI chondrites have been suggested as good analogues for the surfaces of Ceres, Bennu and Ch and Cgh type asteroids (Bus-DeMeo scheme) in the main asteroid belt (Rivkin et al., 2015, Takir et al., 2015, De Sanctis et al., 2015, 2018, McSween et al., 2017, Hamilton et al., 2019). However, most previous spectral studies have instead focused on the partially altered CM2 chondrites (Salisbury et al., 1991, Cloutis et al., 2011b, McAdam et al., 2015, Beck et al., 2018), and if type 1 chondrites are included, they're treated more as endmembers of the petrologic sequence. This chapter therefore focuses on establishing trends in reflectance spectra with aqueous alteration extending into the highly aqueously altered petrologic type 1 chondrites, as these

relationships will be used to infer asteroid surface mineralogy and alteration histories (which will be explored in chapter 6). A number of spectral parameters are discussed: the near infrared (NIR) spectral slope, the position and area of the hydroxyl stretching feature near 3 µm, the Christiansen feature (CF) and the transparency feature (TF).

3.2 Experimental

In this chapter, 18 meteorite samples, ranging from partially aqueously altered CM2 chondrites to fully hydrated CM1 and CI1 chondrites were investigated. For 13 of these samples, modal mineralogy was determined by King et al. (2015a) and King et al. (2017b) (section 2.1.1). I also determined the modal mineralogy using PSD-XRD of samples of the CM1/2 ALH 83100, and the CM2s ALH 83102, LEW 85311, LEW 90500 and LON 94101 to increase the petrologic range studied. The PSD-XRD methodology is described in detail in section 2.2.2: modal mineralogy of powdered samples (<35 µm particle size) was determined from XRD patterns collected with a curved PSD using a peak stripping method developed by Cressey and Schofield (1996) (Fig 2.3). For ALH 83100, ALH 83102 and LON 94101, enough sample (Table 2.1) was available to collect XRD patterns from two aliquots of 50 mg (HB2-1 and HB2-2) in order to evaluate whether the samples were homogenised during the grinding of the sample chips.

This chapter presents the NIR reflectance spectra between 1.0 - 1.7 µm of the 13 samples analysed by King et al. (2015a) and King et al. (2017b), and the NIR and MIR reflectance spectra between 2 - 50 µm for all 18 aqueously altered CM and CI samples. Also presented is the NIR and MIR spectra of a sample of the CM2 Murchison. This meteorite was included because it is one of the most studied CM chondrites, and it has a higher petrologic type; 2.5 in the Rubin scheme (Rubin et al., 2007), 1.6 in the Alexander scheme (Alexander et al., 2013) and a PSF petrologic type of 1.5 (Howard et al., 2015), compared to most of the

CM samples in this study. Howard et al. (2015) determined the modal mineralogy for two Murchison samples, and found little variation in the bulk mineralogy. As such, I will use the average modal mineralogy quoted by Howard et al. 2015 when discussing the Murchison spectrum.

Details about the methodology used to collect spectra are described in chapter 2. Briefly, diffuse reflectance spectra were collected from powdered samples. MIR observations were made before and after heating the sample for 2.5 hours in a vacuum oven, in order to reduce spectral effects from terrestrial adsorbed water. The samples of ALH 83100, ALH 83102 and LON 94101 had sufficient mass (Table 2.1) to use the larger sample cup (200 mg) when collecting reflectance spectra. The other meteorite samples used the smaller sample cup (50 mg). Diagnostic spectral features were identified and compared to standard spectra I collected as well as published standard spectra.

3.3 Results

3.3.1 Modal mineralogy of ALH 83100, ALH 83102, LEW 85311, LEW 90500 and LON 94101

Figure 3.1 shows PSD-XRD patterns for LEW 85311, LEW 90500, ALH 83100, ALH 83102 and LON 94101. Each pattern has diffraction peaks at ~12^{o} and ~25^{o}, consistent with Fe-cronstedtite, and broad features near ~19^{o} and ~61^{o}, which are due to Mg-serpentine, indicating the presence of phyllosilicates in these meteorites. These peaks are typical of CM chondrites (Howard et al., 2009, 2011, 2015, King et al., 2017b). The sample of LEW 85311 consists of 17 vol% primary olivine, 15 vol pyroxene, 1 vol% magnetite, <1 vol% Fe-sulfide, <1 vol% metal, 2 vol% gypsum (likely terrestrial, Lee, 1993) and 64 vol% phyllosilicate, giving a PSF petrologic type of 1.7. The XRD pattern and mineral abundances are consistent with those given by Lee et al. (2019) (section 2.1.1) and indicate that LEW 85311 is one of

the least altered CM chondrites (Howard et al., 2015). The bulk modal mineralogy of LEW 90500 is 10 vol% primary olivine, 3 vol% pyroxene, 1 vol% magnetite, <1 vol% Fe-sulfide, carbonate, and metal, and 83 vol% phyllosilicate, giving a PSF petrologic type of 1.3. This suggests it is more aqueously altered than the sample of LEW 90500 investigated by Howard et al. (2015), which had a PSF petrologic type of 1.5. The XRD patterns of both LEW 85311 and LEW 90500 also show a diffraction peak near 16° that is consistent with the presence of tochilinite. As there was no tochilinite standard pattern available for the peak stripping, I was unable to determine its abundance, however as the final residual for both meteorite patterns following subtraction of all other mineral phases was zero it can be assumed that the tochilinite abundance is likely minor (<2 vol%, Howard et al., 2009, 2015, King et al., 2017b).

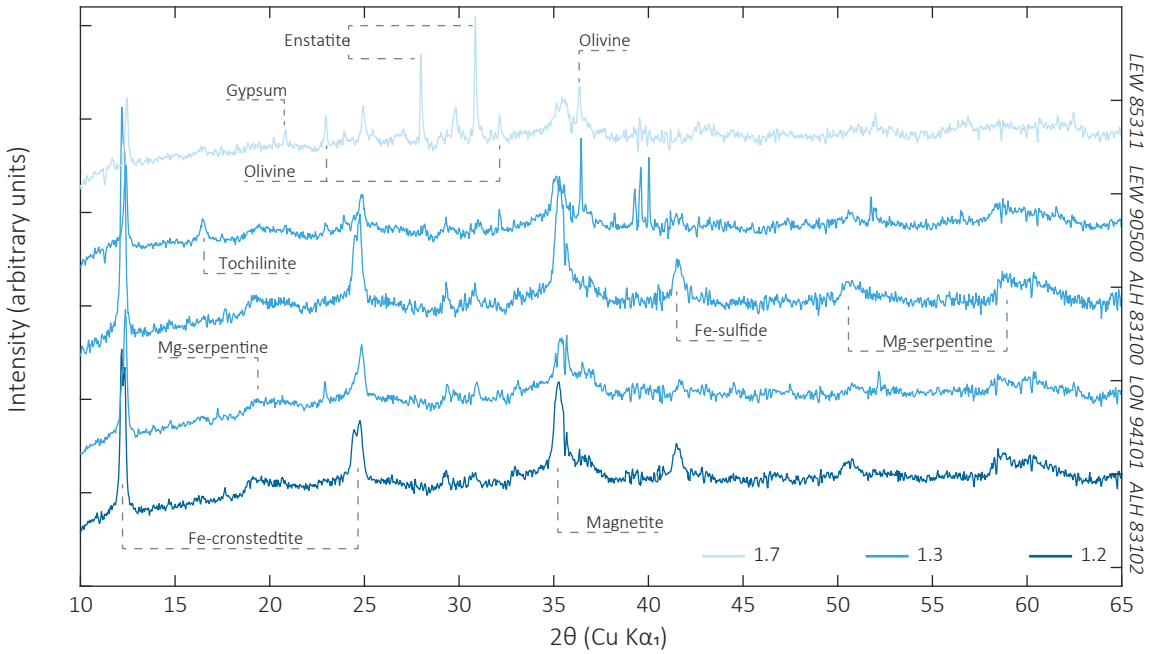


Figure 3.1: *PSD-XRD patterns for LEW 85311, LEW 90500, ALH 83100, LON 94101 and ALH 83102. Patterns are offset on the y axis.*

The subsamples of ALH 83100, ALH 83102 and LON 94101 showed a similar mineralogy, with mineral abundances within error of each other (Table 3.1), demonstrating samples

were homogenised before the aliquots were removed. In the following text I will refer to an average mineralogy for each of these samples. The modal mineralogy for the ALH 83100 sample is 8 vol% unaltered olivine, 4 vol% pyroxene, 4 vol% magnetite, 1 vol% Fe-sulfide, 1 vol% carbonate and 82 vol% phyllosilicate. This gives a PSF petrologic type of 1.3, which indicates my subsample is slightly less aqueously altered than the sample of the same meteorite investigated by Howard et al. (2015), which had a petrologic type of 1.2. ALH 83102 has been reported to be paired with ALH 83100 (Grossman, 1994) but has not previously been analysed using PSD-XRD. Its modal mineralogy consists of 7 vol% unaltered olivine, 2 vol% pyroxene, 3 vol% magnetite, 1 vol% Fe-sulfide, <1 vol% carbonate and 86 vol% phyllosilicate. This gives a PSF petrologic type of 1.2, suggesting it is slightly more aqueously altered than the ALH 83100 sample in this study. The bulk modal mineralogy of the sample of LON 94101 in this study is ~9 vol% unaltered olivine, 3 vol% pyroxene, 2 vol% magnetite, <1 vol% Fe-sulfide and carbonate, and 86 vol% phyllosilicate. This gives a PSF petrologic type of 1.3, which is consistent with the PSF petrologic type determined for LON 94102 (which is paired with LON 94101) by Howard et al. (2015).

3.3.2 NIR

Figure 3.2 shows the spectra between 0.8 and 1.7 µm for the 13 CM2, CM1/2, CM1 and CI1 chondrites characterised by King et al. (2015a) and King et al. (2017b). Figure 2.7a in chapter 2 shows the same wavelength range for the phyllosilicate standards. The meteorite spectra lack strong absorption features and generally show a red slope (increasing reflectance with increasing wavelength). NWA 8534, NWA 4765 and Moapa Valley show the flattest spectra, with slopes of 0.96, 0.98 and 1.08, compared to the steeper slopes (1.23 - 1.61) of the other CMs. Orgueil and Ivuna show spectral slopes of 1.35 and 1.37 respectively (Table 3.2)

The red slopes are partly influenced by particle size (Cloutis et al., 2011b), however meteorite samples (and standards) were all prepared in the same way and have similar

Sample		Classification	PSF Petrologic Type	Olivine (vol%)	Enstatite (vol%)	Magnetite (vol%)	Sulfide (vol%)	Carbonates (vol%)	Gypsum (vol%)	Ferrihydrite (vol%)	Metal (vol%)	Fe-cronstedtite (vol%)	Mg-serpentine (vol%)	Mg-serpentine/Fe-cronstedtite	Total Phyllosilicate (vol%)
LEW 85311	**HB1**	**CM2**	**1.7**	**17**	**15**	**1**	**1**	**-**	**2**	**-**	**<1**	**39**	**25**	**0.6**	**64**
LAP 031214	AK1	CM2[a]	1.5	18	6	2	1	1	<1	-	-	31	40	1.3	71
Murchison	-	CM2	1.5	15	8	1	2	1	-	-	-	50	22	0.4	73
MCY 05231	AK-1	CM2[a]	1.5	20	3	2	1	1	-	-	-	37	36	1.0	73
LEW 90500	**HB1**	**CM2**	**1.3**	**10**	**3**	**1**	**1**	**1**	**1**	**-**	**<1**	**24**	**58**	**2.4**	**83**
ALH 83100	**HB2-1**	**CM1/2**	*1.3*	*10*	*4*	*5*	*1*	*1*	*-*	*-*	*-*	*23*	*56*	*2.4*	*79*
	HB2-2		*1.2*	*7*	*3*	*4*	*1*	*1*	*-*	*-*	*-*	*17*	*67*	*3.9*	*84*
	Ave.		**1.3**	**8**	**4**	**4**	**1**	**1**	**-**	**-**	**-**	**20**	**62**	**3.0**	**82**
LON 94101	**HB2-1**	**CM2**	*1.3*	*9*	*3*	*2*	*1*	*1*	*-*	*-*	*-*	*26*	*59*	*2.3*	*85*
	HB2-2		*1.3*	*9*	*3*	*2*	*1*	*1*	*-*	*-*	*-*	*19*	*67*	*3.6*	*87*
	Ave.		**1.3**	**9**	**3**	**2**	**1**	**1**	**-**	**-**	**-**	**22**	**63**	**2.8**	**85**
ALH 83102	**HB2-1**	**CM2**	*1.3*	*8*	*3*	*3*	*1*	*1*	*-*	*-*	*-*	*18*	*66*	*3.7*	*84*
	HB2-2		*1.2*	*7*	*1*	*3*	*1*	*1*	*-*	*-*	*-*	*17*	*70*	*4.2*	*87*
	Ave.		**1.2**	**7**	**2**	**3**	**1**	**1**	**-**	**-**	**-**	**17**	**68**	**3.9**	**86**
GRO 95645	AK-1	CM1	1.2	8	-	3	3	1	-	-	-	32	52	1.6	84
MIL 090288	AK-1	CM1/2	1.2	4	3	2	2	1	3	-	-	18	66	3.6	84
NWA 8534	AK-1	CM1/2	1.2	5	2	3	2	1	-	-	-	20	68	3.4	88
LAP 031166	AK-1	CM1/2	1.2	5	2	2	1	1	2	-	-	22	65	3.0	87
NWA 4765	AK-1	CM1	1.2	4	2	3	2	1	-	-	-	16	72	4.5	88
LAP 02277	AK-1	CM1	1.2	5	-	2	2	2	-	-	-	21	68	3.3	89
Moapa Valley	AK-1	CM1	1.1	4	-	3	4	1	-	-	-	20	67	3.3	88
MIL 07689	AK-1	CM1	1.1	4	-	3	<1	<1	2	-	-	21	70	3.4	90
MIL 05137	AK-1	CM1	1.1	4	-	3	2	1	2	-	-	18	71	4.0	89
Orgueil	Org-1	CI1	1.1	-	-	7	6	-	1	2	-	-	-	-	84
Ivuna	Ivu-1	CI1	1.1	-	-	8	6	2	-	-	-	-	-	-	84

Table 3.1: *The modal mineralogy of the aqueously altered CM2, CM1/2, CM1 and CI1 chondrites. Numbers in bold are my calculations, numbers for the CM1/2 and CM1 chondrites not in bold were determined by King et al. (2017b) and the CI chondrite mineralogy was determined by King et al. (2015a). The Murchison mineralogy is an average from the values determined for two different Murchison samples by Howard et al. (2015), who found the samples to have mineral abundances within error of each other.* [a]*These meteorites are officially classified as CM1/2, however King et al. (2017b) suggested they are CM2s.*

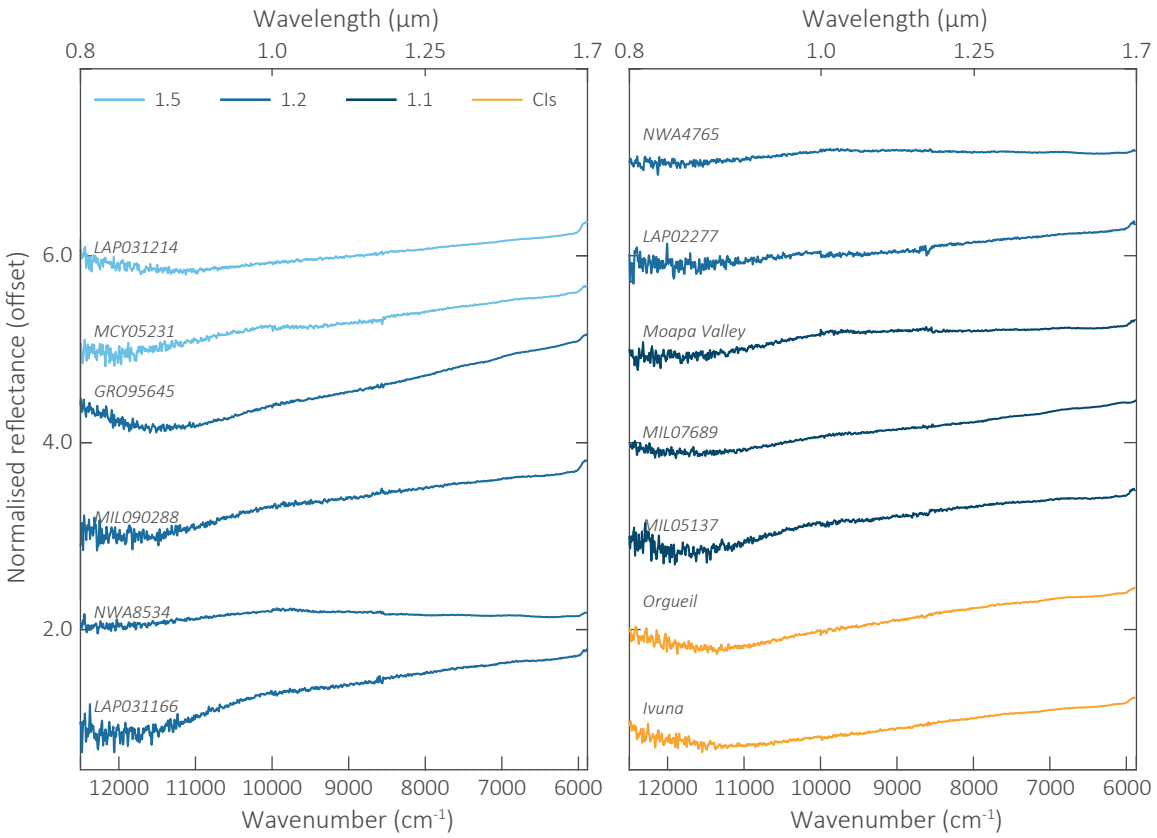


Figure 3.2: *NIR spectra of CM1/2, CM1 and CI1 chondrites, normalised to unity at 0.8 µm and offset on the y axis (+ a multiple of 1). The spectra do not show strong features but do exhibit an increase in reflectance with increasing wavelength (red slope).*

particle sizes of <35 µm (e.g. King et al., 2015a, 2017b), so any variation in slope within the suite should be a function of mineralogy. Based on this assumption, the spectral red slope in most of the meteorite samples is likely due to their high phyllosilicate abundances (71 - 90 vol%), as the representative mineral end members also show red spectral slopes (Fig. 2.7a).

All the meteorite spectra show a large, asymmetric absorption feature between 2.70 - 4.00 µm (Fig. 3.3, Table 3.2), suggesting they all contain mineral phases that have bound -OH or H_2O. As the samples were heated prior to measurement, and spectra were collected under vacuum, I attribute these features to the presence of hydrated mineral phases rather

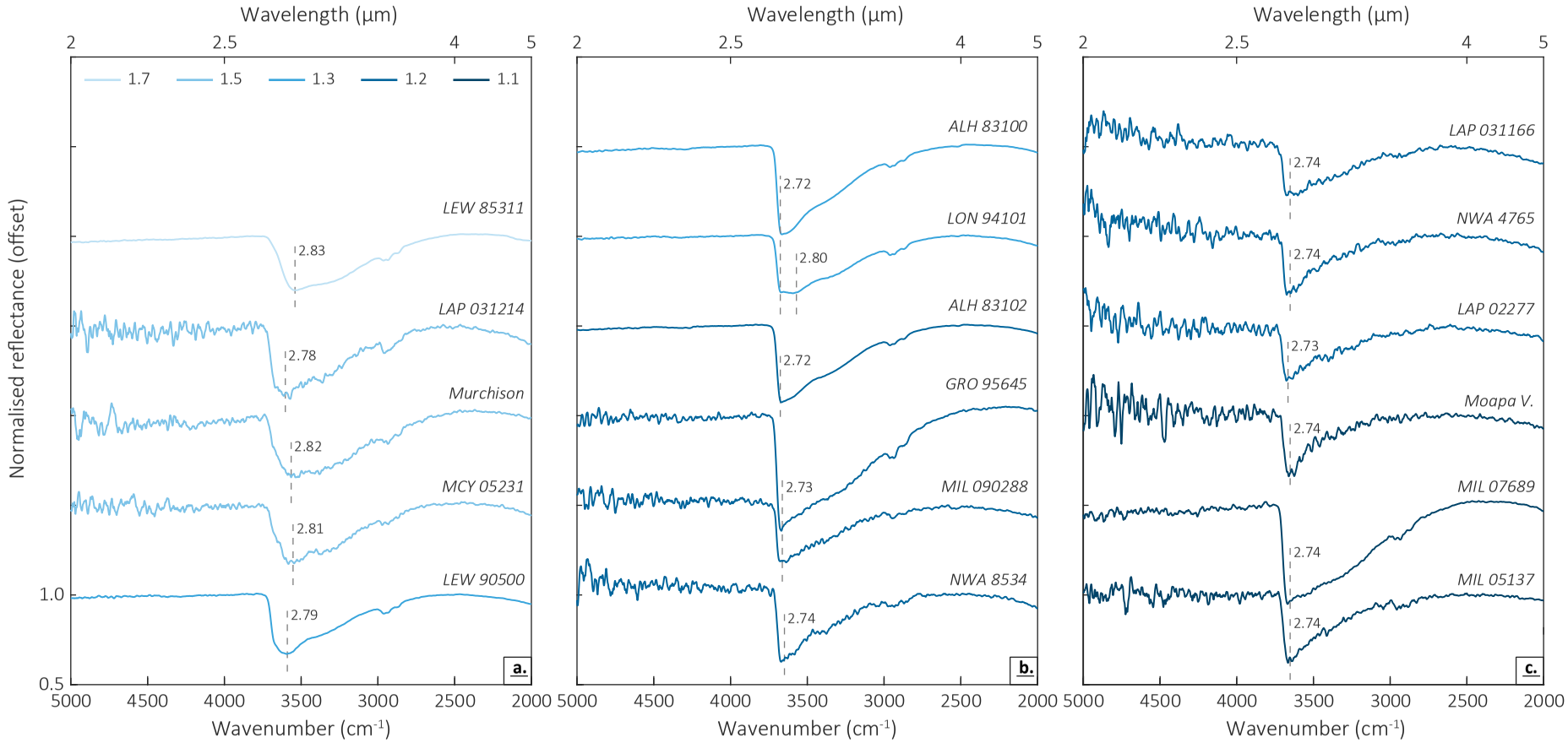


Figure 3.3: *The 3 µm feature for the CM2, CM1/2 and CM1 chondrites, which are ordered by increasing aqueous alteration. Spectra are continuum normalised and offset on the y axis (+ a multiple of 0.5). The features are characterised by a centre between 2.73 – 2.83 µm, the location of which depends on the phyllosilicate composition. Some samples also show a minor feature at 3.40 µm attributed to organics.*

Sample	Classification	NIR slope	3 μm feature (μm)	3 μm feature area (μm^{-1})	6 μm feature (μm)	Christiansen feature (μm)	Transparency feature (μm)
LEW 85311	CM2	-	2.83 ± 0.01	0.16 ± 0.01	6.08 ± 0.01	8.58 ± 0.02	12.20 ± 0.03
LAP 031214	CM2[a]	1.38 ± 0.08	2.78 ± 0.01	0.15 ± 0.03	6.13 ± 0.01	8.98 ± 0.02	11.82 ± 0.06
Murchison	CM2	-	2.82 ± 0.01	0.18 ± 0.02	6.14 ± 0.01	9.12 ± 0.04	12.51 ± 0.07
MCY 05231	CM2[a]	1.31 ± 0.04	2.81 ± 0.01	0.14 ± 0.02	6.15 ± 0.01	9.10 ± 0.03	12.31 ± 0.09
LEW 90500	CM2	-	2.79 ± 0.01	0.13 ± 0.02	6.15 ± 0.01	8.93 ± 0.02	11.33 ± 0.03
ALH 83100	CM1/2	-	2.72 ± 0.01	0.16 ± 0.04	6.15 ± 0.01	8.88 ± 0.02	11.50 ± 0.01
LON 94101	CM2	-	2.80 ± 0.01	0.14 ± 0.03	6.24 ± 0.03	8.88 ± 0.01	11.28 ± 0.03
ALH 83102	CM2	-	2.72 ± 0.01	0.14 ± 0.04	6.15 ± 0.02	8.82 ± 0.02	11.29 ± 0.05
GRO 95645	CM1	1.61 ± 0.10	2.73 ± 0.01	0.26 ± 0.06	6.15 ± 0.01	8.86 ± 0.03	11.53 ± 0.10
MIL 090288	CM1/2	1.24 ± 0.05	2.73 ± 0.01	0.09 ± 0.04	6.14 ± 0.01	9.01 ± 0.05	11.73 ± 0.07
NWA 8534	CM1/2	0.96 ± 0.01	2.74 ± 0.01	0.10 ± 0.03	6.26 ± 0.01	9.05 ± 0.06	11.74 ± 0.06
LAP 031166	CM1/2	1.28 ± 0.04	2.74 ± 0.01	0.08 ± 0.03	6.10 ± 0.01	8.88 ± 0.04	11.36 ± 0.10
NWA 4765	CM1	0.98 ± 0.04	2.74 ± 0.01	0.06 ± 0.03	6.18 ± 0.02	8.88 ± 0.05	11.53 ± 0.10
LAP 02277	CM1	1.25 ± 0.03	2.73 ± 0.01	0.06 ± 0.04	6.19 ± 0.03	8.96 ± 0.05	11.67 ± 0.08
Moapa Valley	CM1	1.08 ± 0.03	2.74 ± 0.01	0.05 ± 0.03	6.24 ± 0.05	9.06 ± 0.06	11.95 ± 0.09
MIL 07689	CM1	1.3 ± 0.04	2.74 ± 0.01	0.23 ± 0.05	6.17 ± 0.01	8.85 ± 0.03	11.62 ± 0.08
MIL 05137	CM1	1.23 ± 0.04	2.74 ± 0.01	0.09 ± 0.04	6.13 ± 0.01	9.01 ± 0.05	11.69 ± 0.07
Orgueil	CI1	1.35 ± 0.06	2.72 ± 0.01	0.23 ± 0.01	6.12 ± 0.02	8.79 ± 0.03	11.58 ± 0.06
Ivuna	CI1	1.37 ± 0.06	2.72 ± 0.01	0.22 ± 0.01	6.10 ± 0.03	8.80 ± 0.02	11.56 ± 0.08

Table 3.2: *The NIR and MIR parameters determined for the highly aqueously altered CI and CM chondrite samples. Dashes represent those samples were not analysed over that wavelength range.*

than adsorbed terrestrial water. There may still be some water trapped in high-energy sites that may contribute to the 3 μm feature (Beck et al., 2010), however TGA shows most of the molecular and mesopore water is removed on heating up to 150 - 200 ^{o}C (Garenne et al., 2014). The LEW 85311, LAP 031214, Murchison, MCY 05231 and LEW 90500 spectra show rounded features, with centres between 2.79 - 2.83 μm (Fig. 3.3a), whereas the other CM1/2 and CM1 chondrite spectra have much sharper features, with centres between 2.73 - 2.74 μm (Figs. 3.3b and 3.3c). The LON 94101 spectrum seems to show two features in this region, at 2.72 and at 2.80 μm (Fig. 3.3b), suggesting it could represent a transitional feature between the more and less aqueously altered sample spectra. Most meteorite spectra also show a minor feature near 3.40 μm, which in previous studies has been attributed to organics (Takir et al., 2013). Band areas in this region are between 0.05 and 0.18 μm^{-1}, except for MIL 07689 and GRO 95645, which have larger band areas of 0.23 μm^{-1} and 0.26 μm^{-1}, respectively (Table 3.2).

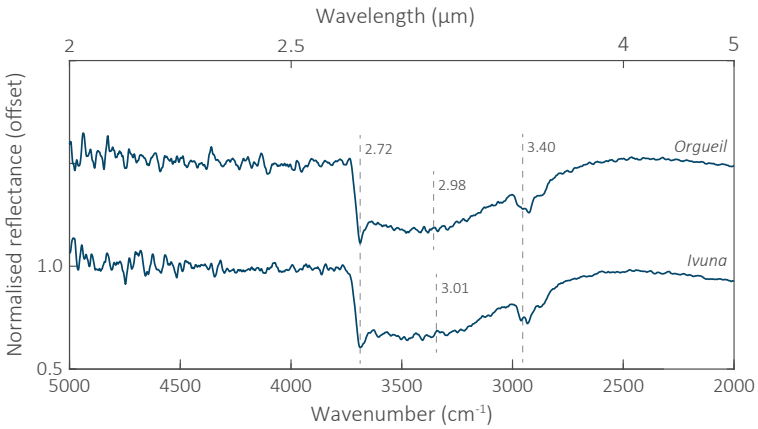


Figure 3.4: *The 3 μm feature for the CI chondrites Orgueil and Ivuna. The blue spectra reflect the PSF petrologic type 1.1. Spectra are continuum normalised and offset on the y axis (Ivuna + 0.5). There are three components to the 3 μm feature in the CIs: at 2.72 μm due to Mg-OH at 2.72 μm, at ~3.00 μm due to bound H_2O and at 3.40 μm due to organics.*

Spectra of the CI1 chondrites Orgueil and Ivuna show a sharp feature at 2.72 μm, alongside a broader feature centred at 2.98 and 3.01 μm, respectively (Fig. 3.4). The band area is 0.23 μm^{-1} for Orgueil and 0.22 μm^{-1} for Ivuna, and spectra for both also show an organic feature near 3.40 μm. The shape and position of these features in my meteorite spectra are similar to the features in the spectra of the phyllosilicate standards I measured, and are consistent with previous spectral measurements in other carbonaceous chondrites (e.g. Takir et al., 2013).

3.3.3 MIR

Figures 3.5 and 3.6 show the MIR spectra of the CM2, CM1/2, CM1 and CI1 chondrites. Figure 2.7c in chapter 2 shows the MIR spectra for the phyllosilicate standards and Figure 2.9 shows the MIR emissivity spectrum for San Carlos Olivine. In the 5.0 - 6.5 μm range, all the CM chondrite spectra show a feature between 6.08 - 6.26 μm. The CI1 chondrite spectra also show features in this region, at 6.12 μm and 6.10 μm respectively (Fig. 3.6). Between 5 - 7 μm, Si-O, -OH and H_2O all have vibrational features, and as such all standard spectra also show features in this region (Figs. 2.7c and 2.9). As with the 3 μm feature, there is a

possibility that some water remains in high-energy sites and could be contributing to these features (Beck et al., 2010). Additionally, some organics are known to have features in this region, for example carbonyl near 5.9 µm and aromatic carbon near 6.25 µm (Battandier et al., 2018). However, due to the presence of features between 5.0 - 6.5 µm in the silicate standards, and because my samples were heated prior to measurement and spectra were collected under vacuum, I assume that these spectral features are related to mineralogy rather than adsorbed terrestrial water. Due to their high abundance in CM and CI chondrites, I propose the features in this region are more likely associated with hydrated phyllosilicates rather than anhydrous silicate minerals. This is consistent with the spectra, as the positions of the 6 µm features plot within the phyllosilicate range, and the vibrational features in olivine are observed at shorter wavelengths (~5.65 and 6.00 µm, Fig. 2.9).

Most spectra show features between 6.9 - 7.2 µm, the positions of which are consistent with carbonates (Lane and Christensen, 1997, Beck et al., 2018). It should be noted that features in this range are also observed in the cronstedtite and saponite phyllosilicate spectra (Fig. 2.7c). Carbonates are detected in all meteorite samples except for the CM LEW 85311 and the CI Orgueil. Beck et al. (2018) discussed the possibility of identifying Ca- and Mg-rich carbonate components based on the position of the features in this region, however there is not a strong difference between the position of the feature in the CI Ivuna spectrum, which contains dolomite, and the features in the CM spectra, which tend to contain more calcite. The Orgueil spectrum shows a feature in this region, however no carbonates were identified in the PSD-XRD pattern (therefore abundance was not determined). This might imply that the features in smectite phyllosilicates may be more responsible for features in this range in the CI chondrite spectra. Dolomite has however been observed in petrographic observations of Orgueil (Endress and Bischoff, 1996).

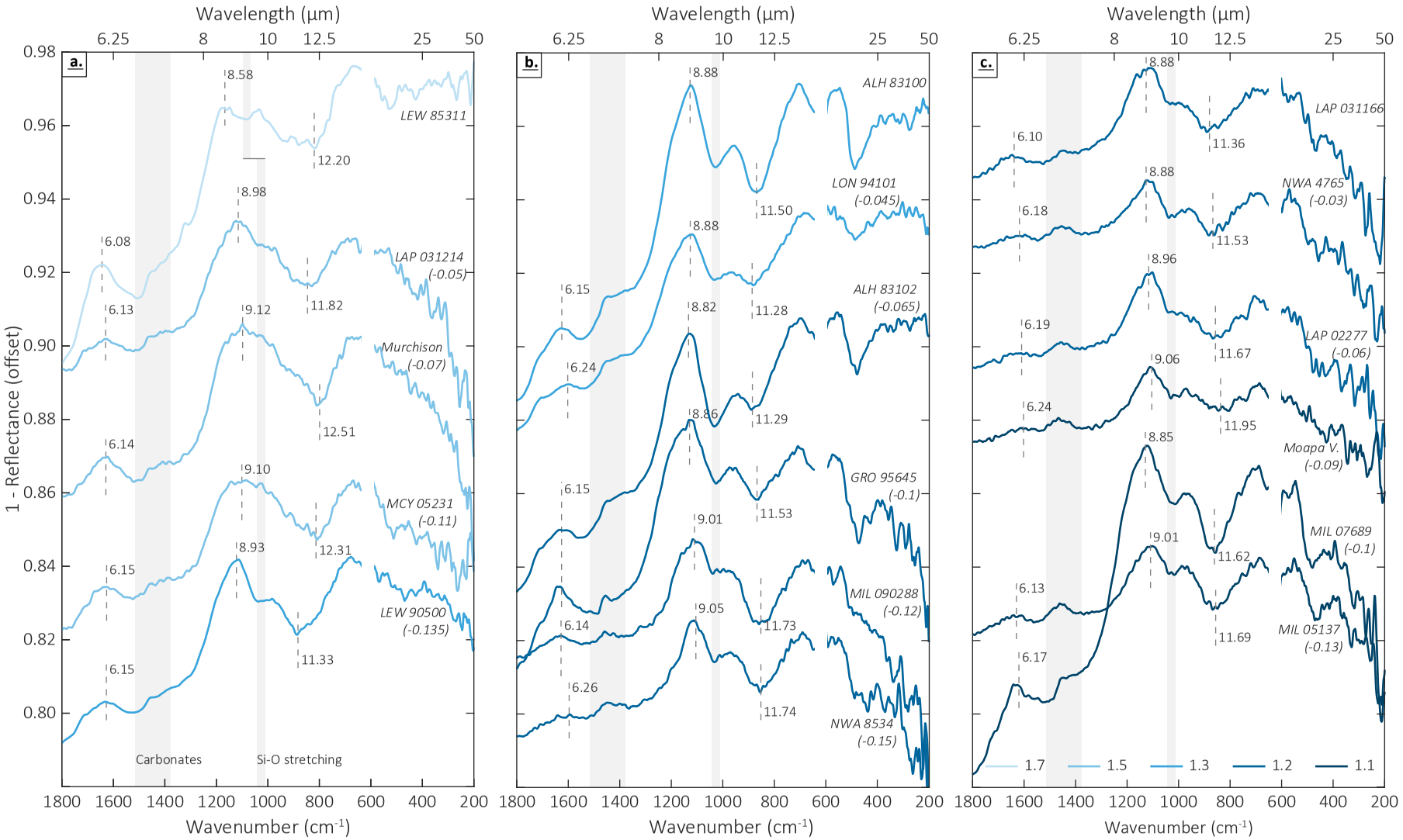


Figure 3.5: *MIR spectra for the CM2, CM1/2 and CM1 chondrites, which are ordered by increasing aqueous alteration. Spectra are inverted and offset on the y axis (by the number in brackets following the meteorite name). All spectra show a feature near 6 µm due to combination and overtone vibrations of phyllosilicates, vibrational features near 7 µm consistent with carbonates, a Christiansen feature (CF) related to the optical constants of the constituent mineralogy, Si-O stretching vibrational features and a transparency feature (TF) in a region of optical transparency in fine-grained samples. The gap in the spectra is a region of low signal-to-noise due to the beam-splitter.*

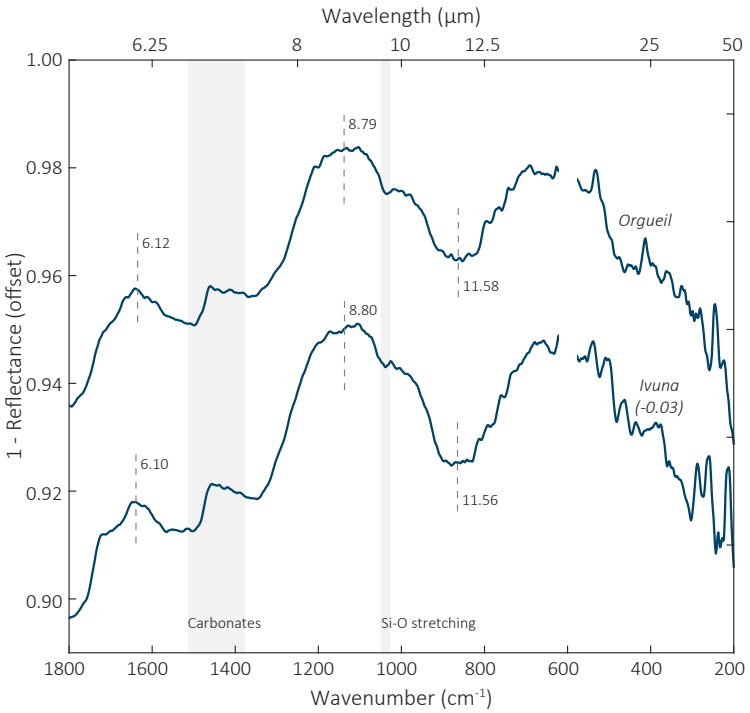


Figure 3.6: *MIR spectra for CI1 chondrites. The blue spectra reflect the PSF petrologic type 1.1. Spectra are inverted and offset on the y axis (by the number in brackets following the meteorite name). Both spectra show similar features to the CMs; near 6 and 7 µm, a Christiansen feature (CF), Si-O stretching vibrational feature and a transparency feature (TF). The gap in the spectra is a region of low signal-to-noise due to the beam-splitter.*

All the meteorite spectra show a Christiansen feature (CF) between 8.88 - 9.12 µm, except LEW 85311, which has a CF at 8.58 µm (Figs. 3.5 - 3.6). The LEW 85311 CF is likely affected by the high pyroxene abundance in this sample (15 vol%), as pyroxene has a CF at shorter wavelengths (Hamilton, 2000, Donaldson Hanna et al., 2012a). The Murchison and MCY 05231 spectra show broad features at 9.12 µm and 9.10 µm, respectively. The remaining CM spectra show sharper features at shorter wavelengths, between 8.75 - 9.06 µm. The CI chondrite spectra show broad features centred at 8.87 and 8.94 µm. Following the CF, vibrational features associated with Si-O stretching are observed. In most CM spectra (except for LEW 85311, MCY 95231 and Murchison) there is a feature ~9.75 µm, which is consistent with the feature observed in the Mg-rich serpentine lizardite spectra (Figure 2.7c). It is difficult to distinguish any vibrational features in the MCY 05231 and Murchison

spectra due to their broad CFs. The LEW 85311 spectrum has a feature at 9.26 µm, which is consistent with the Si-O vibrational features observed in the spectrum of pyroxene (Hamilton, 2000). The Orgueil and Ivuna spectra have Si-O features near 9.65 µm, at a shorter wavelength than the CM spectra likely because of their smectite phyllosilicate component: the saponite spectrum has a Si-O feature near 9.27 µm (Figure 2.7c). Between 11 - 13 µm all samples show a TF as a reflectance maximum (emissivity minimum). The LEW 85311, Murchison and MCY 05231 spectra have TFs at slightly longer wavelengths than the other CMs at 12.20, 12.51 and 12.31 µm, respectively. The remaining CM spectra show a spread of TFs between 11.28 and 11.95 µm. The CI spectra have TFs at 11.50 and 11.73 µm.

Apart from the CF and Si-O stretching feature in the LEW 85311 spectrum, the positions of the CFs, vibrational features and TFs are consistent with the positions of the same features in the spectra of olivine and phyllosilicate mineral standards (Figs. 2.7 and 2.9), and are consistent with previous observations of CM and CI chondrite spectra (e.g. McAdam et al., 2015). There does however appear to be a change in both shape and position of the CF and in position of the TF as aqueous alteration proceeds, which will be discussed further below.

3.4 Discussion

3.4.1 NIR spectral relationships to mineralogy

NIR slope

Cloutis et al. (2011a,b) showed that the spectral slope of CM and CI chondrites in the NIR region is highly variable, ranging from red to blue (decreasing reflectance with increasing wavelength), and does not correlate with phyllosilicate composition. They also demonstrated that the same meteorite could show large differences in slopes between different samples. Opaque phases (e.g. complex organics, iron sulfide, magnetite) are expected to cause no change, or only modest reddening, in the NIR slope of CM chondrites due to their

low abundances (<5 vol% Cloutis et al., 2011b, Howard et al., 2015, King et al., 2017b). In contrast, CI chondrites contain abundant magnetite (~10 vol%), which can cause a decrease in absorption band depths and overall reflectance (Cloutis et al., 2011a). The NIR spectral slope of both CMs and CIs has also been found to be affected by physical properties such as particle size, with finer particle sizes, like the ones measured in this study (<35 µm), generally resulting in redder slopes (Cloutis et al., 2011a,b). McAdam et al. (2015) investigated a suite of CM chondrites ranging from petrologic type 2 to more aqueously altered type 1s, plus a single CI1 chondrite (Orgueil), and did find a relationship between spectral slope (0.56 - 2.4 µm) and mineralogy. They reported that the spectral slope becomes bluer and approached unity with increasing phyllosilicate abundance. Despite this trend, they suggested that NIR spectral slope is not a reliable metric for distinguishing composition due to the influence of other properties such as particle size, terrestrial weathering and viewing geometry (McAdam et al., 2015).

The CM chondrite spectra with the reddest slope in this study is GRO 95645, with a slope of 1.61. This meteorite appears to have experienced significant terrestrial weathering, with a grade of B/Ce indicating the presence of visible evaporites and rusts (Grossman, 1998). The CM1 chondrite MIL 07689 also has a high weathering grade of C (Ruzicka et al., 2015), and whilst it does not have the reddest spectral slope in the suite, its slope of 1.30 is higher than expected (see discussion below). Additionally, King et al. (2018a) reported that the bulk oxygen isotopic compositions of GRO 95645 and MIL 07689 have clearly been influenced by Antarctic water. To test this further I analysed GRO 95645 and MIL 07689 using TGA (for further details see Appendix C), which is a useful technique for identifying the presence and nature of hydrated phases. Previous analyses of CM chondrites using TGA have shown that common terrestrial weathering products (e.g. ferrihydrite and other Fe-(oxy)hydroxides) dehydrate and subsequently lose mass when heated to temperatures of

200 - 400 °C (Garenne et al., 2014, King et al., 2015b). GRO 95645 and MIL 07689 both show a major mass loss event at ~225 °C (Fig. C.1) consistent with the dehydration of ferrihydrite (Garenne et al., 2014, King et al., 2015b). This mass loss event was also observed during TGA analysis of ALH 83100 and ALH 83102 but was not seen for the other CM1/2 and CM1 chondrites. Spectra between 0.8 - 1.7 μm were not collected for these meteorites in this work, but ALH 83100 and ALH 83102 also have weathering grades of Be and B/Ce, and Cloutis et al. (2011b) described a spectrum (0.3 - 2.5 μm) of ALH 83100 as being redder than other CM spectra. This observation confirms that ALH 83100, ALH 83102, GRO 95645 and MIL 07689 are the most weathered meteorites analysed in this study and contain hydrated minerals formed by terrestrial weathering processes.

Cloutis et al. (2011b) showed that terrestrial weathering and the formation of rusts can make the spectral slopes of meteorites redder. For example, they attributed the strong red spectral slope (between 0.8 and 2.3 μm) of the highly weathered (grade Ce) Antarctic CM2 meteorite LEW 88001 to the presence of terrestrial Fe-(oxy)hydroxides, which have strong red slopes in the NIR wavelength ranges. Garenne et al. (2016) also suggested the presence of these terrestrial phases cause redder slopes in CR chondrite spectra. Similarly, I suggest that the red spectral slopes of GRO 95645 and MIL 07689 are the result of terrestrial weathering during the meteorites' residence in Antarctica. I note that all the CM chondrites in this study (except Murchison) are finds and likely experienced some terrestrial weathering. However, the absence of a dehydration event at ~225 °C in the TGA indicates that weathering was less severe for the other CM chondrites, making the spectral slope more reliable for identifying mineralogy associated with parent body alteration.

Phyllosilicates are the main minerals in CM and CI chondrites, and in general their abundance increases with aqueous alteration (Howard et al., 2009, 2011). I find a weak relationship (R^2 value of 0.27) between phyllosilicate abundance and spectral slope (Fig. 3.7a), with

decreasing spectral slope as total phyllosilicate abundance increases (note that this trend does not include GRO 95645 and MIL 07689 as these spectra have redder slopes than expected for their phyllosilicate content due to terrestrial weathering). This relationship was also observed by McAdam et al. (2015), but is in contrast to observations by Cloutis et al. (2011a,b), although in the case of the latter, only one CM1/2 was included in the study. Magnetite abundance has also been found to increase with aqueous alteration, and Cloutis et al. (2011a) showed that the addition of as little as 5 vol% magnetite to phyllosilicates causes the spectral slope to become bluer. I find NIR spectral slope does decrease with increasing magnetite content in the CM1/2 and CM1 chondrites (excluding GRO 95645 and MIL 07689 and the CI chondrites) (Fig. 3.7b), and this correlation is stronger (R^2 value of 0.69) than the relationship between spectral slope and total phyllosilicate abundance. Thus, I conclude that magnetite is a more important control on NIR spectral slope in the CM chondrites.

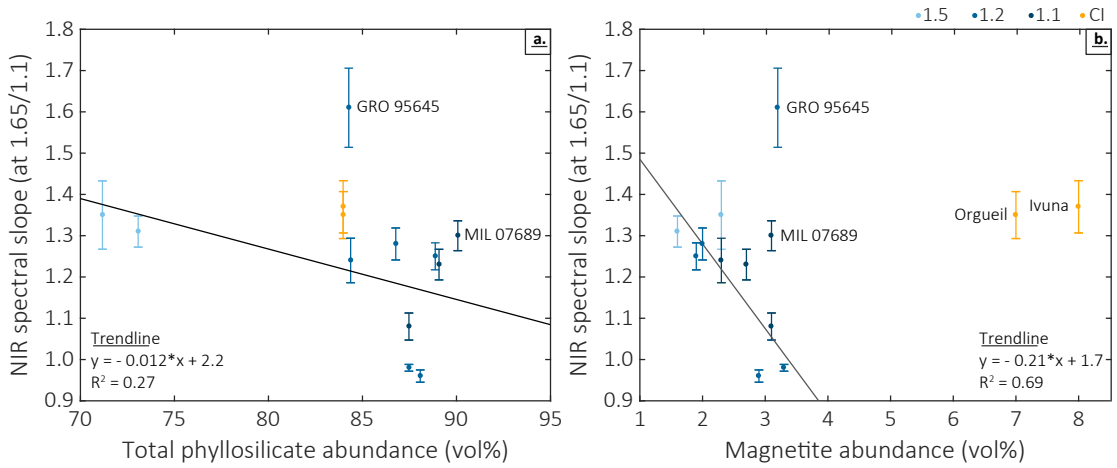


Figure 3.7: *NIR spectral slope as calculated by the reflectance at 1.65 µm divided by the reflectance at 1.05 µm against (a) phyllosilicate and (b) magnetite abundances. The spectral slopes of the CM2, CM1/2 and CM1 chondrites decrease with increasing magnetite and phyllosilicate contents, which are both products of increasing degrees of aqueous alteration. GRO 95645 and MIL 07689 plot away from these trends because they contain Fe-(oxy)hydroxides formed during terrestrial weathering. The CI chondrites have unsually steep spectral slopes for their high magnetite abundance (~8 vol%). This may be due to the CIs having different physical properties to the CMs.*

The spectra of the CI chondrites Orgueil and Ivuna show redder spectral slopes (1.35

and 1.37 respectively) than most of the CMs (Fig. 3.2). This is consistent with the observations of McAdam et al. (2015), who found that their Orgueil spectra had a redder slope than the most altered CM chondrites they investigated. Slopes >1.3 are approximately what I would expect if phyllosilicate abundance was the main control on spectral slope (Fig. 3.7a). However, Figure 3.7b demonstrates the importance of magnetite content in the meteorites and CI chondrites have high magnetite abundances (~8 vol%), which the spectral slope does not seem to reflect. One explanation is that the spectral slopes are reflecting the phyllosilicate content of the CIs and are not affected by the magnetite abundances: CI chondrites are composed of intergrown serpentine and saponite and the spectra of my phyllosilicate standards also show strong red slopes (Fig. 2.7a). Alternatively, the Fe-(oxy)hydroxide ferrihydrite might be affecting slope. Ferrihydrite is a red-sloped material, and is present in Orgueil (King et al., 2015a). However, the similarity between the spectral slope in Ivuna and Orgueil suggests this is not the case, as ferrihydrite was not detected in Ivuna by King et al. (2015a). It appears that the red spectral slopes I observe for the CIs are not reflecting mineralogy (e.g. high abundances of magnetite) and cannot easily be tied to composition. The difference in spectral trends between CM and CI chondrites may therefore be related to physical properties, such as grain size or crystallinity: Cloutis et al. (2011a) suggested the smaller grain size of mineral phases in CI chondrites may cause the observed red slopes.

Whilst there is a trend of decreasing slope with increasing aqueous alteration in CM and CI chondrites, and a trend of decreasing slope with increasing magnetite content in the CM chondrites, the NIR slope appears to be affected by weathering products, and based on this and its relationship to other physical properties such as grain size, I agree with the conclusions of McAdam et al. (2015) that it may not be the best spectral metric for determining mineralogy.

3 μM FEATURE

The 3 μm absorption is caused by the stretching, bending and overtone vibrations of H_2O and the stretching vibration of -OH. Water causes features near 3.1 μm, whereas the exact position of the feature caused by the -OH depends on the bonded cation, and tends to be between 2.5 - 3.0 μm (Gaffey et al., 1993). The CM2, CM1/2, CM1 and CI1 chondrites are comprised mostly (~70- 90 vol%) of serpentine-group phyllosilicates (Table 3.1, Howard et al., 2015, King et al., 2015a, 2017b), which contain -OH anions bonded to Mg^{2+} and Fe^{2+} cations. I therefore expect the 3 μm feature in the spectra of the highly altered CM and CI chondrites to have shapes and positions similar to serpentine group phyllosilicate standards, and to vary depending on the composition of the phyllosilicates, which changes with increasing degrees of aqueous alteration.

Studies of the 3 μm region for CM and CI chondrites show a correlation between the position of the feature and the mineralogy of the meteorite. Beck et al. (2010) investigated transmission IR spectra of CM and CI chondrites and saw a shift to shorter wavelength of the 3 μm feature due to progressive enrichment of Mg in serpentine phyllosilicate minerals as the degree of aqueous alteration increased. This was also observed by Takir et al. (2013), who found that intermediately altered CM chondrites show spectral features consistent with Fe-cronstedtite and highly altered CM chondrites have spectral features that resemble Mg-serpentines. Note that both studies heated their samples prior to measurements to minimise the effects of terrestrial adsorbed water.

LEW 85311, LAP 031214, LEW 90500, MCY 05231, and Murchison spectra show rounded features at 2.78 - 2.83 μm (Fig. 3.3a). These are the least aqueously altered samples in this investigation and contain the lowest phyllosilicate abundances (~64 - 83 vol%, Table 3.1), and have the highest PSF petrologic types (1.3 - 1.7). The composition of their phyllosilicates is more Fe-rich than the other CM1/2 and CM1s, with Mg-serpentine/Fe-cronstedtite

ratios of 0.4 - 2.4 in comparison with >2.8 (although this excludes GRO 95645, which has a Mg-serpentine/Fe-cronstedtite ratio of 1.6). I suggest that the 3 µm features of these samples therefore reflect the higher component of Fe-cronstedtite, the spectra of which has a feature at longer wavelengths than the more Mg-rich phyllosilicate species (Fig. 2.7b). King et al. (2017b) suggested the CM1/2s MCY 05231 and LAP 031214 samples be reclassified as CM2 chondrites, and their spectral signature supports this conclusion.

The spectra of the CM2 LON 94101 shows two features in this region, at 2.72 and 2.80 µm, the former consistent with the more Mg-serpentine phyllosilicate standard spectra and the latter with the Fe-cronstedtite spectra (Fig. 2.7b). This meteorite contains a higher abundance of Mg-serpentine (~63 vol%) than the other CM2 chondrites (<40 %, including LAP 031214 and MCY 05231), yet still a lower Mg/Fe ratio of its phyllosilicates (2.8) in comparison to most of the more altered CM1/2 and CM1s (>3). If phyllosilicate composition is assumed to become increasingly Mg-rich as aqueous alteration proceeds, this Mg/Fe ratio suggests LON 94101 has experienced a lower degree of aqueous alteration than the CM1/2 and CM1s. The shape of this 3 µm feature is consistent with the spectra collected by Takir et al. (2013) who determined this shape representative of intermediate alteration. Both the modal mineralogy and the spectra presented here suggest LON 94101 is an intermediately aqueously altered CM between the less altered CM2s and more aqueously altered CM1/2s. In the spectra of the more altered CM1/2s and CM1s, features at 2.72 - 2.74 µm correspond well with my Mg-serpentine standards, consistent with the more Mg-rich compositions of the phyllosilicates in these meteorites (Mg-serpentine abundances in these samples vary between 52 - 72 vol%).

The 3 µm feature, particularly in the GRO 95645, LEW 85311 and LEW 90500 spectra, is also likely affected by tochilinite, which was identified in these three samples (section 3.3.1, King et al., 2017b). Tochilinite shows spectral features in the 3 µm region between 2.71 -

2.79 µm, depending on whether it's Mg- (shorter wavelengths) or Fe-rich (longer wavelengths) (Moroz et al., 2006, Hanna et al., 2020). The lack of a sharp peak often associated with Mg-rich tochilinite near 2.71 µm in the LEW 85311 and LEW 90500 spectrum suggests the tochilinite present in these samples is Fe-rich, however a feature due to Fe-rich tochilinite near 2.79 µm may be indistinguishable from the Fe-cronstedtite phyllosilicate features observed (Hanna et al., 2020). The opposite may be the case for GRO 95645 - there is no feature near 2.79 µm suggesting the tochilinite present is Mg-rich, although a feature due to Mg-rich tochilinite may be indistinguishable from the Mg-serpentine feature observed near 2.73 µm in the GRO 95645 spectrum.

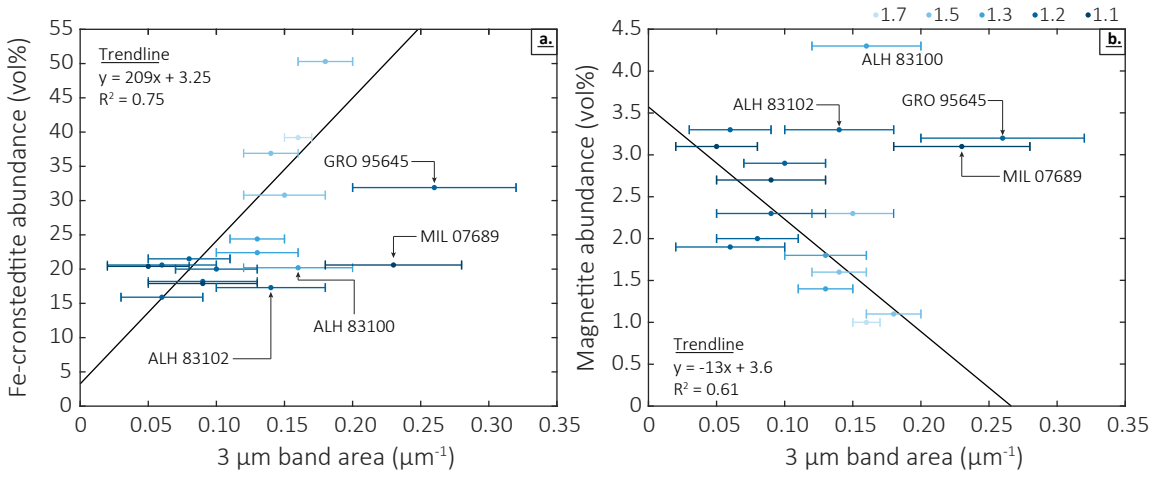


Figure 3.8: *Fe-cronstedtite abundance versus 3 µm band area (a) and magnetite abundance versus 3 µm band area (b) for the CM2, CM1/2 and CM1 chondrites. The 3 µm band area is correlated with both Fe-cronstedtite and magnetite: increasing with increasing Fe-cronstedtite and decreasing with increasing magnetite. The four outliers with larger band areas yet higher magnetite abundances are ALH 83100, ALH 83102, GRO 95645 and MIL 07689, which are highly weathered and contain Fe-(oxy)hydroxides (see text for details).*

Overall, I see a shift in the band centre of the 3 µm feature from longer wavelengths in the samples with the lowest phyllosilicate abundances (e.g. LEW 85311 with ~64 vol% and MCY 05231 with ~73 vol%), to shorter wavelengths in the intensely altered samples with the highest phyllosilicate abundances (82 - 90 vol%). This shift occurs due to changes in phyllosilicate composition, with removal of heavier Fe^{2+} cations from the phyllosilicate

structure, coupled with an increase in more Mg-rich phyllosilicate species, as total phyllosilicate abundance increases with progressive aqueous alteration (King et al., 2017b). The feature also seems to be affected by the presence and chemistry of tochilinite. The shift to shorter wavelengths with increasing degree of aqueous alteration is consistent with previous spectral results of CM chondrites, and likely a useful parameter for remotely inferring the mineralogy and aqueous alteration state of asteroid surfaces (Beck et al., 2010, Takir et al., 2013).

I find that the area of the asymmetrical 3 µm feature appears to be influenced by aqueous alteration extent in CM chondrites, with band area decreasing as total phyllosilicate abundance increases. This is likely caused by changes in phyllosilicate chemistry and increasing magnetite abundances. Qualitative examination of the CM chondrite spectra shows the 3 µm feature to be much broader than those of the Mg-serpentine phyllosilicate standards (note that standards were not heated prior to measurements). The 2.87 µm feature in the spectra of the Fe-cronstedtite standard is broader than the 2.72 µm in the Mg-serpentine, and its calculated area over the range 2.67 - 3.85 is much larger than the feature in the Mg-serpentine standard spectra (0.54 μm^{-1} in comparison to 0.32 - 0.37 μm^{-1}). Fe-cronstedtite therefore acts to increase 3 µm band area, and so the CM chondrites with the highest Fe-cronstedtite abundances have the largest areas, shown in Figure 3.8a. Figure 3.8b shows that increasing magnetite content also correlates with decreasing band area, which is expected as magnetite is known to act as an opaque and can subdue features as its abundance increases (Cloutis et al., 1990). Therefore, the samples with highest magnetite contents show the smallest band areas. As discussed above magnetite has been shown to increase with increasing aqueous alteration, and so this mineralogical change, coupled with decreasing Fe-cronstedtite abundances, act to reduce 3 µm band area as aqueous alteration extent increases.

There are four outliers in Figure 3.8, which do not adhere to the trends observed; ALH 83100, ALH 83102, GRO 95645 and MIL 07689, which as discussed above, are the most terrestrially weathered meteorites analysed in this study. TGA indicates that they contain terrestrial weathering products that would not be removed upon heating to 150 ^{o}C and therefore still contribute to the 3 µm feature. Ferrihydrite, for example, has a strong absorption feature at ~3 µm (Bishop et al., 1993), and its presence could explain the larger band area in these four samples.

The 3 µm region in the CI chondrite spectra show two distinctive features (Fig. 3.4); a sharp absorption at 2.72 µm followed by a broader feature between 2.75 - 3.30 µm. My Mg-serpentine and saponite standard spectra show a feature at 2.72 µm (Fig. 2.7b), suggesting the initial sharp feature is caused by Mg-OH, as with the feature in the same location in the CM1/2 and CM1 chondrites. The broad feature centred at 2.98 µm in the spectrum of Orgueil, and at 3.01 µm in the spectrum of Ivuna, is caused by H_2O. As the meteorite samples were heated to above 150 ^{o}C I can assume this feature is not caused by terrestrially adsorbed water, rather bound interlayer water in smectite phyllosilicates that was not removed on heating (Bishop et al., 1993, and references therin). The contribution of ferrihydrite, which was found in Orgueil but not Ivuna (King et al., 2015a), is probably small due to the similarity between the spectral shape and position of the features in the CI spectra.

3.4.2 MIR SPECTRAL RELATIONSHIPS TO MINERALOGY

6 µM FEATURE

The region between 5.0 - 6.5 µm can be challenging to disentangle in the spectra of CM and CI chondrites as it contains features that are related to the overtones and combination tones of Si-O in the anhydrous minerals as well as the bending of H_2O and -OH that are

present in phyllosilicates (Salisbury et al., 1991, Lucey et al., 2017). I see features in this region in my phyllosilicate standard spectra (Fig. 2.7c), but also in the emissivity spectra of olivine (Fig. 2.3). Beck et al. (2018) found an absorption feature in the IR reflectance spectra of all CM chondrites near 6 µm, and suggested it was due to interlayer H_2O in phyllosilicates or adsorbed water as samples were not heated prior to measurement. I observe features in this region in all the spectra of the CM2, CM1/2, CM1 and CI1 chondrites (Figs. 3.5 and 3.6). As my samples were heated prior to measurement, I suggest that the features here are related to mineralogy rather than adsorbed water.

The Fe-cronstedtite spectrum has a broad feature centred at 5.97 µm, while lizardite and antigorite show multiple features with maxima between 5.89 - 6.34 µm (Fig. 2.7c). The spectrum for the olivine standard also shows a doublet feature in this region, near 5.65 and 6.00 µm (Fig. 2.3). The band centres in the CM1/2 and CM1 chondrite spectra plot within the range of those for the phyllosilicates, suggesting that the 6 µm feature is controlled by the phyllosilicates that dominate the bulk mineralogy of the meteorites, rather than the anhydrous olivine that is present in some of the samples. The spectra of Orgueil and Ivuna have broad 6 µm features with centres at 6.12 and 6.10 µm, respectively, and a shoulder at ~5.8 µm. These positions are similar to the spectra for the CM1/2 and CM1 chondrites and the phyllosilicate standards. The saponite spectrum in particular has a doublet feature with centres at 5.89 µm and 6.18 µm, and considering the phyllosilicates in CIs are a serpentine-saponite mixture (Bland et al., 2004), the 6 µm feature in the CI spectra might be a combination of the different phyllosilicate compositions.

Unlike the 3 µm region, there does not appear to be a trend in position of the 6 µm feature with mineralogy, likely because the features are complex, and it is difficult to identify a trend even within the phyllosilicate endmember standards. As both the hydrated and

anhydrous minerals have features in this region, it may not be a useful metric for establishing whether hydration has taken place.

Christiansen feature

Trends have been observed with the shape and position of the CF in CM and CI chondrites in previous investigations: Hanna et al. (2020) found the CF was at longer wavelengths in CM chondrites with lower petrologic types, and McAdam et al. (2015) reported a change in the shape of the CF, with features becoming sharper and more distinct with increasing alteration. All CFs in the spectra of the CM1/2 and CM1 chondrites are identified between 8.88 - 9.12 µm (Fig. 3.5), excluding the CF in the spectra of LEW 85311, which is at 8.58 µm. The CF of enstatite, the Mg-rich orthopyroxene that was used to determine modal mineralogy, has been observed at 8.33 µm (Donaldson Hanna et al., 2012a), and the presence of a high abundance of pyroxene (15 vol%) in LEW 85311, compared to the other CMs investigated (<6 vol%) likely results in the CF at shorter wavelengths. As discussed in section 3.3.3, the other meteorites show CF at positions consistent with the phyllosilicate standard spectra.

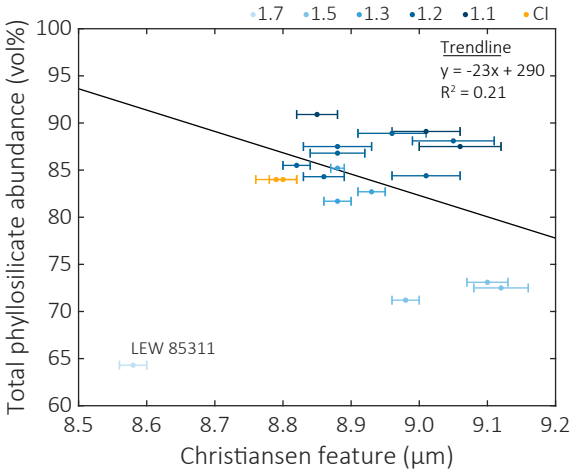


Figure 3.9: *Total phyllosilicate abundance in CM2, CM1/2, CM1 and CI1 chondrites vs the position of the Christiansen feature (CF) in MIR spectra. There is only a weak relationship between position and phyllosilicate abundance, but intermediately altered CMs seem to cluster at longer wavelengths than the highly altered CMs and CIs. LAP 031214 and LEW 85311 are anomalous due to their Mg-rich phyllosilicate composition and enstatite abundance, respectively (see text for details).*

In Figure 3.9, there is only a weak relationship (R^2 of 0.21) between the position of the CF and total phyllosilicate abundance. However, the intermediately altered MCY 05231 spectrum does have a CF at longer wavelengths (9.12 µm) and is similar to the CM2 Murchison spectrum (9.10 µm), whereas the CF in the other CM2, CM1/2 and CM1 chondrite spectra cluster between 8.88 - 9.06 µm (Fig. 3.9). My Fe-cronstedtite spectrum has a CF at 9.66 µm and the Mg-serpentine CF is identified at 8.58 µm (Fig. 2.7c). The difference in CF position between intermediately and highly altered CMs could therefore reflect changes in phyllosilicate composition, which becomes increasingly Mg-rich as aqueous alteration proceeds. Highly aqueously altered CM spectra have CFs at shorter wavelengths, due to higher Mg-serpentine abundances, and intermediately altered CM spectra have CFs at longer wavelengths, due to higher Fe-cronstedtite abundances. This does not corroborate with the trend determined by Hanna et al. (2020), who found the CF shifted to longer wavelengths with decreasing petrologic type in CM chondrite spectra, however they investigated a much larger petrologic range (2.7 to 2.1 in the Rubin scheme) and this study focuses only on the most aqueously altered CMs. Additionally they collected spectra of polished thin sections and this study looks at powdered material. Within the highly altered CM spectra there are no further trends in position of the CF, indicating that the CF position can only provide coarse resolution between mildly, intermediately and highly altered meteorites.

The influence of phyllosilicate composition is further emphasised by the position of the CF in the CM1/2 LAP 031214 spectrum. LAP 031214 has a similar mineralogy to MCY 05231 and Murchison (~20 vol% anhydrous silicates, ~70 vol% phyllosilicates) but a much sharper CF with a position at a shorter wavelength (8.98 µm). Despite comparable total phyllosilicate abundances, the Mg-serpentine/Fe-cronstedtite ratio is higher for LAP 031214 (1.3) than MCY 05231 (1.0) and Murchison (0.4), suggesting that its phyllosilicates are more Mg-rich and it underwent a higher degree of aqueous alteration (King et al., 2017b). This suggests

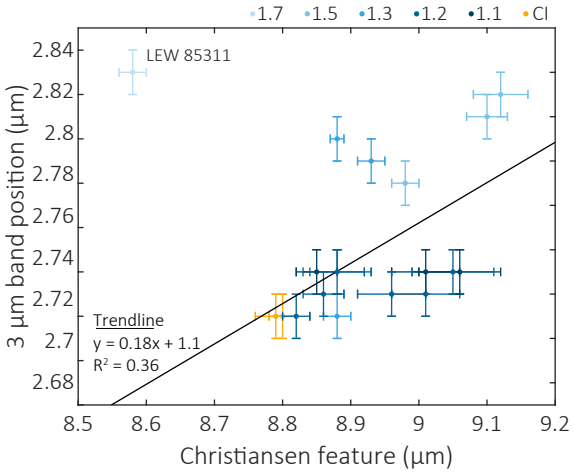


Figure 3.10: *The position of the 3 µm feature and its relationship to the position of the CF. These two features can be used in conjunction to constrain aqueous alteration extent, as shifts in feature position are caused by different mechanisms: the 3 µm position is controlled by total phyllosilicate abundances, and the CF is controlled changes in phyllosilicate chemistry. The CM2s LEW 90500 and LON 94101 and the CM1/2 LAP 031214 are likely more aqueously altered than the CM1/2 MCY 05231 and the CM2 Murchison.*

phyllosilicate composition is a more important control than total phyllosilicate abundance on the position of the CF, in contrast to the 3 µm region, where the position of the feature is controlled more by total phyllosilicate abundance: both LAP 031214 and LEW 90500 (which has a Mg-serpentine/Fe-cronstedtite ratio of 2.1) show 3 µm features associated with Fe-cronstedtite, but CFs consistent with more Mg-rich phyllosilicate. The CF in the spectra of LON 94101, which showed an 'intermediate' 3 µm feature, is consistent with the highly aqueously altered spectra. I therefore propose that as the degree of aqueous alteration increases in CM chondrites the CF position shifts to shorter wavelengths before the 3 µm band shifts to shorter wavelengths, and the two features should be used in combination to constrain the extent of hydration. The relationship between these two features is shown in Figure 3.10, and LEW 85311, as expected, is an outlier. In addition, I also find that the shape of the CF becomes sharper and distinct with increasing aqueous alteration. This is due to the increasing dominance of Mg-serpentine as alteration progresses, and extends the trend in CF shape first observed by McAdam et al. (2015).

The spectra of Orgueil and Ivuna have CFs at similar positions to the spectra of the highly altered CM chondrites, at 8.79 µm and 8.80 µm, respectively, however the features are broader. Unlike the highly altered CMs, where the phyllosilicate composition is dominated by Mg-serpentine, the phyllosilicates in the highly altered CI1s are a serpentine-saponite mixture, and the CFs seen in their spectra are likely combinations of the CFs of these different phyllosilicates. The Mg-serpentine and saponite spectra have CFs near 8.58 µm and 8.21 µm, respectively, and with both present in the CI chondrites it is difficult to identify a single diagnostic peak.

Transparency feature

The TF is a reflectance maximum (emissivity minimum) between 11 - 13 µm that appears in spectra of fine grained samples and has been found to correlate with aqueous alteration. McAdam et al. (2015) identified a trend in the position of the TF peak in the spectra of CM and CI chondrites, with centres shifting to shorter wavelengths with increasing phyllosilicate abundance. They found less altered meteorites with lower phyllosilicate abundances had centres near 12.3 µm, and more altered meteorites with higher phyllosilicate abundances had centres near 11.4 µm. In addition, they found carbonaceous chondrites with intermediate levels of aqueous alteration showed a doublet feature. Furthermore, Beck et al. (2018) found a correlation between the 12.4/11.4 µm reflectance ratio (which corresponds to an olivine feature) and water content in CM chondrites.

I observe a similar trend, with the TFs shifting to shorter wavelengths with increasing total phyllosilicate abundance (Fig. 3.11a). However, the LAP 031214 spectra, as in the CF region, show a TF more consistent with the highly altered CM1/2 and CM1 chondrites. I propose the TF, like the CF, is also affected by phyllosilicate composition in addition to total phyllosilicate abundance. This can be demonstrated by the trend between TF position

and the Mg-serpentine/Fe-cronstedtite ratio of the phyllosilicates in the CM chondrites (Fig. 3.11b), with the TF shifting to shorter wavelengths as Mg-serpentine (TF at ~11.64 µm) becomes more abundant than Fe-cronstedtite (TF at 12.28 µm). This ratio is highest in the most altered CM chondrites as phyllosilicates get progressively more Mg-rich with aqueous alteration (King et al., 2017b). The spectra of LEW 85311, Murchison and MCY 05231, which have the lowest Mg-serpentine/Fe-cronstedtite ratios (0.4 - 1.0), have TF features at the longest wavelengths (12.20 - 12.51 µm), which additionally correspond with the positions of the TF in the spectra of the least altered samples investigated by McAdam et al. (2015). These positions could also be influenced by the higher abundance of olivine (~17 vol% in LEW 85311, ~15 vol% in Murchison and ~20 vol% in MCY 05231), the spectrum of which shows a TF at 12.90 µm (Fig. 2.3).

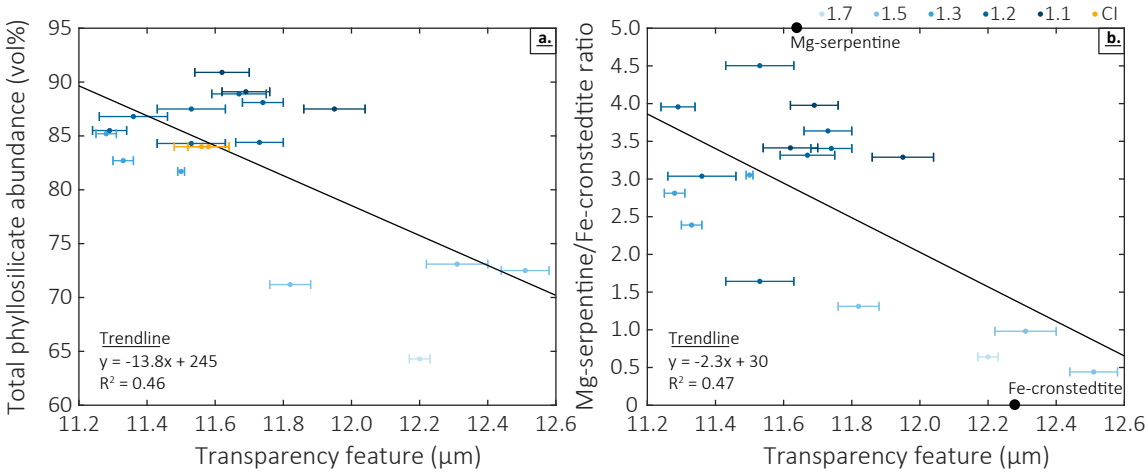


Figure 3.11: *The position of the TF in the CM2, CM1/2, CM1 and CI1 chondrite spectra and its relationship to (a) total phyllosilicate abundance and (b) the Mg-serpentine/Fe-cronstedtite ratio of the phyllosilicates. Both total phyllosilicate abundance and phyllosilicate composition show a relationship to the position of the TF, with the feature shifting to shorter wavelengths with increasing phyllosilicate abundance, and a change to more Mg-rich phyllosilicate. Both are associated with higher degrees of aqueous alteration.*

The spectra of the highly altered CI chondrites Orgueil and Ivuna follow the same trend, with TF positions (11.58 µm and 11.56 µm) shifted to shorter wavelengths (Fig. 3.11a). The similarity of the TFs in the spectra of Orgueil and Ivuna to those in the spectra of the most

altered CM chondrites suggests the TF might be a useful parameter in assessing the degree of aqueous alteration across different chondrite groups and in remote sensing observations of asteroids with fine particulate surfaces. This is in contrast with the variation in the shape and position of the CF between the most aqueously altered CM chondrites and CI chondrites.

There is a correlation between TF position and phyllosilicate abundance, although composition of the phyllosilicates also plays a role. For the highly aqueously altered chondrites, the TFs are identified at short wavelengths (11.33 - 11.95 μm), whereas for the intermediately and mildly altered samples they occur at longer wavelengths (12.20 - 12.51 μm). Both the CF and TF are more sensitive to the phyllosilicate composition than the NIR spectral slope and 3 μm features, so using both in conjunction can help constrain the extent of aqueous alteration.

3.4.3 Spectral parameters for mineral identification

I have examined a number of parameters in the NIR and MIR spectra of CM and CI chondrites and established how they vary with mineralogy. The NIR slope is sensitive to several physical properties (e.g. grain size) and terrestrial weathering of a sample, but if these are well characterised, variations in the slope can be tied to the opaque content of a meteorite. In the CM chondrites, spectral slope decreases with increasing magnetite content (Fig. 3.7b), which reflects the extent of aqueous alteration. Furthermore, there is a reasonable trend between spectral slope and phyllosilicate abundance of the CM chondrites (Fig. 3.7a). The 6 μm feature appears to be indicative of hydration in CM and CI chondrites, although there is no trend with mineralogy or extent of alteration, and as this region also has contributions from anhydrous silicates it is complex to disentangle composition. The 3 μm feature, CF and TF show trends related to the degree of aqueous alteration, with all three parameters shifting to shorter wavelengths with increasing hydration. In particular, the position and

shape of the 3 μm feature is useful: intermediately altered CMs have rounded features at ~2.8 μm, and with increasing aqueous alteration these features become sharper and shift to shorter wavelengths. This is related to increasing phyllosilicate abundance, an increasing fraction of which is Mg-serpentine. Additionally, I suggest that band area may decrease with increasing aqueous alteration due to decreasing Fe-cronstedtite and increasing magnetite. The CF and TF are sensitive to phyllosilicate composition, shifting to shorter wavelengths as the Mg-serpentine/Fe-cronstedtite ratio of the phyllosilicates increases. As both total phyllosilicate abundance and Mg-serpentine phyllosilicate abundance are related to aqueous alteration extent, all three spectral parameters can be used to constrain the alteration history of a sample.

3.5 Conclusions

In this chapter, 18 aqueously altered CM2, CM1/2, CM1 and CI1 chondrites were investigated with the aim of determining spectral trends that can be correlated with known mineralogy and aqueous alteration. The parameters identified included the NIR spectral slope, the position and area of the 3 μm feature, and the position of the CF and TFs, although I show that terrestrial alteration products can affect the former two. I demonstrate that combining spectral parameters across different wavelength ranges can help to determine subtle variations in the extent of aqueous alteration.

However, it has been demonstrated that processing on asteroids is not limited to aqueous alteration alone. There is evidence for dehydration on the surfaces of some C-complex asteroids and this is supported by the number of aqueously and thermally altered chondrites currently identified in meteorite collections, implying complex alteration conditions on their asteroid parent bodies. Chapter 4 therefore aims to identify trends which can help infer both aqueous and thermal alteration history by determining correlations between

spectra and mineralogy of aqueously and thermally altered carbonaceous chondrites (question A-2, chapter 1).

Chapter 4: Linking the reflectance spectroscopy and mineralogy of aqueously and thermally altered CM and CY carbonaceous chondrites

4.1 Introduction

Chapter 3 showed that trends associated with the mineralogy of aqueously altered CM and CI carbonaceous chondrites can be identified in reflectance spectra. These spectral parameters, including the 3 μm feature, Christiansen feature (CF) and transparency feature (TF), can therefore be used to constrain the extent of aqueous alteration in meteorites. Alteration of the carbonaceous chondrites is not limited to hydration however, with several studies showing that some CM chondrites also experienced thermal metamorphism after aqueous alteration, to temperatures of >700 ^{o}C (e.g. Nakamura, 2005, Nakato et al., 2008, Tonui et al., 2014, King et al., 2019). Hiroi et al. (1993) suggested that aqueously and thermally altered chondrites may be good analogues for the surfaces of C-complex asteroids, and more recent observations of Ryugu by the Hayabusa2 spacecraft have indicated the asteroid surface may be dehydrated (Kitazato et al., 2019). It is therefore important to define spectral parameters that can be applied to remote observations in order to determine the complete alteration history of asteroid surfaces. The aim of this chapter is to elaborate on the trends identified in chapter 3 to establish whether there are spectral trends and parameters that correlate with the mineralogy of aqueously and thermally altered carbonaceous chondrites (question A-2, chapter 1).

4.2 Experimental

In this study 21 meteorites have been identified as aqueously and thermally altered: 16 that are classified as CM or CM-anomalous, and five that have been identified as CY chondrites. For CY chondrites Y 86720 and Y 86789, I was allocated two different chips: Y 86720, 61 and Y 86720, 54; and Y 86789, 60 and Y 86789, 70, allowing the heterogeneity of the meteorites to be investigated. High resolution XRD patterns were collected from every meteorite (Table 2.1), except Dho 2046 (CM2-an), Dho 225 (CM-an), Dho 735 (CM2), WIS 91600 (CM-an) and Y 980115 (CY) due to either limited sample mass or laboratory access constraints. The bulk modal mineralogy of all the meteorites was determined using PSD-XRD. For EET 96029 (CM2), PCA 02010 (CM2), PCA 02012 (CM2), WIS 91600 (CM-an), Y 793321 (CM2), Y 86720,54 (CY), Y 86789,70 (CY) and Y 980115 (CY) the sample mass was large enough (Table 2.1) to collect PSD-XRD patterns from two separate aliquots (HB2-1 and HB2-2). This was done to ensure the mineralogy determined from PSD-XRD is representative of the whole sample. Following PSD-XRD analysis small aliquots of all samples were analysed using TGA, with the exception of Dho 225 and Dho 735 due to the limited sample mass available for any destructive analysis. Reflectance spectra across the NIR (2 - 5 µm, 5000 - 2000 cm^{-1}) and MIR (5.55 - 50 µm, 1800 - 200 cm^{-1}) were then collected from the same powders in order to directly relate spectral trends to specific mineralogy. For details on all experimental procedures see chapter 2.

4.3 Results

4.3.1 X-ray diffraction

Aqueously and thermally altered CM chondrites

Ten meteorite samples were determined to be aqueously and thermally altered CM chondrites and assigned a heating stage: two stage Is (DOM 03183 and Y 793595), six stage IIs (A 881334, EET 96029, MIL 07700, PCA 91084, Y 793321 and Y 794080) and two stage IVs (PCA 02010 and PCA 02012). There were no stage III CM chondrites in the sample suite. Representative high-resolution XRD patterns of heating stages I, II and IV are shown in Figure 4.1, and PSD-XRD patterns of the same samples are shown in Figure 4.2. The stage I samples consist mostly of Fe- and Mg-rich serpentines, magnetite, olivine and gypsum (likely terrestrial, Lee, 1993). There are also small peaks associated with calcite, enstatite, tochilinite and Fe-sulfide. The olivine in the stage I samples is primary (Figs 4.1b and 4.1c). Modal mineralogy determined from PSD-XRD for the stage I sample CMs is ~11 vol% primary olivine, ~6 vol% enstatite, ~2 vol% magnetite, ~2 vol% gypsum ~1 vol% Fe-sulfide, ~1 vol% calcite and ~79 vol% crystalline phyllosilicate (Table 4.1). A petrologic type can then be determined from the PSF (section 2.2.2, Howard et al., 2011). DOM 03183 has a PSF petrologic type is 1.5 and Y 793595 has a PSF petrologic type of 1.2.

Stage II sample patterns show diffraction peaks due to primary olivine, enstatite, gypsum, calcite, magnetite and Fe-sulfide (troilite), but do not show diffraction peaks associated with phyllosilicates (Figure 4.1). Modal mineralogies for the stage II samples are 5 - 16 vol% primary olivine, 1 - 13 vol% enstatite, 1 - 2 vol% magnetite, <2 vol% Fe-sulfide, <1 vol% calcite, <2 vol% gypsum and 67 - 91 vol% disordered phase (Table 4.1). Assuming the disordered phases were once phyllosilicates (section 2.2.2, King et al., 2019), this gives

Meteorite	Sample	Classification	Primary olivine (vol%)	Secondary olivine (vol%)	Enstatite (vol%)	Magnetite (vol%)	Sulfide (vol%)	Carbonate (vol%)	Gypsum (vol%)	Anhydrite (vol%)	Feldspar (vol%)	Metal (vol%)	Rusts (vol%)	Phyllosilicate (vol%)	Disordered phyllosilicate (vol%)	Total (vol%)	PSF petrologic type	Nakamura heating stage
A 881334	HB1	CM2	15	-	8	2	1	<1	1	-	-	<1	-	-	72	100	1.5	2
A 881655	HB1	CM2	-	14	4	7	4	1	2	-	-	-	-	-	67	100	1.2	3
B 7904	HB2-1	C2-ung/CY	23	51	8	-	18	-	-	-	-	1	-	-	-	100	1.8	4
	HB2-2	C2-ung/CY	27	49	10	-	11	2	-	-	-	1	-	-	-	100	1.9	4
Dho 225	HB1	CM-an	6	6	-	-	3	<1	-	-	-	-	-	-	84	100	1.2	3
Dho 735	HB1	CM2	7	12	2	-	4	1	-	-	-	<1	-	-	74	100	1.2	3
Dho 2046	HB1	CM2-an	16	20	2	-	10	-	-	-	-	<1	-	-	51	100	1.5	4
DOM 03183	HB1	CM2	12	-	10	2	-	<1	2	-	-	<1	-	73	-	99	1.5	1
EET 96010	HB1	CM2	41	24	9	-	19	2	-	-	-	1	3	-	-	100	2.4	4
EET 96029	HB2-1	CM2	11	-	9	2	1	<1	1	-	-	<1	-	-	76	100	1.5	2
	HB2-2	CM2	10	-	6	2	1	<1	1	-	-	<1	-	-	80	100	1.4	2
MIL 07700	HB1	CM2	5	-	1	1	2	1	-	<1	-	-	-	-	91	100	1.2	2
PCA 02010	HB2-1	CM2	16	58	16	-	8	-	-	-	2	<1	-	-	-	100	1.8	4
	HB2-2	CM2	13	63	15	-	8	-	-	-	1	<1	-	-	-	100	1.7	4
PCA 02012	HB2-1	CM2	27	21	15	-	8	1	-	-	1	<1	-	-	27	100	2.0	4
	HB2-2	CM2	27	20	14	-	9	1	-	-	1	<1	-	-	28	100	2.0	4
PCA 91084	HB1	CM2	8	-	5	1	<1	<1	1	-	-	<1	-	-	85	99	1.3	2
WIS 91600	HB2-1	CM-an	10	-	3	9	4	1	-	-	-	-	-	-	73	100	1.4	2
	HB2-2	CM-an	14	-	2	9	3	1	-	-	-	-	-	-	70	100	1.4	2
Y 793321	HB2-1	CM2	12	-	7	2	1	1	-	-	-	<1	-	-	76	100	1.5	2
	HB2-2	CM2	10	-	6	1	1	1	-	-	-	<1	-	-	81	100	1.4	2
Y 793595	HB1	CM2	8	-	1	2	1	1	2	-	-	-	-	85	-	100	1.2	1
Y 794080	HB1	CM2	16	-	12	1	1	<1	2	-	-	<1	-	-	67	99	1.6	2
Y 86029	HB1	CI1/CY	-	9	-	5	19	-	-	-	-	-	-	-	67	100	1.0	3
Y 86720,61	HB1	C2-ung/CY	-	58	11	-	29	-	-	-	-	2	-	-	-	100	1.4	4
Y 86720,54	HB2-1	C2-ung/CY	-	60	5	-	33	-	-	-	-	2	-	-	-	100	1.2	4
	HB2-2	C2-ung/CY	-	57	11	-	30	-	-	-	-	2	-	-	-	100	1.4	4
Y 86789,60	HB1	C2-ung/CY	-	63	7	-	28	-	-	-	-	2	-	-	-	100	1.1	4
Y 86789,70	HB2-1	C2-ung/CY	-	60	5	-	32	-	-	-	-	3	-	-	-	100	1.2	4
	HB2-2	C2-ung/CY	-	62	5	-	31	-	-	-	-	2	-	-	-	100	1.2	4
Y 980115	HB2-1	CI1/CY	-	8	-	2	12	-	-	-	-	<1	-	-	78	100	1.0	3
	HB2-2	CI1/CY	-	8	-	2	10	-	-	-	-	<1	-	-	80	100	1.0	3

Table 4.1: *Modal mineralogy of the CM, CY and CM/CY-anomalous samples*

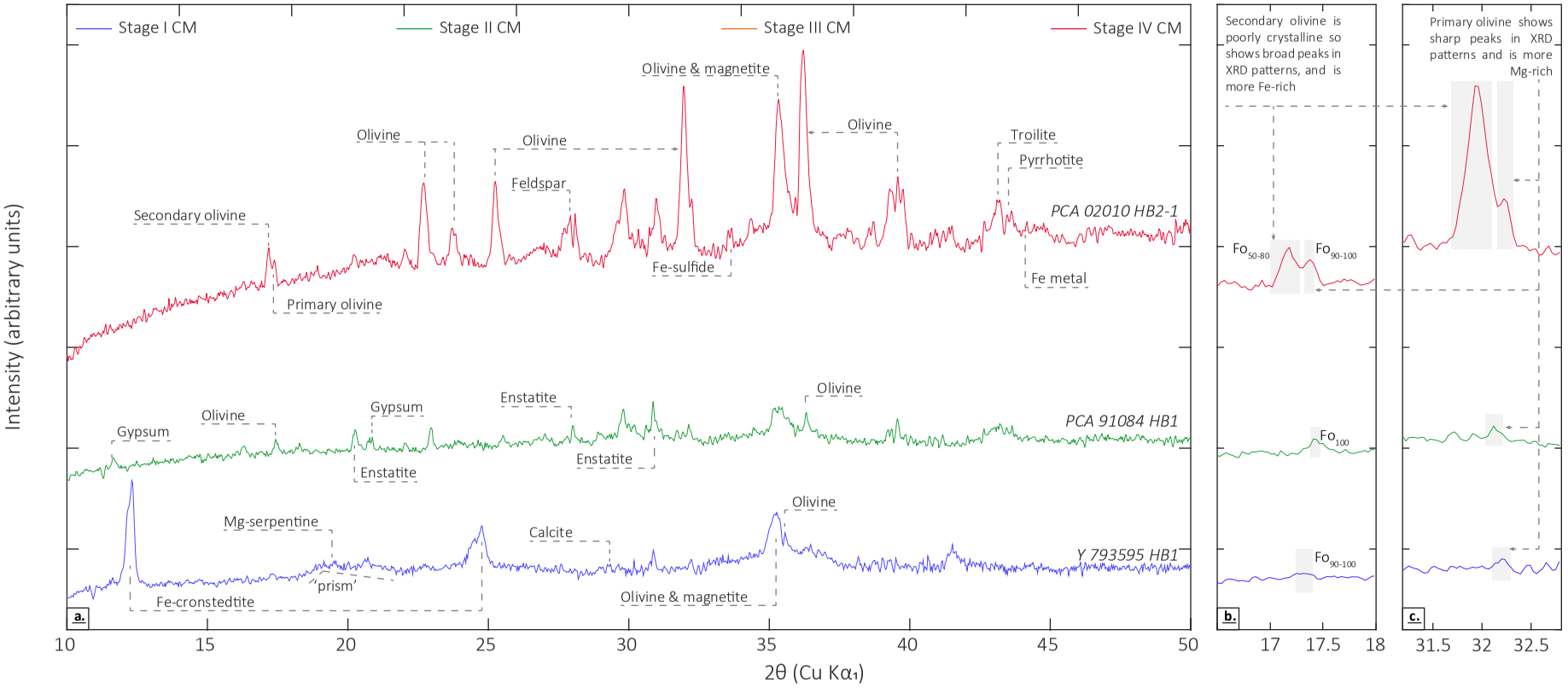


Figure 4.1: *(a) PSD-XRD patterns of representative thermally altered CMs (offset on the y axis). Subsections of the XRD patterns are shown, between 16.5 - 18 ° (b) and 31.2 - 32.8 ° (c), which is where diffraction peaks due to olivine are located. These ranges show the same diffraction peaks as are shown in Figure 4.1b and 4.1c, shifted in position due to the use of Cu radiation in the PSD-XRD as opposed to Co radiation for the high resolution XRD.*

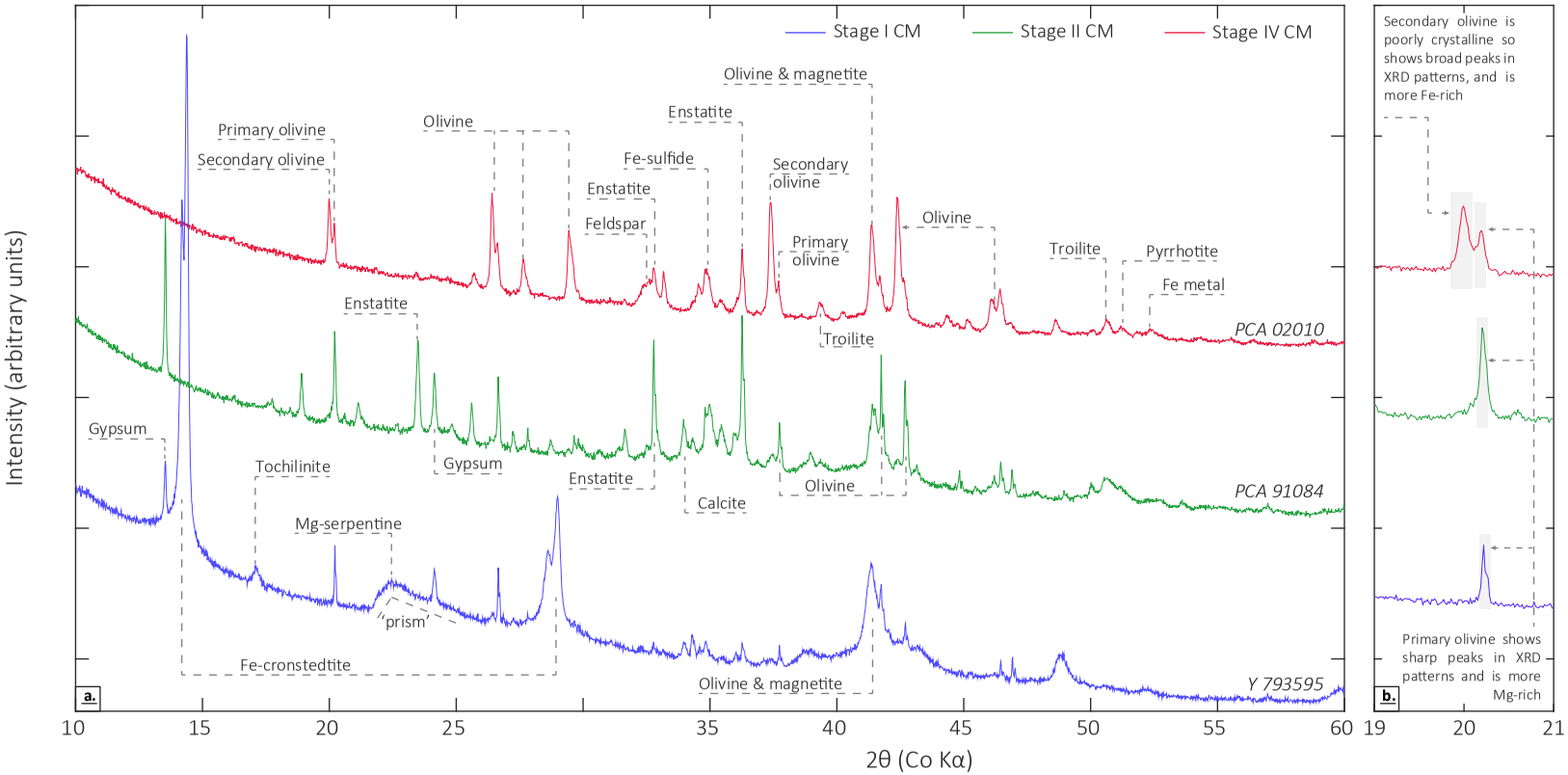


Figure 4.2: *(a) High resolution XRD patterns of representative thermally altered CMs (offset on the y axis). Subsections of the XRD patterns are shown, between 19 – 21 o (b) and 36.5 – 38.5 o (c), which is where diffraction peaks due to olivine are located.*

petrologic types of 1.2 - 1.6. Of the stage II CMs, EET 96029 and Y 793321 had modal mineralogy determined for two aliquots of the meteorite (subsamples HB2-1 and HB2-2), and the abundances were found to be within error of each other, indicating the samples were well mixed during preparation. The EET 96029 sample in this study has a lower enstatite abundance, and as a result a lower PSF petrologic type, than that determined for a different sample of the same meteorite by Lee et al. (2016).

Stage IV patterns show diffraction peaks associated with olivine, enstatite, gypsum, Fe-sulfide (troilite and pyrrhotite), feldspar and metal, and no diffraction peaks due to phyllosilicates. In Figures 4.1b and 4.1c, the two stage IV patterns have peaks near 20.2 and 37.7 ^{o} attributed to Fo_{90-100} primary olivine, however they also show additional broad peaks near 20 and 37.4 ^{o} consistent with poorly crystalline, ~Fo_{60} olivine (Gates-Rector and Blanton, 2019). The more Fe-rich composition and low crystallinity of the olivine indicates they are recrystallised, secondary products resulting from thermal alteration. The stage IV PCA 02010 contains ~15 vol% primary olivine, ~61 vol% secondary olivine, ~16 vol% enstatite, ~8 vol% Fe-sulfide and ~2 vol% feldspar. Assuming all recrystallised phases were once phyllosilicates, a PSF petrologic type can be determined. This is complicated by the enstatite abundance, as at temperatures >700 ^{o}C secondary pyroxene does begin to recrystallise (Nakamura, 2005), however it is difficult to identify as a secondary phase in XRD. Therefore, I only assume recrystallised olivines were once phyllosilicates. This gives a PSF petrologic type of PCA 02010 of 1.7. This mineralogy is consistent with that determined for a different sample of PCA 02010 by Hanna et al. (2020). The stage IV PCA 02012 consists of ~27 vol% primary olivine, ~21 vol% secondary olivine, ~15 vol% enstatite, 9 vol% Fe-sulfide and ~1 vol% feldspar, giving it a PSF petrologic type of 2.0. Its modal mineralogy suggests that PCA 02012 is less aqueously altered than the PCA 02010, and its lower secondary olivine abundance suggests it has experienced less thermal alteration, assuming similar thermal

alteration conditions. Both aliquots (subsamples HB2-1 and HB2-2) of each meteorite gave modal mineralogies within error of each other.

Aqueously and thermally altered CY chondrites

Five of the meteorites studied are classified as CY chondrites; two stage IIIs (Y 86029 and Y 980115) and three stage IVs (Y 86720, Y 86789 and B 7904), and Figure 4.3 shows high-resolution XRD and PSD-XRD patterns for representative samples from both stages. In the high-resolution patterns (Fig. 4.3a), no diffraction peaks associated with crystalline phyllosilicates were present in any of the CY samples. The stage III patterns show diffraction peaks due to Fo_{60-70} olivine that are broad, indicating they are poorly crystalline and secondary. It also shows peaks consistent with troilite and magnetite. The stage IV samples show peaks due to olivine, enstatite, Fe-metal and Fe-sulfide (troilite and pyrrhotite). Figure 4.3b shows high-resolution XRD patterns for representative CY samples between 19 - 21 ^{o}. The Y 86720 and Y 86029 patterns show only one peak due to olivine, consistent with a chemistry of Fo_{60-70}, whereas the B 7904 pattern shows doublets, with a sharp peak due to Fo_{90-100} and a broader peak due to Fo_{60-70} (Gates-Rector and Blanton, 2019). The Fo_{60-70} peaks are broad in comparison to the Fo_{90-100} peaks, indicating they are secondary phases, and the more Mg-rich olivine is primary.

PSD-XRD patterns for representative CYs are shown in Figure 4.3c. Stage III CYs contain ~8 vol% secondary olivine, ~3 vol% magnetite and ~14 vol% Fe-sulfide (Table 4.1). Y 86029 contains 67 vol% disordered phyllosilicate, and Y 980115 contains ~79 vol% disordered phyllosilicate but their PSF petrologic types are both 1.0, as neither meteorites contain primary olivine or any enstatite. The multiple aliquots of Y 980115 show results within error of each other. This is consistent with previously determined mineralogies for stage III CYs (King et al., 2019).

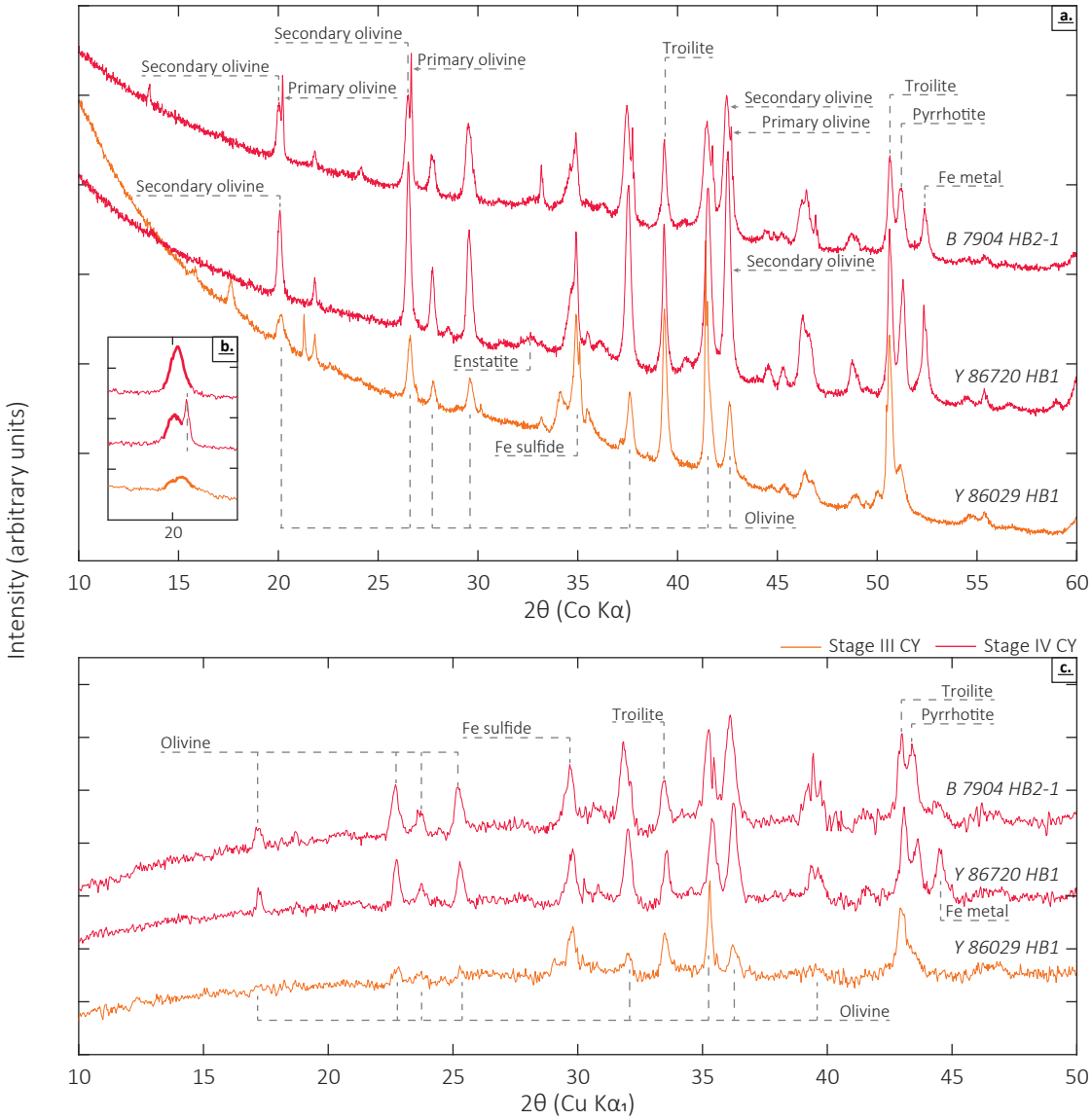


Figure 4.3: *(a) High-resolution XRD patterns of representative CYs offset on the y axis. A subsection of the XRD pattern is shown in (b), between 19 – 21 °, showing the different primary olivine peak in the B 7904 pattern. (c) PSD-XRD patterns of representative CYs.*

The stage IV CY B 7904 contains ~25 vol% primary olivine, ~50 vol% secondary olivine, ~9 vol% enstatite, ~14 vol% Fe-sulfide, <2 vol% calcite and ~1 vol% metal, and has a PSF petrologic type of 1.9. This is consistent with previous investigations of B 7904 (King et al., 2019). The modal mineralogies for the stage IV CYs Y 86720 and Y 86789 are 58 - 63 vol% secondary olivine, 5 - 11 vol% enstatite, 28 - 33 vol% Fe-sulfide and 2 - 3 vol% Fe-metal.

As shown in Table 4.1, the modal mineralogy for the two samples (HB1 and HB2) of each meteorite were within error of each other, indicating that the meteorites are relatively homogeneous at this scale (ie. 50 mg chips). The multiple subsamples of B 7904, Y 86720,54 (HB2) and Y 86789,70 (HB2) produced similar mineralogies, apart from a difference of 7 vol% in the Fe-sulfide abundance in the B 7904 subsamples and a difference in enstatite abundance of 6 vol% in the Y 86720 subsamples.

Anomalous CM chondrites

The remaining six samples are all classified as either CM2 or CM-anomalous and have been suggested in the literature to be thermally metamorphosed (Chapter 2). However, they differ from the thermally altered CM chondrites, either in their mineral assemblages determined here, or through previous investigation (for example in the case of Dho 2046, Dho225 and Dho 735, their oxygen isotopic composition falls outside typical CM values).

EET 96010 was originally classified as a CV3 chondrite (Grossman, 1998), but it shows a different oxygen isotopic composition from the CV group, and similar elemental abundances to CM chondrites that have experienced temperatures of >700 ^{o}C (Moriarty et al., 2009). Figure 4.4 shows that EET 96010 contains both primary and secondary olivine, enstatite, calcite, Fe-sulfide (troilite and pyrrhotite), Fe-metal and some rusts. From PSD-XRD analysis, the bulk mineralogy of EET 96010 is 41 vol% primary olivine, 24 vol% secondary olivine, 9 vol% enstatite, 19 vol% Fe-sulfide, 2 vol% calcite, 1 vol% Fe-metal and 3 vol% rust. Its PSF petrologic type is 2.4.

The PSD-XRD patterns of Dho 2046, Dho 225 and Dho 735 are shown in Figure 4.4c. Dho 2046 has a mineralogy consisting of 16 vol% primary olivine, 20 vol% secondary olivine, 2 vol% enstatite, 10 vol% Fe-sulfide and 51 vol% disordered phyllosilicate. It has a PSF petrologic type of 1.5. Dho 225 and Dho 735 consist of ~7 vol% primary olivine, ~9 vol% secondary

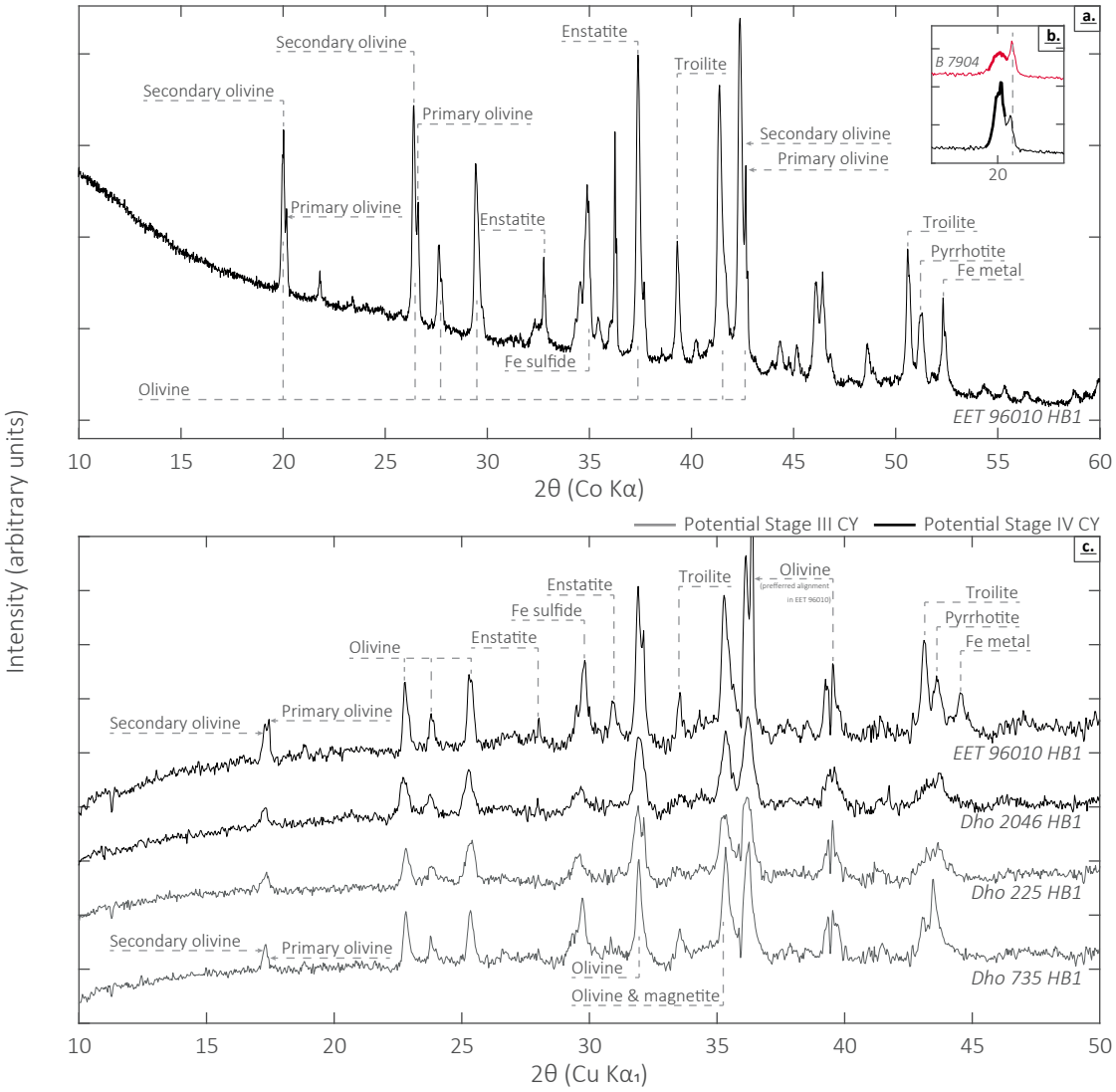


Figure 4.4: *(a) High-resolution XRD pattern of EET 96010, with relevant diffraction peaks labelled. A subsection of the XRD pattern is shown in (b), between 19 – 21 °, along with the same range for the B 7904 pattern for comparison. (c) PSD-XRD patterns of EET 96010, Dho 2046, Dho 225 and Dho 735, offset on the y axis, with relevant peaks labelled.*

olivine, ~4 vol% Fe-sulfide, <2 vol% enstatite, <1 vol% calcite and ~79 vol% disordered phyllosilicate. Both samples have PSF petrologic types of 1.2.

Figure 4.5a shows the high resolution XRD pattern of the CM2 A 881655. It shows diffraction peaks due to gypsum, calcite, enstatite, olivine, Fe-sulfide (troilite and pyrrhotite) and magnetite. The magnetite peaks are significantly more intense than those observed in high-resolution XRD patterns of other CM chondrites (e.g. Figure 4.1). There is a subtle

'prism ' feature near 22.6 °, which is consistent with the presence of partially dehydrated Mg-rich serpentine and smectite phyllosilicates (Nakamura, 2005, Tonui et al., 2014). The olivine diffraction peaks for A 881655 show a similar chemistry and crystallinity to the olivine peaks in the CY chondrite patterns (Fig. 4.5b). They are consistent with a chemistry of Fo_{70-90}, and they are broad suggesting they are poorly crystalline and secondary. The PSD-XRD pattern of A 881655 is shown in Figure 4.5c. The mineralogy of A 881655 is determined to be 14 vol% secondary olivine, 4 vol% enstatite, 7 vol% magnetite, 4 vol% Fe-sulfide, 1 vol% calcite, 2 vol% gypsum and 67 vol% disordered phyllosilicate.

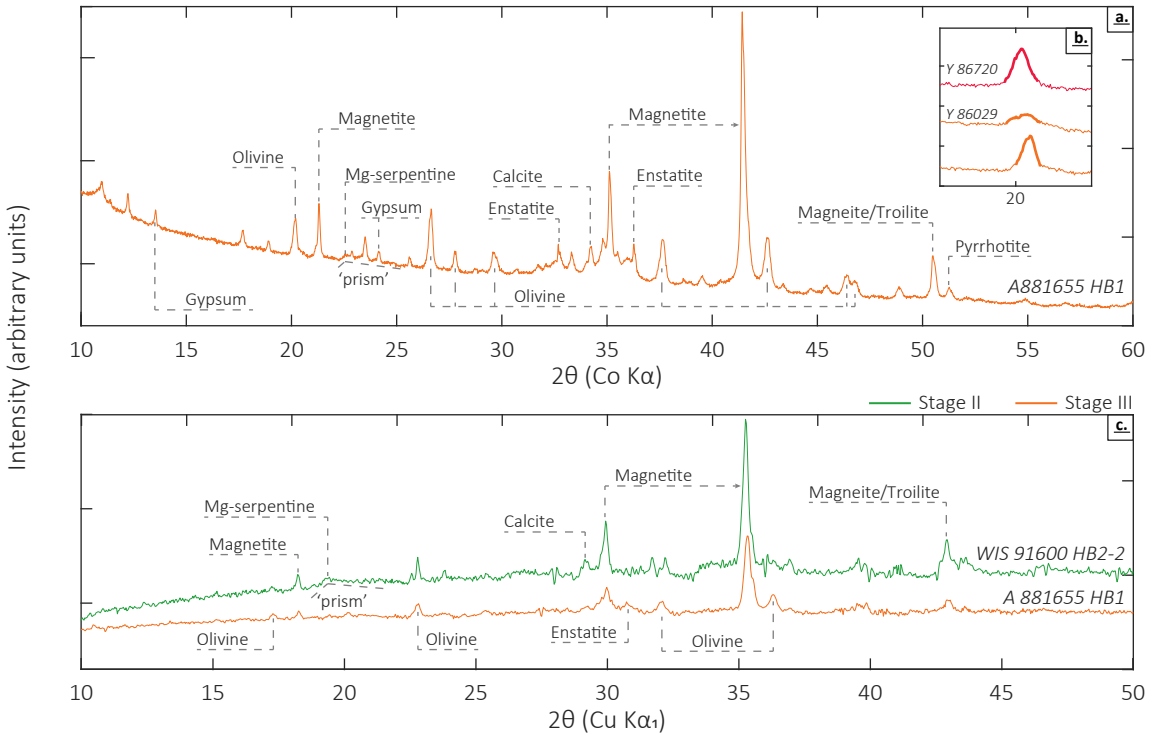


Figure 4.5: *(a) High-resolution XRD pattern of A 881655, with relevant diffraction peaks labelled. A subsection of the XRD pattern is shown in (b), between 19 – 21 °, along with the same range for the Y 86720 and Y 86029 pattern for comparison. (c) PSD-XRD patterns of WIS 91600 and A 881655, offset on the y axis, with relevant peaks labelled.*

Figure 4.5c also shows the PSD-XRD pattern of the CM2 WIS 91600. It has diffraction peaks due to olivine, enstatite, calcite, Fe-sulfide (troilite) and magnetite. As with the PSD-XRD pattern of A 881655, the magnetite peak in the WIS 91600 pattern is intense. The

'prism' feature associated with dehydrated Mg-rich serpentines and smectites is also resolvable. The modal mineralogy of WIS 91600 is determined to be ~12 vol% primary olivine, ~3 vol% enstatite, ~9 vol% magnetite, ~4 vol% Fe-sulfide, ~1 vol% calcite and ~72 vol% phyllosilicate, with a PSF petrologic type of 1.4. The subsamples of WIS 91600 gave results that were within error of one another (Table 4.1), and the mineralogy determined is consistent with values determined for a different sample of WIS 91600 by Howard et al. (2015).

4.3.2 Reflectance spectra

Sample		Classification	3 μm feature (μm)	3 μm feature area (μm^{-1})	6 μm feature (μm)	Christiansen feature (μm)	Transparency feature (μm)	Si-O bending feature (μm)
A 881334	HB1	CM2	2.90 ± 0.01	0.07 ± 0.01	6.24 ± 0.01	8.55 ± 0.02	12.21 ± 0.02	19.15 ± 0.11
A 881655	HB1	CM2	2.90 ± 0.01	0.06 ± 0.01	6.15 ± 0.02	8.48 ± 0.01	12.31 ± 0.02	18.45 ± 0.07
B 7904	HB2	C2-ung/CY	2.90 ± 0.01	0.03 ± 0.01	6.37 ± 0.02	8.90 ± 0.02	12.55 ± 0.07	18.86 ± 0.12
Dho 225	HB1	CM-an	2.90 ± 0.01	0.04 ± 0.01	6.20 ± 0.01	9.04 ± 0.04	12.67 ± 0.07	19.54 ± 0.14
Dho 735	HB1	CM2	2.92 ± 0.01	0.07 ± 0.01	6.19 ± 0.01	9.17 ± 0.02	12.47 ± 0.04	19.15 ± 0.22
Dho 2046	HB1	CM2-an	2.93 ± 0.01	0.04 ± 0.01	6.13 ± 0.01	9.09 ± 0.03	12.58 ± 0.04	19.22 ± 0.27
DOM 03183	HB1	CM2	2.83 ± 0.01	0.12 ± 0.02	6.30 ± 0.01	8.61 ± 0.03	12.16 ± 0.03	19.06 ± 0.09
EET 96010	HB1	CM2	2.91 ± 0.01	0.04 ± 0.01	-	8.58 ± 0.04	12.49 ± 0.03	19.07 ± 0.07
EET 96029	HB2	CM2	2.93 ± 0.01	0.08 ± 0.01	6.18 ± 0.02	8.56 ± 0.02	12.28 ± 0.02	19.29 ± 0.11
MIL 07700	HB1	CM2	2.87 ± 0.01	0.07 ± 0.01	6.17 ± 0.02	8.86 ± 0.01	12.16 ± 0.02	19.95 ± 0.28
PCA 02010	HB2	CM2	3.02 ± 0.04	0.17 ± 0.01	6.12 ± 0.01	8.56 ± 0.02	12.34 ± 0.04	19.23 ± 0.07
PCA 02012	HB2	CM2	2.94 ± 0.01	0.15 ± 0.01	6.11 ± 0.01	8.51 ± 0.02	12.41 ± 0.05	18.92 ± 0.08
PCA 91084	HB1	CM2	2.89 ± 0.01	0.07 ± 0.01	6.13 ± 0.01	8.44 ± 0.02	12.14 ± 0.02	19.10 ± 0.32
WIS 91600	HB2	CM-an	2.90 ± 0.01	0.04 ± 0.01	6.15 ± 0.02, 6.93 ± 0.01	8.76 ± 0.01	12.16 ± 0.03	19.65 ± 0.16
Y 793321	HB2	CM2	2.88 ± 0.01	0.05 ± 0.01	6.23 ± 0.05	8.52 ± 0.02	12.29 ± 0.02	19.09 ± 0.15
Y 793595	HB1	CM2	2.82 ± 0.01a	0.27 ± 0.05	6.13 ± 0.01	8.78 ± 0.03	11.36 ± 0.05	20.79 ± 0.03
Y 794080	HB1	CM2	2.89 ± 0.01	0.11 ± 0.01	6.12 ± 0.01	8.60 ± 0.02	12.45 ± 0.01	19.31 ± 0.09
Y 86029	HB1	CI1/CY	2.89 ± 0.01	0.05 ± 0.01	6.61 ± 0.01, 6.88 ± 0.02	8.93 ± 0.01	12.06 ± 0.04	19.91 ± 0.28
Y 86720,61	HB1	C2-ung/CY	2.92 ± 0.01	0.06 ± 0.01	-	9.47 ± 0.02	-	-
Y 86720,54	HB2	C2-ung/CY	2.91 ± 0.01	0.07 ± 0.01	6.32 ± 0.04	8.85 ± 0.02	12.31 ± 0.07	19.04 ± 0.06
Y 86789,60	HB1	C2-ung/CY	2.91 ± 0.01	0.04 ± 0.01	6.30 ± 0.01	9.03 ± 0.04	12.48 ± 0.05	19.39 ± 0.12
Y 86789,70	HB2	C2-ung/CY	2.91 ± 0.01	0.05 ± 0.01	6.19 ± 0.02	8.89 ± 0.02	12.41 ± 0.04	18.99 ± 0.05
Y 980115	HB2	CI1/CY	2.89 ± 0.01	0.07 ± 0.01	6.58 ± 0.01, 6.93 ± 0.03	8.89 ± 0.01	12.14 ± 0.03	-

Table 4.2: *The NIR and MIR parameters determined for the aqueously and thermally altered CM, CY and CM-CY-anomalous samples.*

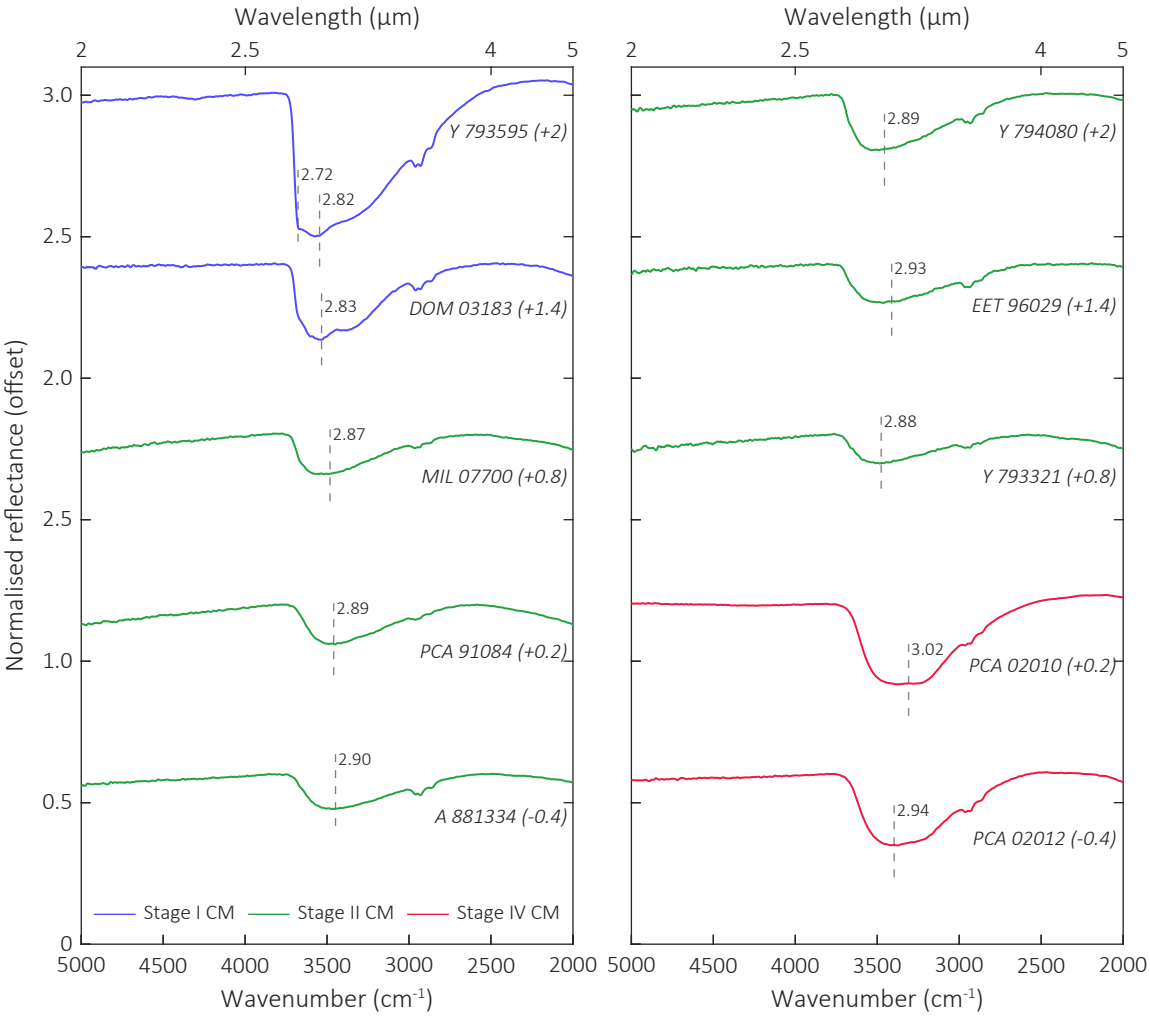


Figure 4.6: *The 3 µm feature from the thermally altered CM spectra investigated in this chapter. All spectra are normalised to a linear continuum between 2.67 – 3.87 µm and offset on the y axis (by the value in brackets after the meteorite name).*

NIR

All meteorites show a broad, asymmetric feature near 3 µm , and these are shown in Figures 4.6 - 4.9. All also show a small feature near 3.40 µm consistent with organics (Takir et al., 2013). The positions of these features are given in Table 4.2. The stage I DOM 03183 spectrum shows a feature at 2.83 µm (Figure 4.6a), which is consistent with the features observed in unheated CM chondrites with PSF petrologic types of 1.3 – 1.5, shown in chapter 3 (Figure 3.3). This is in agreement with the PSF petrologic type of 1.5 for DOM 03183.

The stage I Y 793595 shows features at 2.72 and 2.82 µm (Figure 4.6a), which resemble the feature observed in the unheated LON 94101 spectrum (Figure 3.3). LON 94101 has a petrologic type of 1.3 and its spectrum is suggested to show 'intermediate' behaviour between the more and less aqueously altered CM chondrite spectra (Chapter 3). Stage II CM sample spectra show features in the region between 2.87 – 2.93 µm (Table 4.2, Figures 4.6a and 4.6b). These features show a reduced 3 µm band area (0.04 – 0.11 μm^{-1}) in comparison to the stage I spectra (~0.20 μm^{-1}). The stage IV CM spectra show features at longer wavelengths, 3.02 and 2.94 µm (Figure 4.6b), with areas of 0.17 and 0.15 μm^{-1}.

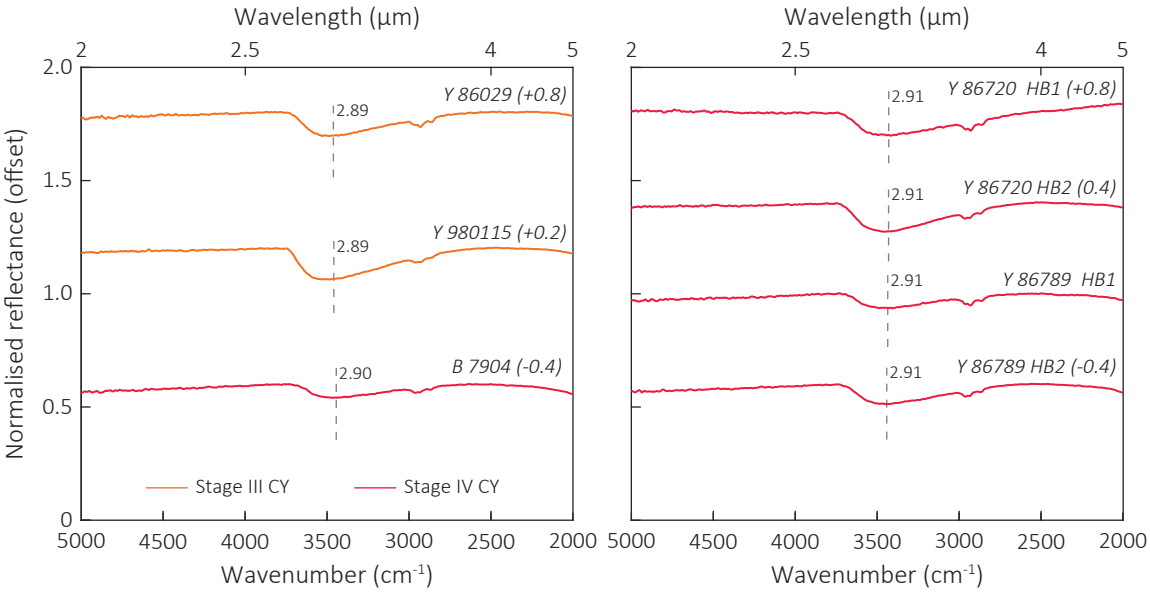


Figure 4.7: *The 3 µm feature from the thermally altered CY spectra investigated in this chapter. All spectra are normalised to a linear continuum between 2.67 – 3.87 µm and offset on the y axis (by the value in brackets after the meteorite name).*

Figure 4.7 shows the 3 µm features for the CY chondrite spectra. Stage III spectra show a feature near 2.89 µm, and stage IV CY spectra show a feature near 2.91 µm (Table 4.2). The band area of these features does not change significantly either, from ~0.06 μm^{-1} to ~0.05 μm^{-1}. As these parameters are both within error of each other, there is no obvious change of the 3 µm feature with increasing thermal alteration in the CY spectra. (Table 4.1, section 4.3.1). Figure 4.8 shows the 3 µm region for the EET 96010, Dho 2046, Dho 225

and Dho 735 meteorites that share some affinities with CY chondrites. They show similar features to the CY spectra at 2.90 - 2.93 µm, with band areas of ~0.05 μm^{-1} (Table 4.2).

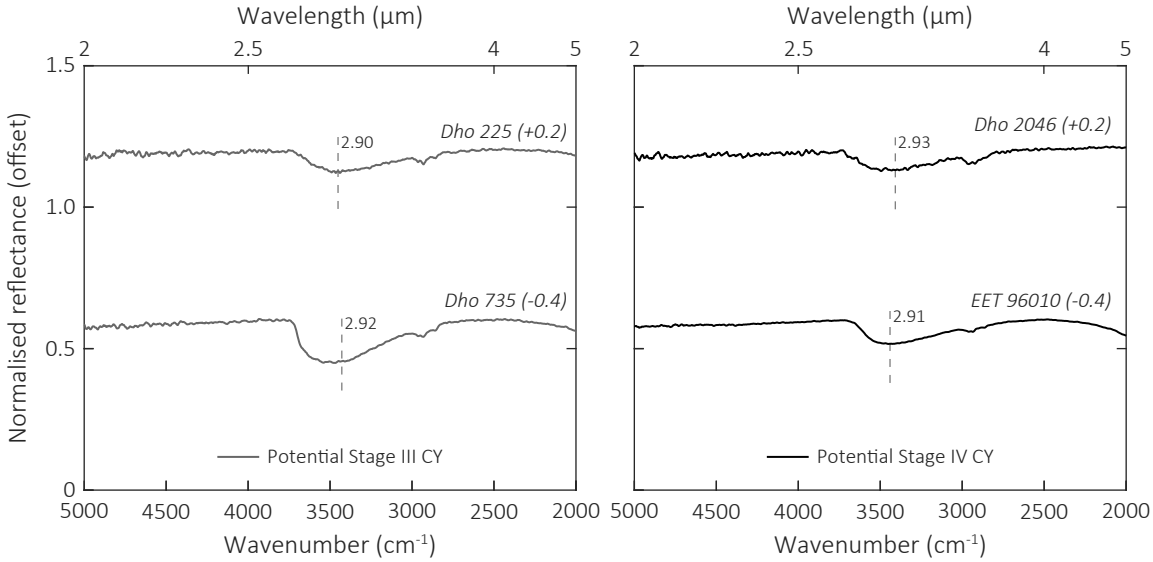


Figure 4.8: *The 3 µm feature from the spectra of EET 96010, Dho 2046, Dho 225 and Dho 735. All spectra are normalised to a linear continuum between 2.67 – 3.87 µm and offset on the y axis (by the value in brackets after the meteorite name).*

Figure 4.9 shows the 3 µm features for A 881655 and WIS 91600. They both show a sharp feature near 2.72 µm, and a broader feature near 2.90 µm. The spectral shape is similar to that of the unheated CI chondrite 3 µm region (Figure 3.4) and is attributed to the presence of both serpentine and smectite phyllosilicates, the latter of which contains interlayer H_2O (chapter 3).

MIR

Figures 4.10 – 4.13 show the spectra between 5 – 50 µm of all samples in this chapter, and the positions of identified features are given in Table 4.2. The stage I CMs Y 793595 and DOM 03183 spectra show vibrational features at 6.13 and 6.30 µm, respectively (Fig. 4.10a). As discussed in chapter 3, these features are likely affected by adsorbed terrestrial

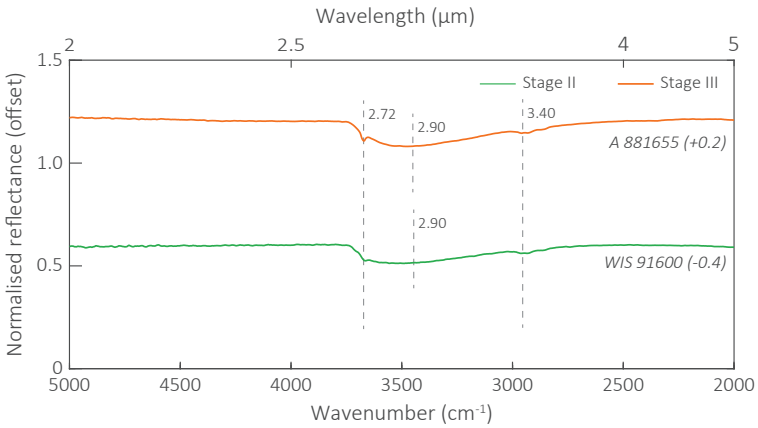


Figure 4.9: *The 3 µm feature from the spectra of A 881655 and WIS 91600. Both spectra are normalised to a linear continuum between 2.67 – 3.87 µm and offset on the y axis (by the value in brackets after the meteorite name).*

water, but as the samples were heated prior to having spectra collected and all observations were done under a vacuum, I assume that there is a mineralogical component to this feature. The stage I CM spectra have CFs that are within the wavelength range determined for the unheated CM spectra (8.58 – 9.12 µm, Table 3.2, Figure 3.5). The CF determined for the DOM 03183 spectrum at 8.61 µm is consistent with its pyroxene abundance of 10 vol% (as observed for LEW 85311, section 3.3.3), and the Y 793595 spectrum shows a CF at 8.78 µm, consistent with the CF determined for Mg-serpentine phyllosilicate standards (chapter 2). The TF for the stage I spectra are identified near 11.36 and 12.16 µm for Y 793595 and DOM 03183, respectively. This is consistent with DOM 03183 being less aqueously altered than Y 793595 (Chapter 3). In the Si-O stretching region between 9.5 – 11.5 µm, and the Si-O bending region between 18.0 – 25.0 µm, the stage I Y 793595 CM spectrum shows vibrational features at 9.65 and 20.79 µm, which are consistent with the Mg-rich phyllosilicate standard spectrum of lizardite shown in chapter 2 (Figure 2.7). The stage I DOM 03183 spectrum shows a combination of the Mg-olivine and Mg-phyllosilicate vibration features, near 9.62 (phyllosilicate), 10.10, 10.70 and 19.06 µm (all olivine). This suggests olivine is spectrally dominant even in low quantities (DOM 03183 only has 12 vol% olivine) and again

supports the conclusion that DOM 03183 is less aqueously altered than Y 793595.

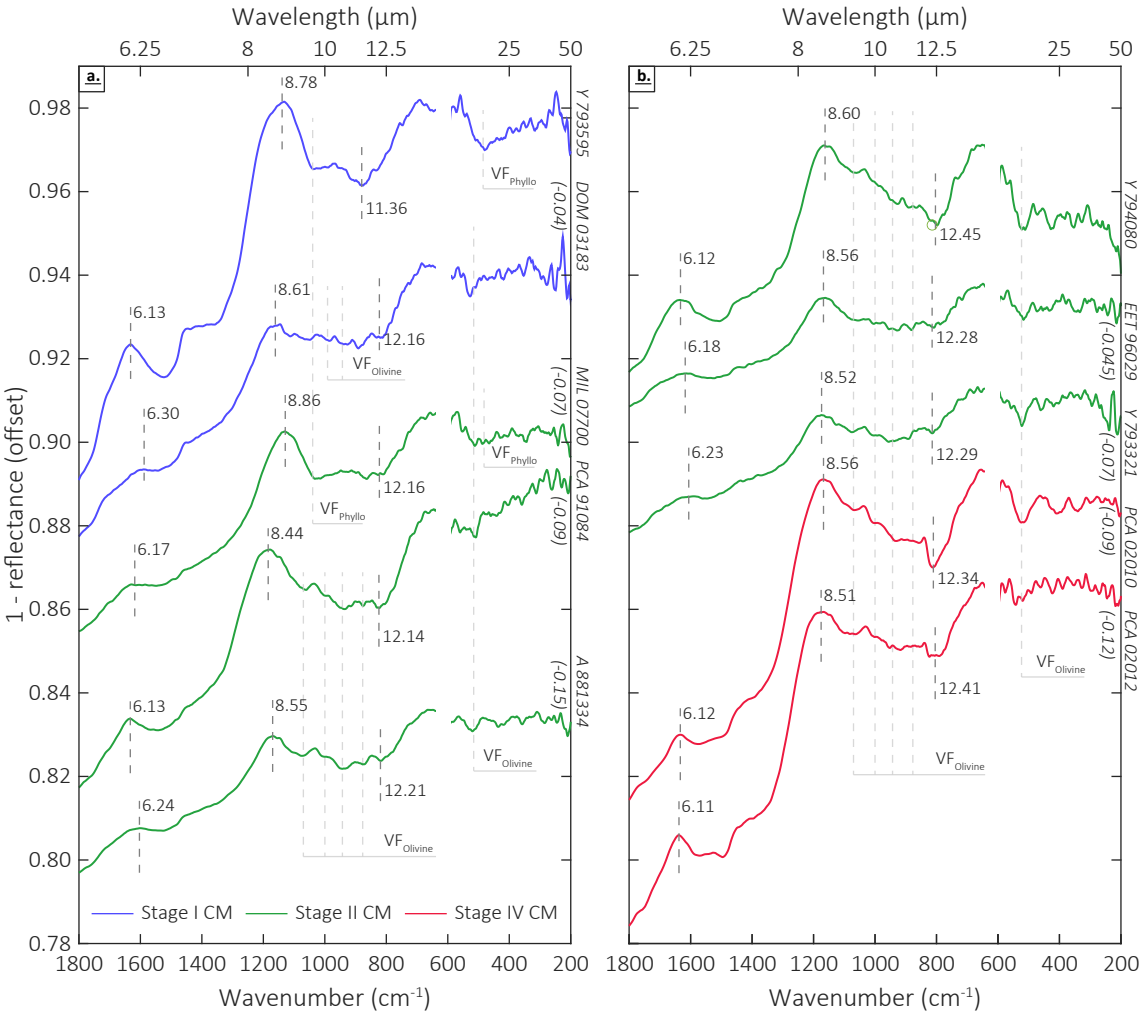


Figure 4.10: *The MIR spectra from the thermally altered CM meteorites investigated in this chapter. All spectra are offset on the y axis ((by the value in brackets after the meteorite name).*

Stage II and stage IV CM spectra are shown in Figure 4.10a and 4.10b. The stage II spectra show features between 6.12 - 6.24 µm, and CFs between 8.44 - 8.86 µm. Stage IV CM spectra show features at ~6.12 µm, and CFs near 8.54 µm. The CFs determined for all thermally altered CM spectra (8.44 - 8.86 µm) are generally at shorter wavelengths than those determined for the unheated and stage I CM spectra (8.58 - 9.12 µm). The stage II and stage IV CM spectra show TFs between 12.16 - 12.41 µm. There does seem to be a shift to longer wavelengths of the TF with increasing thermal alteration. The stage II and stage IV

CM spectra show a number of vibrational features in the Si-O stretching and bending regions that are consistent with Mg-rich olivine, near 9.35, 10.00, 10.60, 11.40 and 19.10 µm (Figure 2.9, Hamilton 2010). The stage II MIL 07700 spectrum shows a single feature near 9.69 µm and a Si-O bending feature at 19.95 µm (Figure 4.10a), both of which are more consistent with Mg-serpentine than Mg-olivine, which is what seems to be influencing the spectral signature in the other stage II CM spectra. MIL 07700 has a low petrologic type, however, indicating it was heavily aqueously altered prior to thermal alteration. It only has an olivine abundance of 5 vol%, and a disordered phyllosilicate abundance of 91 vol%, making it likely this phyllosilicate is the spectrally dominant phase.

Unlike the CM spectra, between 5 – 7 µm the CY spectra show a change in spectral signature with thermal alteration (Figure 4.11). The stage III CY spectra show broad features with double peaks near 6.60 and 6.90 µm, whereas the stage IV CY spectra show features at shorter wavelengths 6.19 - 6.37 µm, with much less spectral contrast. The stage IV features are spectrally similar to the features observed in the thermally altered CM chondrite spectra in Figure 4.10. The broad features in the stage III CY chondrite spectra occur at the same positions as features in emissivity spectra of mineral mixtures that contain carbonates (Donaldson Hanna et al., 2019), however no carbonates were identified in the mineralogy of the samples here. However, both unheated and thermally decomposed ankerite and siderite have been observed in Y 86029 by Tonui et al. (2003), and if these phases are decomposed in my sample of the stage III CYs, they may be difficult to identify in XRD patterns.

The CY spectra show CFs near 8.89 – 9.03 µm, with no trend with increasing thermal alteration between stage III and stage IV spectra. The Y 86720 HB1 sample spectrum shows a CF at 9.47 µm, however it is likely this is due to sample packing effects - the spectrum shows lower spectral contrast of features than other spectra, and the absence of a distinct

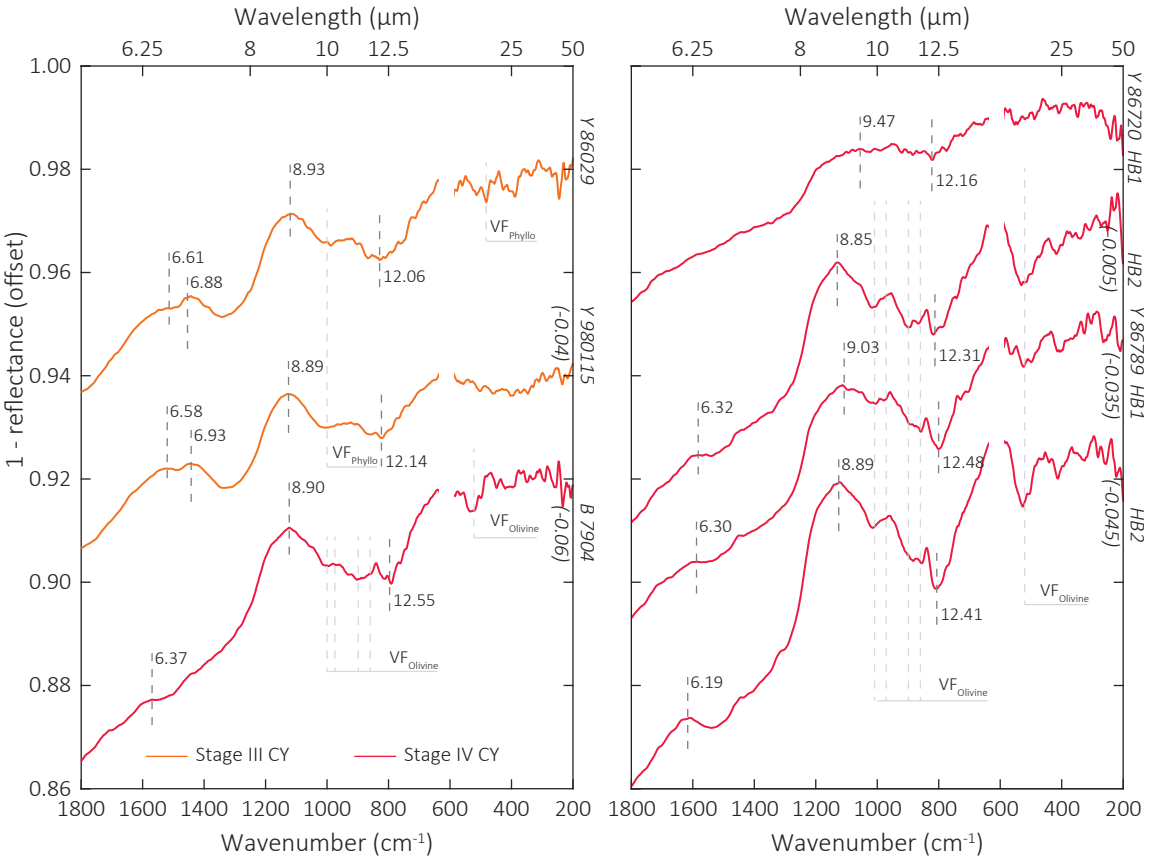


Figure 4.11: *The MIR spectra from the thermally altered CY meteorites investigated in this chapter. All spectra are offset on the y axis (by the value in brackets after the meteorite name).*

TF suggests the powder was 'tightly' packed into the sample cup (section 2.4.1.1). This appears to have shifted the apparent position of the CF in this particular spectrum to a longer wavelength. Both stage III CY spectra show TFs near 12.10 μm. As with the CM spectra, there seems to be a shift to longer wavelengths with increasing thermal alteration, with the stage IV CY spectra showing TFs between 12.31 - 12.55 μm. In the Si-O stretching region, the stage III CY spectra show a single vibrational feature near 10 μm. This feature, whilst located in the same position as the olivine features in stage II and stage IV CM spectra, has a similar spectral shape to the phyllosilicate features identified in the stage I and unheated CM spectra. Additionally, the Y 86029 spectrum shows a feature near 19.91 μm (the Y 980115 spectrum has no distinguishable features in the Si-O bending region) that is more consistent

with Mg-rich phyllosilicates. The cause of this feature in these spectra is therefore likely to be disordered phyllosilicate (similar to my observations for the stage II CM MIL 07700 spectrum). The stage IV CY spectra show features near 9.85, 10.25, 11.20, 11.60 and 19.00 µm. These features show similar spectral shape to the olivine vibrational features in the stage II and stage IV CM spectra, but excluding the 19.00 µm feature, plot at longer wavelengths. This shift is likely due to the higher abundances of secondary, more Fe-rich olivine compared to stage II and stage IV CM chondrites (Table 4.2). Increasing Fe content in olivine is known to cause shifts to longer wavelengths (Hamilton, 2010, Lane et al., 2011).

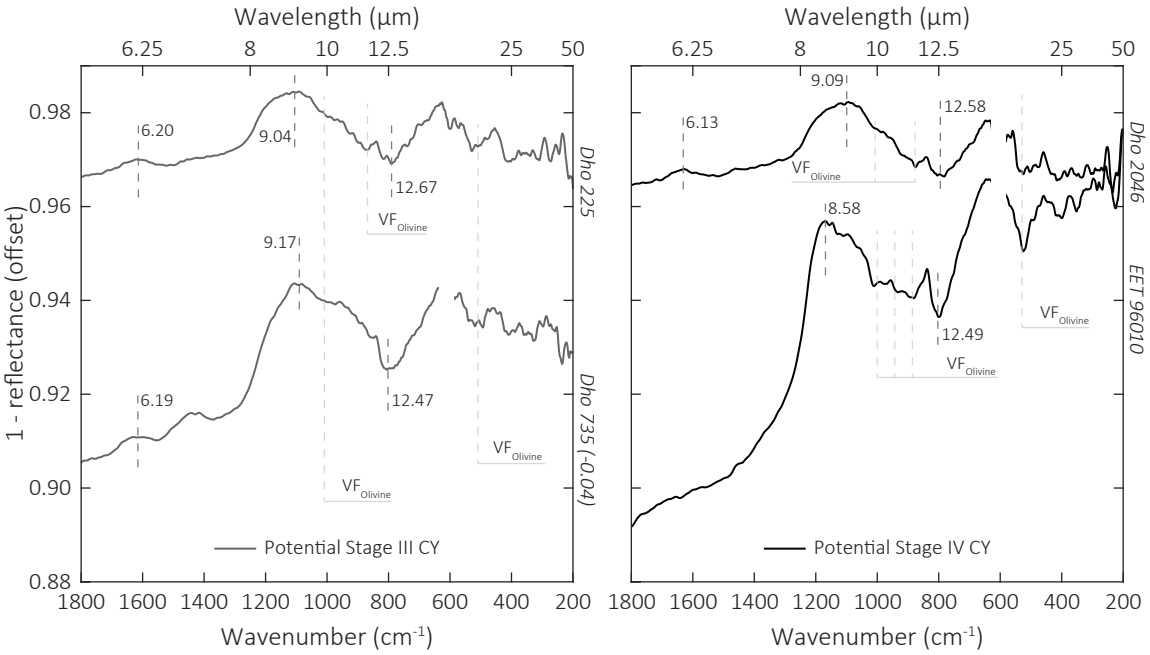


Figure 4.12: *The MIR spectra from EET 96010, Dho 2046, Dho 225 and Dho 735. All spectra are offset on the y axis (by the value in brackets after the meteorite name).*

The EET 96010, Dho 2046, Dho 225 and Dho 735 MIR spectra are shown in Figure 4.12. The Dho 2046, Dho 225 and Dho 735 spectra show features between 6.13 - 6.20 µm, and CFs between 9.04 - 9.17 µm (Figure 4.12, Table 4.3). These are similar to the CFs observed in the least aqueously altered CM chondrites in chapter 3 and are at longer wavelengths than the CFs observed in both the thermally altered CM and CY spectra. The TF observed

in these three spectra are between 12.47 - 12.67 µm, which are at the longest wavelengths identified for thermally altered CM and CY spectra. All three spectra show weak olivine vibrational features near 9.85 and 19.30 µm, and the Dho 225 and Dho 2046 spectra show an olivine feature near 11.50 µm. The EET 96010 spectrum shows no features between 5 - 7 µm, a CF at 8.58 µm, and olivine vibrational features near 10.00, 10.60, 11.40 and 19.10 µm. Its CF and Si–O stretching region are spectrally more similar to the stage IV CM chondrite spectra than the CY spectra.

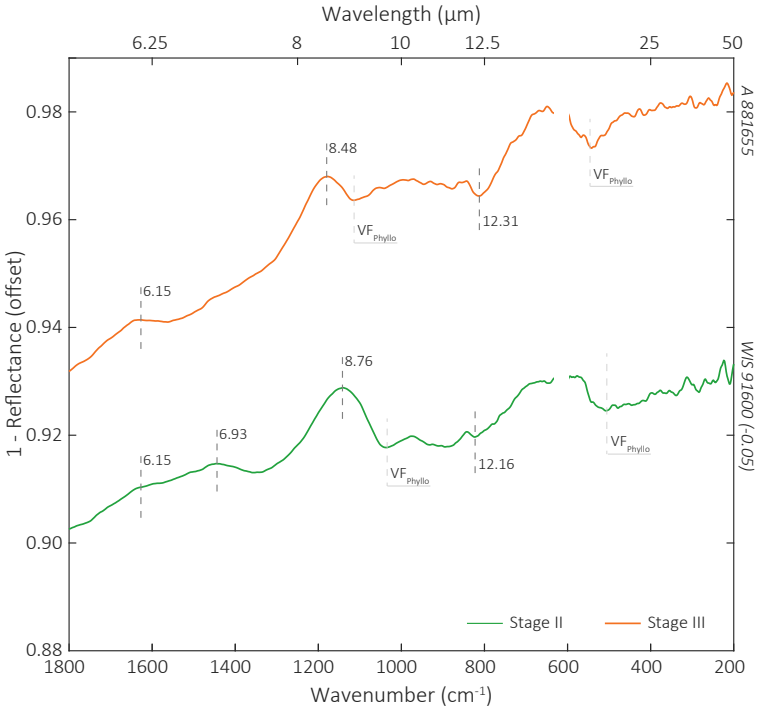


Figure 4.13: *The MIR spectra from A 881655 and WIS 91600. Both spectra are offset on the y axis (by the value in brackets after the meteorite name).*

Figure 4.13 shows the MIR spectra of A 881655 and WIS 91600. The A 881655 spectrum resembles the unheated and thermally altered CM spectra (Fig. 4.13), with a feature near 6.15 µm, however WIS 91600 shows a broader feature, comparable to the stage III CY spectra, although the double peak is less pronounced. The CFs for A 881655 and WIS 91600 are 8.48 and 8.76 µm, respectively (Fig. 4.13). These are within the range for CFs identified

for thermally altered CM spectra. The WIS 91600 spectrum has a TF at 12.16 µm, and the A 881655 spectrum has a TF at 12.31 µm, both within the range of TF positions identified for thermally altered CM and CY spectra. WIS 91600 shows a vibrational feature near 9.60 µm that is consistent with the phyllosilicate features observed in the stage I Y 793595 and the stage II MIL 07700 spectra. It also shows a broad feature near 19.65 µm. A 881655 shows vibrational features at 9.01 and 18.45 µm. These features are most consistent with vibrational features identified in spectra collected for a saponite standard (Fig. 2.7), which supports observations of smectite phyllosilicates in this sample (Lipschutz et al., 1999).

4.4 Discussion

4.4.1 Mineralogy of thermally altered CM and CY chondrites

Heating stages of thermally altered CM chondrites in this chapter were determined based on characteristics and mineralogical changes described by Nakamura (2005). Previous studies estimated peak temperatures of <250 ^{o}C for Y 793595 and DOM 03183 based on decomposition of serpentine in TEM observations of Y 793595 (Nakamura, 2005), and bulk H, C and N isotopes of DOM 03183 (Alexander et al., 2013). However, XRD patterns of Y 793595 and DOM 03183 are the same as unheated CM XRD patterns, with coherent diffraction peaks from phyllosilicates. This implies that if they were heated, it was at a very low temperature (<300 ^{o}C) as the phyllosilicates were not significantly dehydrated (Akai, 1992, Lindgren et al., 2020). TGA is also unable to distinguish between unheated and stage I samples (Table C.1): mass loss during TGA in the 300 - 800 ^{o}C temperature ranges is correlated with the abundance of phyllosilicates present (Garenne et al., 2014, King et al., 2015b), and for the Y 793595 and DOM 03183 samples mass loss in this temperature range are similar to unheated CM chondrites (Table C.1, Fig. C.2). This supports the conclusion that if heating has occurred the temperatures experienced were <300 ^{o}C: i.e. not high enough to dehydrate

phyllosilicates (Akai, 1992, Lindgren et al., 2020). These results show XRD and TGA alone cannot distinguish between unheated CM and stage I samples.

XRD patterns of stage II CM samples show no diffraction peaks associated with phyllosilicates, implying that these phases have dehydrated into a disordered phase that no longer causes coherent diffraction. Stage II CM chondrites are therefore characterised by high abundances (67 – 91 vol%) of dehydrated, disordered phyllosilicate, with some primary olivine and pyroxene. There are no recrystallised secondary phases in the stage II samples, however the disordered phase is assumed to have been crystalline phyllosilicate, prior to thermal alteration. The resulting petrologic types in the stage II CMs suggests variable degrees of aqueous alteration. Akai (1992) suggested temperatures of 300 – 500 ^{o}C were adequate to dehydrate phyllosilicates in experimentally heated Murchison. Furthermore, Lindgren et al. (2020) showed phyllosilicates still had diffraction peaks in XRD patterns of a sample of the CM2 ALH 83100 that had been experimentally heated to 400 ^{o}C, implying phyllosilicates survive dehydration until this temperature (although this sample was only held at this temperature for 24 hours). The lack of coherent diffraction peaks in stage II XRD patterns therefore implies they have experienced tempeartues of at least 400 ^{o}C.

I measured no stage III CM chondrites in this study, however there are two stage III CY samples: Y 86029 and Y 980115. These meteorites are characterised by the presence of both disordered phyllosilicates and recrystallised, secondary phases. Stage IV CM and CY chondrites are characterised by high abundances of re-crystallized, secondary phases, and low to negligible abundances of disordered phyllosilicates. These samples also show limited mass loss (0 – 4.1 wt%, Table C.1) between 300 – 800 ^{o}C, in comparison to unheated, stage I, stage II CMs and stage III CY samples (4.8 – 11.9 wt%, Table C.1).

4.4.2 Potential CY chondrites

CY chondrites have distinct characteristics from CM, CI and thermally altered CM chondrites (Chapter 1). Some of their defining characteristics are high sulfide abundances and heavy oxygen isotopic compositions in comparison to the other carbonaceous chondrite groups. Four samples investigated here share some characteristics with the CY chondrites: EET 96010 (CM2), Dho 2046 (CM2-an), Dho 225 (CM-an) and Dho 735 (CM2).

EET 96010 has Fe-sulfide abundances higher than other stage IV CMs (19 vol% in comparison to ~8 vol%), instead more comparable to the stage IV CY B 7904 (~14 vol%). Its bulk oxygen isotopic composition is however not as heavy as those of the CY group, instead plotting closer to the CI field (Clayton and Mayeda, 2003, Moriarty et al., 2009). This could reflect reduced aqueous alteration relative to other members of the CY group, as progressive hydration results in heavier oxygen isotopic compositions (in a closed system, Clayton and Mayeda, 1999), or EET 96010 could be a CM chondrite with heavier oxygen isotopes due to thermal alteration, and therefore is distinct from the CY group. The spectral signature of EET 96010 (Figure 4.12b) supports a relationship with the CMs, as it is more consistent with the stage IV CM spectra: the CY spectra show CFs and olivine vibrational features at longer wavelengths than those observed in EET 96010.

In contrast, Dho 2046, Dho 225 and Dho 735 show oxygen isotopic compositions that are in good agreement with the CY group (Ivanova et al., 2010, Bouvier et al., 2017). Of these meteorites, Dho 2046 has Fe-sulfide abundances similar to the stage III CYs (10 vol% compared to ~14 vol%). Dho 2046 has disordered phyllosilicate (51 vol%) and based on the thermal alteration classification scheme from Nakamura (2005), its mineralogy implies it is a stage III sample. TGA, however, indicates that its phyllosilicates have completely dehydrated, and it falls into the same mass loss field expected for stage IV CM and CY samples

(Figure C.2). Additionally, the Dho 2046 spectrum does not show the strong doublet features that seem to be characteristic of the stage III CY spectra. The Dho 2046 spectrum is in fact more consistent with stage IV CY spectra, showing similar Si-O stretching vibrational features. I therefore suggest it is a stage IV sample, however its maximum temperature is between that experienced by stage III Y 86029 and stage IV PCA 02012. The high sulfide abundance of Dho 2046, similar spectral signature and similar oxygen isotopic composition to the CYs suggest that it is likely a CY chondrite.

Dho 225 and Dho 735 show lower abundances of Fe-sulfides than the stage III CY chondrites, and instead are more comparable to the stage II and stage IV CM chondrites (~4 vol%). Their mineralogy is consistent with the stage III CY meteorites, however their spectra do not resemble the stage IIIs Y 86029 and Y 980115 due to the absence of the 6.6 – 6.9 feature, CFs and TFs both at longer wavelengths, and the presence of features near 9.85 and 11.50 μm rather than a single feature near 10 μm. My data suggests they are stage III CM chondrites, however previous analyses have confirmed a distinct oxygen isotopic composition from typical CM chondrites and similar to CY chondrites, indicating they are anomalous. This is consistent with conclusions from Ivanova et al. (2010) who suggested Dho 225 and Dho 735 had a different primary material from B 7904 and CM chondrits but formed in the same oxygen reservoir as B 7904.

4.4.3 A 881655 and WIS 91600

WIS 91600 is a CM-an chondrite with a magnetite abundance of ~9 vol%. The mineralogy determined here is consistent with a stage II sample. This agrees with previous estimations that WIS 91600 has been dehydrated to temperatures of 400 - 500 ^{o}C (Tonui et al., 2014). The similar magnetite abundances in WIS 91600 and A 881655 suggest a relationship between the two meteorites. The XRD patterns and mineralogy of A 881655 are consistent with a stage III sample. It has previously been determined as dehydrated to temperatures

of 500 - 750 ^{o}C (section 2.1.2, Hiroi et al., 1997, Nakamura, 2005, Kimura et al., 2011, Tonui et al., 2001, 2014, Mahan et al., 2018), but has often been discussed as a typical dehydrated CM. The results here support this temperature estimation, I however suggest that its high magnetite abundance (~7 vol%) in comparison to other dehydrated CM chondrites (1 - 2 vol%) means it is an anomalous CM chondrite.

Another similarity between the two meteorites is the presence of the Mg-rich phyllosilicate 'prism' in the high-resolution XRD pattern of A 881655 and the PSD-XRD pattern of WIS 91600. The prism feature has been observed previously in XRD patterns of WIS 91600 (Nakamura, 2005, Tonui et al., 2014), and attributed to the presence of dehydrated phyllosilicates. Note that the prism is also present in the XRD patterns of unheated CI and CM spectra indicative of unheated phyllosilicates, however in the WIS 91600 and A 881655 patterns it is a less intense peak. This is supported by Che et al. (2011), who collected the XRD patterns of dehydrated serpentine and smectite group phyllosilicates and showed that they retain broad diffraction peaks between 20 - 30 ^{o} (Cu Ka1) even after heating to 800 ^{o}C (at a rate of 10 ^{o}C/min). No other dehydrated meteorite here shows this prism feature however, indicating the phyllosilicates in WIS 91600 and A 881655 are distinct from the phyllosilicates in CM and CY chondrites. Petrographic observations of these meteorites show their phyllosilicates to be serpentine and smectites, which suggest a similar, pre-thermally altered mineralogy to the phyllosilicates in CI chondrites (Lipschutz et al., 1999, Tonui et al., 2014). This similarity to CI chondrites is supported by the oxygen isotopic composition of WIS 91600 (Figure 1.6), which is within the CI field, and the high magnetite abundances in both WIS 91600 and A 881655. CI chondrites have the heaviest oxygen isotopic composition of the carbonaceous chondrites, apart from the CY chondrites (Figure 1.6), and contain 6 - 10 vol% magnetite and abundant serpentine interlayed with saponite (Tomeoka

and Buseck, 1988, Tomeoka, 1990, Brearley, 1992, Zolensky et al., 1993, King et al., 2015a, 2020). WIS 91600 and A 881655 could represent thermally altered CI material.

4.4.4 NIR SPECTRAL RELATIONSHIPS TO MINERALOGY

All thermally altered CM, CY and anomalous spectra show a 3 μm feature. As spectra were collected on samples that had been gently heated to drive off adsorbed terrestrial water, the presence of a 3 μm feature indicates that a hydrated component remains in these meteorites despite them being thermally altered. In unheated CM and CI spectra, the position of the 3 μm feature is controlled by the phyllosilicate composition, with more aqueously altered meteorites showing features near ~2.74 μm, consistent with Mg-rich phyllosilicates, and less aqueously altered samples show features near 2.78 - 2.83 μm, consistent with Fe-rich phyllosilicate. The area of the features is controlled by Fe-cronstedtite and magnetite abundance: samples with higher Fe-cronstedtite and lower magnetite abundances have band areas ~0.15 μm^{-1} and samples with lower Fe-cronstedtite and higher magnetite abundances show smaller band areas of ~0.08 μm^{-1} (chapter 3). Consistent with unheated CM samples, the 3 μm features of the weakly heated stage I CM chondrites also seem to reflect the phyllosilicate composition, as their phyllosilicate phases are not dehydrated and have not lost their -OH components. DOM 03183 has a petrologic type of 1.5 and its spectrum has a rounded feature near 2.83 μm. The feature is similar to that observed in the least aqueously altered CM spectra in chapter 3: LEW 85311, LAP 031214, LEW 90500, MCY 05231 and Murchison. The Y 793595 spectrum shows features at 2.72 and 2.82 μm, consistent with 'intermediate' levels of aqueous alteration (chapter 3, Takir et al., 2013).

Typically, the 3 μm features in the stage II, III and IV sample (regardless of meteorite type) spectra show features between 2.87 - 2.93 μm (Figs. 4.6 – 4.8). Unlike the unheated and stage I CM spectra, the position of these features is not influenced by the degree of aqueous alteration: for example, the position and shape of the 3 μm feature in the stage

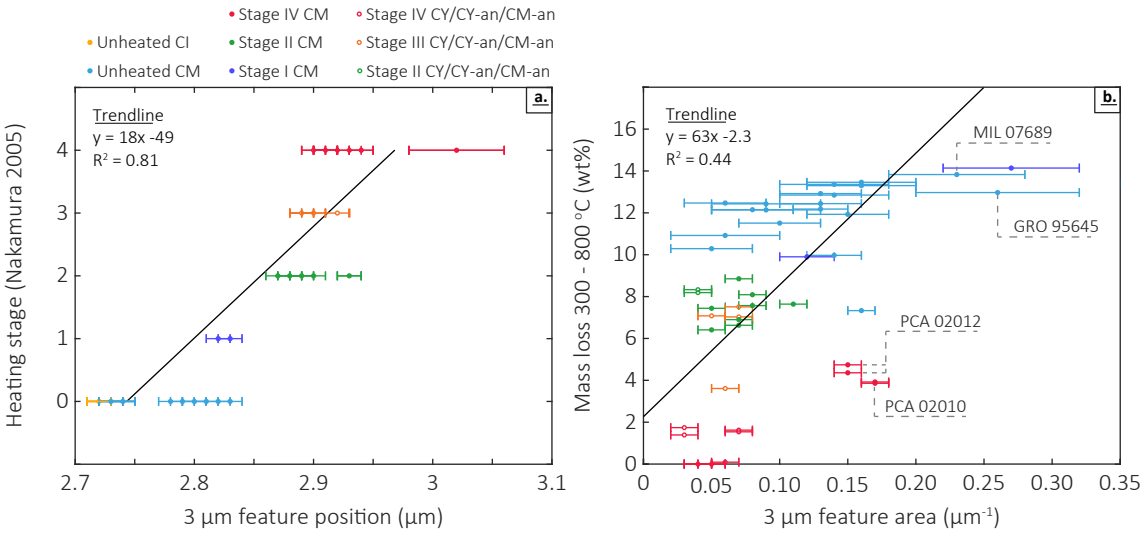


Figure 4.14: *(a) The position of the 3 µm feature against heating stage for heated CM, CY and CM/CY-anomalous meteorites. With increasing metamorphic temperature, the position shifts to longer wavelengths. (b) The band area of the 3 µm feature against mass loss between 300 - 800 °C for the thermally altered and unheated samples. With increased thermal metamorphism, the band area and mass loss get smaller. This indicates the feature is influenced by the disordered phyllosilicate content. The trend calculated does not include the unheated GRO 95645 and MIL 07689 and the stage IV CM PCA 02010 and PCA 02012, all of which showed anomalously large band areas due to terrestrial weathering products (see text for details).*

II spectra do not vary with disordered phyllosilicate abundance. Figure 4.14a shows that with increasing metamorphic temperature, the position of the 3 µm feature shifts to longer wavelengths (all unheated samples are given the heating stage 0). Of particular use is the fact that unheated and stage I samples can be clearly resolved from stage IIs and above. These spectral observations are consistent with previous measurements of thermally altered CM and CY chondrites (Hiroi et al., 1996, 1997). The difference between unheated and dehydrated CM spectra is also demonstrated in the experimentally heated Murchison spectra from Tonui et al. (2014), who showed that the unheated Murchison spectrum has a 3 µm feature near 2.80 µm (consistent with the spectra of Murchison in chapter 3), but this shifts to 2.90 µm upon heating to 400 °C.

This trend is complicated by the causes of the features in the thermally altered samples. The lack of variation in spectral shape between the different thermally altered samples could

suggest the 3 µm feature is a result of terrestrial contaminants such as rusts, which could be present in all samples. Rusts and other Fe-(oxy)hydroxides dehydrate between 200 - 400 ^{o}C (Garenne et al., 2014, King et al., 2015b), so it is possible some may remain even after samples were heated at 150 ^{o}C for 2 hours prior to having their spectra collected. However, the area of the 3 µm features does not correlate well with TGA mass loss between 200 - 400 ^{o}C. Figure 4.14b shows there is a better relationship between 3 µm band area and mass loss calculated over 300 - 800 ^{o}C, which is the temperature range over which phyllosilicates dehydrate (King et al., 2015b). This suggests that the 3 µm feature in the thermally altered samples is affected by the disordered phyllosilicates present in the samples, and its shift to longer wavelengths is a real result of thermal alteration, and not just reflecting terrestrial contamination. The results from the experimentally heated Murchison support this, as the meteorite is a fall and the same trend is observed (Tonui et al., 2014). The change in 3 µm feature with heating has been observed in previous studies: Alemanno et al. (2020) experimentally heated samples of a serpentine and measured the changes in the 3 µm feature. They observed the 2.72 µm becoming more indistinct (although not disappearing) and a widening of a feature near 3 µm, both with increasing temperature and increasing duration of heating.

The stage IV CM spectra show features at 2.94 and 3.02 µm (Fig. 4.6a, Table 4.2), and they show larger band areas (~0.16 µm^{-1}) than in any other thermally altered spectra. This is consistent with previous spectral observations of PCA 02010, and the large band depth has been attributed to the presence of rusts (Hanna et al., 2020). Rusts are very poorly crystalline, and so are difficult to analyse using XRD; however, TGA shows that PCA 02010 and PCA 02012 lose 1.4 - 1.6 wt % mass between 200 - 400 ^{o}C, which is higher than the mass loss measured for the other stage IV CM-an and CY samples (0 - 0.9 wt%, Table C.1), suggesting the two PCA samples may contain rusts. Both also show a mass loss event at

~225 ^{o}C, similar to the dehydration event observed in the CM1 GRO 95645 and MIL 07689 samples (Figure C.3). In these CM1 samples I suggested this phase contributed to the increased band area in their 3 µm features, and this may also be the case for PCA 02010 and PCA 02012.

WIS 91600 and A 881655 show 3 µm features that share some similarity to the features observed in CI spectra (Fig 3.4), with a sharp feature near 2.72 µm, and a broad feature centred near 2.90 µm. As suggested for the CI spectra, this likely reflects Mg-rich smectite in WIS 91600 and A 881655, which is supported by the features identified in XRD patterns (section 4.4.3). The band areas calculated for the WIS 91600 and A 881655 3 µm feature are however smaller than those calculated for the CI spectra, 0.04 - 0.06 µm^{-1} compared to 0.22 and 0.23 µm^{-1}, and are instead more consistent with the areas measured in the stage II CM spectra (Table 4.2). Unlike the thermally altered CM spectra, there is no shift in the position of the 3 µm feature between A 881655 and WIS 91600. Experimentally heated Ivuna shows a 3 µm feature that remains at 2.72 µm even at temperatures of 600 ^{o}C, although the depth of the feature is reduced from the unheated spectra (Hiroi and Pieters, 1996). This may be due to the smectite phyllosilicate component of the CI chondrite, with Alemanno et al. (2020) showing that the 3 µm feature of saponite retains its sharp 2.72 µm feature upon experimental heating to 700 ^{o}C, whereas the 2.72 µm feature in the spectra of serpentine samples becomes less distinct at similar temperatures. This is therefore further evidence that A 881655 and WIS 91600 contain dehydrated smectite phyllosilicates.

4.4.5 MIR spectral relationships to mineralogy

5 - 7 µm region

Features between 6.11 - 6.24 µm are observed in all dehydrated CM spectra. These are within the range of features that are identified in the spectra of unheated CMs and CIs in

chapter 3. In the unheated CM and CI spectra I suggest these features are due to phyllosilicates, and Alemanno et al. (2020) showed that features in this region remain when phyllosilicates are experimentally heated. In the thermally altered CM sample spectra, there does not appear to be any trends associated with metamorphic or aqueous alteration. Most spectra show subtle features near 6.90 μm (Figs. 4.10 – 4.13). Carbonates are known to have features at these wavelengths (Lane and Christensen, 1997, Beck et al., 2018), and features at 6.90 μm appear in emissivity spectra of mineral mixtures containing carbonates (Donaldson Hanna et al., 2019). However, the appearance of these features in the spectra here does not correlate with the abundance (0- 2 vol%) of carbonates as determined through PSD-XRD.

The stage III CY spectra show an additional feature near 6.60 μm, creating a doublet peak with the 6.90 μm feature (Fig 4.11a). This is consistent with previous spectral observations of the stage III CY chondrites (Miyamoto, 1992). They attributed the 6.60 μm feature in a stage III CY (Y 82162, which was not included in this project) to terrestrial weathering products, and the 6.90 μm feature to the incomplete break down of calcite. It is not convincing that the 6.60 μm feature is a result of weathering, given that it is not present in spectra that show increased 3 μm band areas as a result of weathering products (eg. GRO 95645 in chapter 3, PCA 02010 in this chapter). A number of different carbonates have been identified in petrographic studies of the stage III CYs, including dolomite in Y 82029, Y 980115 and Y 82162 (Fujiya et al., 2013, King et al., 2019), and also magnesite, ankerite and siderite in Y 86029 (Tonui et al., 2003). These carbonates show features at shorter wavelengths than calcite, and it may be that the features in the stage III spectra reflect the different chemistries of the carbonates in the CYs compared to the CMs (Lane and Christensen, 1997). These phases are not identified in XRD patterns and so are either in low abundance or decomposed due to thermal alteration, therefore it is surprising they can be observed in the spectra. It is clear

the causes of features in this region require further study. The 6.60 and 6.90 µm features are not observed in stage IV CY spectra (if they are due to carbonates this indicates these phases have fully broken down by the temperatures experienced by the stage IV samples), therefore their presence could be used to distinguish different degrees of thermal alteration in the CYs.

Christiansen feature

The CF is a complex region to disentangle in CM, CI and CY chondrites. Olivine and phyllosilicates, the two primary mineral phases in these meteorites, have similar spectral ranges for their CFs. Both shift to longer wavelengths with increasing Fe: in phyllosilicates the CF shifts from 8.71 µm in lizardite to 9.66 µm in cronstedtite (Figure 2.7c), and in olivine, forsterite has a CF near 8.79 µm and fayalite has a CF near 9.39 µm (Hamilton, 2010). As described in chapter 3, increasing aqueous alteration in CM and CIs causes an increase in abundance and proportion of Mg-rich phyllosilicates, which acts to shift the CF to shorter wavelengths (Fig. 3.9). However, figure 4.15a shows there is no convincing correlation between CF and the abundance of secondary olivine (R^2 of 0.08). This indicates the CF cannot characterise degree of thermal alteration. This is likely because the samples have experienced multiple episodes of alteration: firstly, they were aqueously altered, which would have shifted the positions of their CFs depending on the degree of hydration. As the degree varied, the CFs of the pre-metamorphosed samples would have covered a range of positions. Subsequently, they were heated, affecting the positions of the CF again. Therefore, different degrees of thermal alteration would variably shift the positions of CFs which were already diverse.

Whilst disentangling the effects of aqueous and thermal alteration on the position of the CF is challenging, enstatite abundance correlates with the position of the CF regardless of whether the spectra is of an unheated or dehydrated sample. Figure 4.15b shows the CF

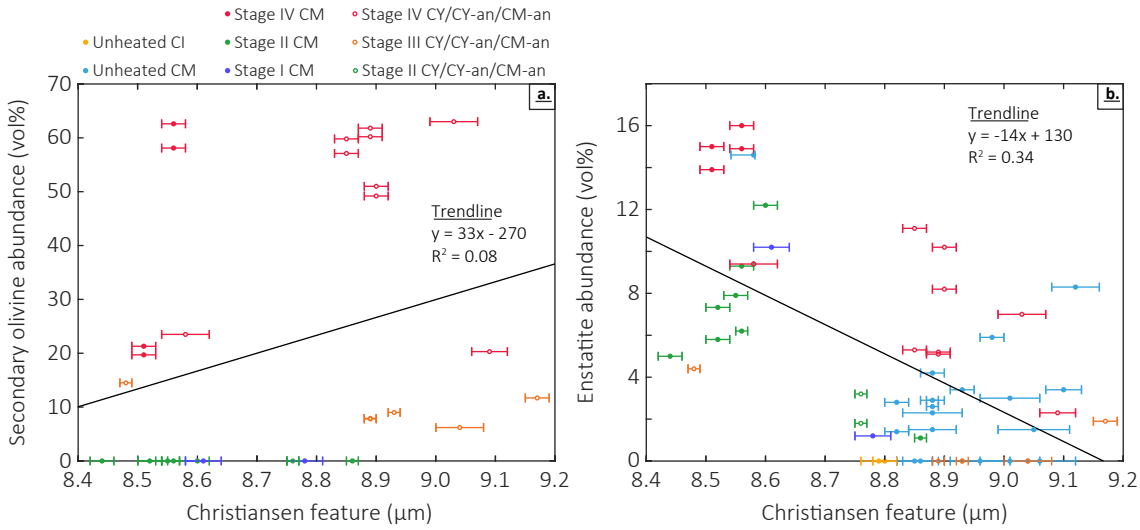


Figure 4.15: *(a) The abundance of secondary olivine against position of the CF. (b) The position of the CF against enstatite abundance, for all hydrated and dehydrated samples, showing the influence of enstatite on the CF.*

position shifts to shorter wavelength with increasing abundance of enstatite as a proportion of total anhydrous silicate. Enstatite has a CF near 8.33 µm (Donaldson Hanna et al., 2012a), and Figure 4.15b shows that in abundances of >5 vol% it seems to influence the CF, particularly in the CM samples. The enstatite abundance however cannot be associated with different degrees of thermal alteration; as Figure 4.15b shows, there does not appear to be a consistent relationship between heating and enstatite abundance.

Transparency feature

The TF behaves in a similar way to the CF, with features due to olivine and phyllosilicate both shifting to longer wavelengths with increasing Fe content (Hamilton, 2010). Unlike the CF, the position of the TF in phyllosilicate and olivine standard spectra shift over different wavelength ranges depending on their chemistry: lizardite has a TF near 11.75 µm and Fe-cronstedtite has a TF near 12.28 µm (Fig. 2.7), whereas forsteritic olivine has a TF near 12.90 µm and fayalite has a TF near 13.80 µm (Figure 2.9, Lane et al., 2011).

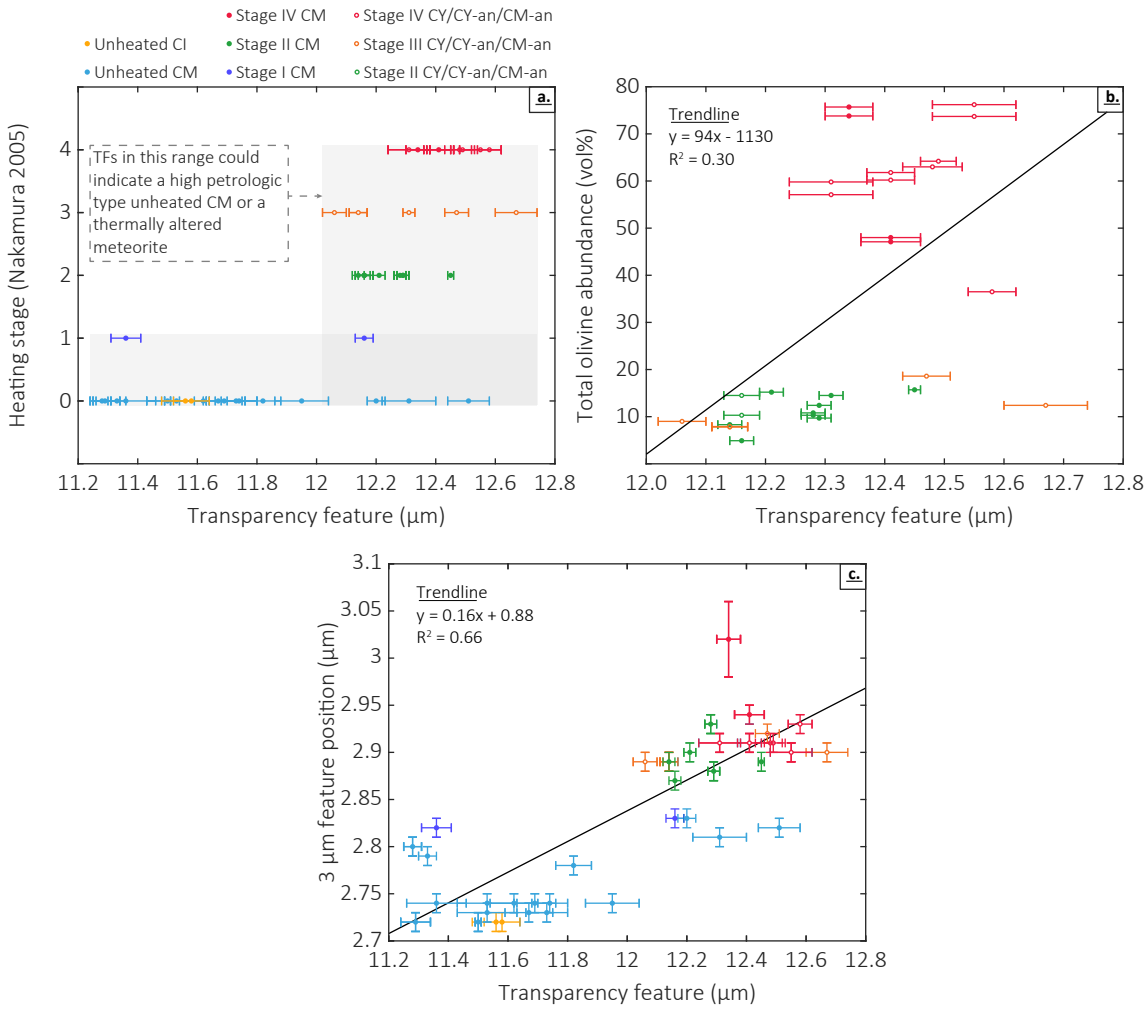


Figure 4.16: *(a) The position of the TF against heating stage for heated CM, CY and CM/CY-anomalous meteorites. (b) the relationship between the TF and total olivine abundance (primary + secondary olivine). (c) The relationship between the position of the TF and the position of the 3 µm feature (A 881655 and WIS 91600 are not included due to the presence of multiple features in the 3 µm range). This relationship can help distinguish between the effects of aqueous and thermal alteration on the position of the TF.*

Figure 4.16a shows the relationship between TF and the heating stage of all samples in chapters 3 and 4 (again, all unheated samples are given the heating stage 0). The thermally altered meteorites show TFs in similar positions to those in the least aqueously altered CM2s from chapter 3. Within the thermally altered meteorites however, there is no convincing trend in TF position, however it does appear as though the TF can be used to indicate whether thermal alteration has occurred. This is demonstrated by the TF observed

in the spectra of the stage II CM MIL 07700. This sample has a PSF petrologic type of 1.2, with 5 vol% primary olivine and 91% disordered phyllosilicate. This disordered phyllosilicate was modelled using 85 vol% Mg-serpentine and 6 vol% Fe-cronstedtite (Fig. 2.4), a composition which in an unheated sample would result in a TF at shorter wavelengths. Unheated CM chondrites with PSF petrologic types of 1.2 show TFs between 11.29 - 11.73 µm (Table 3.2), whereas MIL 07700 has a TF at 12.16 µm. This shift implies the disordered phyllosilicate does not influence the position of the TF, and that it is now controlled by the olivine abundance. This is demonstrated in Figure 4.16b, where the TF of thermally altered samples (excluding stage I samples, which do seem to be influenced by phyllosilicate abundance) shows a weak correlation with total olivine abundance (primary + secondary olivine, if present). There are two distinct groups: those samples with higher olivine abundances show TFs at longer wavelengths, whereas those with lower olivine abundances show TFs at shorter wavelengths.

The position of the TF in the MIL 07700 spectrum suggests that regardless of the degree of aqueous alteration, the TF in thermally altered samples is at longer wavelengths. The caveat to this is that the position of the TFs for the thermally altered samples are within the same range as those measured in the higher petrologic type unheated CM samples. In order to distinguish between aqueous and thermal alteration, the 3 µm feature, which shows a good relationship in its position with both aqueous alteration (chapter 3) and thermal alteration (Fig. 4.14), can be combined with observations of the TF. Figure 4.16c shows the TF position is correlated with 3 µm feature position and as the 3 µm feature of unheated samples is at shorter wavelength than the 3 µm feature in thermally altered samples, the trend is able to distinguish between unheated samples with high petrologic type, and samples that are thermally altered but experienced a high degree of aqueous alteration.

Si-O stretching and bending

In the 9.5 - 10.5 μm and 18 - 25 μm ranges, olivine and phyllosilicates both show vibrational features associated with Si-O stretching and bending absorptions, respectively (Reynard, 1991, Michalski et al., 2006, Hamilton, 2010). As suggested in section 4.3.3, in the Si-O stretching region (9.5 - 10.5 μm), features consistent with olivine become apparent as thermal alteration increases, with unheated and stage I spectra showing features in agreement with phyllosilicate spectra, and stage II to stage IV CM and CY spectra with olivine. Of these spectra, the stage I DOM 03183 and the stage II MIL 07700 spectra show some interesting characteristics. The DOM 03183 spectrum shows features associated with both olivine and phyllosilicates (Fig. 4.10). The phyllosilicate features in this region are so broad that the olivine spectral signature can easily overprint on top of them, even in low quantities (DOM 03183 only has 12 vol% olivine). The MIL 07700 spectrum shows features consistent with phyllosilicates (Fig. 4.10). MIL 07700 only has an olivine abundance of 5 vol%, which may be low enough that it does not have a strong influence on vibrational features that instead reflect the disordered phyllosilicate abundance. This is in contrast to the position of the 3 μm feature and the TF in the MIL 07700 spectrum, at 2.87 and 12.16 μm, which are consistent with other stage II spectra. The 3 μm feature and TF seem to be more sensitive to thermal alteration and olivine abundance, respectively, than the vibrational features. Therefore, identifying phyllosilicate vibrational features in the Si-O stretching region in the spectra of meteorites that have 3 μm features and TFs suggesting some degree of thermal alteration could constrain the degree of aqueous alteration prior to thermal alteration.

Between 18 - 25 μm, the meteorite spectra tend to show a single, easily distinguishable feature. Much like the CF and TF, the position of this Si-O bending feature in olivine and phyllosilicates varies with chemistry: forsterite has a feature near 18.70 μm and fayalite has a feature near 19.75 μm (Figure 2.9, Hamilton 2010, Lane et al. 2011), while Mg-

serpentines have a feature near 20.00 µm, and more Fe-rich serpentines shift features to longer wavelengths (e.g. antigorite has a feature near 23.00 µm, Figure 2.7c, Christensen et al., 2000). As with the TF, the position of the Si-O bending feature in the thermally altered samples is similar to the position of the Si-O bending feature in the unheated, high petrologic type CM2 samples (Figure 4.17a). Like the TF, the Si-O bending feature in the MIL 07700 spectrum (at 19.95 µm) is within error of the features observed in the other stage II spectra, between 19.10 - 19.65 µm. This suggests the Si-O bending feature is an additional parameter that can be used to identify whether heating has occurred in samples that were highly aqueously altered. This also implies the Si-O bending region is more sensitive to thermal alteration than the Si-O stretching region between 9.5 - 10.5 µm, where the MIL 07700 spectrum shows features consistent with phyllosilicates and therefore similar to its unheated counterparts' spectra. The Si-O stretching features can be used in combination with the Si-O bending feature to validate whether a material has experienced a high degree of aqueous alteration prior to thermal alteration.

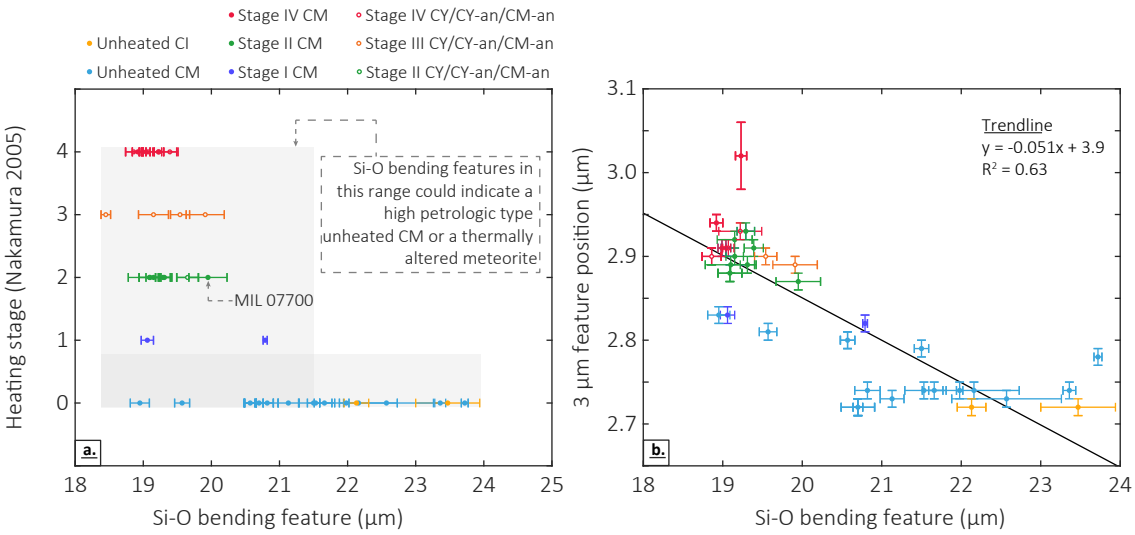


Figure 4.17: *(a) The position of the vibrational feature in the Si-O bending region between 18 – 25 µm against heating stage (b) The relationship between the position of the Si-O bending feature and the position of the 3 µm feature (A 881655 and WIS 91600 are not included due to the presence of multiple features in the 3 µm range). As with the TF, this relationship can help distinguish between the effects of aqueous and thermal alteration.*

The comparison of Si-O stretching and bending features will not be able to distinguish between thermally altered samples that have a PSF petrologic type of >1.4 and high petrologic type unheated samples. High petrologic type unheated and stage I CM spectra show Si-O stretching features that are consistent with anhydrous silicates (e.g. pyroxene in the LEW 85311 spectrum, chapter 3, and olivine in the DOM 03193 spectrum), and these are similar to what is observed in thermally altered spectra. The Si-O bending feature can, however, be combined with the 3 μm feature position to fully distinguish between aqueous and thermal alteration regardless of petrologic type. Figure 4.17b shows this relationship, with the 3 μm feature shifting to increasing wavelengths with thermal alteration, as the Si-O bending vibration shifts to shorter wavelengths. This highlights that to understand the causes of spectral signature, and to unravel the alteration history of a material or surface, it is important to observe samples over multiple spectral ranges.

4.4.6 Spectral parameters for determining thermal alteration

There are a number of changes in spectral signatures as CM, CY and CM/CY-anomalous chondrites experience thermal alteration. These include the position of the 3 μm feature, which varies between 2.72 - 2.83 μm for unheated CM and CI chondrites (chapter 3) but shifts to >2.87 μm for samples that have been heated to stage II. The feature then continues to shift to longer wavelengths as thermal alteration increases. The area of the 3 μm feature is also reduced in comparison to the area measured in unheated CM chondrite spectra. The position of the 3 μm feature can be combined with the positions of the TF and Si-O bending features, effectively providing a distinction between the effects on the spectra of aqueous and thermal alteration, and allowing a unique explanation for the spectral behaviour to be identified. Additionally, the presence or absence of vibrational features can be combined with other spectral parameters: in the CM spectra, the presence of phyllosilicate vibrational features in spectra that show evidence for thermal alteration in other ranges suggest high

degrees of aqueous alteration prior to heating. In the CY spectra, stage IIIs show features near 6.60 and 6.90 µm likely consistent with carbonates that are no longer distinguishable in the stage IV spectra as they have been fully decomposed. I have demonstrated that many of these trends can be explained by a variety of mineralogical changes.

The multiple explanations for trends identified in this chapter highlight the importance of investigating well characterised samples, as only then can the clearest trends be identified and applied to laboratory and remote spectra where the mineralogy and alteration history are not known. This is of course especially valuable for remote observations of asteroids, when mineralogy cannot be established as easily as it can for laboratory samples. Combining multiple spectral parameters, demonstrated here, may help constrain whether a surface has experienced aqueous or thermal alteration or both.

4.5 Conclusions

In this chapter, 21 thermally altered CM, CY and CM/CY-anomalous chondrites were investigated, with the aim of identifying whether thermal alteration history could be inferred from spectral observations. In order to do this, their modal mineralogy was determined, and a heating stage assigned based on the scale determined by Nakamura (2005). There are two stage I CMs, 6 stage II CMs, two stage IV CMs, two stage III CYs and three stage IV CYs. I additionally looked at the anomalous samples EET 96010 (stage IV), Dho 2046 (stage IV), Dho 225 and Dho 735 (both stage III), which share affinities with both CM and CY chondrites, and WIS 91600 (stage II) and A 881655 (stage III), which share affinities with CI chondrites.

A number of trends were identified for evaluating thermal alteration. These include the position of the 3 µm feature, CF, TF and Si-O bending feature, and the presence or absence of olivine and phyllosilicate vibrational features. These trends are complicated by the effects of aqueous alteration, which influences spectral signature in a similar way to thermal

alteration. Distinguishing the two alteration types requires a combination of spectral parameters, for example the 3 μm feature position with the position of the TF and Si-O bending feature.

Chapters 3 and 4 have and demonstrated that reflectance spectroscopy can be used to effectively examine aqueous and thermal alteration (objectives A-1 and A-2, chapter 1). However, reflectance data is only approximately comparable to these observations, as spectral flux from remote bodies is dominated by thermal emission at MIR wavelengths, and not reflected light. Additionally, thermal emission is strongly affected by pressure and temperature and so when emissivity spectra are collected, they need to be under the appropriate near-surface environmental conditions. This will be explored further in chapter 5.

Chapter 5: The emissivity spectra of heated CM and CY carbonaceous chondrites

5.1 Introduction

Chapters 3 and 4 identified a number of trends in the MIR reflectance spectra of aqueously and thermally altered CM, CY and CM/CY-an chondrites that can be used to relate mineralogy and degrees of alteration. However, telescopic and spacecraft remote sensing observations from small Solar System bodies are dominated by thermal emission, which is in turn affected by the near-surface environmental conditions of those bodies (i.e., pressure and temperature). Therefore, to accurately compare laboratory spectra to remote observations, thermal emission spectra under the appropriate environmental conditions need to be collected. This chapter presents the MIR emissivity spectra of 12 meteorites, with the aim of discussing the differences between reflectance and emissivity spectra, and to assess whether there are additional trends in emissivity spectra that can be tied to aqueous or thermal alteration (question B, chapter 1).

5.2 Experimental

Reflectance spectra of 39 meteorites were presented in chapters 3 and 4. For 12 of these meteorites, I also collected emissivity spectra from the same powder. The samples included three unheated CM chondrites: ALH 83100, ALH 83102 and LON 94101; two stage II CM chondrites: EET 96029 and Y 793321; the stage II CM-an WIS 91600; two stage IV CM chondrites: PCA 02010 and PCA 02012; the stage III CY Y 980115; and three stage IV CY

chondrites: B 7904, Y 86720 and Y 86789. Emissivity spectra were collected between 5.5 - 50 µm (1800 - 200 cm^{-1}) under both ambient and SAE conditions. Briefly, under ambient conditions the environment chamber was backfilled with dry nitrogen to a pressure of 1000 mbar and maintained at an ambient temperature. Samples are then heated from below to ~80 ^{o}C. Under SAE conditions, the environment chamber was held under vacuum (<10^{-4} mbar) and the interior cooled to <-150 ^{o}C. Samples were heated from above and below until the maximum brightness temperature was 75 ^{o}C. For details of the experimental procedure used see section 2.3.2 in chapter 2.

5.3 Results

5.3.1 Ambient and SAE MIR spectral features in aqueously altered CM chondrites

Figure 5.1 shows the ambient (black) and SAE (blue) emissivity spectra of the unheated CM chondrites (ALH 83100, ALH 83102 and LON 94101). The positions of the diagnostic features identified in the spectra are given in Table 5.1. The ambient emissivity spectra of the unheated CM chondrites show vibrational features in the 5 - 8 µm range near 6.16, 6.95 and 7.24 µm. These are consistent with the positions of features in the reflectance spectra the same samples. The 6.16 µm feature is likely related to the bending mode of bound molecular water (Bishop et al., 1993), however as discussed in Chapters 3 and 4, the feature likely has some mineralogical contribution. The 6.95 and 7.24 µm features, as suggested in chapters 3 and 4, are consistent with carbonates (Beck et al., 2018).

The unheated CM ambient emissivity spectra show CFs between 9.01 - 9.05 µm, and TFs at 11.43 - 11.56 µm. The transparency feature in the LON 94101 ambient emissivity spectrum has a slight doublet shape with an additional minimum at 12.32 µm that is not distinguishable in its reflectance spectrum. Following the trend established in McAdam et al. (2015) that the TF moves to shorter wavelengths with increasing aqueous alteration,

a. **AMBIENT**

Sample		Classification	Heating Stage	6 μm feautres (μm)			Christiansen feature (μm)	Si-O stretching features (μm)			Transparency feature (μm)	Si-O bending features (μm)				
ALH 83100	HB2	CM2	0	6.16 ± 0.01	6.96 ± 0.01	7.23 ± 0.01	9.05 ± 0.03	-	9.83 ± 0.01	-	-	11.56 ± 0.01	-	-	23.32 ± 0.05	31.29 ± 0.08	36.35 ± 0.14
ALH 83102	HB2	CM2	0	6.16 ± 0.01	6.97 ± 0.01	7.25 ± 0.01	9.06 ± 0.02	-	9.83 ± 0.01	-	-	11.54 ± 0.01	-	-	23.22 ± 0.03	31.23 ± 0.02	36.95 ± 0.06
LON 94101	HB2	CM2	0	6.17 ± 0.01	6.94 ± 0.01	7.24 ± 0.01	9.01 ± 0.03	-	9.82 ± 0.01	-	-	11.30 ± 0.01, 12.32 ± 0.01	-	-	23.76 ± 0.04	31.15 ± 0.04	38.00 ± 0.08
Murchison				*6.17 ± 0.02*	-	*7.17 ± 0.01*	*8.78 ± 0.01*	*9.29 ± 0.01*	*9.90 ± 0.01*	-	-	*11.40 ± 0.01, 12.22 ± 0.01*	*19.72 ± 0.05*	*21.07 ± 0.01*	*24.05 ± 0.03*	-	*34.99 ± 0.01*
WIS 91600	HB2	CM-an	2	-	6.61 ± 0.01	6.90 ± 0.02	9.04 ± 0.01	-	9.81 ± 0.01	10.69 ± 0.01	-	12.53 ± 0.01	-	-	24.36 ± 0.12	29.47 ± 0.15	38.50 ± 0.03
EET 96029	HB2	CM2	2	6.10 ± 0.01	-	-	8.86 ± 0.02	9.38 ± 0.02	9.84 ± 0.01	10.65 ± 0.01	-	12.47 ± 0.01	19.81 ± 0.06	21.17 ± 0.01	24.10 ± 0.01	29.79 ± 0.01	34.86 ± 0.03
Y 793321	HB2	CM2	2	6.17 ± 0.01	-	-	8.89 ± 0.03	9.34 ± 0.02	9.88 ± 0.01	10.65 ± 0.01	-	12.54 ± 0.02	19.59 ± 0.01	21.05 ± 0.01	23.98 ± 0.01	29.96 ± 0.01	35.05 ± 0.03
PCA 02010	HB2	CM2	4	6.10 ± 0.01	-	-	8.75 ± 0.01	9.40 ± 0.01	9.85 ± 0.01	10.66 ± 0.03	11.77 ± 0.01	12.45 ± 0.03	19.79 ± 0.01	20.97 ± 0.02	24.72 ± 0.02	30.04 ± 0.03	35.02 ± 0.02
PCA 02012	HB2	CM2	4	6.09 ± 0.01	-	-	8.47 ± 0.05	9.39 ± 0.01	9.88 ± 0.01	10.62 ± 0.03	11.77 ± 0.01	12.50 ± 0.01	19.76 ± 0.03	21.00 ± 0.01	24.25 ± 0.01	29.86 ± 0.03	34.84 ± 0.02
Y 980115	HB2	CI1/CY	3	-	6.54 ± 0.02	6.93 ± 0.02	9.03 ± 0.02	-	9.85 ± 0.02	-	-	12.61 ± 0.04	-	-	25.72 ± 0.01	-	35.85 ± 0.05
B 7904	HB2	C2-ung/CY	4	-	-	-	9.27 ± 0.02	-	9.73 ± 0.02	10.72 ± 0.01	11.75 ± 0.01	12.61 ± 0.01	20.12 ± 0.16	-	25.49 ± 0.01	30.61 ± 0.03	36.01 ± 0.05
Y 86720	HB2	C2-ung/CY	4	-	-	-	8.99 ± 0.01	9.82 ± 0.01	10.33 ± 0.01	-	11.78 ± 0.01	12.61 ± 0.01	20.15 ± 0.07	-	25.41 ± 0.02	30.87 ± 0.01	35.71 ± 0.04
Y 86789	HB2	C2-ung/CY	4	6.14 ± 0.01	-	-	9.02 ± 0.01	9.80 ± 0.02	10.36 ± 0.01	-	11.77 ± 0.01	12.63 ± 0.02	20.23 ± 0.06	-	25.55 ± 0.03	30.79 ± 0.01	36.18 ± 0.05

b. **SAE**

Sample		Classification	Heating Stage	6 μm feautres (μm)			Christiansen feature (μm)	Si-O stretching features (μm)			Transparency feature (μm)	Si-O bending features (μm)				
ALH 83100	HB2	CM2	0	6.20 ± 0.01	6.89 ± 0.01	7.23 ± 0.01	9.17 ± 0.01	-	9.84 ± 0.04	-	-	11.49 ± 0.01	-	-	23.28 ± 0.05	31.98 ± 0.04	36.62 ± 0.06
ALH 83102	HB2	CM2	0	6.17 ± 0.01	6.86 ± 0.01	7.21 ± 0.01	9.10 ± 0.01	-	9.86 ± 0.06	-	-	11.43 ± 0.01	-	-	23.31 ± 0.03	32.30 ± 0.01	37.61 ± 0.03
LON 94101	HB2	CM2	0	6.24 ± 0.02	6.86 ± 0.01	7.20 ± 0.01	9.16 ± 0.01	-	9.84 ± 0.04	-	-	11.39 ± 0.01, 12.34 ± 0.04	-	-	23.73 ± 0.04	30.73 ± 0.03	37.98 ± 0.07
Murchison				*6.16 ± 0.01*	-	*7.18 ± 0.01*	*8.71 ± 0.01*	*9.34 ± 0.01*	*9.88 ± 0.03*	-	-	*11.46 ± 0.03, 12.26 ± 0.01*	*19.74 ± 0.05*	*21.25 ± 0.01*	*24.00 ± 0.02*	-	*35.06 ± 0.03*
WIS 91600	HB2	CM-an	2	-	6.48 ± 0.02	6.93 ± 0.02	9.32 ± 0.01	-	-	10.74 ± 0.02	-	12.53 ± 0.02	-	-	24.39 ± 0.08	29.54 ± 0.02	35.02 ± 0.05
EET 96029	HB2	CM2	2	6.05 ± 0.02	-	-	8.65 ± 0.02	9.16 ± 0.03	-	10.87 ± 0.03	11.49 ± 0.01	12.51 ± 0.03	19.80 ± 0.04	21.05 ± 0.01	24.11 ± 0.01	30.06 ± 0.06	35.06 ± 0.03
Y 793321	HB2	CM2	2	6.12 ± 0.02	-	-	8.84 ± 0.02	-	-	-	11.62 ± 0.01	12.60 ± 0.01	19.76 ± 0.05	21.00 ± 0.01	24.03 ± 0.02	30.22 ± 0.05	34.97 ± 0.03
PCA 02010	HB2	CM2	4	6.08 ± 0.01	-	-	8.59 ± 0.01	9.38 ± 0.01	9.95 ± 0.01	10.83 ± 0.03	11.69 ± 0.01	12.90 ± 0.03	19.77 ± 0.05	20.97 ± 0.01	24.47 ± 0.04	30.13 ± 0.05	-
PCA 02012	HB2	CM2	4	6.09 ± 0.01	-	-	8.52 ± 0.01	9.41 ± 0.01	9.94 ± 0.02	10.77 ± 0.03	11.78 ± 0.01	12.51 ± 0.03	19.83 ± 0.02	20.97 ± 0.01	24.15 ± 0.03	30.32 ± 0.09	-
Y 980115	HB2	CI1/CY	3	-	6.42 ± 0.01	6.96 ± 0.01	9.23 ± 0.02	-	-	-	-	12.52 ± 0.01	-	-	-	-	-
B 7904	HB2	C2-ung/CY	4	6.26 ± 0.01	-	-	9.23 ± 0.01	-	9.63 ± 0.01	10.58 ± 0.02	11.83 ± 0.01	12.68 ± 0.03	20.10 ± 0.01	-	25.48 ± 0.05	30.78 ± 0.05	-
Y 86720	HB2	C2-ung/CY	4	6.36 ± 0.03	-	-	9.39 ± 0.06	-	10.43 ± 0.01	-	11.76 ± 0.01	12.58 ± 0.03	20.46 ± 0.02	-	25.45 ± 0.03	30.89 ± 0.03	-
Y 86789	HB2	C2-ung/CY	4	6.12 ± 0.01	-	-	9.59 ± 0.07	-	10.44 ± 0.01	-	11.77 ± 0.01	12.60 ± 0.05	20.39 ± 0.02	-	25.49 ± 0.03	30.80 ± 0.03	-

Table 5.1: *Positions of features identified in MIR emissivity spectra collected under (a) ambient and (b) SAE conditions for the CM, CY and CM-an samples*

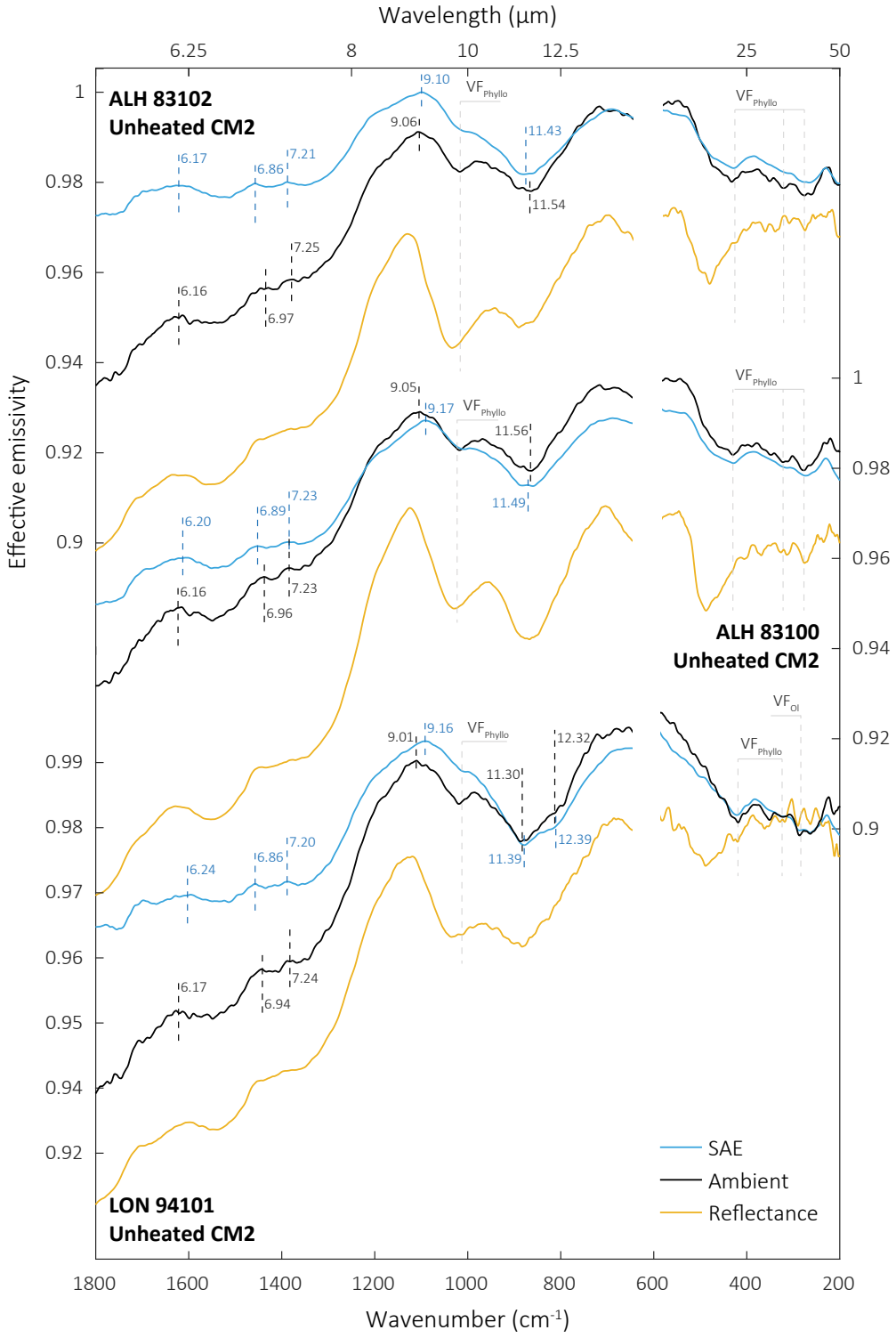


Figure 5.1: *The MIR emissivity spectra for the unheated CM chondrites ALH 83100, ALH 83102 and LON 94101, between 5.5 – 50 µm. Reflectance spectra from chapter 3 for the same material are also included and are plotted as 1 – reflectance. Gaps in the data are due to low signal to noise due to low throughput by the beam splitter at these wavelengths.*

this doublet in the emissivity spectra suggest it has experienced less aqueous alteration than ALH 83100 and ALH 83102, consistent with the petrologic grade (1.3 vs. 1.2) of these meteorites (Table 3.1).

The ambient emissivity spectra of ALH 83100, ALH 83102 and LON 94101 show vibrational features near 9.83 and 23.27 µm. These are the phyllosilicate Si-O stretching and bending vibrational features, respectively (chapters 3 and 4, Michalski et al., 2006). The Si-O bending feature in the LON 94101 emissivity spectrum is at slightly longer wavelengths than in the ALH 83100 and ALH 83102 spectra, at 23.76 µm (Table 5.1), and based on the trend determined by Hanna et al. (2020) that the Si-O bending minimum moves to shorter wavelengths with increasing aqueous alteration, this suggests it is less aqueously altered. This trend was not observed in the reflectance spectra (chapter 3). Between 25 - 50 µm, the ALH 83100 and ALH 83102 emissivity spectra show phyllosilicate vibrational features near 31.26 and 36.65 µm and the LON 94101 emissivity spectra shows features at 31.15 and 34.93 µm, the former of which is due to phyllosilicate and the latter of which is more consistent with olivine (Figs. 2.7 and 2.9, Bishop et al., 2008, Hamilton, 2010, Lane et al., 2011).

Emissivity spectra of the unheated CMs collected under SAE show some differences to the ambient spectra (Fig. 5.1). For example, there is a slight shift (of up to 0.16 µm) to longer wavelengths of the CF. This is in contrast to the study of Donaldson Hanna et al. (2019), who reported a shift of the CF to shorter wavelengths in the spectra of both hydrated physical mixtures and hydrated meteorites collected under similar SAE conditions. In addition, for all unheated CM spectra I observe a decrease in spectral contrast between 5 - 8 µm, and a reduction in contrast of some of the vibrational features between 16.7 - 50.0 µm, notably the feature near 31.25 µm.

5.3.2 Ambient and SAE MIR spectral features in aqueously and thermally altered CM chondrites

Figures 5.2 and 5.3 show the ambient and SAE emissivity spectra of the stage II and stage IV CM chondrites. In the 5 - 8 μm range the stage II CMs EET 96029 and Y 793321 show weak features compared to the unheated CM ambient emissivity spectra. The stage IV CMs PCA 02010 and PCA 02012, which have undergone intense thermal metamorphism on their parent bodies, (Fig. 5.3), show peaks in their ambient emissivity spectra near 6.10 μm. The positions of these features are consistent with bound molecular water and as discussed in chapter 4, these samples have terrestrial alteration products which may be contributing to these features. The samples were gently heated to 80 ^{o}C and 75 ^{o}C when collecting ambient and SAE emissivity spectra, respectively, so it is still likely that adsorbed water was driven off. Olivine spectra also show features in this region (Figure 2.9, Christensen et al., 2000, Baldridge et al., 2009), and considering the olivine dominated mineralogy of PCA 02010 and PCA 02012, these phases may be responsible for these features at 6.10 μm. The EET 96029 and Y 793321 ambient emissivity spectra show CFs and TFs at 8.86 and 8.89 μm, and at 12.47 and 12.54 μm, respectively. The PCA 02010 and PCA 02012 ambient spectra show CFs and TFs at 8.75 and 8.67 μm, and at 12.45 and 12.50 μm.

The ambient emissivity spectra of the stage II and stage IV CMs show vibrational features consistent with spectral measurements of Mg-rich olivine (Fig. 2.9, Lane et al., 2011); near 9.35, 9.85, 10.75, 11.50 and 19.74 μm (Table 5.1). Additionally, features at longer wavelengths (> 20 μm) consistent with Mg-rich olivine are distinguishable in the emissivity spectra, near 21.05, 24.26, 29.91 and 34.94 μm (Fig. 2.9, Hamilton, 2010, Lane et al., 2011).

In the stage II and stage IV emissivity spectra, under SAE conditions I observe a shift of the CF to shorter wavelengths (of up to 0.21 μm) relative to measurements under ambient

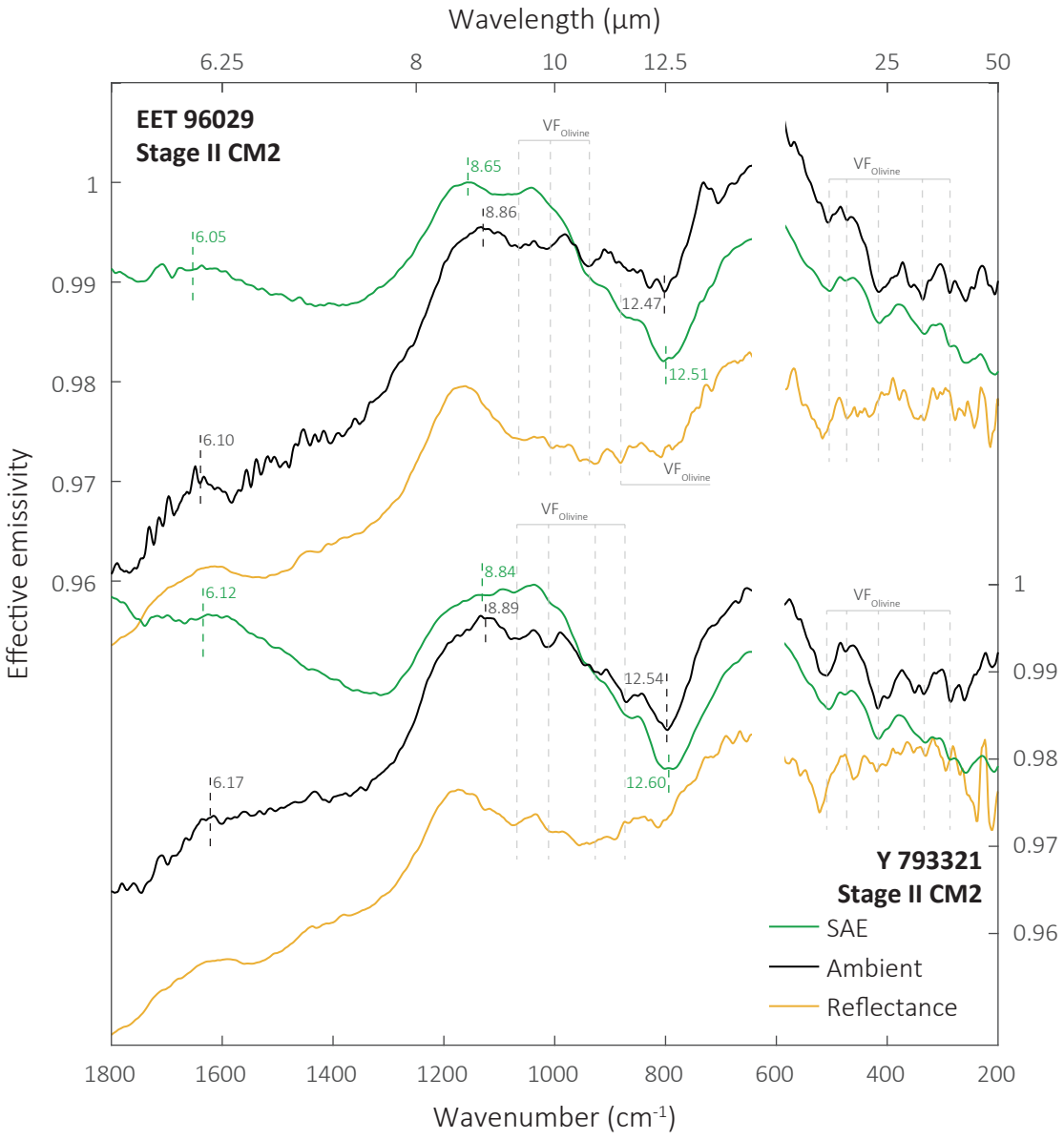


Figure 5.2: *The MIR emissivity spectra for the stage II CM chondrites EET 96029 and Y 793321, between 5.5 – 50 µm. Reflectance spectra from chapter 4 for the same material are also included and are plotted as 1 – reflectance. Gaps in the data are due to a beam splitter error.*

conditions, consistent with previous observations of anhydrous physical mixtures and anhydrous meteorites under SAE conditions (Donaldson Hanna et al., 2019), but opposite to what is observed in the unheated CM spectra, where the CF shifts to longer wavelenghts under SAE conditions. The spectral contrast of some vibrational features in the EET 96029 and Y 793321 spectra are reduced under SAE, although their positions do not change. The one

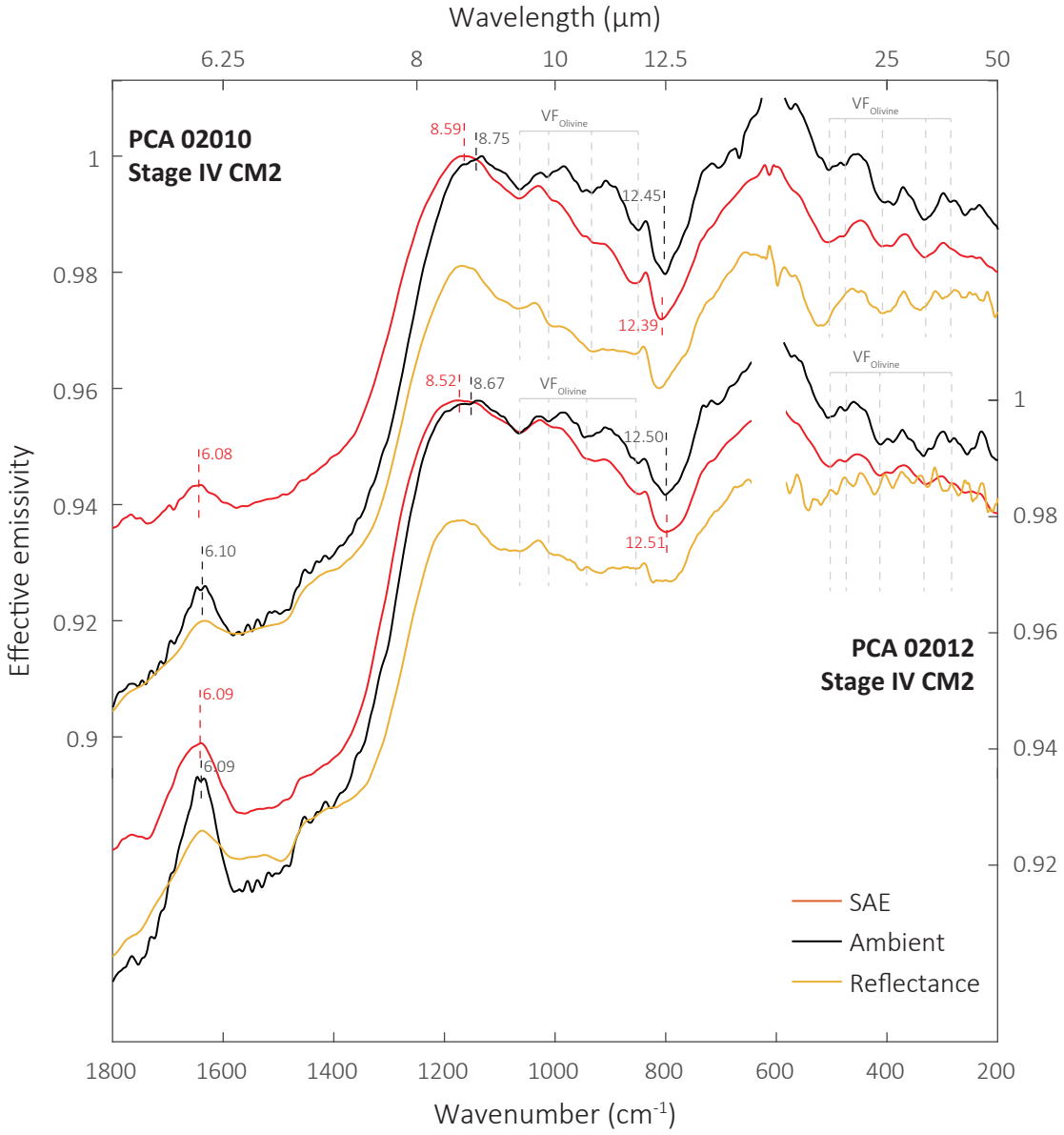


Figure 5.3: *The MIR emissivity spectra for the stage IV CM chondrites PCA 02010 and PCA 02012, between 5.5 – 50 μm. Reflectance spectra from chapter 4 for the same material are also included and are plotted as 1 – reflectance. Gaps in the data are due to a beam splitter error.*

exception is the 9.35 μm feature in the EET 96029 spectrum, which shifts to shorter wavelengths (near 9.17 μm) under SAE conditions. Additionally, in the EET 96029 spectrum, a vibrational feature near 11.50 μm becomes more distinct.

5.3.3 Ambient and SAE MIR spectral features in aqueously and thermally altered CM-anomalous chondrites

Figure 5.4 shows the ambient and SAE emissivity spectra of the stage II CM-an WIS 91600. The reflectance spectrum of the same sample is included for comparison. The ambient emissivity spectrum shows a strong emissivity feature between 5 - 8, with two peaks at 6.61 and 6.90 μm. A vibrational feature at 9.81 μm is likely due to phyllosilicates, some of which are not dehydrated in WIS 91600 (chapter 4). WIS 91600 also contains 12 vol% olivine, resulting in a feature at 10.69 μm. In the Si-O bending region, the ambient spectrum shows features at 24.36 and 34.96 μm that are consistent with Mg-rich olivine (Fig. 2.9, Hamilton, 2010, Lane et al., 2011), although features diagnostic of Mg-rich olivine near 19.75 and 21.05 μm are absent. There is a feature at 29.47 μm that is consistent with olivine, however WIS 91600 contains significant magnetite (~9 vol%, Table 4.1), which also has a feature at that position (Christensen et al., 2000). Thus, I cannot uniquely determine which mineralogy is the cause of this feature.

Under SAE conditions, the main changes in the emissivity spectrum of WIS 91600 occur in the region around the CF. The vibrational feature at 9.81 μm is no longer resolvable, moving the CF to a longer wavelength at 9.32 μm. Between 5 - 8 μm, there is a change in spectral slope, which shifts the initial vibrational feature from 6.61 to 6.48 μm. Across the rest of the spectral range, other vibrational features do not change in position.

5.3.4 Ambient and SAE MIR spectral features in aqueously and thermally altered CY chondrites

The ambient, SAE and reflectance spectra of the stage III and stage IV CY chondrites are shown in Figures 5.5 and 5.6. The ambient emissivity spectrum of Y 980115 shows a strong emissivity feature between 5- 8 μm, with two peaks at 6.54 and 6.93 μm, similar to those observed in the reflectance spectra of the same sample, and in the WIS 91600 emissivity

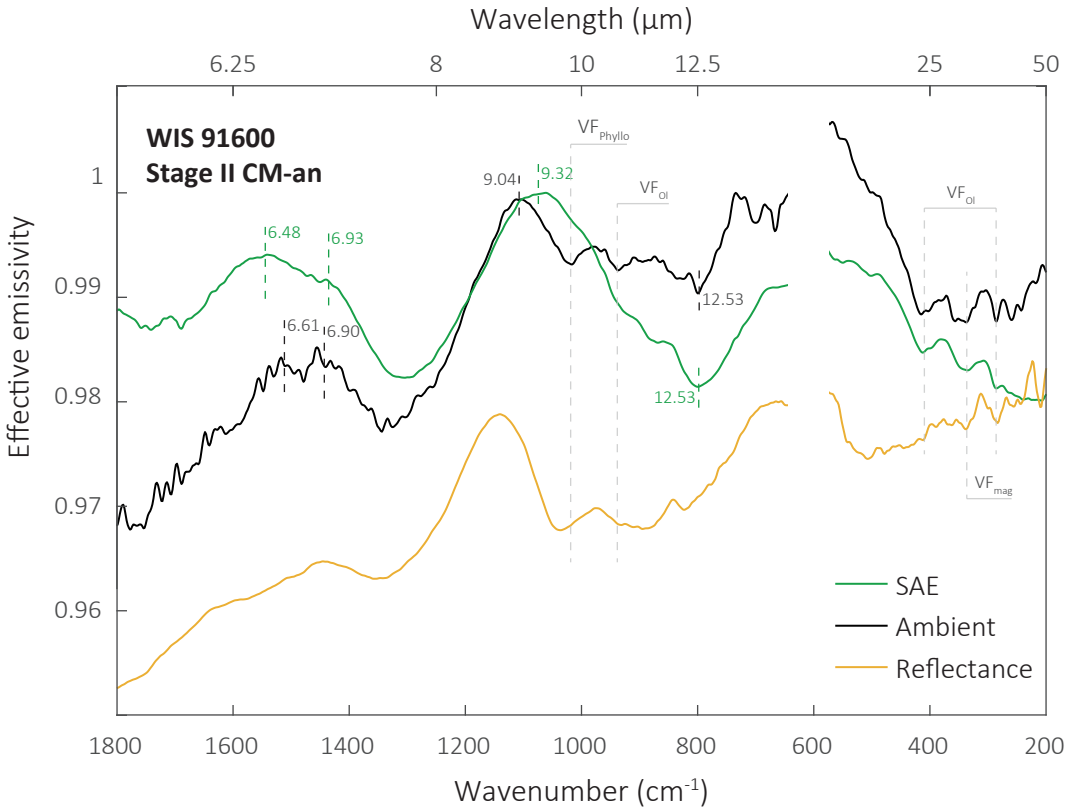


Figure 5.4: *The MIR emissivity spectra for the stage II CM-an chondrite WIS 91600, between 5.5 – 50 µm. The reflectance spectrum from chapter 4 for the same material are also included and are plotted as 1 – reflectance. Gaps in the data are due to a beam splitter error.*

spectra (Figure 5.4). This is due to carbonates in Y 980115 (chapter 4). The ambient spectra of the stage IV CY chondrites have weaker features between 5 - 8 µm (Fig. 5.6). The 5 - 8 µm region can therefore be used to distinguish between stage III and stage IV CY spectra.

The Y 980115 ambient emissivity spectrum has a CF near 9.03 µm and a TF at 12.61 µm. Spectral contrast in the Si-O stretching and bending vibrational regions in the Y 980115 ambient spectrum is lower than that observed for the CM ambient spectra and few diagnostic features are observed, however a feature at 9.85 µm can be identified. Based on the shape of the feature, it is likely due to Si-O stretching in dehydrated phyllosilicates (chapter 4). I observe weak features at wavelengths >20 µm, although their spectral contrast is low, likely due to the high abundance of Fe-sulfides (Table 4.1). Fe-sulfides have low albedo and can act as an opaque agent, reducing the strength of vibrational features and overall spectral

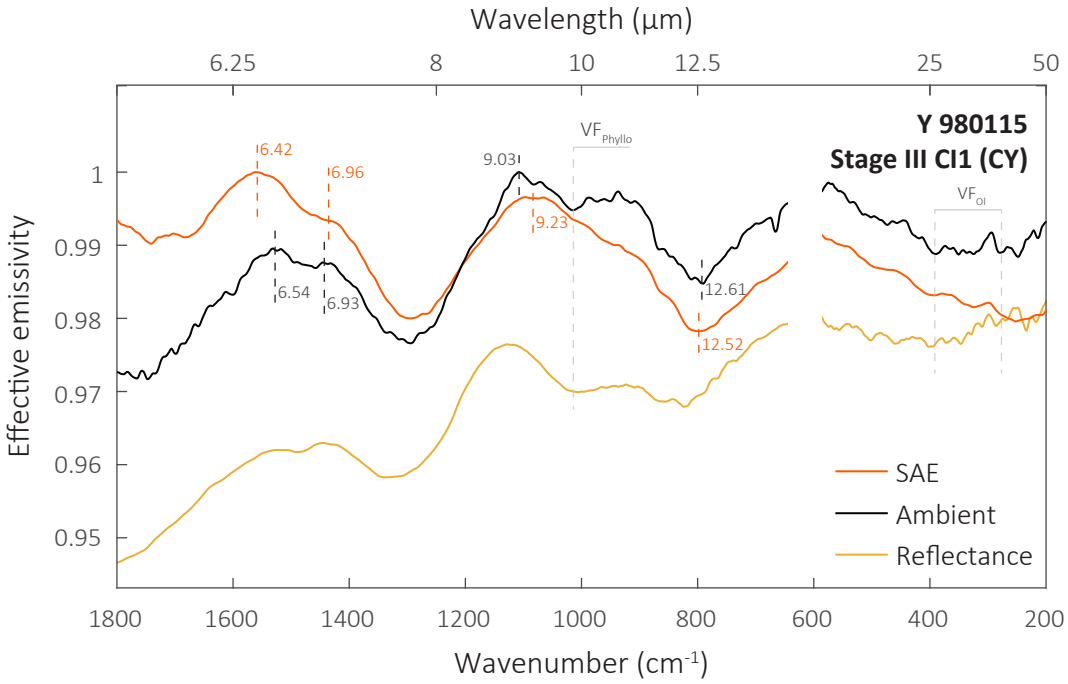


Figure 5.5: *The MIR emissivity spectra for the stage III CY chondrite Y 980115, between 5.5 – 50 µm. The reflectance spectrum from chapter 4 for the same material are also included and are plotted as 1 – reflectance. Gaps in the data are due to a beam splitter error.*

contrast (Cloutis et al., 2011a). Features near 25.72 and 35.85 µm are also identified and are consistent with ~Fo_{60} olivine (Hamilton, 2010, Lane et al., 2011).

The region around the CF in the stage IV CY emissivity spectra is complex and identifying the CF position is challenging. The Y 86720 and Y 86789 ambient emissivity spectra show a shoulder near 8.35 µm that is consistent with the CF of pyroxene (Hamilton, 2000). These meteorites contain 8 and 5 vol% pyroxene respectively (Table 4.1). The 8.35 µm feature is followed by another emissivity peak near 9.00 µm. This 9 µm feature is in a similar position to the CF in the Y 980115 spectrum, but rather than being related to dehydrated phyllosilicates, which are not present in the stage IV CYs (Table 4.1), it likely represents olivine: its position is consistent with the CF in $Fo_{60–80}$ olivine (Hamilton, 2010), which is consistent with the fact that the samples contain ~60 vol% secondary olivine (Table 4.1). There is a TF near 12.60 µm in both stage IV CY spectra. The Y 86720 and Y 86789 ambient spectra also

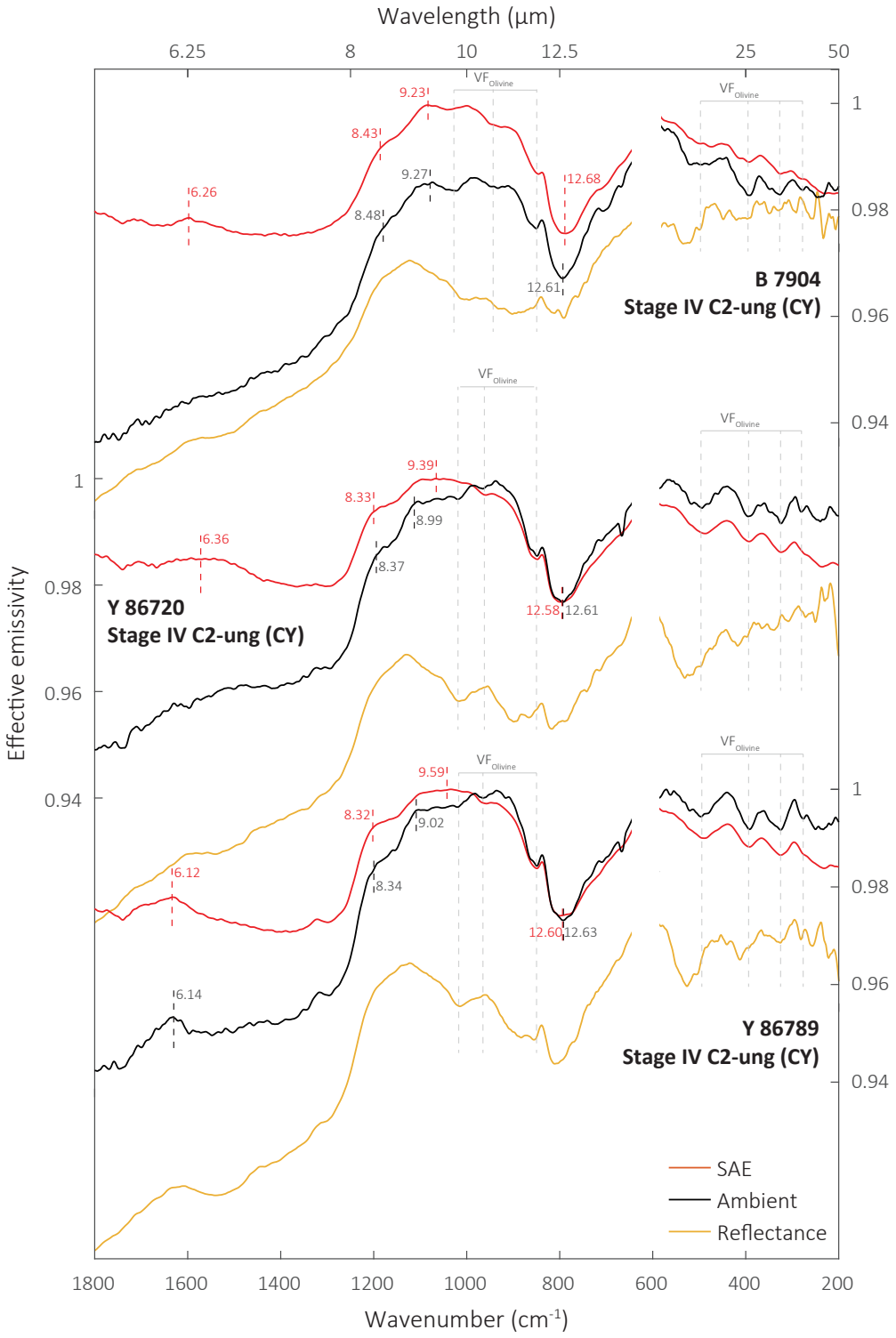


Figure 5.6: *The MIR emissivity spectra for the stage IV CY chondrites B 7904, Y 86720 and Y 86789, between 5.5 – 50 µm. Reflectance spectra from chapter 4 for the same material are also included and are plotted as 1 – reflectance. Gaps in the data are due to a beam splitter error.*

show vibrational features near 9.81, 10.35, 11.78, 20.19, 25.48, 30.83 and 35.95 µm, which are consistent with more Fe-rich olivine (~Fo_{60-70}, Hamilton, 2000).

The B 7904 ambient emissivity spectrum shows a shoulder at 8.48 µm, consistent with the CF of some pyroxenes (Hamilton, 2000, Donaldson Hanna et al., 2012a), and then a CF at 9.27. The spectrum has a transparency feature at 12.61 µm. The B 7904 spectrum shows vibrational features in the Si-O stretching region at 9.73 and 10.72 µm. These are in similar positions to the olivine vibrational features identified in the stage II and stage IV CM ambient emissivity spectra. However, the Si-O bending region of B 7904 resembles the other stage IV CY spectra, with features consistent with Fe-rich olivine at 20.12, 25.49, 30.61, and 36.01 µm. B 7904 contains both ~25 vol% primary, Mg-rich olivine, and ~50 vol% secondary olivine (Table 4.1). This combination of primary and secondary olivine might explain the difference between this spectrum and the other stage IV CY spectra.

Under SAE conditions the CF in the Y 980115 spectrum shifts to slightly lower frequencies, and the vibrational feature at 9.35 µm is no longer identifiable. The spectral contrast in the Si-O bending range is reduced relative to the ambient emissivity spectrum. In the stage IV Y 86720 and Y 86789 spectra under SAE conditions, the feature near 9.81 µm is no longer distinguishable, causing the peak at 9.00 µm to shift to longer wavelengths, to 9.39 µm for Y 86720 and 9.59 µm for Y 86789. The B 7904 emissivity spectrum shows little change in the CF region under SAE conditions, with the feature at 9.73 µm still resolvable and no shift in the CF position. In the Si-O bending region, the SAE spectral signature of all stage IV CYs appears smoother, in contrast to the more complex ambient spectra. However, the positions of the vibrational features do not change under SAE conditions.

5.3.5 Comparing reflectance and emissivity spectra

Included in Figures 5.1 - 5.6 are the reflectance spectra collected for the same samples. Figure 5.7 shows the position of the CFs, TFs and first Si-O bending feature as calculated in

the reflectance and emissivity spectra. The positions of CFs, TFs and first Si-O bending vibrational features in emissivity spectra are consistently at longer wavelengths than those observed in the reflectance spectra, regardless of meteorite type. The shift is greatest for the first Si-O bending feature in the unheated CM and the stage II WIS 91600 spectra. Other differences between reflectance and emissivity is that several features at longer wavelengths (>25 µm) can be identified, which are not discernible in the reflectance data due to low signal to noise.

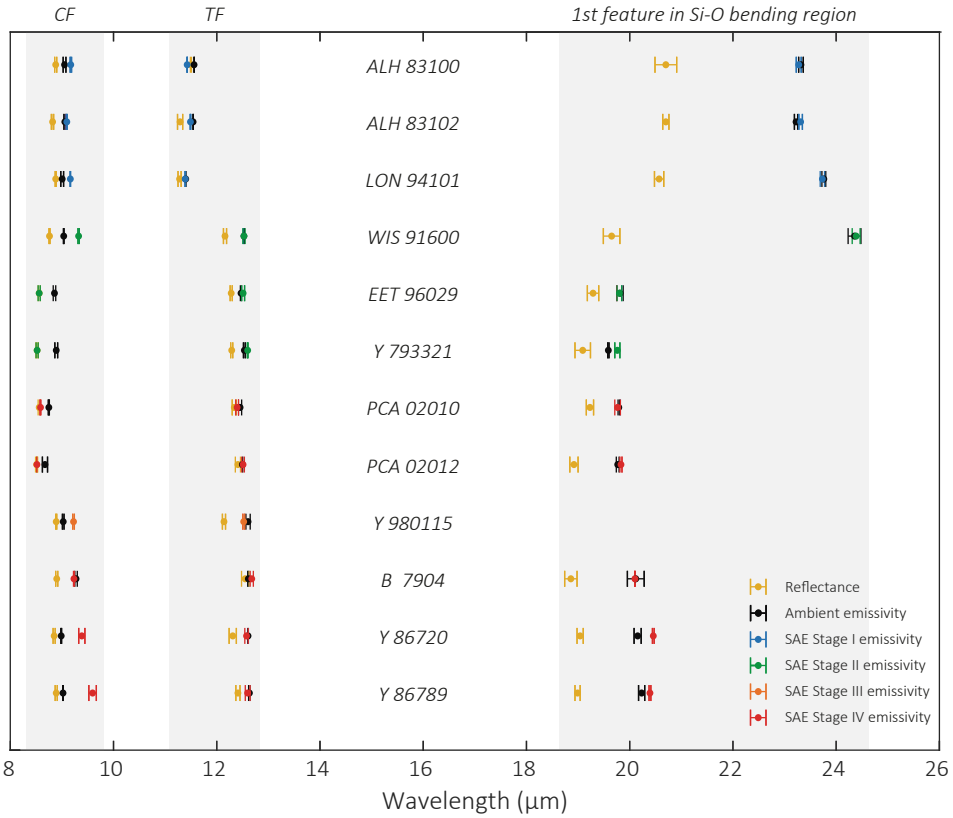


Figure 5.7: *The positions of the CF, TF and first feature in the Si-O bending region as observed in the ambient and SAE emissivity spectra, and the reflectance spectra of the same material.*

The spectral shape of the CF and TF also differ in the emissivity spectra compared to the reflectance spectra. The shape of the CF is broader, particularly evident in the unheated CM and the stage II CM spectra. This widening of the feature may be responsible for the apparent shift of the CF to longer wavelengths. The TF observed in the reflectance spectra

of several samples are also weaker compared to their equivalent emissivity spectra, again regardless of meteorite type. This is not likely to be a result of sample packing, which can cause the TF to be weaker (section 2.3.1.1), as these reflectance spectra do not show any other characteristics of being packed tightly. These stronger TFs enable a doublet to be identified in the LON 94101 emissivity spectra, which is not observed in the reflectance spectrum.

The stage IV CY emissivity spectra show different spectral shapes in their CF regions compared to their equivalent reflectance spectra, where a single CF is easily discernible. It is likely the emissivity peak near 9.00 µm in the ambient emissivity spectra of Y 86720 and Y 86789 is the CF represented in their equivalent reflectance spectra, as the shift between this 9.00 µm feature and the CF in the stage IV CY reflectance spectra (~8.90, Figure 4.11b) is about the same as the difference between the position of the CF in other reflectance and emissivity spectra. I also assume that the CF in the ambient B 7904 µm spectrum is the emissivity peak located at 9.27 µm.

5.4 Discussion

5.4.1 Comparing reflectance and emissivity spectra in the MIR

Reflectance and emissivity spectra

Emissivity spectra are often approximated from reflectance spectra using Kirchhoff's law: E = 1- R (Nicodemus, 1965). Reflectance is traditionally easier than emissivity to measure in the laboratory, but Kirchoff's law can only be applied accurately when directional hemispherical reflectance is measured and when samples are in thermodynamic equilibrium with their environment (Salisbury et al., 1991, Salisbury, 1993, Christensen and Harrison, 1993). In chapters 3 and 4 I presented reflectance spectra that were collected in a bidirectional reflectance geometry (as described in section 2.3.1). As the same samples were used to

collect emissivity spectra, the two spectral measurement types can be compared in order to evaluate how accurate the approximation of Kirchhoff's law is when using bidirectional reflectance, and how well reflectance spectra collected in this manner can be used to interpret remote sensing observations. Figures 5.1 - 5.6 show that for most aqueously and thermally altered samples, shapes and positions of features are qualitatively similar between the reflectance and emissivity spectra, particularly when collected under ambient conditions, although systematic shifts in positions of the CF and TF are observed. Additionally, in the Si-O bending region between 18 - 25 μm, emissivity spectra show vibrational features that are not as easily identified in most reflectance spectra. The stage IV CY emissivity spectra show the greatest deviation from their reflectance spectra, particularly in the CF region. The reflectance spectra for all stage IV CYs show a distinct CF, followed by vibrational features associated with olivine (section 4.3.3). In the emissivity spectra, the region is more complex, with a plateau-like spectral signature. Understanding the cause of this plateau would involve additional lab measurements and analysis, including hemispherical reflectance and analysis of the optical properties of the constituent minerals and so is outside the scope of this thesis.

Figure 5.7 shows the position of the CF, TF and first feature in the Si-O bending region (18 - 25 μm) as determined for the reflectance, ambient and SAE emissivity spectra collected for the same samples of all meteorites in this chapter. In all samples, the CF and TF are consistently at shorter wavelengths in the reflectance spectra than in the emissivity spectra. Christensen and Harrison (1993) showed the CF in emissivity spectra of quartz (with a coarse particulate size of 75 - 250 μm) was at longer wavelengths when compared to the CF observed in biconical reflectance spectra, and I show this is also true when bidirectional reflectance spectra of fine particulate samples are collected. Additionally, in all spectra there is a significant shift (>2σ) in position of the first identifiable feature in the Si-O

bending feature between reflectance and emissivity spectra. This is particularly the case for unheated CM spectra and for the WIS 91600 spectra, which show positions between 23.22 - 24.39 µm in emissivity spectra, but between 19.65 - 20.70 µm in reflectance spectra (Fig. 5.7, Tables 4.2 and 5.1).

Reflectance measurements are highly dependent on the geometry of the experimental system, and although I have attempted to best approximate emission by collecting diffuse reflectance, the bidirectional set up has the incident and reflected light at set angles. Previous laboratory studies have shown that varying the incident and emission angles can vary the positions and shapes of spectral features (e.g. Gradie et al., 1980, Reddy et al., 2012). When collecting my emissivity measurements I heat the samples using heaters and a lamp (see chapter 2), and the sample emits in all directions (hemispherically). This difference (hemispherical emission versus bidirectional reflectance) is likely the cause of the shifts in the positions of the TF and CF observed in the spectra. In the Si-O bending region (where emission is the dominant spectral flux), the reflectance spectra have much lower signal to noise than the emissivity spectra making spectral features difficult to identify from the noise, especially for these low albedo samples. This emphasises that to properly interpret this longer wavelength region, between 18 - 50 µm, in spacecraft and telescopic spectra, laboratory emissivity spectra are required.

Ambient and SAE emissivity spectra

The effect of varying environmental conditions has been discussed previously (e.g. Logan et al., 1973, Salisbury and Walter, 1989, Henderson and Jakosky, 1994, Thomas et al., 2010, Donaldson Hanna et al., 2012a,b, 2019). When asteroid surfaces dominated by fine particulates are heated by the Sun, they absorb visible light and then re-emit infrared radiation, however the emitting layer is shallower than the absorbing layer (due to optical properties

of the materials). This results in a thermal gradient between the upper and lower layers of the surface. This is emphasised by the airless environment and therefore lack of interstitial gases (and therefore lack of convective heat transport) between the particulates making up the surface. SAE conditions reproduce these thermal gradients by heating samples from above and below in a cold, vacuum environment (chapter 2).

Previous lab studies have demonstrated how thermal gradients affect the shape and position of spectral features across thermal infrared wavelengths (e.g. Logan et al., 1973, Salisbury and Walter, 1989, Henderson and Jakosky, 1994, Thomas et al., 2010, Donaldson Hanna et al., 2012a,b, 2019). Typically, introduction of a thermal gradient results in a shift in the CF to shorter wavelengths as a result of the different temperatures between the CF region (where radiation is emitted from the relatively warm interior due to little scattering as it passes through the material) and the vibrational features (where radiation from the relatively cool shallower layers is emitted, due to most materials having high absorption coefficients in these wavelength ranges) (e.g. Logan et al., 1973, Salisbury and Walter, 1989, Henderson and Jakosky, 1994, Donaldson Hanna et al., 2012a,b). The shift of the CF to shorter wavelengths under SAE conditions (when a thermal gradient is present) is observed when comparing the ambient and SAE emissivity spectra of EET 96029, Y 793321, PCA 02010, PCA 02012 and B 7904 (Fig. 5.7). However, all other emissivity spectra show a shift in the opposite direction, to longer wavelengths under SAE conditions. There may be a number of causes for this. First, when calibrating and reducing the spectra to emissivity, a single brightness temperature of the sample is assumed, when in reality several temperatures at varying depths are being detected by the spectrometer. This may cause spectral slopes to appear in the CF region of spectra, which are not a result of the mineralogy of the sample. In the spectra of ALH 83100, ALH 83102 and LON 94101 it appears as though the shift in the CF position to longer wavelengths could be a result of a change in spectral slope.

To investigate whether this is the case, alternative calibration methods could be considered, although this is outside the scope of this thesis.

An alternate explanation for the shift of CFs to longer wavelengths under SAE conditions is the effect of vibrational features appearing and disappearing. This is responsible for the shift in the CF in the WIS 91600, Y 980115, Y 86720 and Y 86789 spectra. One hypothesis is that with the introduction of the thermal gradient in the samples under SAE conditions, different minerals are sampled owing to their optical properties in the resulting emissivity spectrum. Disappearance of features characteristic of certain minerals certainly suggests they are no longer emitting in the same way as they did under ambient conditions. This could be explored by studying further investigating the optical properties of the minerals responsible for the appearing/disappearing features. Unfortunately, exploring these avenues is outside the scope of this thesis.

As bidirectional reflectance and emissivity spectra were collected on the same sample, mineralogy is consistent between measurements, and differences in positions can only be due to collection method. I show that bidirectional reflectance does provide a good approximation for emissivity as long as comparisons are limited to trends rather than exact positions. I demonstrate in the following sections that certain trends apply to both reflectance and emissivity data. However, bidirectional reflectance cannot be quantitatively compared to emissivity measurements, as emissivity spectra show shifts in features and changes in spectral shapes.

5.4.2 Aqueous alteration in MIR emissivity spectra

Chapter 3 identified a number of trends with increasing aqueous alteration in MIR reflectance spectra of CM chondrites, including shifts of the CF and TF to shorter wavelengths with increasing aqueous alteration (Figs. 3.9 and 3.11). The CM2 chondrites in this chapter do not cover the same petrologic range as was covered in chapter 3, however Figure 5.8 shows

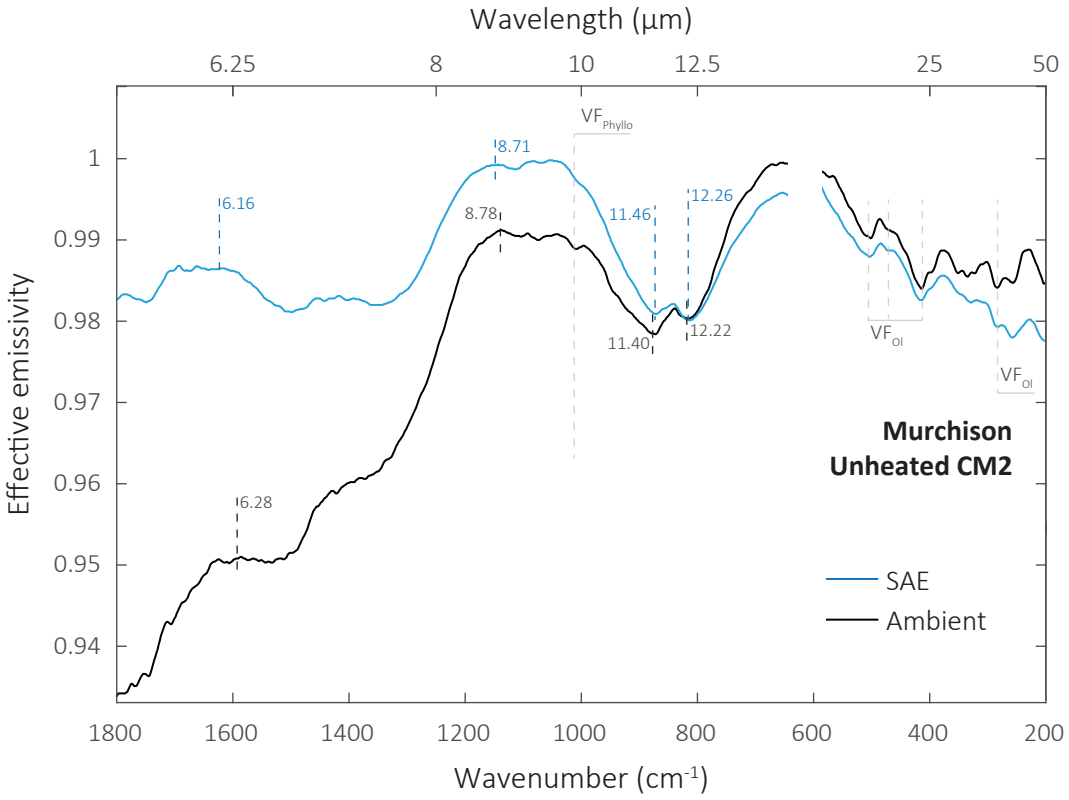


Figure 5.8: *The MIR emissivity spectra for the unheated CM2 chondrite Murchison from Donaldson Hanna et al. 2020, between 5.5 – 50 µm. Gaps in the data are due to a beam splitter error.*

the ambient and SAE spectra of Murchison collected by Donaldson Hanna et al. (2020). Although the emissivity spectra were not collected on the same material as in chapter 3, and so I will not compare differences between the reflectance and emissivity spectra, Murchison has been determined to be less aqueously altered than ALH 83100, ALH 83102 and LON 94101 (Table 3.1 Howard et al., 2015). It must be noted that the Murchison sample represented in Figure 5.8 had a range of particle sizes including coarse particles >150 µm (Donaldson Hanna et al., 2020), therefore only first order comparisons can be made to my spectra, which were collected on samples with particle sizes <35 µm. By comparing the emissivity spectra of ALH 83100, ALH 83102 and LON 94101 in Figure 5.1 to the spectra of Murchison in Figure 5.8, it appears several of the trends identified for evaluating aqueous alteration in reflectance spectra can also be applied to emissivity spectra. For example,

the Murchison and LON 94101 spectra have doublet TFs while ALH 83100 and ALH 83102 emissivity spectra have a single feature at shorter wavelengths, which is consistent with ALH 83100 and ALH 83102 being more aqueously altered than LON 94101 and Murchison (Table 3.1 McAdam et al., 2015). Additionally, the CF changes shape from a relatively broad feature in the Murchison spectra to a sharper feature in the LON 94101, ALH 83100 and ALH 83102 spectra consistent with Murchison being the least aqueously altered (Table 3.1, Howard et al., 2015).

The CF shifts to longer wavelengths in the more aqueously altered spectra, which is inconsistent with what was observed in chapter 3, where there was a shift to shorter wavelengths with increasing alteration due to increasing Mg-serpentine abundances. Here I show that for the ambient emissivity spectra, Murchison has a CF at 8.78 µm, but the more altered ALH 83100, ALH 83102 and LON 94101 have CFs near 9.01- 9.05 µm. This may be due to the higher signal to noise of these emissivity spectra in comparison to reflectance measurements in chapter 3, allowing the CF to be clearly identified. In the reflectance spectra of Murchison in chapter 3, the CF was identified as the centre of a broad zone, whereas in the emissivity spectrum in this chapter, vibrational features can be identified, resulting in the CF being more distinguishable.

Si-O bending

As features in the Si-O bending region (wavelengths >18 µm) are more identifiable in emissivity spectra compared to reflectance spectra, trends with aqueous alteration at longer wavelengths can be evaluated. Figure 5.9a compares the ambient and SAE emissivity spectra in this range for ALH 83100, ALH 83102, LON94101 and Murchison with the ambient emissivity spectrum of Mg-rich olivine and the reflectance spectrum of Mg-serpentine. The Murchison emissivity spectra show features consistent with Mg-rich olivine at 19.72, 21.07,

24.05 and 34.99 µm, despite having ~75 vol% phyllosilicates and ~15 vol% primary olivine (Table 3.1, Howard et al., 2015). Donaldson Hanna et al. (2019) showed that addition of as little as 5 vol% olivine to a predominately phyllosilicate physical mixture (85.5 vol%) changes the position of the CF, and the Murchison spectra here show that an olivine abundance of ~15 vol% is great enough to superimpose olivine features over the broad phyllosilicate features in the Si-O bending region. In contrast, the more aqueously altered ALH 83100 and ALH 83102 spectra only show features in this region consistent with phyllosilicates (Fig. 5.9a) because they contain less primary olivine (~8 vol%) and more phyllosilicates (~84 vol%) (Table 3.1).

The LON 94101 ambient and SAE spectra show an intermediate behaviour. The spectra have a feature near 23.75 µm, which is between the Mg-serpentine features identified in the ALH 83100 and ALH 83102 spectra at 23.25 µm and the olivine feature in the Murchison spectra at 24.05 µm. The LON 94101 spectra have a phyllosilicate feature at 31.25 µm and an olivine feature near 34.93 µm, but do not show the Mg-olivine features near 19.72 and 21.07 µm that are seen in the Murchison spectra. This supports conclusions from Hanna et al. (2020), who identified a feature within this 23.25 - 24.04 µm Si-O bending region that shifted to shorter wavelengths as alteration increased (Fig. 5.9b).

5.4.3 Thermal alteration in MIR emissivity spectra

Chapter 4 identified a number of parameters in reflectance MIR spectra that could be used to identify thermal alteration. These included features between 5 - 8 µm in the CY chondrite reflectance spectra: stage III samples show strong carbonate features which then break down in the stage IV chondrites (Fig. 4.12). Additionally, the TF and first Si-O bending feature shift to longer and shorter wavelengths respectively in thermally altered samples (Figs.

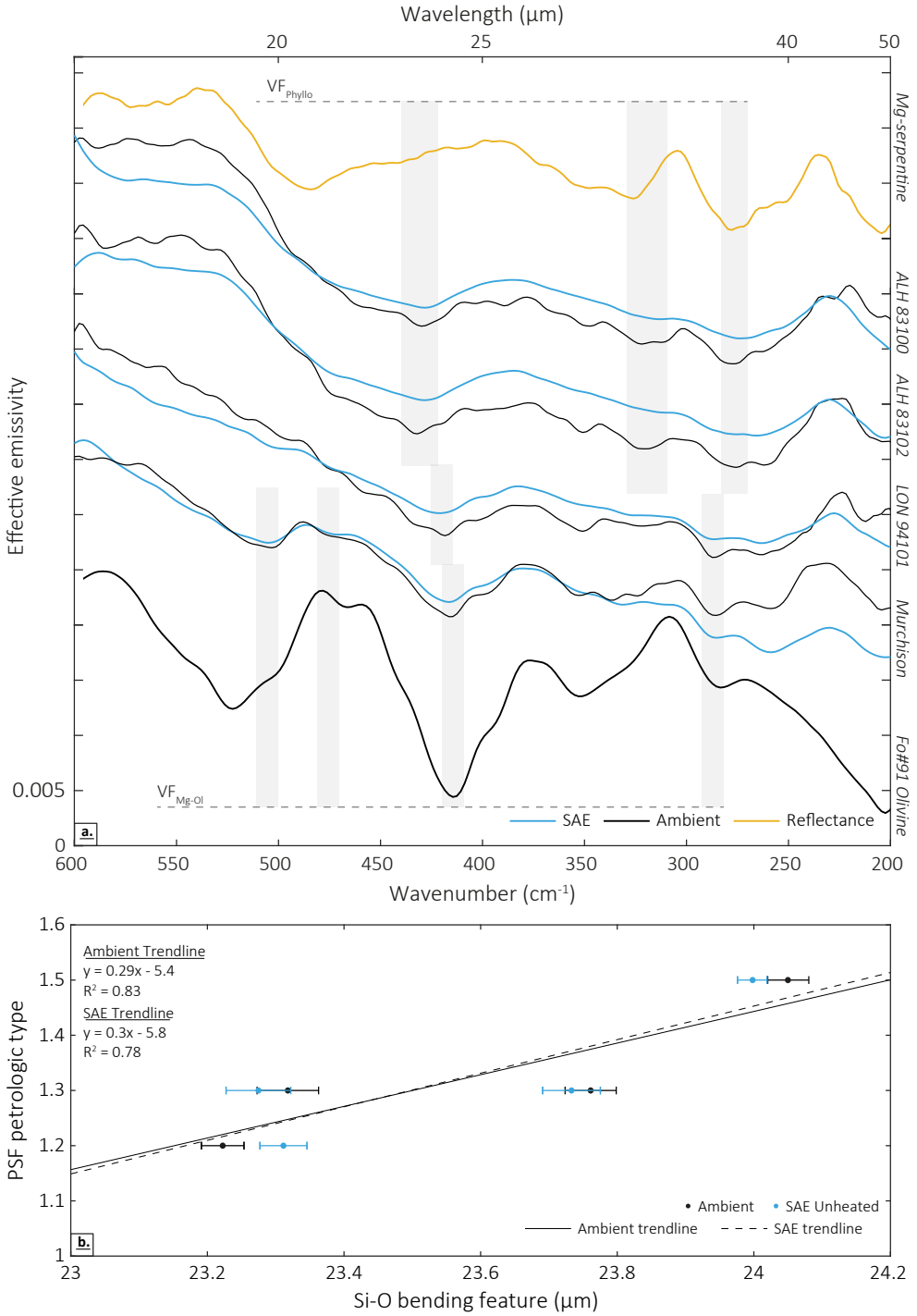


Figure 5.9: *(a) The Si-O bending region, between 16.7 - 50 µm from the emissivity spectra of the unheated CMs in this chapter, including the emissivity spectra of Murchison. Ambient and SAE spectra are offset so they plot on top of each other for the same meteorite. The ambient spectrum of San Carlos Olivine (Fo_{91}) and the reflectance spectrum of the Mg-rich serpentine lizardite are also included for comparison. (b) The position of the Si-O bend feature between 23 - 26 µm against petrologic type as determined by PSD-XRD.*

4.17a, 4.18a). The shifts of the TF and Si-O bending feature could also be explained by variations in degree of aqueous alteration however, and so are most effective when combined with other spectral observations in the NIR (Figs. 4.17b, 4.18b).

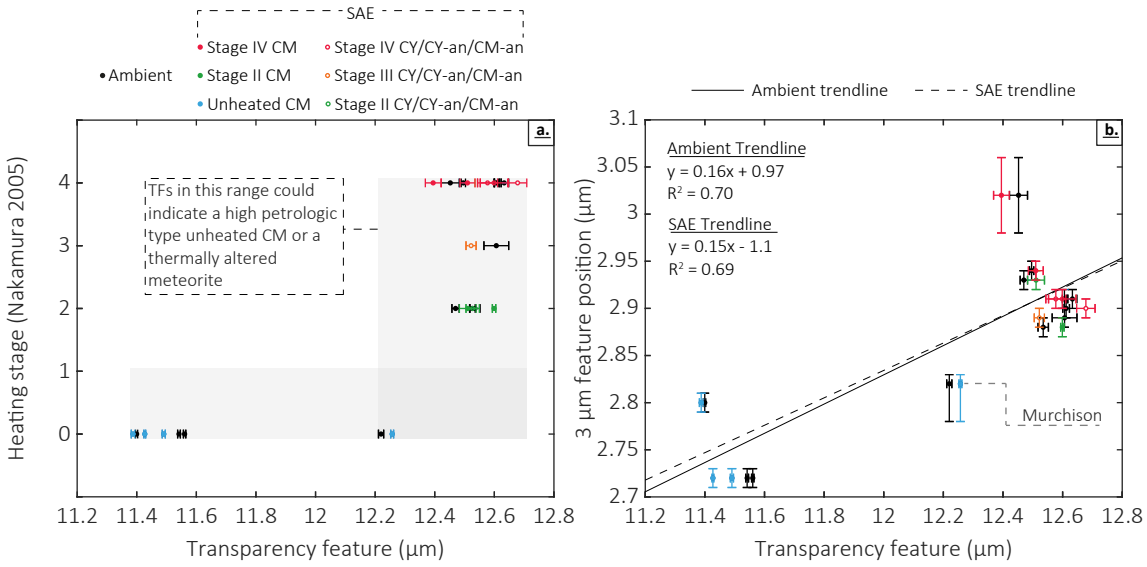


Figure 5.10: *(a) The position of the TF against heating stage, showing that with increasing thermal alteration, the TF shifts to longer wavelengths. (b) The relationship between the position of the TF from the emissivity spectra and the position of the 3 µm feature from reflectance spectra of the same material. The WIS 91600 emissivity spectra were not included due to the multiple features in the 3 µm region (Fig. 4.10, section 4.3.3). This relationship can help distinguish between the effects of aqueous and thermal alteration on the position of the TF.*

In the emissivity spectra, the region between 5 - 8 µm can still be used to determine thermal alteration in the CY chondrites: strong features are present in the stage III Y 980115 spectra but are absent in the stage IV CY spectra. Additionally, the position of the TF is at longer wavelengths in thermally altered samples (Fig. 5.10a). This is likely because of higher olivine abundances in thermally altered CM and CY spectra: the emissivity spectrum of Mg-rich olivine has a transparency feature near 12.82 µm (Fig. 2.3). However, as in the reflectance spectra, unheated spectra with high petrologic types also have TF at longer wavelengths: the Murchison spectra show doublet features with one of the minima near 12.24 µm. Although this does not overlap with the TFs in the dehydrated samples, the

trend does imply a less aqueously altered CM emissivity spectra would have a TF that does overlap. As with some of the parameters discussed in chapter 4, the effects of aqueous and thermal alteration can be distinguished by combining the TF position with the position of the 3 µm feature, which is shown in Figure 5.10b, although this does not resolve between heating stages. The 3 µm position was determined from the reflectance spectra of the same sample so combining observations from multiple spectral ranges can be done without the issue of different samples of the same meteorite showing different spectral features. Given the reflectance and emissivity spectra of Murchison were collected on different samples, I have increased the error of the 3 µm feature in Figure 5.10b to include values determined for multiple different samples by previous studies (Miyamoto, 1992, Calvin and King, 1997, Takir et al., 2013, Garenne et al., 2016, Hanna et al., 2020). Figure 5.10b shows the position of the TF is correlated with the position of the 3 µm feature and the two can be used to distinguish between aqueous and thermal alteration.

Si-O bending

As discussed in section 5.4.1, the first feature in the Si-O bending region is shifted relative to its position in reflectance spectra of the same subsamples, particularly for the unheated CM spectra. Subsequently, the shift to shorter wavelengths of the first Si-O bending feature with thermal alteration described in chapter 4 does not apply to the emissivity spectra. However, there are multiple features in the Si-O bending region of the emissivity spectra that are not identifiable in reflectance spectra but are useful.

Figure 5.11a shows the spectra between ~16.5 - 50 µm for representative unheated CM and thermally altered CM, CM-an and CY spectra. In the thermally altered CM and CY spectra, the features in this region are consistent with olivine, although the positions of these features are at longer wavelengths for the CYs than the CMs. Features at longer wavelengths

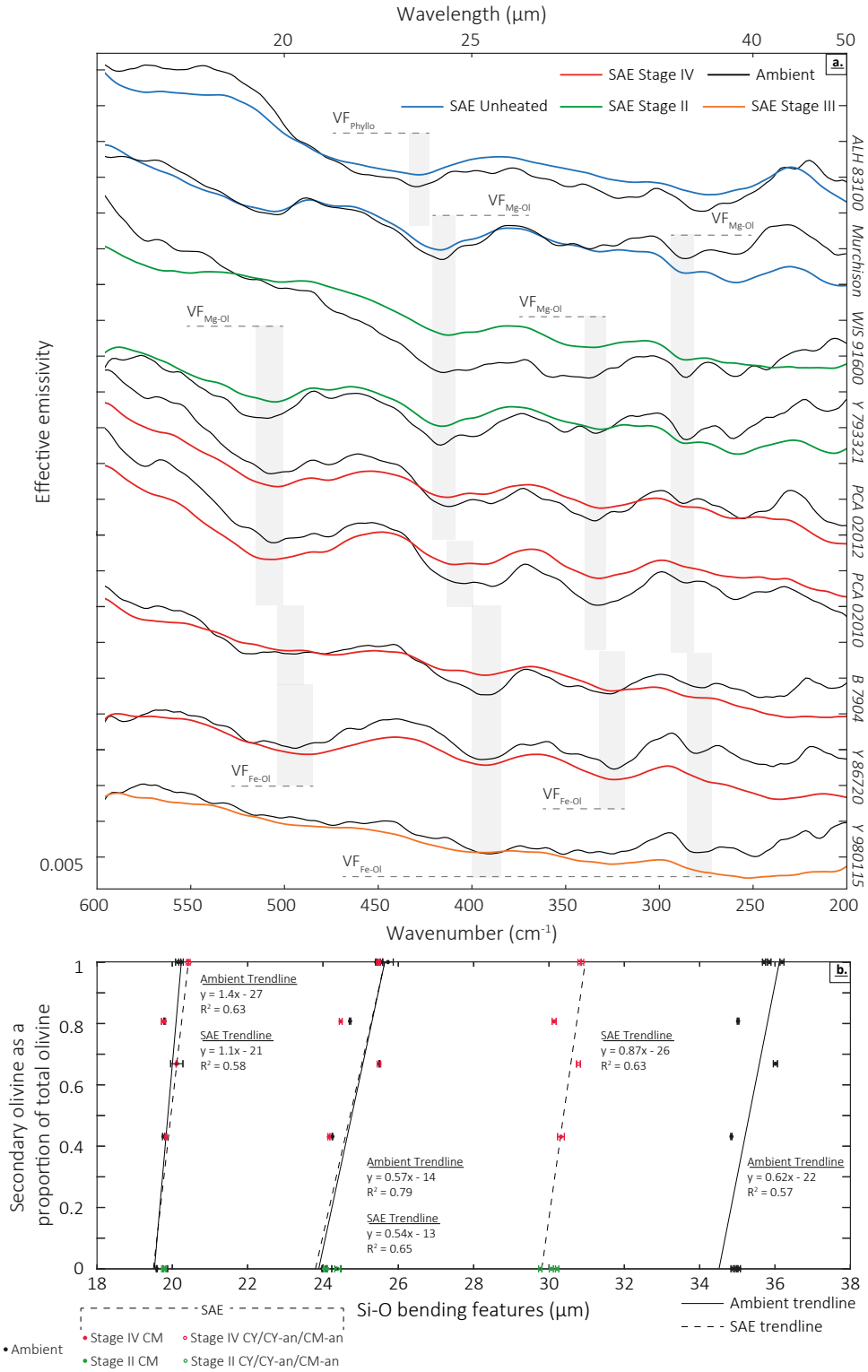


Figure 5.11: *(a) The Si-O bending region, between 16.7 – 50 µm from the emissivity spectra of representative CM, CM-an and CY chondrites in this chapter, including the emissivity spectra of Murchison. Ambient and SAE spectra are offset so they plot on top of each other for the same meteorite. (b) The position of features in the Si-O bending region against secondary olivine as a proportion of total anhydrous silicate as determined through PSD-XRD. Features show a shift to longer wavelengths with increasing secondary olivine*

are consistent with the olivine containing more iron (Hamilton, 2010, Lane et al., 2011), in agreement with the mineralogy of the CY chondrites (Table 4.1). Y 86720, Y 86789 and Y 980115 experienced near complete aqueous alteration prior to thermal metamorphism, so contain abundant Fe-rich secondary olivine and no primary Mg-rich olivine. In contrast, the thermally altered CM chondrites typically contain more primary olivine (11 - 27 vol%, Table 4.1), which influences the position of features, shifting them to shorter wavelengths. This results in features at longer wavelengths in the spectra of thermally altered samples with more secondary olivine, shown in Figure 5.11b. Additionally, TEM studies and XRD analysis shows that the secondary olivine is poorly crystalline (chapter 4, Nakamura, 2005), which appears to cause a 'smoothing out' of spectral features, particularly under SAE conditions. Poorly crystalline, or amorphous phases have been shown to have broader features with less spectral structure than seen in the spectra of more crystalline materials (e.g. Minitti and Hamilton, 2010).

PCA 02010 and B 7904 both contain primary Mg-rich olivine (~15 and ~25 vol%, respectively) and significant secondary olivine (~61 and ~50 vol%, respectively). Figure 5.11b shows that the positions of features between 18 - 38 µm can help constrain the abundance of the secondary olivine in these samples, as they show features at longer wavelengths than observed in samples with no secondary olivine. The presence of primary olivine can be confirmed by looking at other wavelength ranges, for example in the Si-O stretching region the B 7904 and PCA 02010 ambient spectra show features at 9.73 and 10.72 µm, and 9.85 and 10.66 µm, respectively. Combining observations across multiple wavelength ranges can therefore help identify the presence of both primary and secondary olivine.

Figure 5.11a also shows how the feature between 23 - 26 µm can be used to distinguish between aqueous and thermal alteration. Figure 5.12a shows the feature shifts to longer wavelengths with increasing heating stage. However, this shift to longer wavelengths is also

consistent with a lower degree of aqueous alteration: the Murchison spectra shows a feature similar to that observed in the stage II and stage IV spectra due to its higher olivine abundance compared to ALH 83100, ALH 83102 and LON 94101 (Table 4.1). In order to help distinguish between aqueous and thermal alteration, the Si-O bending feature can be combined with the position of the 3 µm feature (Figure 5.12b). This relationship only works for the unheated and dehydrated CM chondrites, as the CY chondrite features are influenced by the presence of only secondary olivine, shifting the features to even longer wavelengths, but not changing the position of the 3 µm feature. As in Figure 5.9b, the error for the Murchison 3 µm feature is increased to include determinations from previous studies.

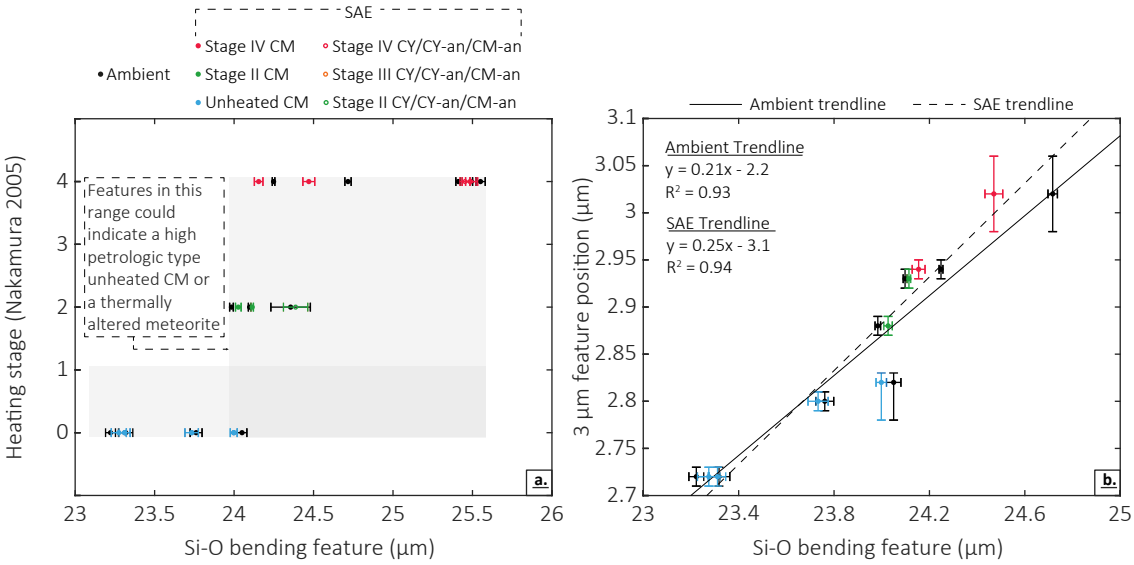


Figure 5.12: *(a) The position of the feature between 23 – 26 µm against heating stage, showing that with increasing thermal alteration, the feature shifts to longer wavelengths. No distinguishable feature in the Y 980115 spectra could be identified. (b) The relationship between the position of the feature between 23 – 26 µm from the emissivity spectra and the position of the 3 µm feature from reflectance spectra of the same material. The WIS 91600 emissivity spectra were not included due to the multiple features in the 3 µm region (Fig. 4.10, section 4.3.3). This relationship can help distinguish between the effects of aqueous and thermal alteration on the position of the Si-O bending feature.*

5.4.4 Spectral parameters in emissivity spectra for identifying aqueous and thermal alteration

The parameters and trends discussed in chapters 3 and 4 for reflectance spectra that can be used to evaluate aqueous and thermal alteration can largely be applied to both the SAE and ambient emissivity spectra in this chapter:

- The CF becomes sharper as aqueous alteration increases.
- The TF shows a shift to shorter wavelengths with increasing aqueous alteration.
- The TF is at longer wavelengths in thermal altered sample spectra, and additionally correlates with the position of the 3 μm feature.
- Features between 5- 8 μm can distinguish between stage III and stage IV CY spectra, with features due to carbonates disappearing as they dehydrate at high temperatures.

The comparison implies that bidirectional reflectance is a good approximation for emissivity. However, some trends identified in chapters 3 and 4 are not present in the emissivity spectra. The CF shifts to longer wavelengths with increasing aqueous alteration, which is inconsistent with the results of chapter 3. The position of the first Si-O bending feature is shifted from what was observed in reflectance spectra, therefore the trend of it moving to shorter wavelengths with increasing thermal alteration also does not apply to the emissivity spectra.

The emissivity spectra do show some additional trends, however. The Si-O bending region appears to be sensitive to both aqueous alteration and secondary olivine abundance. Most features shift to longer wavelengths with increasing proportion of secondary olivine (Fig. 5.11b), as more Fe in olivine results in features at longer wavelengths. The diagnostic

feature between 23 - 26 μm shifts to shorter wavelengths with increasing aqueous alteration (Fig. 5.9b), but also correlates with increasing thermal alteration (Fig. 5.12a). This feature therefore correlates well with the 3 μm feature and can be used to distinguish between aqueous and thermal alteration in CM chondrites (Fig. 5.12b).

5.5 Conclusions

In this chapter, the emissivity spectra of 12 aqueously and thermally altered CM, CM-an and CY chondrites were presented. The emissivity spectra were collected on the same material for which reflectance spectra were acquired. I showed differences between the two measurement types, supporting the conclusion that bidirectional reflectance cannot be quantitatively compared to emissivity data. I do find, however, that emissivity spectra show similar trends to those observed in reflectance spectra. These include the position of the TF, which can be used to estimate both aqueous and thermal alteration, the presence of features between 5 - 8 μm, and the spectral signature of the CF. The emissivity spectra also indicate the Si-O bending region is sensitive to mineralogy and can be used to further constrain degrees of aqueous and thermal alteration.

By identifying trends in meteorite spectra, I can now apply them to remote data in order to evaluate the mineralogy and processing that occurs on the surfaces of small Solar System bodies. In the following chapter I will compare some of the meteorite spectra presented in chapters 3 - 5 to telescopic and spacecraft data from a number of asteroids. If the trends can help identify the mineralogy and alteration on these bodies, conclusions can begin to be made about the processes that have acted to modify their surfaces (objective C, chapter 1).

Chapter 6: Comparing laboratory data to remote observations

6.1 Introduction

The aim of this chapter is to showcase how the spectra of aqueously and thermally altered CI, CM, CY and CM/CY-anomalous chondrites can be used to interpret remote data from small Solar System bodies (objective C, chapter 1). The C-complex asteroids have generally been linked to aqueously altered carbonaceous chondrites based on features near 0.7 and 3 µm that are associated with hydrated minerals (chapter 1, Vilas et al., 1994, Hiroi et al., 1996, Rivkin et al., 2005, Rivkin and Emery, 2010, Takir and Emery, 2012, Takir et al., 2015). There is additional evidence that the surfaces of some C-complex asteroids experienced thermal alteration (chapter 1, Hiroi et al., 1993, 1996, Clark et al., 2010, Takir et al., 2020). The previous chapters have shown that the MIR spectral range is valuable, when combined with observations in the NIR, for determining degrees of both aqueous and thermal alteration. Observing asteroids in the MIR range should help further constrain their composition and processing histories.

In sections 6.2 and 6.3 the spectra collected in this study are used to understand and evaluate data from the OSIRIS-REx and Hayabusa2 sample return missions, and how they might determine the presence of fine particulate material or certain compositions on the surfaces of the target asteroids. Section 6.4 compares the spectra of aqueously altered CI and CM chondrites with the NIR spectra of Ceres collected by NASA's Dawn mission. Section 6.5 highlights an intriguing similarity between the emissivity spectra of the Jupiter

Trojan asteroids and the CY chondrites and discusses the implications for the processing histories of the Trojans and the dynamical evolution of the Solar System. Finally, section 6.6 showcases a larger study applying some of the trends determined in previous chapters to a population of outer main belt asteroids.

6.2 Bennu

NASA's OSIRIS-REx mission is currently in orbit around the B-type asteroid 101955 Bennu and aims to return samples in 2023 following successful sampling of the asteroid surface in October 2020 (chapter 1, Lauretta et al., 2017). The spacecraft has two spectrometers on board for characterizing Bennu's surface composition: the OSIRIS-REx Visible and InfraRed Spectrometer (OVIRS), covering the 0.4 - 4.3 µm spectral range (Reuter et al., 2018), and the OSIRIS-REx Thermal Emission Spectrometer (OTES), which covers the 5.7 - 50 µm range (Christensen et al., 2018). During the approach phase of the mission disk-resolved observations showed there are hydrated Mg-rich phyllosilicate minerals on the surface of Bennu, based on the presence of an absorption feature at 2.74 µm in spectra collected by OVIRS (Hamilton et al., 2019). This is similar to the 3 µm features observed in CM1/2 and CM1 chondrite spectra (chapter 3, Takir et al., 2013). The OTES spectra collected from the approach phase of the OSIRIS-REx mission also showed some similarity with CM1/2 and CM1 chondrite spectra, with a CF near 9.00 µm and a Si-O bending feature near 22.70 µm (Hamilton et al., 2019). The positions of these features are consistent with the CF and Si-O bending features observed in the emissivity spectra of the ALH 83100, ALH 83102 and LON 94101 spectra in chapter 5. The meteorite emissivity spectra were collected under SAE conditions that were designed specifically to mimic the temperatures and thermal gradients on the surface of Bennu (chapter 2), which further reinforces the similarity between the surface of Bennu and the aqueously altered CM spectra.

The MIR spectral range is sensitive to particle size, and some spectral parameters will only be applicable to fine particulate material. For example, the TF is only distinguishable in optically thin material, or a fine particulate size (<75 μm, Salibsury 1993). Whether the surface of an asteroid is covered with a fine particulate regolith can be estimated by values of thermal inertia <~100 $Js^{-1}/2K^{-1}m^{-2}$ (Delbo and Tanga, 2009, Gundlach and Blum, 2013). The meteorite spectra from chapters 3, 4 and 5 will therefore only be comparable to regions of the surface of Bennu spectrally dominated by fines.

On approach, OSIRIS-REx discovered the global average thermal inertia of Bennu to be 350 ± 20 $Js^{-1}/2K^{-1}m^{-2}$, which suggests a surface dominated by 0.5 - 5 cm particles. However, in contrast to this thermal inertia, the pre-encounter radar characteristics, which predicted a loose particulate regolith on the Bennu surface (Nolan et al., 2013), and observations of other small bodies visited by spacecraft (e.g. Miyamoto et al., 2007), resolved images of Bennu showed a surface dominated by boulders >1 m, with more than 200 boulders >10 m in size (DellaGiustina et al., 2019). Additionally, OTES spectra from the approach phase showed more spectral similarity to whole rock meteorite observations; for example, there is no obvious TF and the spectral slope between 6.6 - 9.0 μm is relatively shallow (Hamilton et al., 2019). Despite this, the spectra did show a widening of the Si-O stretching feature which was deemed evidence for some amount of fines. Additionally, there are boulders that appear to be covered in a low-albedo dust (DellaGiustina et al., 2019), and some areas within craters that show evidence of fine particulates (Lauretta et al., 2019a, Walsh et al., 2019). Thus, we should expect some variation in the spectra collected in the upcoming phases of the mission, depending on whether the area of the surface observed has a fine particulate regolith, fine particulate coating, or is dominated by coarser particles and boulders.

Figures 6.1a and 6.1b show the emissivity spectra of fine-particulate ALH 83100 and WIS 91600 from chapter 5, collected under Bennu-like conditions. Also included are average reflectance spectra collected from thin sections of the same meteorites (although not the same samples) by Lindgren et al. (2020) and Hanna et al. (2020), respectively. Spectra from thin sections, which behave similarly to coarse-particulates, do not show the effects of volume scattering (such as transparency features); therefore, the figures show the range of spectral behaviour that could be observed on the surface of Bennu in areas dominated by fine and coarse particulates. The thin section spectra also show slight differences in the position of the CF in comparison to the fine-particulate spectra, which has been observed previously when comparing coarse and fine particulate samples (Shirley and Glotch, 2019), although it may be also due to observations being made on different samples. ALH 83100 was chosen for comparison as it shows similar features to those observed in the Bennu OVIRS and OTES spectra, with a 3 µm feature at 2.72 µm in its NIR spectrum (chapter 3), and a CF at 9.17 µm in its SAE emissivity spectrum (chapter 5). I am also showing WIS 91600, which has a higher magnetite abundance (~9 vol%) than most CM chondrites, but with the OTES spectra of Bennu showing features near 18.00 and 29.40 µm consistent with magnetite (Christensen et al., 2000), comparing the two might give an indication of the abundance of magnetite on the Bennu surface. The WIS 91600 emissivity spectrum collected under SAE does not have a magnetite feature distinguishable near 18 µm (chapter 5), which implies that if the Bennu surface does contain magnetite it likely has an abundance of >10 vol%.

Following the phases of the mission where the spacecraft moves closer to the asteroid, the spectra presented in this project (particularly those collected under Bennu-like conditions in chapter 5) should provide useful comparisons with OTES spectra in order to better

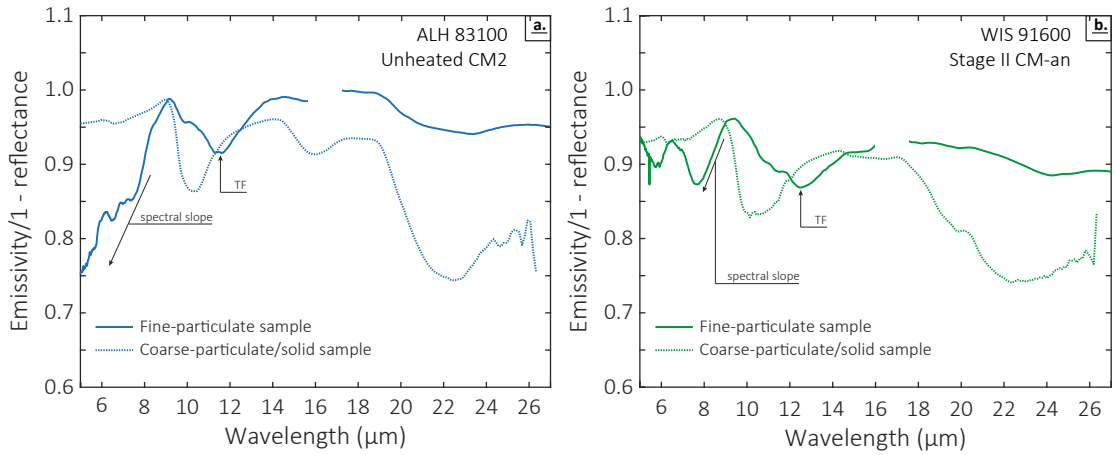


Figure 6.1: *The spectra of (a) ALH 83100 and (b) WIS 91600 collected for fine-particulate samples and coarse-particulate/solid samples. Fine-particulate sample emissivity spectra were collected under SAE conditions (see chapter 5) and have been scaled by a factor of 3 and offset to aid comparison. Coarse-particulate sample reflectance spectra from Lindgren et al. (2020) (ALH 83100) and Hanna et al. (2020) (WIS 91600) were collected using a Thermo Scientific iN10 FTIR microscope and approximated as emissivity using Kirchoff's law. The spectral slope and TF identified on the figures are areas where the spectra are affected by transparency and volume scattering effects in the fine-particulate sample spectra.*

understand the mineralogy and therefore alteration history of the surface material. Furthermore, the spectra will help identify regions where the surface may be dominated by fine particulate material. Fine particulate material is expected to have been produced on Bennu from boulder fracturing (Molaro et al., 2020), impact events (Ballouz et al., 2020) and erosion during movement of material (Walsh et al., 2019), and the lack of a widespread regolith suggests some mechanism by which this fine particulate material is lost. Mapping the presence of regolith on the surface will help understand how and why this occurs and will help model surface processes active on small asteroids.

6.2.1 3200 Phaethon

The asteroid 3200 Phaethon has the same classification as Bennu, B-type, and shows a similar spectral slope in the VNIR between 0.5 - 2.5 µm. Both are active asteroids, with multiple ejection events having been observed at Bennu (Lauretta et al., 2019b), and Phaethon is

thought to be the source of the Geminid meteor shower (Jewitt and Li, 2010, Jewitt et al., 2013). However, despite showing similarity at wavelengths less than 2.5 µm, at higher wavelengths there are differences in the spectra of the two bodies, emphasising the need to use multiple wavelengths when observing and classifying asteroids. Phaethon shows a featureless spectrum across the 2.5 - 4 µm range, suggesting an absence of hydrated minerals (Takir et al., 2020). Based on its similar spectral slope in the NIR to Bennu and other B-type asteroids, Phaethon is believed to have once been a volatile-rich asteroid that became dehydrated as it reached perihelion at 0.14 AU from the Sun (Hanuš et al., 2016). However, the timing of the dehydration remains unknown and is not the driver of the current asteroid activity (Jewitt et al., 2013, Takir et al., 2020). Alternatively, Phaethon was never hydrated, which would imply a different formation and evolution from Bennu, despite showing similar NIR spectral slopes (Takir et al., 2020).

In 2022, JAXA's Destiny+ (Demonstration and Experiment of Space Technology for Interplanetary voYage, Phaethon fLyby and dUst Science) will perform a high-speed flyby of asteroid Phaethon, collecting data that may reveal the alteration history of the surface materials and establish the relationship between Phaethon and other small bodies such as Bennu. The results of chapters 4 and 5 will help constrain the processes that may have acted on Phaethon earlier in its evolution.

6.3 Ryugu

JAXA's Hayabusa2 mission sampled the surface of the Cg-type asteroid 162173 Ryugu and returned this sample to Earth on the 6th December 2020 (Morota et al., 2020). The spacecraft has on board the Optical Navigation Camera Telescope (ONC-T), which has seven filters covering the visible spectral range (0.3 - 1.0 µm) (Kameda et al., 2017), the Near Infrared Spectrometer (NIRS3) covering the 1.8 - 3.2 µm spectral range (Iwata et al., 2017), and it

also carried the Mobile Asteroid Scout (MASCOT) Radiometer (MARA), which has a series of channels covering some of the MIR spectral range (5 - 15.5 µm) (Grott et al., 2019). Thermal inertia values of Ryugu determined from Hayabusa2 observations and in situ data collected by the MASCOT rover were determined to be 225 - 282 $Js^{-1}/2K^{-1}m^{-2}$ (Grott et al., 2019, Shimaki et al., 2020), values which suggested the presence of a fine-grained regolith (Gundlach and Blum, 2013). However, as with Bennu, images of Ryugu showed a surface covered in boulders with some as large as > 20m (Sugita et al., 2019). Nevertheless, images did show some abundance of fine-grained material, with some regolith covered boulders, and evidence for movement of regolith within crater walls and around the equatorial ridge (Sugita et al., 2019). ONC-T and NIRS3 spectra collected across the surface of Ryugu show a flat, featureless spectral slope in the NIR range <2.5 µm, and a shallow, narrow absorption at 2.72 µm consistent with the presence of Mg-rich phyllosilicates. The albedo of the surface of Ryugu is very low (4.5 ± 0.2 %, Kitazato et al., 2019), lower than most laboratory measurements of carbonaceous chondrites, apart from some measurements of CY chondrites (King et al., 2017a). Additionally, the shallow depth of the 2.72 µm feature best matches the spectra of experimentally heated (to 500 ^{o}C) Ivuna and MET 01072, a shocked CM2 (Kitazato et al., 2019). It has therefore been suggested that the surface of Ryugu has experienced some degree of dehydration (Sugita et al., 2019, Michel et al., 2020).

The 3 µm feature of Ryugu's surface can be compared to the 3 µm feature of dehydrated CM and CY chondrites in chapter 4 in order to evaluate whether the asteroid has a similar composition to these meteorites. The NIR spectra showing the 3 µm feature of the dehydrated CM and CY chondrites are shown in Figures 4.7 and 4.8. None show a feature near 2.72 µm, instead having broad features with centres between 2.88 - 3.04 µm that I suggest result from the dehydration and amorphization of the phyllosilicate structure and are not

due to terrestrial contamination (section 4.4.4). The lack of this feature in even the moderately heated stage II samples suggests these thermally altered CM and CY chondrites may not be a good representation of the globally averaged surface composition of Ryugu, or at least that the heating these meteorites experienced may not be an adequate representation of the metamorphism on Ryugu. The NIR spectra of WIS 91600, A 881655 (Fig. 4.9) and experimentally heated Ivuna (Hiroi and Pieters, 1996) all show a subtle 2.72 µm feature that is similar to the one observed in the Ryugu spectra. The link between these three samples is the presence of Mg-rich smectite-like phyllosilicates that have been partially dehydrated by thermal metamorphism (chapter 4, Lipschutz et al., 1999, Tonui et al., 2014). As the surface of Ryugu is heated but its spectrum still shows a 2.72 µm feature, this could imply a similar composition of dehydrated Mg-rich smectite phyllosilicates as observed in A 881655 and WIS 91600. Smectites are a result of high water/rock ratios during aqueous alteration on asteroid parent bodies (Bourcier and Zolensky, 1992). Smectites were formed on the CI parent body, which may have had a high initial ice content and therefore high water/rock ratio as a result of its formation in the outer Solar System (> 15 AU based on refractory element and CAI abundances, Desch et al., 2018), and smectites must also have been present on the parent body of WIS 91600, which is also hypothesised to have an outer Solar System origin (~10 AU) based on its magnetic properties (Bryson et al., 2020). If there is a similar composition of phyllosilicates on Ryugu, this could be a result of high water/rock ratios in the outer Solar System during its parent body formation, and the dehydration could have been caused by the collisional event that led to its present-day rubble structure (Michel et al., 2020) or solar radiation during closer orbits of the Sun.

The MARA instrument operated as part of the MASCOT rover on the surface of Ryugu, and so its observations are likely of specific lithologies in the area where the MASCOT rover

landed; thus are not necessarily representative of the average Ryugu composition. The primary aim of MASCOT was to evaluate the temperature of surface; however, it did have four wide-band channels (5.0 - 7.0 µm, 8.0 - 9.5 µm, 9.5 - 11.5 µm and 13.5 - 15.5 µm) covering the MIR wavelength range. These filters had transmissions of 80 %, 65 %, 60 % and 50 %, respectively (Grott et al., 2017). The spectra presented in chapter 5 can be re-sampled to these channels by multiplying the calibrated emissivity by the transmission of each filter, and then averaging the emissivity across the wavelength range of each filter. These laboratory spectra are especially valuable as they were collected under SAE conditions, and although these were selected based on Bennu, the temperatures and resulting thermal gradients are expected to be similar on Ryugu (Wada et al., 2018). As previously discussed, the spectral measurements of meteorites are only applicable to areas on the surface of Ryugu dominated by fines. Images of Ryugu appear to show a proportion of the surface covered in a fine-particulate regolith (Sugita et al., 2019), and with MASCOT being in contact with the surface, ideally MARA can observe areas dominated by this regolith.

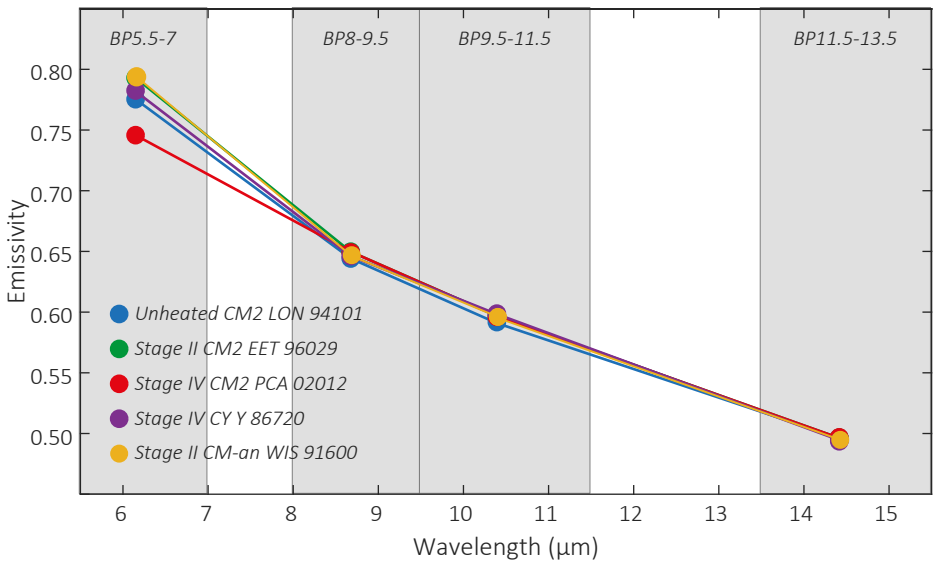


Figure 6.2: *The SAE emissivity spectra of the unheated CM2 LON 94101, the stage II CM2 EET 96029, the stage IV CM2 PCA 02012, the stage IV CY Y 86720 and the stage II CM-an WIS 91600. Spectra have been re-sampled using the MARA filter parameters, in order to evaluate what different surface compositions on Ryugu would look like when observed with the MARA instrument.*

Figure 6.2 shows the emissivity spectra collected under SAE conditions of LON 94101, EET 96029, PCA 02012, Y 86720 and WIS 91600, re-sampled to the MARA filters. There is little difference between the spectra of the meteorites, and it is not possible to uniquely determine whether WIS 91600 is a better match for Ryugu from MARA data, as suggested by its 2.72 µm feature. This is due to the spectral range covered by the filters, so when re-sampling, unique spectral features are averaged out. However, in the first filter the spectrum of PCA 02012, a stage IV CM2, shows a lower emissivity than the other CM and CY meteorites. Based on the radiometric performance given in Grott et al. (2013), MARA observations should be capable of discriminating this difference in emissivity. As discussed in chapter 5, the spectrally dominant mineralogy in PCA 02012 is primary Mg-rich olivine, and this implies MARA should be able to identify regions dominated by Mg-rich olivine, which will help in mapping composition and processing in the area observed by MASCOT.

6.4 Ceres

The relationship between the dwarf planet 1 Ceres and other C-complex asteroids such as Bennu and Ryugu is not well understood. Ceres is classified as a C-type dwarf planet (DeMeo et al., 2009), is the most massive object in the asteroid belt (Pitjeva and Pitjev, 2015) and is thought to be differentiated with an icy core (Castillo-Rogez and McCord, 2010). Early ground based telescopic observations of Ceres suggested the surface may be composed of carbonaceous chondrite-like material (Larson et al., 1979, Lebofsky et al., 1981), and later water vapour was identified outgassing from areas on the surface (Küppers et al., 2014). NASA's Dawn mission characterised the physical and compositional properties of both Ceres and asteroid 4 Vesta, and had on board the VIR imaging spectrometer, capable of observing the surfaces of these bodies between 0.25 and 5.1 µm (De Sanctis et al., 2012).

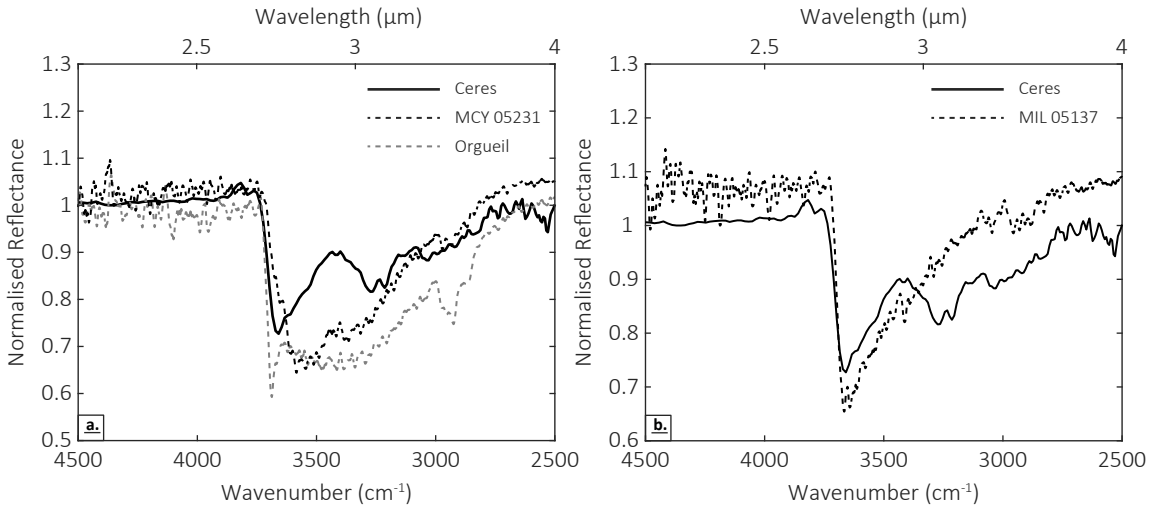


Figure 6.3: *The 3 μm feature of 1 Ceres compared to the spectra of (a) the CM2 MCY 05231 and the CI1 Orgueil, and (b) the CM1 MIL 05137. The Ceres spectrum is from De Sanctis et al. (2018). All spectra are continuum removed and normalised to unity at 2.3 μm. This figure was published in Bates et al. (2020).*

Figure 6.3 shows the average spectrum of Ceres between 1.0 - 4.3 μm, collected by the VIR instrument (De Sanctis et al., 2015, 2018). There is a broad asymmetric feature observed between 2.6 - 4.2 μm, with a number of distinct absorption features at 2.72 μm, 3.05 - 3.10 μm, 3.3 - 3.5 μm and 3.95 μm. De Sanctis et al. (2018) attributed these to -OH, NH^{4+}, organics and CO^{3-}, respectively. The spectrum in Figure 6.3 is a global average, but the spectral features described are present in all individual spectra collected across the surface of Ceres (De Sanctis et al., 2018). Additionally, in some visibly brighter areas of Ceres' surface the 2.72 μm feature is at longer wavelengths, closer to 2.78 μm (De Sanctis et al., 2018).

To date, Ceres has mainly been compared to the spectra of CM2 and CI1 chondrites (McSween et al., 2017, De Sanctis et al., 2018). Figure 6.3a compares the spectra of Ceres with the CM2 MCY 05231 and the CI1 Orgueil, and Figure 6.3b compares the 3 μm feature of Ceres with the most altered CM1 chondrite in this project MIL 05137. The Ceres spectrum shows a feature near 2.72 μm, consistent with Mg-OH in phyllosilicates, that is

best matched by the feature in the MIL 05137 spectrum. This suggests that the surface of Ceres consists of highly altered CM1-like materials, in agreement with the conclusions of McSween et al. (2017). In areas where this feature is at longer wavelengths, closer to 2.78 µm, this is more consistent with features due to Fe-OH in Fe-rich phyllosilicates (chapter 3) and Al-OH in Al-rich phyllosilicates (De Sanctis et al., 2016). Areas with spectral features at longer wavelengths therefore probably contain materials that experienced less aqueous alteration. One of the regions where this occurs is in the bright material found in the centres of several craters, where Na-carbonates are also prevalent (De Sanctis et al., 2016, Palomba et al., 2017, Carrozzo et al., 2018), suggesting there is a lower degree of aqueous alteration in these spots. However, this anti-correlation between carbonate presence and degree of aqueous alteration is not understood.

The feature at 3.07 µm in the Ceres spectrum has been hypothesised to be caused by ammoniated phyllosilicates (De Sanctis et al., 2015). Ammoniated phyllosilicates have also been suggested as the cause of 3.05 µm features in the spectra of the C-type asteroid 10 Hygiea and the CP-type 324 Bamberga (Takir and Emery, 2012) implying this mineralogy is not unique to Ceres. This feature is not observed in any of the meteorite spectra in chapters 3 or 4, but due to the volatile nature of ammonia this does not indicate that ammoniated phyllosilicates were never present in the meteorites prior to them arriving on Earth. In fact, ammonia-bearing organic compounds have been identified in the CI and CM chondrites (Pizzarello and Williams, 2012).

The presence of ammoniated phyllosilicates on Ceres has been attributed to a formation scenario for Ceres whereby it accreted significant amounts of ammonia ice (De Sanctis et al., 2018). This could have occurred in the proto-Kuiper belt (McKinnon, 2012), a model supported by the identification of ammonia ice on Kuiper belt objects (DeMeo et al., 2015b).

However, Figure 6.3b suggests some similar mineralogy between it and highly aqueously altered CM chondrites, and therefore some similar alteration histories between Ceres and the CM parent body. If this is the case, Ceres may have formed near the CM parent bodies at a smaller heliocentric distance (~3.76 AU, Desch et al., 2018). Ammonia bearing species from the outer Solar System could have been delivered to this CM/Ceres forming region (Mousis and Alibert, 2005), or ammonia ice could have been directly accreted as its snow-line has been shown to move inwards to ~2.7 AU 10,000 years after CAI formation (Dodson-Robinson et al., 2009). Ammonia bearing organics could then form through aqueous alteration on the CM parent body (Brearley 2006), and hydrothermal circulation on Ceres could form ammoniated phyllosilicates (Pizzarello and Williams, 2012, McSween et al., 2017).

At wavelengths longer than 5 μm, the similarity between Ceres and the highly altered CM1 chondrites is less robust. Vernazza et al. (2017) observed Ceres between 5 - 12 μm using the Stratospheric Observatory for Infrared Astronomy (SOFIA) and the Infrared Space Observatory (ISO) using the Faint Object infraRed Camera for the SOFIA Telescope (FORCAST), and identified emissivity features near 7, 10 (which has two peaks at 9.80 and 10.65 μm) and 22 μm. This is consistent with previous measurements of Ceres using the NASA Ames High-efficiency Infrared Faint-Object Grating Spectrograph (HIFOGS) spectrometer on the Kuiper Airborne Observatory (Cohen et al., 1998). The feature near 7 μm in the MIR Ceres spectrum has been attributed to carbonates or ammoniated phyllosilicates (Milliken and Rivkin, 2009, Vernazza et al., 2017). Mg or Mg-Ca carbonates (eg. Magnesite, dolomite) and Na-carbonates (natrite) are widespread on the surface of Ceres (Carrozzo et al., 2018). Features near 7 μm are identified in the reflectance and emissivity MIR spectra of the highly aqueously altered CI1, CM1 and CM1/2 spectra (chapters 3 and 5), however these do not match the spectral shape of the feature in the Ceres spectrum. Neither the reflectance or emissivity spectra of the highly aqueously altered CM chondrite replicate the features in

the CF region of the Ceres MIR spectrum near 9.80 and 10.65 µm. The spectral signature in this region can be reproduced by linear mixtures of the hydroxide brucite, magnesite, cronstedtite and magnetite (Milliken and Rivkin, 2009), a mineral combination that is not observed in any known meteorite.

The differences between the spectrum of Ceres and the aqueously altered CM1 and CM1/2 spectra across multiple wavelengths implies that these meteorites may only be a partial spectral match to Ceres and highlights the importance of using multiple wavelength ranges when interpreting the evolution of these bodies. There is also a clear difference between the 3 µm feature observed in the Ceres spectrum and the 3 µm features observed in other C-complex asteroids, including Ryugu and Bennu (Takir and Emery, 2012, Hamilton et al., 2019, Kitazato et al., 2019). This indicates that the mineralogy on the surface of Ceres, although not unique due to the presence of the 3.05 µm feature in the 10 Hygeia and 324 Bamberga spectra, is not common. The shared Mg-OH feature near 2.72 µm in the NIR spectra of Ryugu, Bennu, Ceres and of the CM1 and CM1/2 chondrites indicates the presence of Mg-rich phyllosilicates. However, the presence of this mineralogy does not imply that Ceres experienced a similar alteration history to these other bodies and to the CM parent body. The different evolution of Ceres is clear due to the presence of ammoniated phyllosilicates identified in the NIR spectra, but also due to the high abundance of carbonates in bright zones indicative of a potential subsurface cryosphere (Carrozzo et al., 2018) and the likely differentiation of the dwarf planet (Ermakov et al., 2017). The Mg-rich phyllosilicates are consistent however with a high degree of aqueous alteration on the surface of Ceres.

6.5 Jupiter Trojans

In addition to interpreting spectral observations of single objects, the spectra in this project can also be used to infer the mineralogy of specific asteroid populations. One example is

the Jupiter Trojans; currently trapped in stable Lagrange points in Jupiter's orbit, they offer an insight into the events and processes occurring in the outer Solar System early in its evolution. However, the initial formation locations, compositions and structures of the Trojan asteroids are not well constrained. Are they Kuiper belt objects that were brought forward during a period of orbital migration or did they form in the vicinity of Jupiter? The MIR spectra of Jupiter Trojans show some similarity to the spectra of comet comae, including the presence of broad 10 μm 'plateaus', and features near 15, 19 and 23 μm, suggesting similar physical and/or mineralogical characteristics (Crovisier et al., 1997, Stansberry et al., 2004, Emery et al., 2006, Mueller et al., 2010). Due to the similarity between the asteroid and comet comae spectra, it has been proposed that the 10 μm feature is evidence that the surfaces of the Trojans have physical properties that resemble coma-like emission (Emery et al., 2006). These explanations include fine-particulate silicates in an under-dense ('fairy-castle') structure, embedded within a MIR transparent matrix (Emery et al., 2006), or suspended in salts that were deposited as briny fluids evaporated after being exposed at the surface by impacts (Yang et al., 2013). Vernazza et al. (2012) suggested that the surface porosity could be as high as >90%, although the mechanism for producing this porosity structure remains unknown.

Spectra presented by Kelley et al. (2017) showed that comet nuclei also have similar 10 μm plateaus, implying that coma-like structures may not be required to explain this spectral feature. Efforts to find appropriate compositional analogues from meteorite collections and physical mixtures of mineral separates that can explain the features seen in the MIR spectra of the Trojans and comet nuclei have been limited. Previously, the meteorites that provided the best spectral match to the Trojan's 10 μm plateaus were the anhydrous CO and CV carbonaceous chondrites (Emery et al., 2006, Vernazza et al., 2012), although the plateau feature is not satisfactorily reproduced by these samples (Emery et al., 2006). However,

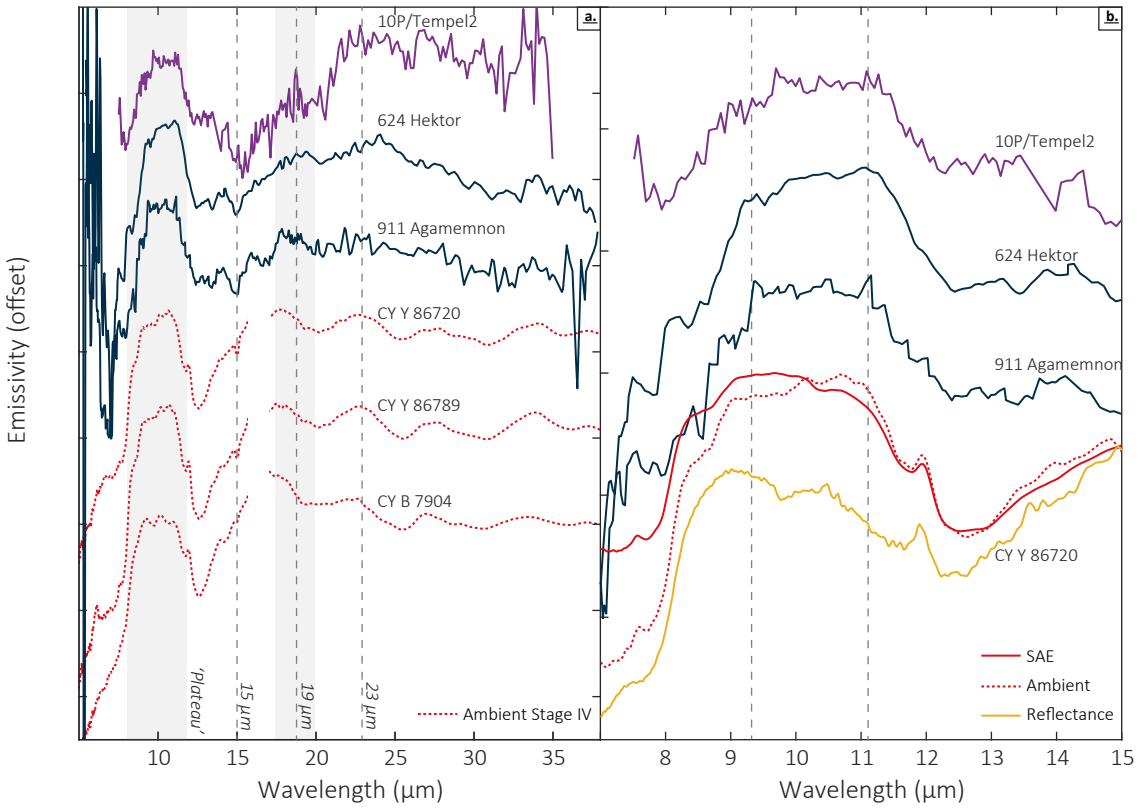


Figure 6.4: *Remote emissivity spectra of comet 10P/Tempel2 (Kelley et al., 2017) and Jupiter Trojan asteroids 624 Hektor and 911 Agamemnon (Emery et al., 2006) compared to emissivity and reflectance spectra of stage IV CY chondrites. Meteorite spectra have been scaled by a factor of 5 to aid comparison. Common features of interest are labelled in (a) and the beginning and end of the plateau feature in 624 Hektor are labelled in (b).*

Vernazza et al. (2015) did find a good match between the MIR spectra of D-type asteroids (which make up ~70% of the taxa of Trojans Bendjoya et al., 2004) and individual olivine- and pyroxene-rich interplanetary dust particles (IDPs), further supporting the idea that the 10 μm plateau could be a compositional effect.

Chapter 5 presented emissivity spectra of stage IV CY chondrites that show features closely resembling the 10 μm plateau observed in the Trojan and comet nuclei spectra. Figure 6.4a shows the ambient spectra of these CYs with the emissivity spectra of the Jupiter Trojan asteroids 624 Hektor and 911 Agamemnon, and the nucleus of comet 10P/Tempel2. Figure 6.4b compares the emissivity (ambient and SAE) and reflectance spectra of Y 86720

with the same Trojan and comet spectra. In addition to the similar 10 µm plateaus, the CY ambient emissivity spectra show features near 15, 19 and 23 µm that are consistent with features identified in the spectra of Trojans and comet nuclei. The vibrational features that result in the emissivity peaks near 19 and 23 µm in stage IV CY chondrite spectra are due to the presence of secondary Fe-rich olivine (chapter 5). Slight differences in the position of these peaks in the remote spectra may result from variable olivine chemistry; for example, changing from a Mg- to an Fe-rich olivine composition causes a shift of features to longer wavelengths in the CM and CY emissivity spectra (chapter 5).

The change in shape of the CY chondrite plateau feature under SAE conditions results in a less convincing spectral match with the remote data, particularly as it starts at shorter wavelengths than any of the plateaus in the Trojan or comet nuclei spectra (Fig. 6.4b). However, as described in chapter 2, these SAE conditions were designed to mimic the near-surface environment of Bennu (Donaldson Hanna et al., 2019) and may not be representative of conditions on the surface of Trojan asteroids or comet nuclei. The reflectance spectrum of Y 86720 in Figure 6.4b also does not provide a satisfactory spectral match, showing a distinct Christiansen feature instead of the complex plateau feature. This difference in spectral shape between the emissivity and reflectance spectra emphasizes the importance of measuring samples under appropriate conditions (chapter 5, Donaldson Hanna et al., 2012a,b, 2019, Thomas et al., 2012).

The spectral similarity between the remote emissivity spectra and the CY chondrite spectra suggest that the surfaces of the Jupiter Trojan asteroids may contain abundant poorly crystalline Fe-rich olivine. Vernazza et al. (2015) reached a similar conclusion, proposing that the surfaces of many D-type asteroids could be covered by materials comparable to olivine- and pyroxene-rich IDPs. In general, IDPs are amongst the most pristine extraterrestrial samples having experienced minimal alteration (Bradley, 2014), whereas the CY chon-

drites suffered extensive hydration followed by thermal metamorphism at temperatures >750°C (King et al., 2019). The conclusions reached by the Vernazza et al. (2015) study were however based on comparisons between the Trojan spectra and transmission spectra of IDPs. As demonstrated in chapter 5, and also in Figure 6.4b, features can differ when measuring transmission, reflectance, emissivity and when measuring under SAE. In order to properly evaluate whether the IDPs are a better spectral match for the Trojans than the CYs, their emissivity spectra should be collected, although this will be challenging due to the mass constraints required to adequately replicate thermal gradients of airless bodies.

If the surfaces of the Trojans experienced both aqueous and thermal processing, this would constrain their history. Trojans could have formed in the vicinity of where they are currently located, consistent with them not spectrally matching Kuiper Belt Objects (Emery et al., 2015), and accreted water ice that resulted in aqueous alteration. Their surfaces could then have been dehydrated via impacts, with models predicting high collision rates in the Trojan population (Dell'oro et al., 1998), or possibly through radiation from the early Jupiter (Marley et al., 2007). Alternatively, Trojans could have accreted and been aqueously altered in the Kuiper Belt, before being scattered inwards to <2 AU resulting in dehydration from solar radiation (Morbidelli et al., 2005, 2015). During the inward journey, comet like activity may have occurred on their surfaces, potentially explaining the mismatch between the spectra of the Trojan surfaces and those of KBOs. However, if the silicates on the surface of the Trojans were minimally altered, to avoid aqueous alteration the bodies either did not accrete water ice, or accreted water ice that was not melted. The presence of minimally altered material might imply the Trojans formed in a drier, different part of the Solar System than suggested by the above explanations, which put them accreting beyond the snow-line.

Distinguishing between whether the silicates on the surfaces of the Trojans are minimally altered (IDP-like), or aqueously and thermally altered (CYs) is difficult from telescopic

MIR spectral observations alone. It is likely that the upcoming reconnaissance mission, Lucy, to six Jupiter Trojans (Levison, 2016) will help unravel their history. Lucy will have onboard the Lucy thermal emission spectrometer (L'TES), which may provide additional MIR spectra of the Trojan targets (although the L'TES focus will be on obtaining temperatures rather than spectra), as well as a panchromatic and colour visible imager (0.4 - 0.85 μm) and infrared spectrometer (1.0 - 3.6 μm), and a high-resolution telescope for imaging the surfaces of the target Trojans (Levison, 2016).

6.6 Main belt volatile-rich asteroids

The main asteroid belt is concentrated between Mars and Jupiter, and is separated into 'inner', 'middle' and 'outer' regions. These were carved out by the v6 secular resonance with Saturn near 2 AU, and the 3:1 and 5:2 mean-motion resonances with Jupiter near 2.5 and 2.8 AU, respectively (e.g. DeMeo et al., 2015a). As discussed in chapter 1, C-complex asteroids are associated with aqueously altered carbonaceous chondrites and so are likely hydrated. These bodies are found throughout the different regions of the main belt (Figure 1.3). There have been hypotheses that there is a relationship between degree of aqueous alteration and heliocentric distance, as asteroids beyond the snow-line which formed closer to the Sun accreted more ^{26}Al, which radioactively decayed and released heat, resulting in a higher degree of aqueous alteration (Grimm and Mcsween, 1989, Grimm and McSween, 1993, Jones et al., 1990). However, there is no correlation observed between either the presence of spectral features associated with hydration, or the strength of hydration features with heliocentric distance (Rivkin, 2002, Rivkin et al., 2003, Takir and Emery, 2012, Rivkin et al., 2015, Takir et al., 2015). The lack of correlation is hypothesised to be a result of mixing of planetesimals during the Grand Tack and Nice scenarios (Gomes et al., 2005, Walsh et al., 2012). There is a relationship observed between asteroid diameter and the

presence and strength of spectral features associated with hydration that has been proposed to result from increased hydrothermal circulation in larger bodies (Florczak et al., 1999, Takir and Emery, 2012). Notably, these conclusions were based on single spectral parameters assumed to be proxies for degree of alteration. In the previous chapters I have tied spectral parameters to specific compositions and shown that combining observations over multiple wavelengths is useful for further constraining mineralogy. In the following section I aim to demonstrate whether there is a correlation between mineralogy and properties, such as heliocentric distance and size, of water-rich asteroids in the main belt. This should help further constrain the mineralogy of the surfaces of hydrous asteroids, which has implications for their formation and the dynamical evolution of the asteroid belt.

Features near 3 μm associated with the presence of hydrated phases have been observed in the spectra of several main belt C-complex and X-complex asteroids (Lebofsky, 1980, Jones et al., 1990, Rivkin, 2002, Takir and Emery, 2012, Usui et al., 2018). As discussed in chapter 1, observing asteroids with ground-based telescopes in the NIR range is complicated as Earth's atmosphere masks the spectral flux received from a remote body between 2.5 - 2.85 μm. Chapters 3 and 4 demonstrated that spectra of aqueously altered CI and CMs show band minima in this region between 2.72 - 2.83 μm consistent with Mg- and Fe-rich phyllosilicates. The terrestrial atmosphere therefore makes it difficult to identify if there is a band minimum consistent with phyllosilicates present in the asteroid spectra. Despite this challenge, the spectral signature surrounding the range masked by the atmosphere can indicate whether the shape of the 3 μm feature in remote spectra is qualitatively similar to that observed in aqueously altered CI and CM spectra; for example Takir and Emery (2012) and Usui et al. (2018) identified 'sharp' features, Rivkin (2002) called the spectra 'checkmark shaped' and Rivkin et al. (2015) described the spectra as 'Pallas-shaped'. I use the terminology 'sharp' to describe this spectral shape for the rest of this section.

Rivkin et al. (2015) suggested asteroids with 'sharp' 3 µm features have similar H/Si ratios to CM chondrites (with H/Si ratio calculated from reflectance ratios at 2.9/2.5 µm and 3.2/2.5 µm). They also demonstrated that 'sharp' 3 µm features have similar band depths to 3 µm features observed in CM chondrites that had been gently heated prior to measurements in order to drive off adsorbed water (Takir et al., 2013). Takir et al. (2015) went further and proposed that 'sharp' 3 µm features are similar to the 3 µm features observed in the spectra of the most altered CM chondrites (types 2.2/2.1 in the Rubin scale). They therefore suggested that the asteroids showing sharp 3 µm features had surfaces which were CM-like and highly aqueously altered. Based on these conclusions, the spectral parameters determined in chapter 3 are useful for constraining the mineralogy of these asteroid surfaces.

Table 6.1 lists 19 asteroids that have been identified as having 3 µm band shapes that are 'sharp' (Takir and Emery, 2012, Rivkin et al., 2015, Takir et al., 2015). These asteroids were chosen as they had NIR data available that extended up to and including the 3 µm feature. All of the selected asteroids are C-complex, apart from 308 Polyxo, which is a T-type (other complex). The NIR spectra between 0.8 - 2.5 µm of these asteroids are available through the Small Main-belt Asteroid Spectroscopic Survey and MIT-Hawaii Near-Earth Object Spectroscopic Survey (SMASS-MITHNEOS Binzel et al., 2019) and the small body data ferret of NASA's Planetary Data System (PDS, Reddy and Sanchez, 2016). These data were collected by Reddy and Sanchez (2016) and Binzel et al. (2019) using the SpeX instrument at the NASA Infrared Telescope Facility. The spectral slope between 1.1 and 1.6 µm is given in Table 6.1, and this parameter can be directly compared to the equivalent spectral slope of the aqueously altered CM and CI chondrites from chapter 3. The slopes determined for the asteroids (1.03 - 1.26) fall within the same range of as those for the CM chondrites with PSF petrologic types 1.2 and 1.1 (0.96 - 1.28 excluding weathered samples), supporting the

Asteroid	Classification	Diameter (km)[d]	Heliocentric distance (AU)[d]	VNIR slope	Magnetite abundance from VNIR slope (vol%)	Phyllosilicate abundance from VNIR slope (vol%)	3 μm band area (μm^{-1})	Magnetite abundance from 3 μm feature area (vol%)	Fe-cronstedtite abundance from 3 μm feature area (vol%)	Mg/Fe phyllosilicate ratio from VNIR	TF (μm)[k]	Phyllosilicate abundance from TF (vol%)	Mg/Fe phyllosilicate ratio from TF
13 Egeria	G[a], Ch[b], Ch[c]	202.636	2.58	1.07 ± 0.01[e]	3 ± 1	94 ± 1	0.11 ± 0.01[h]	2 ± 1	26 ± 1	2.57	-	-	-
19 Fortuna	G[a], Ch[b], Ch[c]	200	2.44	1.17 ± 0.01[e]	3 ± 1	86 ± 1	0.06 ± 0.01[i]	3 ± 1	16 ± 1	4.32	-	-	-
34 Circe	C[a], Ch[b], Ch[c]	132.992	2.69	1.05 ± 0.01[e]	3 ± 1	96 ± 1	0.09 ± 0.03[h]	2 ± 1	22 ± 1	3.33	-	-	-
36 Atalante	C[a]	132.842	2.75	1.13 ± 0.01[e]	3 ± 1	89 ± 2	0.08 ± 0.03[j]	3 ± 1	20 ± 1	3.47	-	-	-
41 Daphne	C[a], Ch[b], Ch[c]	205.495	2.76	1.03 ± 0.01[e]	3 ± 1	98 ± 1	0.09 ± 0.05[h]	3 ± 1	22 ± 1	3.52	-	-	-
48 Doris	CG[a], Ch[b], Ch[c]	216.473	3.11	1.03 ± 0.01[e]	3 ± 1	98 ± 1	0.11 ± 0.02[h]	2 ± 1	27 ± 1	2.60	-	-	-
51 Nemausa	CU[a], Ch[b], Cgh[c]	138.159	2.36	1.26 ± 0.02[f]	2 ± 1	78 ± 2	0.17 ± 0.01[i]	1 ± 1	39 ± 1	1.03	-	-	-
54 Alexandra	C[a], C[b], Cgh[c]	160.12	2.71	1.08 ± 0.01[e]	3 ± 1	93 ± 2	0.04 ± 0.04[j]	3 ± 1	12 ± 1	7.04	-	-	-
78 Diana	C[a], Ch[b], Ch[c]	120.6	2.62	1.07 ± 0.01[e]	3 ± 1	94 ± 1	0.07 ± 0.01[i]	3 ± 1	18 ± 1	4.32	-	-	-
105 Artemis	C[a], Ch[b], Ch[c]	94.864	2.37	1.09 ± 0.01[e]	3 ± 1	93 ± 2	0.06 ± 0.01[i]	3 ± 1	17 ± 1	4.59	-	-	-
121 Hermione	C[a], Ch[b]	209	3.46	1.12 ± 0.01[e]	3 ± 1	90 ± 2	0.11 ± 0.01[j]	2 ± 1	26 ± 1	2.43	12.10 ± 0.02	78 ± 1	2.18
130 Elektra	G[a], Ch[b], Ch[c]	180.652	3.13	1.17 ± 0.01[g]	3 ± 1	86 ± 1	0.11 ± 0.05[h]	2 ± 1	26 ± 1	2.25	11.92 ± 0.04	80 ± 1	2.58
308 Polyxo	T[a], T[b], T[c]	128.578	2.75	1.14 ± 0.02[e]	3 ± 1	88 ± 2	0.08 ± 0.02[j]	3 ± 1	20 ± 1	3.42	-	-	-
334 Chicago	C[a]	158.5	3.89	1.08 ± 0.02[e]	3 ± 1	93 ± 3	0.07 ± 0.03[j]	3 ± 1	18 ± 1	4.22	-	-	-
345 Tercidina	C[a], Ch[b], Ch[c]	90.243	2.32	1.11 ± 0.01[e]	3 ± 1	91 ± 1	0.08 ± 0.01[i]	3 ± 1	19 ± 1	3.75	-	-	-
511 Davida	C[a], C[b]	270.327	3.16	1.06 ± 0.01[g]	3 ± 1	95 ± 1	0.07 ± 0.02[j]	3 ± 1	18 ± 1	4.31	-	-	-
554 Peraga	FC[a], Ch[b]	95.87	2.38	1.04 ± 0.01[f]	3 ± 1	97 ± 1	0.06 ± 0.01[i]	3 ± 1	16 ± 1	4.88	-	-	-
704 Interamnia	F[a], B[b]	306.313	3.06	1.12 ± 0.01[f]	3 ± 1	90 ± 2	0.05 ± 0.03[j]	3 ± 1	14 ± 1	5.57	-	-	-
776 Berbericia	C[a], Cgh[b], Cgh[c]	151.711	2.93	1.05 ± 0.01[e]	3 ± 1	96 ± 1	0.12 ± 0.01[i]	2 ± 1	27 ± 1	2.51	-	-	-

Table 6.1: *NIR and MIR parameters calculated for 19 asteroids which are hypothesised to have experienced aqueous alteration.* [a]*Tholen 1984,* [b]*Bus and Binzel 2002,* [c]*DeMeo et al. 2009,* [d]*http://ssd.jpl.nasa.gov/sbdb.cgi,* [e]*SMASS-MIT-Hawaii Near-Earth Object Spectroscopic Survey,* [f]*Reddy and Sanchez 2016 (small body data ferret, PDS),* [g]*SMASS (Burbine 2000, Burbine and Binzel 2002),* [h]*average values from Takir et al. 2015 and Rivkin et al. 2015,* [i]*Rivkin et al. 2015,* [j]*Takir et al. 2015,* [k]*Marchis et al. 2012*

conclusions by Takir et al. (2015) that the surfaces of these asteroids are similar to highly aqueously altered CMs.

Table 6.1 also gives the area of the 'sharp' 3 μm feature for these asteroids. Due to complications with the terrestrial atmosphere when observing asteroids in this range, band area is calculated as: band area = 0.0045*(band depth at 2.9 μm) - 0.0016. This relationship between band area and band depth at 2.9 μm was established by Takir et al. (2013) for meteorite spectra and gives a method to determine band area in remote spectra despite the gap in data between 2.5 - 2.85 μm. As with the spectral slopes, band areas are mostly within the range determined for CM chondrites with PSF petrologic type 1.2 and 1.1 (0.05 - 0.14 μm^{-1} excluding weathered samples). Figure 6.5 shows the 3 μm features of four representative asteroids (51 Nemausa, 776 Berbericia, 345 Tercindina and 554 Peraga) compared with the CM chondrites that show the most similar 3 μm band areas. The asteroid 51 Nemausa has a band area of 0.17 μm^{-1}, which is larger than the other asteroids and within the range of areas determined for CM chondrites with PSF petrologic types of 1.2 - 1.7 (0.14 - 0.18 μm^{-1}). This coupled with its spectral slope of 1.26, which is also higher than the spectral slopes of the other asteroids, suggests that its surface is the least altered of the asteroids considered here. This is supported by its best spectral match being ALH 83100, which has a PSF petrologic type of 1.3. One caveat to this match is the 3 μm feature of ALH 83100 is at least partly influenced by terrestrial weathering (chapter 3).

The spectral slope and band area can be used to help constrain total phyllosilicate, magnetite and Fe-cronstedtite abundance on the surfaces of asteroids using the relationships determined in chapter 3 (Table 6.1). The magnetite abundances calculated from the spectral slope and band area are within error of each other and are similar in value to the calculated magnetite abundances in the highly aqueously altered CM chondrites (1.5 - 3.3 vol% in PSF petrologic types 1.2 and 1.1, Table 3.1, King et al. 2017). In contrast, the phyllosilicate

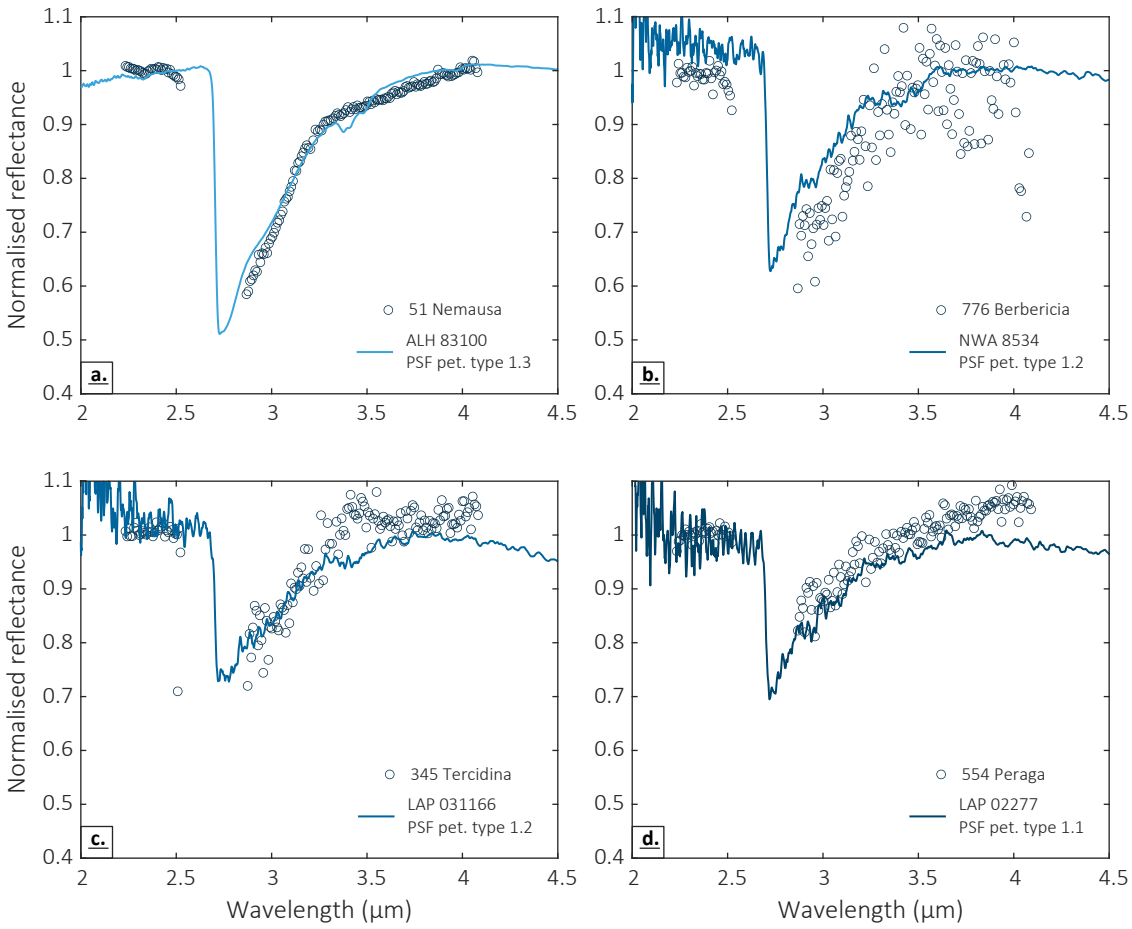


Figure 6.5: *The spectra of four asteroids that show 'sharp' 3 µm features: (a) 51 Nemausa, (b) 776 Berbericia, (c) 345 Tercidina and (d) 554 Peraga, all from Rivkin et al. 2015. The asteroid data is continuum removed and normalised to unity at 2.3 µm. Also included are the 3 µm features of CM meteorites from chapter 3 that show the most similar band areas to the asteroids. The meteorite spectra have been normalised to a continuum between 2.67 – 3.87 µm.*

abundance calculated from the spectral slope is generally higher in abundance than calculated for the CMs (78 - 98 vol% for the asteroid surfaces, 84.3 - 90.1 vol% for PSF petrologic types 1.2 and 1.1).

Total phyllosilicate abundance can be combined with the Fe-cronstedtite abundances to give a Mg-phyllosilicate/Fe-phyllosilicate ratio, which is a useful proxy for determining the degree of aqueous alteration (chapter 3). Figure 6.6 shows that with increasing degree of aqueous alteration, both the total abundance of phyllosilicate, and the proportion of phyllosilicate that is Mg-serpentine, increase in abundance within CM chondrites (King et al.,

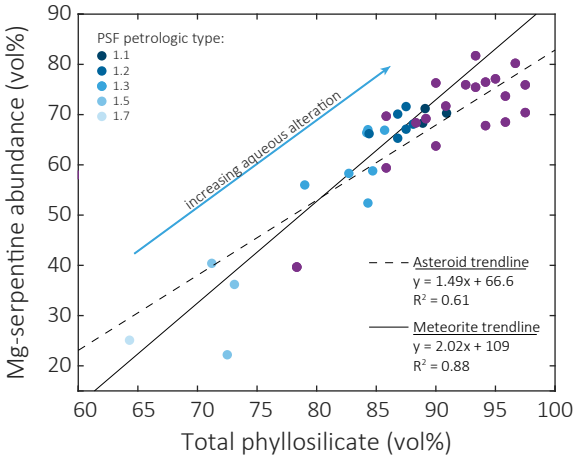


Figure 6.6: *The Mg-serpentine abundance against total phyllosilicate abundance for the asteroids (purple) investigated in this section, and for the CM meteorites (blues) from chapter 3. The meteorite abundances are calculated from PSD-XRD and the multiple aliquots of ALH 83100, ALH 83102 and LON 94101 are included as separate points. The asteroid abundances are estimated from relationships between spectral parameters and mineralogy.*

2017b). The values determined from the asteroid spectral parameters adhere nicely to this trend and suggest the asteroids analysed in this section are potentially more aqueously altered than the highly hydrated CM chondrites investigated in chapter 3. This is an interesting conclusion, as this implies near complete hydration of the asteroid surfaces. The increased degree of aqueous alteration in CM1 chondrites compared to CM2 chondrites has been proposed to result from elevated temperatures (>120 ^{o}C compared to <100 ^{o}C for CM2s) or higher water/rock ratios on their parent bodies (King et al., 2017b). In accordance with this, if the asteroid surfaces experienced even higher degrees of hydration, they may have experienced even higher temperatures or water/rock ratios. Higher water/rock ratios than the CM1 and CM2 chondrites seems unlikely: water abundances have been estimated for a number of the asteroid surfaces here and are lower than water abundances found in all CM chondrite meteorites (Rivkin et al., 2003). Additionally, the NIR spectral slope overestimating total phyllosilicate abundance cannot be ruled out: space weathering can cause the NIR spectral slope to decrease (Thompson et al., 2018), which would result in a higher total

phyllosilicate estimate. This may also be the cause of the slightly higher magnetite abundances estimated from the NIR spectral slope compared to the 3 µm band area, although the magnetite estimates are within error of each other.

In terms of a relationship between aqueous alteration and heliocentric distance, I find no correlation between total phyllosilicate abundance or Mg-phyllosilicate/Fe-phyllosilicate ratio with semi major axis (Figure 6.7a), consistent with previous observations (Rivkin, 2002, Takir and Emery, 2012). This supports models of orbital migration mixing planetesimal populations throughout the inner and outer Solar System (chapter 1, Gomes et al., 2005, Walsh et al., 2011). There is also no correlation between total phyllosilicate abundance or Mg-phyllosilicate/Fe-phyllosilicate ratio with asteroid diameter (Figure 6.7b). Such a relationship has been proposed due to correlations of both the presence of 0.7 µm features and 3 µm band depth with diameter (Florczak et al., 1999, Takir and Emery, 2012) and is suggested to result from greater degrees of hydrothermal circulation on larger asteroids (Rivkin, 2002, Grimm and Mcsween, 1989). The results here do not fully rule out a relationship between degree of alteration and diameter, as the asteroid spectra represent the mineralogy on the surface, and only suggest that if there is increased hydrothermal circulation in larger bodies it is not reflected in the regolith material.

6.6.1 MIR: 121 Hermione, 130 Elektra

Based on interpretation of NIR spectral data for the asteroids here, I can assume features in the MIR of the same asteroids are due to aqueous alteration. However, available MIR spectra of the asteroids in Table 6.1 are limited to only 121 Hermione and 130 Elektra (Marchis et al., 2012). Comparisons in the MIR between meteorites and asteroids are only valid for surfaces covered in fines, as discussed previously. Thermal inertia for 121 Hermione and 130 Elektra were determined by Marchis et al. (2012) to be 5 - 60 and 5 - 65 $Js^{-1}/2K^{-1}m^{-2}$,

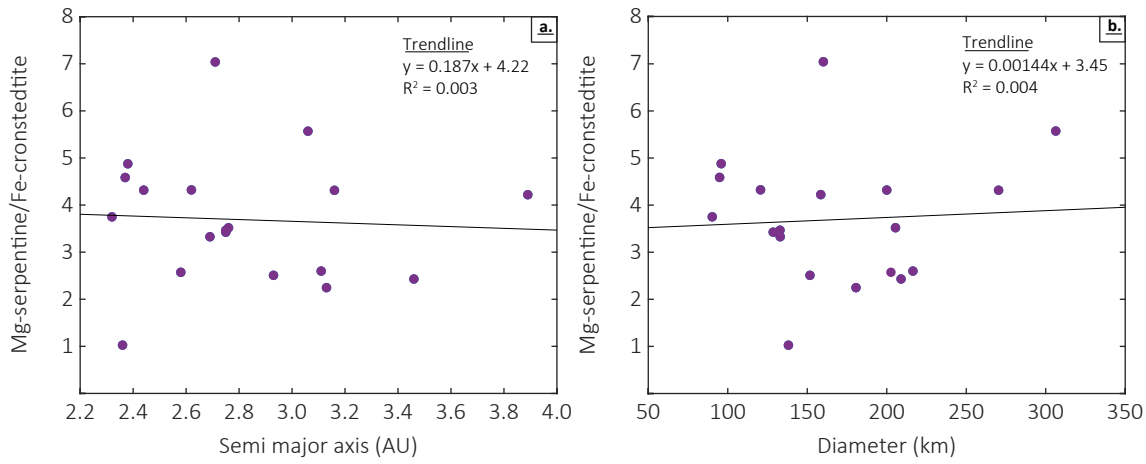


Figure 6.7: *The relationship between Mg-serpentine/Fe-cronstedtite and (a) semi major axis and (b) asteroid diameter.*

respectively. These values are consistent with surfaces covered in fine particulate material (30 - 500 µm Gundlach and Blum, 2013).

The MIR spectral data of 121 Hermione and 130 Elektra are shown in Figure 6.8. The asteroid spectra were collected using the Infrared Spectrograph from the Spitzer Space Telescope (Marchis et al., 2012). Also included are the MIR reflectance spectra of representative CMs from each PSF petrologic type investigated in chapter 3, as the asteroid NIR spectral parameters are similar to those observed in the aqueously altered CM reflectance spectra. Figure 6.8b shows the same asteroids compared to the spectra of CM chondrites collected under SAE conditions from chapter 5. Between 5 - 8 µm, the asteroid spectra show features near 6.1 and 6.7 µm. These correspond to features observed in the meteorite spectra that are attributed to phyllosilicates and carbonates (section 3.4.2, section 4.4.5), suggesting the presence of these phases on the asteroids.

Christiansen feature

The meteorite and asteroid spectra differ in the region surrounding the CF. 121 Hermione shows a CF near 8.20 µm and a possible vibrational feature near 9.20 µm, and 130 Elektra

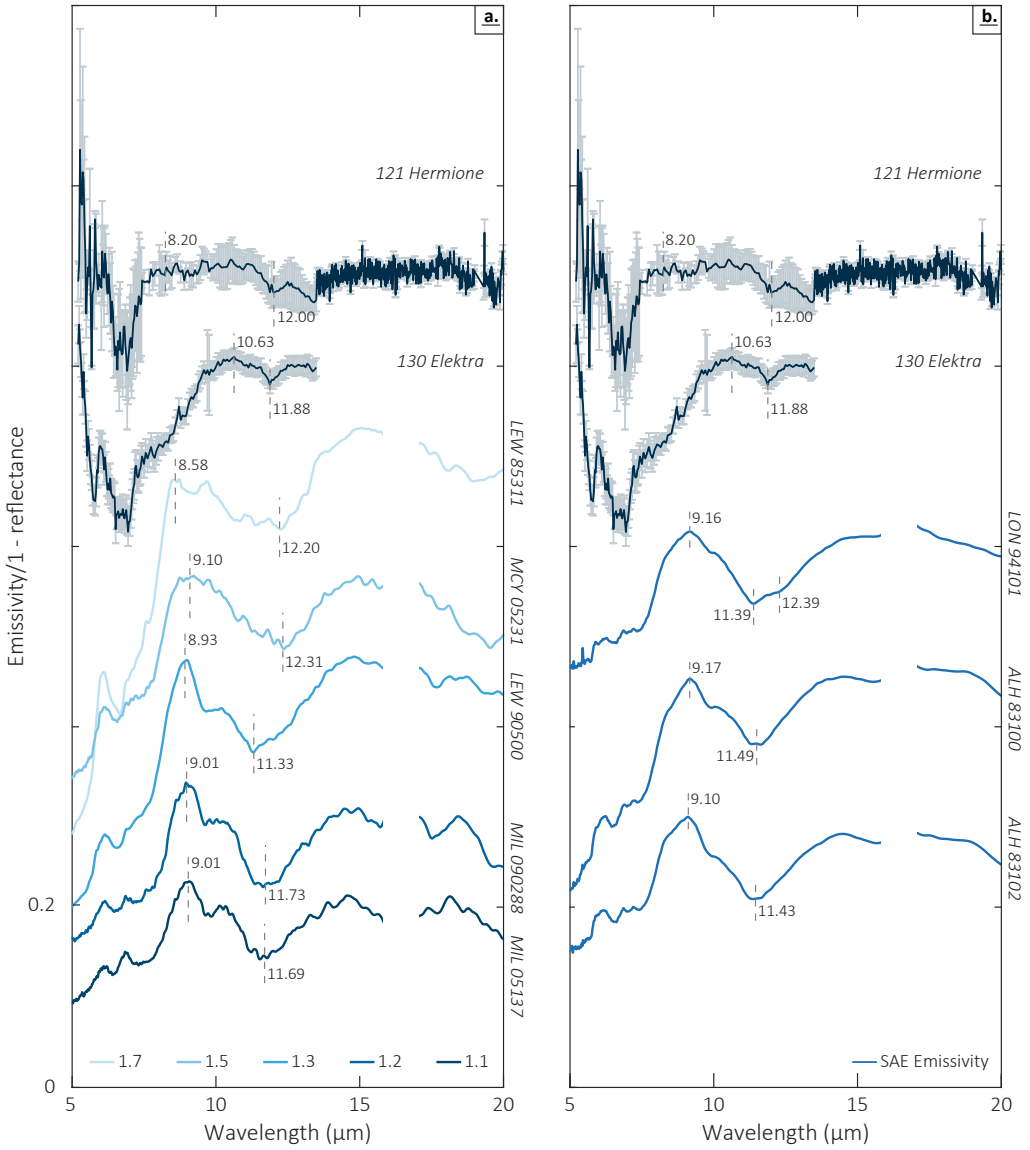


Figure 6.8: *The MIR emissivity spectra of asteroids 121 Hermione and 130 Elektra from Marchis et al. (2012). (a) Reflectance spectra of representative CM chondrites from each PSF petrologic type, approximated as emissivity using Kirchoff's law, and (b) Emissivity spectra for ALH 83100, ALH 83102 and LON 94101 collected under SAE conditions. Neither the reflectance or the emissivity spectra satisfactorily reproduce the CF region observed in the asteroid spectra.*

shows a CF at longer wavelengths near 10.70 µm. It has been suggested that the shape of the CF region for the 121 Hermione spectrum is similar to the 10 µm 'plateau' features observed in the spectra of Jupiter Trojans (Marchis et al., 2012). The plateau feature in the Jupiter Trojan spectra could result from a surface covered in a highly porous, fine particulate material, with particles potentially embedded in a transparent matrix (section 6.5,

Emery et al., 2006, Vernazza et al., 2012, Hargrove et al., 2012, Landsman et al., 2016). A similar scenario has therefore been proposed for Hermione (Marchis et al., 2012). The discrepancy between the asteroid and meteorite spectra may therefore be due to a difference in the physical rather than mineralogical properties of the asteroid surface. However, as discussed in section 6.5, the plateau feature can also be reproduced in the spectra of the thermally altered stage IV CY chondrites (Figs. 5.6 and 6.4), suggesting the plateau features observed in both these asteroids and the Jupiter Trojans may also have a compositional explanation. If it is a compositional effect, then the aqueously altered CM chondrites may not be appropriate analogues for the surfaces of Hermione, a conclusion that does not support the NIR observations. I note that the Hermione spectrum only shows some similarity with the Trojan spectra: it shows a different spectral shape at wavelengths shorter than the CF, and additionally the 'plateau' does not show as much spectral contrast as observed in the Trojan spectra.

The Elektra spectrum shows a different spectral signature to both the Hermione and Trojan spectra. As the NIR spectra suggest Elektra has a mineralogy similar to the CM1 chondrites, this does suggest the CF is affected by something other than the composition, as the CFs in the CM1 spectra are at lower wavelengths. In fact, the Elektra CF is at longer wavelengths than any meteorite CF observed in this project. It is clear that further work is required to determine the cause of the shape of the CF region in remote spectra.

Transparency feature

If the asteroids do have a highly porous surface, a TF should remain identifiable. Martin et al. (2019) showed in the spectra of fine particulate silicate mixed with KBr (which is optically transparent in the MIR so acts to increase the porosity of a sample) a TF is still distinguishable. Emissivity minima between 10 - 13 µm are present in the 121 Hermione and 130

Elektra near 12.10 and 11.92 μm, respectively. If these are TFs, the 130 Elektra value is within the range of TFs determined for CM chondrites with PSF petrologic types of 1.2 and 1.1 and therefore consistent with the NIR parameters, however the 121 Hermione TF is at slightly longer wavelengths, in better agreement with CMs that have a PSF petrologic type of 1.5.

The phyllosilicate abundances and Mg-phyllosilicate/Fe-phyllosilicate ratios determined from the TFs in the 121 Hermione and 130 Elektra are given in Table 6.1. The phyllosilicate values determined from the MIR spectra are lower than their abundance determined from the NIR spectral slope; 121 Hermione has 90 vol% phyllosilicate as determined from its NIR spectra, and 78 vol% phyllosilicate as determined by its TF, which as described above is more consistent with the TFs determined in the spectra of CMs that have petrologic types of 1.5. The difference in the values for 130 Elektra is not as high: 86 vol% from the NIR spectral slope compared to 80 vol% from the TF. The difference in phyllosilicate estimates does support the suggestion that the value from the NIR spectral slope is an overestimate, however the phyllosilicate abundance from the MIR parameters is also lower than the phyllosilicate abundance determined for the CMs with petrologic types of 1.2 and 1.1 (84.3 - 90.1 vol%). Combining the two estimates gives values of ~84 vol% for the surfaces of both Hermione and Elektra, which seems more consistent with the values determined for the meteorites. This emphasises the importance of observing over multiple wavelength ranges as multiple spectral parameters can help to better constrain mineralogy.

6.7 Conclusions

In this chapter I have shown how reflectance and emissivity measurements of aqueously altered CM, CI, CY and CM/CY-anomalous carbonaceous chondrites can be used to evaluate and interpret remote spectra of primitive Solar System airless bodies. For example, the fine

particulate spectra that I have collected in this project can be combined with coarse particulate spectra of the same meteorites in order to predict the variation of spectra that might be observed in the OSIRIS-REx spectra collected at Bennu. Additionally, I have demonstrated how MARA data may be able to identify regions of Mg-rich olivine on the surface of Ryugu.

The relationships determined between mineralogy and spectral parameters also allow inferences of the composition and processing that occurred on the surfaces of asteroids and dwarf planets. For example, the presence of Mg-rich phyllosilicates on the surface of Ceres suggests it experienced similar alteration to the CM chondrite parent body. Additionally, Jupiter Trojans may have an aqueously and thermally altered component, implying they were dehydrated by impacts or solar heating. I also suggest some outer main belt asteroids may have experienced a higher degree of aqueous alteration than the most aqueously altered CM meteorites we have available on Earth.

Following the retirement of NASA's Spitzer Space Telescope in early 2020, the James Webb Space Telescope (JWST) should take over producing spectra of asteroids. Due to launch in 2021 and capable of observing both the VNIR and MIR ranges, the JWST will be capable of observing asteroids with improved spatial resolution (Rivkin et al., 2016). When interpreting the asteroid spectra produced by JWST, meteorite spectral data acquired under appropriate environmental conditions, such as described in the preceding chapters, will be invaluable.

Chapter 7: Conclusions and future work

7.1 Introduction

Volatile-rich asteroids are thought to have contributed water and other volatiles to the inner Solar System (Alexander et al., 2013). These bodies are primitive, left-over material from the initial stage of planetary building, and so studying them offers an opportunity to evaluate the processing occurring at this early stage of Solar System evolution. Remote observations show these bodies have a variety of compositions, suggesting a complex record of hydration and dehydration, however these alteration histories are not well understood. The aqueously and thermally altered CI, CM and CY carbonaceous chondrites are thought to come from volatile-rich asteroids, so characterising them can help to understand more about their parent bodies. This thesis aimed to identify spectral trends and parameters related to mineralogy and alteration history of these carbonaceous chondrites which could be applied to remote observations.

7.2 Spectral relationships with aqueous alteration

Chapter 3 presented the reflectance spectra for 18 meteorites, from partially altered CM2 chondrites to highly hydrated CM1 and CI1 chondrites. Reflectance spectra were collected from powdered samples for which bulk mineralogy had previously been determined, enabling spectral features to be directly related to specific mineral phases. Chapter 5 also presented the emissivity spectra for 3 well characterised aqueously altered CM2 and CM1/2

chondrites. Several trends and parameters in both reflectance and emissivity spectra were identified which varied with degree of aqueous alteration, and these are summarised in Figure 7.1.

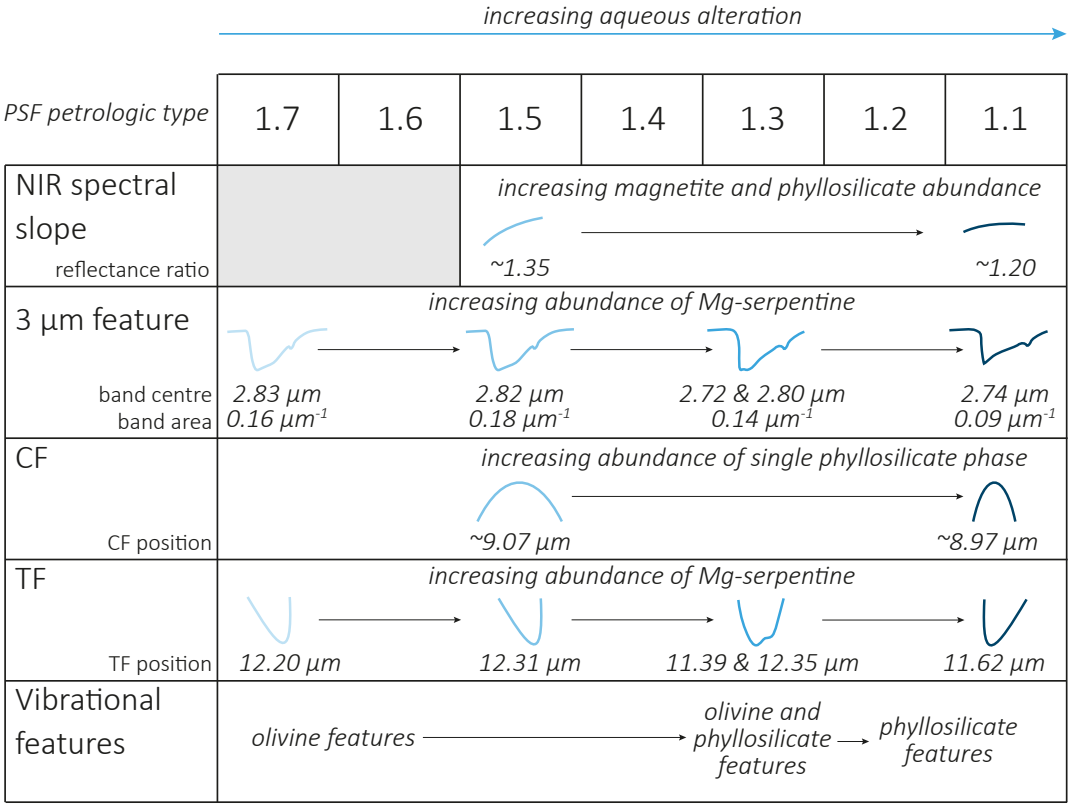


Figure 7.1: *A summary of the spectral trends and parameters which correlate with degree of aqueous alteration, with cartoons showing the changes in the spectra. The sharpening of the CF, the shift of the TF and the change in vibrational features are trends which are observed in both reflectance and emissivity spectra. The grey box indicates where NIR spectra of the CM chondrites with PSF petrologic types of 1.6 and 1.7 were not collected.*

In the NIR wavelength range in reflectance spectra, both the spectral slope and the 3 µm feature show correlations with degree of aqueous alteration that can be applied to remote spectra. This was demonstrated for several Ch and Cgh-type asteroids in chapter 6, where I determined a phyllosilicate and Fe-cronstedtite abundance for the asteroid surfaces based on their NIR spectral slope and 3 µm band area, respectively, and used this to estimate a degree of hydration (Fig. 6.6). The results suggested the asteroids had experienced a higher degree of aqueous alteration than the most altered CM1 chondrites, which may be a result

of aqueous alteration at high water/rock ratios or higher alteration temperatures than experienced by the CM1 chondrites. A caveat to this is the asteroid spectral slope may be overestimating the abundance of phyllosilicate. The spectral slope of the Ch and Cgh asteroids are generally lower than the spectral slope determined for CI and CM spectra, resulting in the determination of higher phyllosilicate abundances on the asteroid surfaces. However, space weathering can also cause spectral slope to decrease (Thompson et al., 2018), implying lower slopes in asteroid spectra may be a result of this process. One way to investigate this further would be to evaluate the effects of simulated space weathering on the spectra of the exact same powders used in this study. This would ensure that spectral differences can be tied specifically to space weathering influence and not meteorite heterogeneity.

In the MIR wavelength range, I demonstrated that bidirectional reflectance measurements of aqueously altered CM chondrites are a reasonable approximation for emissivity measurements of the same samples. However, some of the trends identified in the reflectance spectra were proven to not be reliable parameters for determining alteration history as they were not observed in emissivity spectra. This is the case for the CF, which was observed to shift with increasing alteration to longer wavelengths in reflectance spectra, but to shorter wavelengths in emissivity spectra. Additionally, trends in Si-O bending features were not consistent between reflectance and emissivity spectra.

The CF and Si-O bending features were challenging to interpret in remote observations. Most asteroid spectra examined in chapter 6 show complex plateau features between 8 - 11 µm or CFs at longer wavelengths than observed in any meteorite spectra in this study. This could be related to physical properties of the asteroid surfaces affecting the spectra, such as high porosity or the presence of salts on the asteroid surfaces (Emery et al., 2006, Vernazza et al., 2012, Yang et al., 2013). Alternatively it could be that the asteroids investigated are not compositionally represented in the current meteorite collection. Additionally, Si-O bending

features could not be identified in remote spectra due to the low signal to noise of most telescopic asteroid data. However, OSIRIS-REx observations of Bennu do show a CF and Si-O bending feature at similar positions to that observed in the more aqueously altered CM emissivity spectra, indicating that higher signal-to-noise spectra may be able to resolve these features. This is supported by the observations of Bennu by Emery et al. (2014) using the Spitzer space telescope, where no features can be resolved across the MIR.

In contrast, the TF was found to be consistent in both position and trends with degree of aqueous alteration in reflectance and emissivity spectra, showing trends with phyllosilicate abundance and with Mg-serpentine/Fe-cronstedtite ratios. TFs have also been observed in asteroid spectra. For two of the Ch-type asteroids I examined, I demonstrated the TF position in their MIR spectra could also be used to estimate a degree of hydration for the asteroid surfaces. The results further imply the phyllosilicate abundance estimated from the NIR spectral slope may be an overestimation, possibly due to space weathering effects, emphasising the need for interpretation over multiple wavelength ranges. The TF being a more reliable parameter than the CF in asteroid spectra is a useful consideration, as the CF is usually used for compositional analysis when looking at laboratory data (e.g. Logan et al., 1973, Salisbury et al., 1991) and other Solar System bodies (e.g. Donaldson Hanna et al., 2012a). However, it is important to note the TF will only be present in surfaces dominated by fine-particulate material.

7.3 Spectral relationships with aqueous and thermal alteration

Chapter 4 presented the reflectance spectra for 21 aqueously and thermally altered carbonaceous chondrites. Spectra were collected on the same powdered samples for which mineralogy was identified using PSD-XRD. Chapter 5 presented emissivity spectra for 9 of

the same samples. The spectral trends and parameters identified are summarised in Figure 7.2.

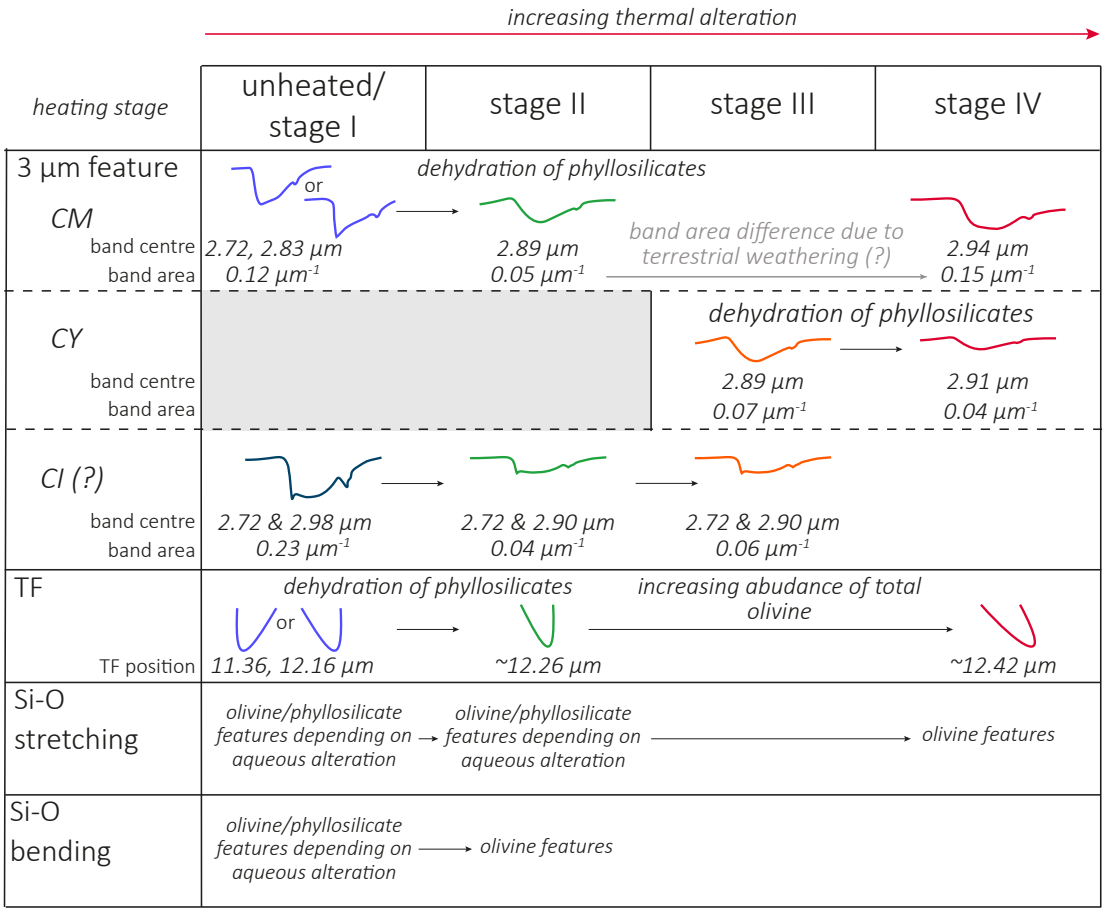


Figure 7.2: *A summary of the spectral trends and parameters which correlate with degree of thermal alteration, with cartoons showing the changes in the spectra. The TF, Si-O stretching and Si-O bending parameters apply to all meteorite types investigated, therefore they have not been separated as was done for the 3 µm feature. These three parameters also apply to both reflectance and emissivity spectra. The grey box indicates that were there no CY chondrite samples investigated which have experienced temperatures <500 °C.*

In the NIR spectral range, the 3 µm region changes from sharp features at shorter wavelengths representing the phyllosilicate compositions in unheated spectra, to rounded features with centres at longer wavelengths in the spectra of samples which have experienced moderate heating (stage II: 400 - 500 °C). These features remain rounded and at longer wavelengths in those CM and CY chondrites which have experienced higher temperatures

(up to 700 ^{o}C). Features similar to these rounded 3 µm shapes have yet to be identified in remote spectra yet, although a number of asteroids are suggested to be dehydrated, including Ryugu (Kitazato et al., 2019, Michel et al., 2020). However, the Ryugu NIR spectrum shows a sharp, narrow feature at 2.72 µm (Kitazato et al., 2019) that is more consistent in shape with the features observed in A 881655, WIS 91600 and experimentally heated Ivuna, than the features observed in the thermally altered CM and CY spectra.

As with the unheated CM spectra, the MIR bidirectional reflectance spectra were found to be a reasonable approximation for emissivity for the thermally altered CM spectra, however there were significant differences between the reflectance and emissivity measurements of the CY spectra. The emissivity spectra of the CYs show a plateau shape in the CF region that is similar to the plateau observed in the spectra of Jupiter Trojans and comet nuclei (as suggested in the previous section, the plateau feature is also observed in other asteroid types, including members of the C-complex). The presence of the plateau in the CY emissivity spectra implies there may be an alternative, mineralogical explanation for the presence of this feature in remote spectra. If the Trojans and comets share some similar mineralogy with the CY chondrites, this could imply they are dehydrated, potentially as a result of either impacts or orbital migration into the inner Solar System at some point in their histories.

The TF and associated trends were applicable to both reflectance and emissivity spectra of aqueously and thermally altered chondrites. Therefore, the TF may be a useful parameter in remote sensing observations, for identifying whether dehydration has occurred on asteroids which have a fine-particulate regolith. The Si-O bending region also proved to be useful in emissivity spectra to investigate for identifying the presence of Fe-rich olivine in the highly dehydrated CM and CY chondrites. The Trojan and comet spectra show some

discernible features in the Si-O bending region, and their positions imply a Fe-rich olivine component, lending further similarity to the CY chondrites.

Unfortunately, compared to the number of asteroids which have been identified as hydrated, spectra are not as readily available for asteroids which are suggested as dehydrated. However, the growing number of dehydrated meteorites identified and the discovery that Ryugu may have experienced thermal alteration suggests these asteroids or fragments of these asteroids may be prevalent throughout the Solar System. Inevitably, further dehydrated asteroids will be discovered, and their spectra collected. At that point, the spectra in this study will be useful for determining degree of thermal alteration.

7.4 Future work

During my project it has become clear that several key areas would benefit from future work. Most notably, Ryugu and Bennu are suggested to share affinities with dehydrated CM, CI or CY chondrites and highly aqueously altered CM1/2 and CM1 chondrites, respectively, based on previous spectral observations both in this thesis and in previous studies (Kitazato et al., 2019, Hamilton et al., 2019). When these samples are returned to Earth and analysed in laboratories, they can be compared directly to the samples which provided the best spectral matches. How the returned samples relate to the samples predicted to be similar to the surfaces of these asteroids will help our understanding of how remote and laboratory spectra can be compared. For example, if the samples returned from Bennu do not look like an aqueously altered CM chondrite, why are OVIRS and OTES spectra similar to CM chondrite spectra? Once this is fully explored the trends and parameters identified in chapters 3, 4 and 5 can be more confidently applied to other small body spectra. The available spectra will be increased by the launch of the James Webb Space Telescope (JWST) in 2021. The

JWST will be capable of observing over the VNIR and MIR wavelengths, with the Near InfraRed Camera (NIRCam) and Near InfraRed Spectrograph (NIRSpec) covering 0.6 - 5 µm, and the Mid Infrared Instrument (MIRI), which has a series of grating channels covering 5 - 28 µm (Horner and Rieke, 2004, Wells et al., 2006, Bagnasco et al., 2007). NIRCam will have a spatial resolution of 45 km at 2 AU and 80 km at 2.8 AU, and NIRSpec should be capable of observing a 0.5 km size object with 5% albedo at 2.5 AU with a signal-to-noise of 10 at 3 µm in 1000s (Rivkin et al., 2016). MIRI should be able to observe the 10 µm region of bodies which are maximum 330 km in size at a distance of 5.2 AU without being saturated. As the largest Jupiter Trojans are below this diameter (Emery et al., 2015), MIRI spectra should provide spectra covering the 10 µm plateau at an increased sensitivity compared to current ground based telescopic spectra (Rivkin et al., 2016).

A further area of interest is the origin of the plateau feature in the CF region in the spectra of Jupiter Trojans, which is currently not well understood. It can be explained by physical characteristics of the asteroid surfaces (Emery et al., 2006, Yang et al., 2013), but the plateau is also reproduced in the CY spectra, suggesting a compositional explanation for the plateau in the remote spectra. Observations by JWST with MIRI of Jupiter Trojans using the 10 µm grating will provide further opportunities to investigate the plateau in the remote spectra, however the cause of the feature in the CY spectra requires further exploration. One of the characteristics of the CY chondrites is a high sulfide abundance. Varatharajan et al. (2019) showed the emissivity spectra of several sulfides had broad features in the CF region (although Fe-sulfides, which are the phases in the CYs, did not show as significant features as other sulfide phases). The effect of sulfide abundance in the CYs could be investigated by collecting the emissivity spectra of physical mixtures containing up to 30 vol% sulfide, to see if these phases are the cause of the plateau feature. Another option would be to try and recreate some of the physical characteristics identified as causing plateau features in the CY

chondrites. This could be done by mixing some CY sample with KBr, which is transparent in the MIR and so acts to increase the porosity of the sample (Vernazza et al., 2012, Martin et al., 2019). Also contributing to this area will be the Lucy mission, which is due to launch in 2021. Lucy will visit 6 Jupiter Trojan asteroids and should be able to evaluate some of their surface compositions, unravelling the cause of the plateau feature.

The final area of future work is regarding further laboratory measurements of different meteorites. I have demonstrated how dehydrated CM chondrite MIR spectra have a lot of similarity with anhydrous silicate spectra. Other meteorite groups are composed primarily of anhydrous silicates that have never been significantly hydrated, such as the CO and CV chondrites. It would be useful to perform a similar suite of measurements as was done in this study on these meteorite groups, in order to identify spectral parameters that are able to tell between samples which have always been anhydrous and those that have experienced dehydration. An example of where this might benefit is for asteroid 3200 Phaethon, where it is unknown whether it has always been anhydrous or is dehydrated. Donaldson Hanna et al. 2019 presented some MIR emissivity spectra of some CV chondrites, which do not resemble the dehydrated CM chondrite spectra I collected, however the CO chondrites in particular are suggested to be similar to precursor CM material (Greenwood and Franchi, 2004, Greenwood et al., 2014). Collecting reflectance and emissivity measurements for a suite of well characterised CO chondrites would therefore be useful for comparison with dehydrated CM spectra.

Bibliography

Akai, J. (1984). Mineralogical characterization of matrix materials in carbonaceous chondrite Yamato 793321 and Belgica-7904 by HREM. In *Proc. NIPR Symp. Antarct. Meteorites*, (pp. 59–61).

Akai, J. (1988). Incompletely transformed serpentine-type phyllosilicates in the matrix of Antarctic CM chondrites. *Geochimica et Cosmochimica Acta*, *52*(6), 1593–1599.

Akai, J. (1990). Mineralogical evidence of heating events in Antarctic carbonaceous chondrites, Y-86720 and Y-82162. *Proc. NIPR Symp. Antarct. Meteorites*, *3*, 55–68.

Akai, J. (1992). T-T-T diagram of serpentine and saponite, and estimation of metamorphic heating degree of Antarctic carbonaceous chondrites. *Proc. NIPR Symp. Antarct. Meteorites*, *5*, 120–135.

Akai, J., and Tari, S. (1997). Thermally Metamorphosed Antarctic CM and CI Carbonaceous Chondrites in Japanese Collections, and Transformation Processes of Phyllosilicates. In *LPI Technical Report*, (pp. 1–2).

Alemanno, G., Maturilli, A., Helbert, J., and D'Amore, M. (2020). Laboratory studies on the 3 µm spectral features of Mg-rich phyllosilicates with temperature variations in support of the interpretation of small asteroid surface spectra. *Earth and Planetary Science Letters*, *546*, 116424.

Alexander, C. M., Bowden, R., Fogel, M. L., Howard, K. T., Herd, C. D. K., and Nittler, L. R. (2012). The provenances of asteroids, and their contributions to the volatile inventories of the terrestrial planets. *Science*, *337*, 721–723.

Alexander, C. M., Greenwood, R. C., Bowden, R., Gibson, J. M., Howard, K. T., and Franchi, I. A. (2018). A mutli-technique search for the most primitive CO chondrites. *Geochimica et Cosmochimica Acta*, *221*, 406–420.

Alexander, C. M., Howard, K. T., Bowden, R., and Fogel, M. L. (2013). The classification of CM and CR chondrites using bulk H, C and N abundances and isotopic compositions. *Geochimica et Cosmochimica Acta*, *123*, 244–260.

Alexander, C. M. O. (2017). The origin of inner Solar System water. *Philosophical Transactions of the Royal Society*, *375*.

Amelin, Y., Kaltenbach, A., Iizuka, T., Stirling, C. H., Ireland, T. R., Petaev, M., and Jacobsen, S. B. (2010). U-Pb chronology of the Solar System's oldest solids with variable 238U/235U. *Earth and Planetary Science Letters*, *300*(3-4), 343–350.

Amelin, Y., Krot, A. N., Hutcheon, I. D., and Ulyanov, A. A. (2002). Lead Isotopic Ages of Chondrules and Calcium-Aluminum-Rich Inclusions. *Science*, *297*(5587).

Apai, D., and Lauretta, D. S. (2010). Planet formation and protoplanetary dust. In *Protoplanetary dust: Astrochemical and cosmochemical perspectives*, chap. 1, (pp. 1 – 19). Cambridge University Press.

Arai, T., Kobayashi, M., Ishibashi, K., Yoshida, F., Kimura, H., Wada, K., Senshu, H., Yamada, M., Okudaira, O., Okamoto, T., Kameda, S., Srama, R., Krüger, H., Ishiguro, M., Yabuta, H., Nakamura, T., Watanabe, J., Ito, T., Ohtsuka, K., Tachibana, S., Mikouchi, T., Komatsu, M., Toyota, H., Kawakatsu, Y., and Takashima, T. (2018). DESTINY+ mission: Flyby of Geminids parent asteriod (3200) Phaethon and in-situ analyses of dust accreting on the Earth. In *49th Lunar and Planetary Science Conference*.

Armitage, P. J. (2007). Massive Planet Migration: Theoretical Predictions and Comparison with Observations. *The Astrophysical Journal*, *665*(2), 1381–1390.

Asphaug, E., Agnor, C. B., and Williams, Q. (2006). Hit-and-run planetary collisions. *Nature*, *439*(7073), 155–160.

Bagnasco, G., Kolm, M., Ferruit, P., Honnen, K., Koehler, J., Lemke, R., Maschmann, M., Melf, M., Noyer, G., Rumler, P., Salvignol, J.-C., Strada, P., and Te Plate, M. (2007). Overview of the near-infrared spectrograph (NIRSpec) instrument on-board the James Webb Space Telescope (JWST). In J. B. Heaney, and L. G. Burriesci (Eds.) *Cryogenic Optical Systems and Instruments XII*, vol. 6692, (p. 66920M). SPIE.

Baldridge, A., Hook, S., Grove, C., and Rivera, G. (2009). The ASTER spectral library version 2.0. *Remote Sensing of Environment*, *113*(4), 711–715.

Ballouz, R. L., Walsh, K. J., Barnouin, O. S., DellaGiustina, D. N., Asad, M. A., Jawin, E. R., Daly, M. G., Bottke, W. F., Michel, P., Avdellidou, C., Delbo, M., Daly, R. T., Asphaug, E., Bennett, C. A., Bierhaus, E. B., Connolly, H. C., Golish, D. R., Molaro, J. L., Nolan, M. C., Pajola, M., Rizk, B., Schwartz, S. R., Trang, D., Wolner, C. W., and Lauretta, D. S. (2020). Bennu's near-Earth lifetime of 1.75 million years inferred from craters on its boulders. *Nature*, *587*(7833), 205–209.

Barrat, J.-A., Zanda, B., Moynier, F., Bollinger, C., Liorzou, C., and Bayon, G. (2012). Geochemistry of CI chondrites: Major and trace elements, and Cu and Zn Isotopes. *Geochimica et Cosmochimica Acta*, *83*, 79–92.

Batchelder, M., and Cressey, G. (1998). Rapid, Accurate Phase Quantification of Clay-Bearing Samples Using a Position-Sensitive X-ray Detector. *Clays and Clay Minerals*, *46*(2), 183–194.

Bates, H. C., King, A. J., Donaldson Hanna, K. L., Bowles, N. E., and Russell, S. S. (2020). Linking mineralogy and spectroscopy of highly aqueously altered CM and CI carbonaceous chondrites in preparation for primitive asteroid sample return. *Meteoritics & Planetary Science*, *55*(1), 77–101.

Battandier, M., Bonal, L., Quirico, E., Beck, P., Engrand, C., Duprat, J., and Dartois, E. (2018). Characterization of the organic matter and hydration state of Antarctic micrometeorites: A reservoir distinct from carbonaceous chondrites. *Icarus*, *306*, 74–93.

Beck, P., Garenne, A., Quirico, E., Bonal, L., Montes-Hernandez, G., Moynier, F., and Schmitt, B. (2014). Transmission infrared spectra (2-25um) of carbonaceous chondrites (CI, CM, CV-CK, CR, C2 ungrouped): Mineralogy, water, and asteroidal processes. *Icarus*, *229*, 263–277.

Beck, P., Maturilli, A., Garenne, A., Vernazza, P., Helbert, J., Quirico, E., and Schmitt, B. (2018). What is controlling the reflectance spectra (0.35–150 μm) of hydrated (and dehydrated) carbonaceous chondrites? *Icarus*, *313*, 124–138.

Beck, P., Quirico, E., Montes-Hernandez, G., Bonal, L., Bollard, J., Orthous-Daunay, F.-R., Howard, K. T., Schmitt, B., Brissaud, O., Deschamps, F., Wunder, B., and Guillot, S. (2010). Hydrous mineralogy of CM and CI chondrites from infrared spectroscopy and their relationship with low albedo asteroids. *Geochimica et Cosmochimica Acta*, *74*, 4881–4892.

Beckett, J. R., Connolly, H. C., and Ebel, D. S. (2009). Chemical Processes in Igneous Calcium-Aluminum-rich Inclusions: A Mostly CMAS View of Melting and Crystallization. In *Meteorites and the early solar system II*, (pp. 399 – 429).

Bell, J., Davis, D. R., Hartmann, W. K., and Gaffey, M. J. (1989). Asteroids- The Big Picture. In *Asteroids II*, (pp. 921–945).

Bendjoya, P., Cellino, A., Di Martino, M., and Saba, L. (2004). Spectroscopic observations of Jupiter Trojans. *Icarus*, *168*(2), 374–384.

Benedix, G. K., and Bland, P. A. (2004). What does the CM chondrite Mineralogic Alteration Index really mean? In *67th Annual Meteoritical Society Meeting*, vol. 43.

Benoit, P. H., Cunningham, J. M., Bland, P. A., Berry, F. J., and Pillinger, C. T. (1996). The pairing of meteorite finds. In *27th Lunar and Planetary Science Conference*.

Binzel, R. P., DeMeo, F. E., Turtelboom, E. V., Bus, S. J., Tokunaga, A., Burbine, T. H., Lantz, C., Polishook, D., Carry, B., Morbidelli, A., Birlan, M., Vernazza, P., Burt, B. J., Moskovitz, N., Slivan, S. M., Thomas, C. A., Rivkin, A. S., Hicks, M. D., Dunn, T., Reddy, V., Sanchez, J. A., Granvik, M., and Kohout, T. (2019). Compositional distributions and evolutionary processes for the near-Earth object population: Results from the MIT-Hawaii Near-Earth Object Spectroscopic Survey (MITHNEOS). *Icarus*, *324*, 41–76.

Binzel, R. P., Rivkin, A. S., Thomas, C. A., Vernazza, P., Burbine, T. H., DeMeo, F. E., Bus, S. J., Tokunaga, A. T., and Birlan, M. (2009). Spectral properties and composition of potentially hazardous Asteroid (99942) Apophis. *Icarus*, *200*(2), 480–485.

Bischoff, A., Geiger, T., Palme, H., Spettel, B., Schultz, L., Scherer, P., Loeken, T., Bland, P., Clayton, R. N., Mayeda, T. K., Herpers, U., Meltzow, B., Michel, R., and Dittrich-Hannen, B. (1994). Acfer 217-A new member of the Rumuruti chondrite group (R). *Meteoritics*, *29*(2), 264–274.

Bischoff, A., and Metzler, K. (1991). Mineralogy and Petrology of the Anomalous Carbonaceous Chondrites, Yamato-86720, Yamato-82162, and Belgica-7904. *Proc. NIPR Symp. Antarct. Meteorites*, *4*, 226–246.

Bishop, J. L., Lane, M. D., Dyar, M. D., and Brown, A. J. (2008). Reflectance and emission spectroscopy study of four groups of phyllosilicates: smectites, kaolinite-serpentines, chlorites and micas. *Clay Minerals*, *43*, 35–54.

Bishop, J. L., Pieters, C. M., and Burns, R. G. (1993). Reflectance and Mössbauer spectroscopy of ferrihydrite-montmorillonite assemblages as Mars soil analog materials. *Geochimica et Cosmochimica Acta*, *57*, 4583–4595.

Bland, P. A., Cressey, G., and Menzies, O. N. (2004). Modal mineralogy of carbonaceous chondrites by X-ray diffraction and Mössbauer spectroscopy. *Meteoritics & Planetary Science*, *39*(1), 3–16.

Bland, P. A., Zolensky, M. E., Benedix, G. K., and Sephton, M. A. (2006). Weathering of Chondritic Meteorites. In *Meteorites and the early solar system II*, (pp. 853–867).

Bollard, J., Connelly, J., and Bizzarro, M. (2015). Pb-Pb dating of individual chondrules from the CBa chondrite Gujba: Assessment of the impact plume formation model. *Meteoritics & Planetary Science*, *50*(7), 1197–1216.

Botta, O., and Bada, J. L. (2002). Extraterrestrial Organic Compounds in Meteorites. *Surveys in Geophysics*, *23*(5), 411–467.

Bottke, W., Vokrouhlicky, D., Nesvorny, D., Shrbeny, L., Bottke, W., Vokrouhlicky, D., Nesvorny, D., and Shrbeny, L. (2010). (6) Hebe Really is the H Chondrite Parent Body. In *DPS*, (p. 46.06).

Bottke, W. F., Durda, D. D., Nesvorný, D., Jedicke, R., Morbidelli, A., Vokrouhlický, D., and Levison, H. (2005). The fossilized size distribution of the main asteroid belt. *Icarus*, *175*(1), 111–140.

Bourcier, W. L., and Zolensky, M. E. (1992). Coumputer modelling of aqueous alteration on carbonaceous chondrite parent bodies. In *23rd Lunar and Planetary Science Conference*, (p. 143).

Bouvier, A., Gattacceca, J., Grossman, J., and Metzler, K. (2017). The Meteoritical Bulletin, No. 105. *Meteoritics & Planetary Science*, *52*(11), 2411.

Bradley, J. P. (2014). *Early Solar Nebula Grains - Interplanetary Dust Particles*, vol. 1. Elsevier Ltd., 2 ed.

Brearley, A. J. (1992). Mineralogy of Fine-Grained Matrix in the Ivuna Carbonaceous Chondrite. In *23rd Lunar and Planetary Science Conference*.

Brearley, A. J. (2006). The action of water. In D. S. Lauretta, and H. Y. McSween (Eds.) *Meteorites and the early solar system II*, (pp. 587–624). The University of Arizona Press.

Brogan, C. L., Perez, L. M., Hunter, T. R., Dent, W. R. F., Hales, A. S., Hills, R., Corder, S., Fomalont, E. B., Vlahakis, C., Asaki, Y., Barkats, D., Hirota, A., Hodge, J. A., Impellizzeri, C. M. V., Kneissl, R., Liuzzo, E., Lucas, R., Marcelino, N., Matsushita, S., Nakanishi, K., Phillips, N., Richards, A. M. S., Toledo, I., Aladro, R., Broguiere, D., Cortes, J. R., Cortes, P. C., Espada, D., Galarza, F., Garcia-Appadoo, D., Guzman-Ramirez, L., Humphreys, E. M., Jung, T., Kameno, S., Laing, R. A., Leon, S., Marconi, G., Mignano, A., Nikolic, B., Nyman, L. A., Radiszcz, M., Remijan, A., Rodon, J. A., Sawada, T., Takahashi, S., Tilanus, R. P. J., Vilaro, B. V., Watson, L. C., Wiklind, T., Akiyama, E., Chapillon, E., de Gregorio-Monsalvo, I., Di Francesco, J., Gueth, F., Kawamura, A., Lee, C. F., Luong, Q. N., Mangum, J., Pietu, V., Sanhueza, P., Saigo, K., Takakuwa, S., Ubach, C., van Kempen, T., Wootten, A., Castro-Carrizo, A., Francke, H., Gallardo, J., Garcia, J., Gonzalez, S., Hill, T., Kaminski, T., Kurono, Y., Liu, H. Y., Lopez, C., Morales, F., Plarre, K., Schieven, G., Testi, L., Videla, L., Villard, E., Andreani, P., Hibbard, J. E., and Tatematsu, K. (2015). First Results from High Angular Resolution ALMA Observations Toward the HL Tau Region. *The Astrophysical Journal Letters*, *808*(1).

Browning, L. B., McSween, H. Y., and Zolensky, M. E. (1996). Correlated alteration effects in CM carbonaceous chondrites. *Geochimica et Cosmochimica Acta*, *60*(14), 2621–2633.

Brunetto, R., Loeffler, M. J., Nesvorný, D., Sasaki, S., and Strazzulla, G. (2015). Asteroid Surface Alteration by Space Weathering Processes Asteroid families View project CODITA View project. In *Asteroids IV*, (pp. 597–616).

Bryson, J. F. J., Weiss, B. P., Biersteker, J. B., King, A. J., and Russell, S. S. (2020). Constraints on the Distances and Timescales of Solid Migration in the Early Solar System from Meteorite Magnetism. *The Astrophysical Journal*, *896*(2), 103.

Bullock, E. S., Gounelle, M., Lauretta, D. S., Grady, M. M., and Russell, S. S. (2005). Mineralogy and texture of Fe-Ni sulfides in CI1 chondrites: Clues to the extent of aqueous alteration on the CI1 parent body. *Geochimica et Cosmochimica Acta*, *69*(10), 2687–2700.

Burbine, T. H. (2017). *Asteroids: Astronomical and Geological Bodies*. Cambridge University Press.

Burbine, T. H., Binzel, R. P., Bus, S. J., and Clark, B. E. (2001). K asteroids and CO3/CV3 chondrites. *Meteoritics & Planetary Science*, *36*(2), 245–253.

Burbine, T. H., McCoy, T. J., Meibom, A., Gladman, B., and Keil, K. (2002). Meteoritic parent bodies: Their number and identification. In *Asteroids III*, (pp. 653–667).

Burgess, R., Wright, I. P., and Pillinger, C. T. (1991). Determination of sulphur-bearing components in C1 and C2 carbonaceous chondrites by stepped combustion. *Meteoritics*, *26*, 55–64.

Bus, S. J. (1999). *Compositional structure in the asteroid belt: Results of a spectroscopic survey*. Ph.D. thesis.

Bus, S. J., and Binzel, R. P. (2002a). Phase II of the Small Main-Belt Asteroid Spectroscopic Survey: A Feature-Based Taxonomy. *Icarus*, *158*, 146–177.

Bus, S. J., and Binzel, R. P. (2002b). Phase II of the Small Main-Belt Asteroid Spectroscopic Survey: The Observations. *Icarus*, *158*, 106–145.

Calvin, W. M., and King, T. V. V. (1997). Spectral characteristics of iron bearing phyllosilicates: Comparison to Orgueil (CI1), Murchison and Murray (CM2). *Meteoritics & Planetary Science*, *32*(5), 693–701.

Carrozzo, F. G., De Sanctis, M. C., Raponi, A., Ammannito, E., Castillo-Rogez, J., Ehlmann, B. L., Marchi, S., Stein, N., Ciarniello, M., Tosi, F., Capaccioni, F., Capria, M. T., Fonte, S., Formisano, M., Frigeri, A., Giardino, M., Longobardo, A., Magni, G., Palomba, E., Zambon, F., Raymond, C. A., and Russell, C. T. (2018). Nature, formation, and distribution of carbonates on Ceres. *Science Advances*, *4*(3), e1701645.

Castillo-Rogez, J. C., and McCord, T. B. (2010). Ceres' evolution and present state constrained by shape data. *Icarus*, *205*(2), 443–459.

Chambers, J. E. (2014). Planet formation. In *Treatise on Geochemistry: Second Edition, Volume 2*, (pp. 55 – 67). 2 ed.

Che, C., Glotch, T. D., Bish, D. L., Michalski, J. R., and Xu, W. (2011). Spectroscopic study of the dehydration and/or dehydroxylation of phyllosilicate and zeolite minerals. *Journal of Geophysical Research*, *116*(E5), E05007.

Choe, W. H., Huber, H., Rubin, A. E., Kallemeyn, G. W., and Wasson, J. T. (2010). Compositions and taxonomy of 15 unusual carbonaceous chondrites. *Meteoritics & Planetary Science*, *45*(4), 531–554.

Christensen, P. R., Bandfield, J. L., Hamilton, V. E., Howard, D. A., Lane, M. D., Piatek, J. L., Ruff, S. W., and Stefanov, W. L. (2000). A thermal emission spectral library of rock-forming minerals. *Journal of Geophysical Research: Planets*, *105*(E4), 9735–9739.

Christensen, P. R., Hamilton, V. E., Mehall, G. L., Pelham, D., O'Donnell, W., Anwar, S., Bowles, H., Chase, S., Fahlgren, J., Farkas, Z., Fisher, T., James, O., Kubik, I., Lazbin, I., Miner, M., Rassas, M., Schulze, L., Shamordola, K., Tourville, T., West, G., Woodward, R., and Lauretta, D. (2018). The OSIRIS-REx Thermal Emission Spectrometer (OTES) instrument. *Space Science Reviews*, *214*(5), 87.

Christensen, P. R., and Harrison, S. T. (1993). Thermal infrared emission spectroscopy of natural surfaces: application to desert varnish coatings on rocks. *Journal of Geophysical Research*, *98*(B11).

Clark, B. E., Bus, S. J., Rivkin, A. S., Shepard, M. K., and Shah, S. (2004). Spectroscopy of X-Type Asteroids. *The Astronomical Journal*, *128*(6), 3070–3081.

Clark, B. E., Ockert-Bell, M. E., Cloutis, E. A., Nesvorny, D., Mothé-Diniz, T., and Bus, S. J. (2009). Spectroscopy of K-complex asteroids: Parent bodies of carbonaceous meteorites? *Icarus*, *202*(1), 119–133.

Clark, B. E., Ziffer, J., Nesvorny, D., Campins, H., Rivkin, A. S., Hiroi, T., Barucci, M. A., Fulchignoni, M., Binzel, R. P., Fornasier, S., Demeo, F., Ockert-Bell, M. E., Licandro, J., and Moth-Diniz, T. (2010). Spectroscopy of B-type asteroids: Subgroups and meteorite analogs. *Journal of Geophysical Research: Planets*, *115*(6), 1 – 22.

Clayton, R. N., and Mayeda, T. K. (1999). Oxygen isotope studies of carbonaceous chondrites. *Geochimica et Cosmochimica Acta*, *63*, 2089–2104.

Clayton, R. N., and Mayeda, T. K. (2003). Oxygen isotopes of carbonaceous chondrites. In *Evolution of Solar System Materials: A New Perspective from Antarctic Meteorites*.

Clayton, R. N., Mayeda, T. K., Goswami, J. N., and Olsen, E. J. (1991). Oxygen isotope studies of ordinary chondrites. *Geochimica et Cosmochimica Acta*, *55*(8), 2317–2337.

Clayton, R. N., Mayeda, T. K., and Rubin, A. E. (1984). Oxygen isotopic compositions of enstatite chondrites and aubrites. *Journal of Geophysical Research*, *89*(S01), C245.

Cloutis, E., Hiroi, T., Gaffey, M., Alexander, C., and Mann, P. (2011a). Spectral reflectance properties of carbonaceous chondrites: 1. CI chondrites. *Icarus*, *212*(1), 180–209.

Cloutis, E., Hudon, P., Hiroi, T., and Gaffey, M. (2012). Spectral reflectance properties of carbonaceous chondrites 4: Aqueously altered and thermally metamorphosed meteorites. *Icarus*, *220*(2), 586–617.

Cloutis, E., Hudon, P., Hiroi, T., Gaffey, M., and Mann, P. (2011b). Spectral reflectance properties of carbonaceous chondrites: 2. CM chondrites. *Icarus*, *216*(1), 309–346.

Cloutis, E. A., Gaffey, M. J., Smith, D. G., and Lambert, R. S. J. (1990). Reflectance spectra of mafic silicate-opaque assemblages with applications to meteorite spectra. *Icarus*, *84*(2), 315–333.

Cohen, M., Witteborn, F. C., Roush, T., Bregman, J., and Wooden, D. (1998). Spectral Irradiance Calibration in the Infrared. VIII. 5–14 Micron Spectroscopy of the Asteroids Ceres, Vesta, and Pallas. *The Astronomical Journal*, *115*(4), 1671–1679.

Conel, J. E. (1969). Infrared emissivities of silicates' experimental results and a cloudy atmosphere model of spectral emission from condensed particulate mediums. *Journal of Geophysical Research*, *74*(15), 1614 – 1634.

Connelly, J. N., Bizzarro, M., Krot, A. N., Nordlund, A., Wielandt, D., and Ivanona, M. A. (2012). The Absolute Chronology and Thermal Processing of Solids in the Solar Protoplanetary Disk. *Science*, *338*, 651–655.

Connolly, H. C., and Jones, R. (2016). Chondrules: The canonical and noncanonical viewsTitle. *Journal of Geophysical Research: Planets*, *121*, 1885–1899.

Cooper, B. L. (2002). Midinfrared spectral features of rocks and their powders. *Journal of Geophysical Research*, *107*(E4), 1–17.

Cressey, G., and Schofield, P. F. (1996). Rapid whole-pattern profile-stripping method for the quantification of multiphase samples. *Powder Diffraction*, *11*, 35–39.

Crovisier, J., Leech, K., Bockelée-Morvan, D., Brooke, T. Y., Hanner, M. S., Altieri, B., Keller, H. U., and Lellouch, E. (1997). The spectrum of Comet Hale-Bopp (C/1995 O1) Observed with the Infrared Space Observatory at 2.9 Astronomical Units from the Sun. *Science*, *275*(5308), 1904–1907.

De Prá, M. N., Pinilla-Alonso, N., Carvano, J. M., Licandro, J., Campins, H., Mothé-Diniz, T., De León, J., and Alí-Lagoa, V. (2018). PRIMASS visits Hilda and Cybele groups. *Icarus*, *311*, 35–51.

De Sanctis, M., Ammannito, E., Carrozzo, F., Ciarniello, M., Giardino, M., Frigeri, A., Fonte, S., McSween, H., Raponi, A., Tosi, F., Zambon, F., Raymond, C., and Russell, C. (2018). Ceres's global and localized mineralogical composition determined by Dawn's Visible and Infrared Spectrometer (VIR). *Meteoritics and Planetary Science*, *22*, 1 – 22.

De Sanctis, M. C., Ammannito, E., Raponi, A., Marchi, S., McCord, T. B., McSween, H. Y., Capaccioni, F., Capria, M. T., Carrozzo, F. G., Ciarniello, M., Longobardo, A., Tosi, F., Fonte, S., Formisano, M., Frigeri, A., Giardino, M., Magni, G., Palomba, E., Turrini, D., Zambon, F., Combe, J. P., Feldman, W., Jaumann, F., McFadden, L. A., Pieters, C. M., Prettyman, T. H., Toplis, M., Raymond, C. A., and Russell, C. T. (2015). Ammoniated phyllosilicates with a likely outer Solar System origin on (1) Ceres. *Nature*, *528*, 241–244.

De Sanctis, M. C., Coradini, A., Ammannito, E., Filacchione, G., Capria, M. T., Fonte, S., Magni, G., Barbis, A., Bini, A., Dami, M., Ficai-Veltroni, I., and Preti, G. (2012). The VIR spectrometer. In *The Dawn Mission to Minor Planets 4 Vesta and 1 Ceres*, vol. 9781461449, (pp. 329–369). Springer New York.

De Sanctis, M. C., Raponi, A., Ammannito, E., Ciarniello, M., Toplis, M. J., Mcsween, H. Y., Castillo-Rogez, J. C., Ehlmann, B. L., Carrozzo, F. G., Marchi, S., Tosi, F., Zambon, F., Capaccioni, F., Capria, M. T., Fonte, S., Formisano, M., Frigeri, A., Giardino, M., Longobardo, A., Magni, G., Palomba, E., Mcfadden, L. A., Pieters, C. M., Jaumann, R., Schenk, P., Mugnuolo, R., Raymond, C. A., and Russell, C. T. (2016). Bright carbonate deposits as evidence of aqueous alteration on (1) Ceres.

Delbo, M., and Tanga, P. (2009). Thermal inertia of main belt asteroids smaller than 100 km from IRAS data. *Planetary and Space Science*, *57*(2), 259–265.

DellaGiustina, D. N., Emery, J. P., Golish, D. R., Rozitis, B., Bennett, C. A., Burke, K. N., Ballouz, R., Becker, K. J., Christensen, P. R., Aubigny, C. Y. D., Hamilton, V. E., Reuter, D. C., Rizk, B., Simon, A. A., Asphaug, E., Bandfield, J. L., Barnouin, O. S., Barucci, M. A., Bierhaus, E. B., Binzel, R. P., Bottke, W. F., Bowles, N. E., Campins, H., Clark, B. C., Clark, B. E., Connolly Jr, H. C., Daly, M. G., de Leon, J., Delbo, M., Deshapriya, J. D. P., Elder, C. M., Fornasier, S., Hergenrother, C. W., Howell, E. S., Jawin, E. R., Kaplan, H. H., Kareta, T. R., LeCorre, L., Li, J. Y., Licandro, J., Lim, L. F., Michel, P., Molaro, J., Nolan, M. C., Pajola, M., Popescu, M., Rizos Garcia, J. L., Ryan, A., Schwartz, S. R., Shultz, N., Siegler, M. A., Smith, P. H., Tatsumi, E., Thomas, C. A., Walsh, K. J., Wolner, C. W. V., Zou, X. D., Lauretta, D. S., and OSIRIS-REx Team, T. (2019). Properties of rubble-pile asteroid (101955) Bennu from OSIRIS-REx imaging and thermal analysis. *Nature Astronomy*.

Dell'oro, A., Paolicchi, P., Marzari, F., Dotto, E., and Vanzani, V. (1998). Trojan collision probability: a statistical approach. *Astron. Astrophys*, *339*, 272–277.

Delsemme, A. H. (1992). Cometary origin of carbon, nitrogen and water on the Earth. *Origins of life and evolution of the biosphere*, *21*(5), 279–298.

DeMeo, F. E., Alexander, D., Walsh, K. J., Chapman, C. R., and Binzel, R. P. (2015a). The Compositional Structure of the Asteroid Belt. In *Asteroids IV*, (pp. 13–42).

DeMeo, F. E., Binzel, R. P., Carry, B., Polishook, D., and Moskovitz, N. A. (2014). Unexpected D-type interlopers in the inner main belt. *Icarus*, *229*, 392–399.

DeMeo, F. E., Binzel, R. P., Slivan, S. M., and Bus, S. J. (2009). An extension of the Bus asteroid taxonomy into the near-infrared. *Icarus*, *202*(1), 16–180.

DeMeo, F. E., and Carry, B. (2014). Solar System evolution from compositional mapping of the asteroid belt. *Nature*, *505*, 629–634.

DeMeo, F. E., Dumas, C., Cook, J. C., Carry, B., Merlin, F., Verbiscer, A. J., and Binzel, R. P. (2015b). Spectral variability of Charon's 2.21-µm feature. *Icarus*, *246*(C), 213–219.

Desch, S. J., Ciesla, F. J., Hood, L. L., and Nakamoto, T. (2005). Heating of Chondritic Materials in Solar Nebula Shocks. In *Chondrites and the Protoplanetary Disk*, vol. 341, (p. 849).

Desch, S. J., and Cuzzi, J. N. (2000). The Generation of Lightning in the Solar Nebula. *Icarus*, *143*(1), 87–105.

Desch, S. J., Kalyaan, A., O', C. M., and Alexander, D. (2018). The Effect of Jupiter's Formation on the Distribution of Refractory Elements and Inclusions in Meteorites. *The Astrophysical Journal Supplement Series*, *238*, 11–42.

Desch, S. J., Morris, M. A., Connolly, H. C., and Boss, A. P. (2010). A critical examination of the X-wind model for chondrule and calcium-rich, aluminium-rich inclusion formation and radionuclide production. *The Astrophysical Journal*, *725*, 692–711.

Dodson-Robinson, S. E., Willacy, K., Bodenheimer, P., Turner, N. J., and Beichman, C. A. (2009). Ice lines, planetesimal composition and solid surface density in the solar nebula. *Icarus*, *200*(2), 672–693.

Donaldson Hanna, K., Wyatt, M. B., Thomas, I. R., Bowles, N. E., Greenhagen, B. T., Maturilli, A., Helbert, J., Paige, D. A., Hanna, D., Wyatt, M. B., Thomas, I. R., Bowles, N. E., Greenhagen, B. T., Maturilli, A., Helbert, J., and Paige, D. A. (2012a). Thermal infrared emissivity measurements under a simulated lunar environment: Application to the Diviner Lunar Radiometer Experiment. *J. Geophys. Res*, *117*, 0–05.

Donaldson Hanna, K. L., Bowles, N. E., Warren, T., Hamilton, V. E., Schrader, D. L., McCoy, T. J., Temple, J., Clack, A., Calcutt, S., and Lauretta, D. S. (2020). Spectral characterization of Bennu analogs using PASCALE: A new experimental set-up for simulating the near-surface conditions of airless bodies. *Journal of Geophysical Research: Planets, submitted*.

Donaldson Hanna, K. L., Schrader, D., Cloutis, E., Cody, G., King, A., McCoy, T., Applin, D., Mann, J., Bowles, N., Brucato, J., Connolly, H., Dotto, E., Keller, L., Lim, L., Clark, B., Hamilton, V., Lantz, C., Lauretta, D., Russell, S., and Schofield, P. (2019). Spectral characterization of analog samples in anticipation of OSIRIS-REx's arrival at Bennu: A blind test study. *Icarus*, *319*, 701–723.

Donaldson Hanna, K. L., Thomas, I. R., Bowles, N. E., Greenhagen, B. T., Pieters, C. M., Mustard, J. F., Jackson, C. R. M., and Wyatt, M. B. (2012b). Laboratory emissivity measurements of the plagioclase solid solution series under varying environmental conditions. *Journal of Geophysical Research: Planets*, *117*(E11), 1 – 7.

DuFresne, E. R., and Anders, E. (1962). On the chemical evolution of the carbonaceous chondrites. *Geochimica et Cosmochimica Acta*, *26*, 1085–1114.

Elkins-Tanton, L., Asphaug, E., Bell, J., Bercovici, D., Bills, B., Binzel, R., Bottke, W., Jun, I., Marchi, S., Oh, D., Polanskey, C., Weiss, B., Wenkert, D., and Zuber, M. (2014). Journey to a metal world: Concept for a discovery mission to Psyche. In *44th Lunar and Planetary Science Conference*.

Emery, J. P., and Brown, R. H. (2003). Constraints on the surface composition of Trojan asteroids from near-infrared (0.8-4.0μm) spectroscopy. *Icarus*, *164*(1), 104–121.

Emery, J. P., Cruikshank, D. P., and Van Cleve, J. (2006). Thermal emission spectroscopy (5.2-38 μm) of three Trojan asteroids with the Spitzer Space Telescope: Detection of fine-grained silicates. *Icarus*, *182*(2), 496–512.

Emery, J. P., Fernández, Y., Kelley, M., Warden, K., Hergenrother, C., Lauretta, D., Drake, M., Campins, H., and Ziffer, J. (2014). Thermal infrared observations and thermophysical characterization of OSIRIS-REx target asteroid (101955) Bennu. *Icarus*, *234*, 17–35.

Emery, J. P., Marzari, F., Morbidelli, A., French, L. M., and Grav, T. (2015). The Complex History of Trojan Asteroids. In *Asteroids IV*, (pp. 203–220).

Endress, M., and Bischoff, A. (1996). Carbonates in CI chondrites: Clues to parent body evolution. *Geochimica et Cosmochimica Acta*, *60*(3), 489–507.

Ermakov, A. I., Fu, R. R., Castillo-Rogez, J. C., Raymond, C. A., Park, R. S., Preusker, F., Russell, C. T., Smith, D. E., and Zuber, M. T. (2017). Constraints on Ceres' Internal Structure and Evolution From Its Shape and Gravity Measured by the Dawn Spacecraft. *Journal of Geophysical Research: Planets*, *122*(11), 2267–2293.

Fassett, C. I., and Minton, D. A. (2013). Impact bombardment of the terrestrial planets and the early history of the Solar System. *Nature Geoscience*, *6*, 520–524.

Florczak, M., Lazzaro, D., Mothé-Diniz, T., Angeli, C. A., and Betzler, A. S. (1999). A spectroscopic study of the Themis family. *Astron. Astrophys. Suppl. Ser*, *134*, 463–471.

Fornasier, S., Lantz, C., Barucci, M. A., and Lazzarin, M. (2014). Aqueous alteration on main belt primitive asteroids: Results from visible spectroscopy. *Icarus*, *2333*, 163–178.

Fornasier, S., Lantz, C., Perna, D., Campins, H., Barucci, M. A., and Nesvorny, D. (2016). Spectral variability on primitive asteroids of the Themis and Beagle families: Space weathering effects or parent body heterogeneity? *Icarus*, *269*, 1–14.

Fornasier, S., Lazzarin, M., Barbieri, C., and Barucci, M. A. (1999). Spectroscopic comparison of aqueous altered asteroids with CM2 carbonaceous chondrite meteorites. *Astron. Astrophys. Suppl. Ser*, *135*, 65–73.

Franchi, I. A., Wright, I. P., Sexton, A. S., and Pillinger, C. T. (1999). The oxygen-isotopic composition of Earth and Mars. *Meteoritics & Planetary Science*, *34*(4), 657–661.

Frank, D. R., Zolensky, M., Martinez, J., Mikouchi, T., Ohsumi, K., Hagiya, K., Satake, W., Le, L., Ross, D., and Peslier, A. (2011). A CAI in the Ivuna CI1 chondrite. In *42nd Lunar and Planetary Science Conference*.

Friedrich, J. M., Abreu, N. M., Wolf, S. F., Troiano, J. M., Stanek, G. L., and Friedrich, J. M. (2018). Redox-influenced trace element compositional differences among variably aqueously altered CM chondrites. *Geochimica et Cosmochimica Acta*, *237*, 1–17.

Fuchs, L. H., Olsen, E., and Jensen, K. J. (1973). Mineralogy, Mineral-Chemistry, and Composition of the Murchison (C2) Meteorite. *Smithsonian Contributions to the Earth Sciences*, *10*, 1–39.

Fujiya, W. (2018). Oxygen isotopic ratios of primordial water in carbonaceous chondrites. *Earth and Planetary Science Letters*, *481*, 264–272.

Fujiya, W., Sugiura, N., Sano, Y., and Hiyagon, H. (2013). Mn-Cr ages of dolomites in CI chondrites and the Tagish Lake ungrouped carbonaceous chondrite. *Earth and Planetary Science Letters*, *362*, 130–142.

Gaffey, M. J. (1976). Spectral reflectance characteristics of the meteorite classes. *Journal of Geophysical Research*, *81*(5), 905–920.

Gaffey, M. J., Bell, J. F., Brown, R. H., Burbine, T. H., Piatek, J. L., Reed, K. L., and Chaky, D. A. (1993). Mineralogical Variations within the S-Type Asteroid Class. *Icarus*, *106*, 573–602.

Gaffey, M. J., Cloutis, E. A., Kelley, M. S., and Reed, K. L. (2006). Mineralogy of Asteroids. In *Meteorites and the early solar system II*, (pp. 183 – 204).

Gaffey, M. J., and Gilbert, S. L. (1998). Asteroid 6 Hebe: The probable parent body of the H-type ordinary chondrites and the IIE iron meteorites. *Meteoritics and Planetary Science*, *33*(6), 1281–1295.

Gardner, J. P., Mather, J. C., Clampin, M., Doyon, R., Greenhouse, M. A., Hammel, H. B., Hutchings, J. B., Jakobsen, P., Lilly, S. J., Long, K. S., Lunine, J. I., Mccaughrean, M. J., Mountain, M., Nella, J., Rieke, G. H., Rieke, M. J., Rix, H.-W., Smith, E. P., Sonneborn, G., Stiavelli, M., Stockman, H. S., Windhorst, R. A., and Wright, G. S. (2006). The James Webb space telescope. *Space Science Reviews*, *123*(4), 485–606.

Garenne, A., Beck, P., Montes-Hernandez, G., Brissaud, O., Schmitt, B., Quirico, E., Bonal, L., Beck, C., and Howard, K. T. (2016). Bidirectional reflectance spectroscopy of carbonaceous chondrites: Implications for water quantification and primary composition. *Icarus*, *264*, 172–183.

Garenne, A., Beck, P., Montes-Hernandez, G., Chiriac, R., Toche, F., Quirico, E., Bonal, L., and Schmitt, B. (2014). The abundance and stability of "water" in type 1 and 2 carbonaceous chondrites (CI, CM and CR). *Geochimica et Cosmochimica Acta*, *137*, 93–112.

Garvie, L. A. J., and Buseck, P. R. (2005). Structure and bonding of carbon in clays from CI carbonaceous chondrites. In *36th Lunar and Planetary Science Conference*.

Gates-Rector, S., and Blanton, T. (2019). The Powder Diffraction File: a quality materials characterization database. *Powder Diffraction*, *34*(4), 352–360.

Gil-Hutton, R., and Licandro, J. (2010). Taxonomy of asteroids in the Cybele region from the analysis of the Sloan Digital Sky Survey colors. *Icarus*, *206*(2), 729–734.

Goldreich, P., Lithwick, Y., and Sari, R. (2004). Planet Formation by Coagulation: A Focus on Uranus and Neptune. *Annual Review of Astronomy and Astrophysics*, *42*(1), 549–601.

Gomes, R., Levison, H. F., Tsiganis, K., and Morbidelli, A. (2005). Origin of the cataclysmic Late Heavy Bombardment period of the terrestrial planets. *Nature*, *435*(7041), 466.

Gounelle, M., and Zolensky, M. E. (2001). A terrestrial origin for sulfate veins in CI1 chondrites. *Meteoritics & Planetary Science*, *36*(10), 1321–1329.

Gradie, J., Veverka, J., and Buratti, B. (1980). The effects of scattering geometry on the spectrophotometric properties of powdered material. In *Proc. Lunar Planet. Sci. Conf. 11th*, (pp. 799–815).

Greenwood, R. C., and Franchi, I. A. (2004). Alteration and metamorphism of CO3 chondrites: Evidence from oxygen and carbon isotopes. Tech. rep.

Greenwood, R. C., Howard, K. T., Fran-Chi, I. A., Zolensky, M. E., Buchanan, P. C., and Gibson, J. M. (2014). Oxygen isotope evidence for the relationship between CM and CO chondrites: could they both coexist on a single asteroid? In *45th Lunar and Planetary Science Conference*.

Grimm, R. E., and Mcsween, H. Y. (1989). Water and the thermal evolution of carbonaceous chondrite parent bodies. *Icarus*, *82*(2), 244–280.

Grimm, R. E., and McSween, H. Y. (1993). Heliocentric zoning of the asteroid belt by aluminium-26 heating. *Science*, *259*, 653–655.

Grossman, J. N. (1994). The Meteoritical Bulletin, No. 76, 1994 January: The U.S. Antarctic Meteorite Collection. *Meteoritics*, *29*(1).

Grossman, J. N. (1998). The Meteoritical Bulletin, No. 82, 1998 July. *Meteoritics & Planetary Science*, *33*, A221–A239.

Grossman, L. (1972). Condensation in the primitive solar nebula. *Geochimica et Cosmochimica Acta*, *36*(5), 597–619.

Grott, M., Knollenberg, J., Borgs, B., Hänschke, F., Kessler, E., Helbert, J., Maturilli, A., and Müller, N. (2017). The MASCOT radiometer MARA for the Hayabusa 2 mission. *Space Science Reviews*, *208*(1-4), 413–431.

Grott, M., Knollenberg, J., Hamm, M., Ogawa, K., Jaumann, R., Otto, K. A., Delbo, M., Michel, P., Biele, J., Neumann, W., Knapmeyer, M., Kührt, E., Senshu, H., Okada, T., Helbert, J., Maturilli, A., Müller, N., Hagermann, A., Sakatani, N., Tanaka, S., Arai, T., Mottola, S., Tachibana, S., Pelivan, I., Drube, L., Vincent, J., Yano, H., Pilorget, C., and Matz, K. D. (2019). Low thermal conductivity boulder with high porosity identified on C-type asteroid (162173) Ryugu. *Nature Astronomy*, *3*(11), 971–976.

Grott, M., Knollenberg, J., Maturilli, A., Helbert, J., Müller, N., and Kührt, E. (2013). Mineralogical Surface Characterization using the MASCOT Radiometer MARA on the Hayabusa 2 Mission. In *44th Lunar and Planetary Science Conference*.

Gundlach, B., and Blum, J. (2013). A new method to determine the grain size of planetary regolith. *Icarus*, *223*(1), 479–492.

Hamilton, V. E. (2000). Thermal infrared emission spectroscopy of the pyroxene mineral series. *Journal of Geophysical Research: Planets*, *105*(E4), 9701–9716.

Hamilton, V. E. (2010). Thermal infrared (vibrational) spectroscopy of Mg-Fe olivines: A review and applications to determining the composition of planetary surfaces. *Chemie der Erde - Geochemistry*, *70*(1), 7–33.

Hamilton, V. E., Simon, A. A., Christensen, P. R., Reuter, D. C., Blark, B. E., Barucci, M. A., Bowles, N. E., Boynton, W. V., Brucato, J. R., Cloutis, E. A., Connolly Jr, H. C., Donaldson Hanna, K. L., Keller, L. P., Lantz, C., Li, J., Lim, L. F., Mccoy, T. J., Merlin, F., Nolan, M. C., Praet, A., Rozitis, B., Sandford, S. A., Schrader, D. L., Thomas, C. A., Zou, X. D., Lauretta, D. S., and OSIRIS-REx Team, T. (2019). Evidence for widespread hydrated minerals on asteroid (101955) Bennu. *Nature Astronomy*, *3*, 332 – 340.

Hanna, R., Hamilton, V., Haberle, C., King, A., Abreu, N., and Friedrich, J. (2020). Distinguishing relative aqueous alteration and heating among CM chondrites with IR spectroscopy. *Icarus*, *346*, 113760.

Hanuš, J., Delbo', M., Vokrouhlický, D., Pravec, P., Emery, J. P., Alí-Lagoa, V., Bolin, B., Devogèle, M., Dyvig, R., Galád, A., Jedicke, R., Kornoš, L., Kušnirák, P., Licandro, J., Reddy, V., Rivet, J.-P., Világi, J., and Warner, B. D. (2016). Near-Earth asteroid (3200) Phaethon: Characterization of its orbit, spin state, and thermophysical parameters. *A&A*, *592*.

Hargrove, K. D., Kelley, M. S., Campins, H., Licandro, J., and Emery, J. (2012). Asteroids (65) Cybele, (107) Camilla and (121) Hermione: Infrared spectral diversity among the Cybeles. *Icarus*, *221*(1), 453–455.

Harris, A. W. (1998). A Thermal Model for Near-Earth Asteroids. *Icarus*, *131*(2), 291–301.

Henderson, B. G., and Jakosky, B. M. (1994). Near-surface thermal gradients and their effects on mid-infrared emission spectra of planetary surfaces. *Journal of Geophysical Research*, *99*(E9), 19063–19073.

Hergenrother, C. W., Antonietta Barucci, M., Barnouin, O., Bierhaus, B., Binzel, R. P., Bottke, W. F., Chesley, S., Clark, B. C., Clark, B. E., Cloutis, E., Drouet, C., Delbo, M., Emery, J., Gaskell, B., Howell, E., Keller, L., Kelley, M., Marshall, J., Michel, P., Nolan, M., Rizk, B., Scheeres, D., Takir, D., Vokrouhlický, D. D., Beshore, E., Lauretta, D. S., Observatory, A., and Rico, P. (2014). The Design Reference Asteroid for the OSIRIS-REx Mission Target (101955) Bennu. Tech. rep.

Hester, J. J., and Desch, S. J. (2005). Understanding our Origins: Star Formation in H ii Region Environments. *Chondrites and the Protoplanetary Disk*, *341*, 107.

Hester, J. J., Desch, S. J., Healy, K. R., and Leshin, L. A. (2004). The cradle of the solar system. *Science*, *304*(5674), 1116–1117.

Hiroi, T., and Pieters, C. M. (1996). Reflectance spectra (UV- 3um) of heated Ivuna (CI) meteorite and newly identified thermally metamorphosed CM chondrites. In *27th Lunar and Planetary Science Conference*, (pp. 551–552).

Hiroi, T., Pieters, C. M., Zolensky, M. E., and Lipschutz, M. E. (1993). Evidence of thermal metamorphism on the C,G,B, and F asteroids. *Science*, *261*, 1016–1018.

Hiroi, T., Zolensky, M. E., and Pieters, C. M. (1997). Characterization of Unusual CI/CM/CR Meteorites from Reflectance Spectroscopy. In *28th Lunar and Planetary Science Conference*, vol. 27, (pp. 577–578).

Hiroi, T., Zolensky, M. E., and Pieters, C. M. (2001). The Tagish Lake Meteorite: A Possible Sample from a D-Type Asteroid. *Science*, *293*(5538), 2234–2236.

Hiroi, T., Zolensky, M. E., Pieters, C. M., and Lipschutz, M. E. (1996). Thermal metamorphism of the C, G, B, and F asteroids seen from the 0.7 µm, 3 µm, and UV absorption strengths in comparison with carbonaceous chondrites. *Meteoritics & Planetary Science*, *31*(3), 321–327.

Horner, S. D., and Rieke, M. J. (2004). The near-infrared camera (NIRCam) for the James Webb Space Telescope (JWST). In J. C. Mather (Ed.) *Optical, Infrared, and Millimeter Space Telescopes*, vol. 5487, (p. 628). SPIE.

Howard, K., Alexander, C., Schrader, D., and Dyl, K. (2015). Classification of hydrous meteorites (CR, CM and C2 ungrouped) by phyllosilicate fraction: PSD-XRD modal mineralogy and planetesimal environments. *Geochimica et Cosmochimica Acta*, *149*, 206–222.

Howard, K., Benedix, G., Bland, P., and Cressey, G. (2009). Modal mineralogy of CM2 chondrites by X-ray diffraction (PSD-XRD). Part 1: Total phyllosilicate abundance and the degree of aqueous alteration. *Geochimica et Cosmochimica Acta*, *73*, 4576–4589.

Howard, K., Benedix, G., Bland, P., and Cressey, G. (2010). Modal mineralogy of CV3 chondrites by X-ray diffraction (PSD-XRD). *Geochimica et Cosmochimica Acta*, *74*(17), 5084–5097.

Howard, K., Benedix, G., Bland, P., and Cressey, G. (2011). Modal mineralogy of CM chondrites by X-ray diffraction (PSD-XRD): Part 2. Degree, nature and settings of aqueous alteration. *Geochimica et Cosmochimica Acta*, *75*(10), 2735–2751.

Hutchison, R. (2004). *Meteorites: A Petrologic, Chemical and Isotopic Synthesis*. Cambridge University Press.

Ikeda, and Yukio (1991). Petrology and mineralogy of the Yamato-82162 chondrite (CI). *Proc. NIPR Symp. Antarct. Meteorites*, *4*, 187–225.

Ikeda, Y. (1992). An overview of the research consortium, "Antarctic carbonaceouschondrites with CI affinities, Yamato-86720, Yamato-82162, and Belgica-7904". *Proc. NIPR Symp. Antarct. Meteorites*, *5*, 49–73.

Inaba, S., Wetherill, G. W., and Ikoma, M. (2003). Formation of gas giant planets: Core accretion models with fragmentation and planetary envelope. *Icarus*, *166*(1), 46–62.

Ivanova, M. A., Lorenz, C. A., Nazarov, M. A., Brandstaetter, F., Franchi, I. A., Moroz, L. V., Clayton, R. N., and Bychkov, A. Y. (2010). Dhofar 225 and Dhofar 735: Relationship to CM2 chondrites and metamorphosed carbonaceous chondrites, Belgica-7904 and Yamato-86720. *Meteoritics & Planetary Science*, *45*, 1108 – 1123.

Iwata, T., Kitazato, K., Abe, M., Ohtake, M., Arai, T., Arai, T., Hirata, N., Hiroi, T., Honda, C., Imae, N., Komatsu, M., Matsunaga, T., Matsuoka, M., Matsuura, S., Nakamura, T., Nakato, A., Nakauchi, Y., Osawa, T., Senshu, H., Takagi, Y., Tsumura, K., Takato, N., Watanabe, S.-i., Barucci, M. A., Palomba, E., and Ozaki, M. (2017). NIRS3: The Near Infrared Spectrometer on Hayabusa2. *Space Science Reviews*, *208*(1-4), 317–337.

Javoy, M. (1995). The integral enstatite chondrite model of the Earth. *Geophysical Research Letters*, *22*(16), 2219–2222.

Javoy, M., Kaminski, E., Guyot, F., Andrault, D., Sanloup, C., Moreira, M., Labrosse, S., Jambon, A., Agrinier, P., Davaille, A., and Jaupart, C. (2010). The chemical composition of the Earth: Enstatite chondrite models. *Earth and Planetary Science Letters*, *293*(3-4), 259–268.

Jenniskens, P., Shaddad, M. H., Numan, D., Elsir, S., Kudoda, A. M., Zolensky, M. E., Le, L., Robinson, G. A., Friedrich, J. M., Rumble, D., Steele, A., Chesley, S. R., Fitzsimmons, A., Duddy, S., Hsieh, H. H., Ramsay, G., Brown, P. G., Edwards, W. N., Tagliaferri, E., Boslough, M. B., Spalding, R. E., Dantowitz, R., Kozubal, M., Pravec, P., Borovicka, J., Charvat, Z., Vaubaillon, J., Kuiper, J., Albers, J., Bishop, J. L., Mancinelli, R. L., Sandford, S. A., Milam, S. N., Nuevo, M., and Worden, S. P. (2009). The impact and recovery of asteroid 2008 TC3. *Nature*, *458*(7237), 485–488.

Jewitt, D., and Li, J. (2010). Activity in Geminid parent (3200) Phaethon. *The Astronomical Journal*, *140*(5), 1519–1527.

Jewitt, D., Li, J., and Agarwal, J. (2013). The dust tail of asteroid (3200) Phaethon. *The Astrophysical Journal Letters*, *771*(5pp), 36.

Johansen, A., Oishi, J. S., Low, M.-M. M., Klahr, H., Henning, T., and Youdin, A. (2007). Rapid planetesimal formation in turbulent circumstellar disks. *Nature*, *448*(7157), 1022–1025.

Jones, T. D., Lebofsky, L. A., Lewis, J. S., and Marley, M. S. (1990). The composition and origin of the C, P, and D asteroids: Water as a tracer of thermal evolution in the outer belt. *Icarus*, *88*(1), 172–192.

Kameda, S., Suzuki, H., Takamatsu, T., Cho, Y., Yasuda, T., Yamada, M., Sawada, H., Honda, R., Morota, T., Honda, C., Sato, M., Okumura, Y., Shibasaki, K., Ikezawa, S., and Sugita, S. (2017). Preflight Calibration Test Results for Optical Navigation Camera Telescope (ONC-T) Onboard the Hayabusa2 Spacecraft. *Space Science Reviews*, *208*(1-4), 17–31.

Kant, I. (1755). *Algemeine Naturgeschichte und Theories des Himmel*.

Kelley, M. S., Woodward, C. E., Gehrz, R. D., Reach, W. T., and Harker, D. E. (2017). Mid-infrared spectra of comet nuclei. *Icarus*, *284*, 344–358.

Kenyon, S. J., and Bromley, B. C. (2006). Terrestrial Planet Formation. I. The Transition from Oligarchic Growth to Chaotic Growth. *The Astronomical Journal*, *131*(3), 1837–1850.

Kimura, M., Grossman, J. N., and Weisberg, M. K. (2011). Fe-Ni metal and sulfide minerals in CM chondrites: An indicator for thermal history. *Meteoritics & Planetary Science*, *46*(3), 431–442.

King, A., Bates, H., Krietsch, D., Busemann, H., Clay, P., Schofield, P., and Russell, S. (2019). The Yamato-type (CY) carbonaceous chondrite group: Analogues for the surface of asteroid Ryugu? *Geochemistry*, *79*(4), 125531.

King, A. J., Greenwood, R. C., Gibson, J. M., Schofield, P. F., Fran-Chi, I. A., and Russell, S. S. (2018a). The Oxygen Isotopic Composition of the Most Aqueously Altered CM Carbonaceous Chondrites. In *49th Lunar and Planetary Science Conference*.

King, A. J., Maturilli, A., Schofield, P. F., Helbert, J., and Russell, S. (2017a). The thermal history of CI and CM chondrites and their relationship to primitive asteroid surfaces. In *80th Annual Meeting of The Meteoritical Society*.

King, A. J., Phillips, K. J., Strekopytov, S., Vita-Finzi, C., and Russell, S. S. (2020). Terrestrial modification of the Ivuna meteorite and a reassessment of the chemical composition of the CI type specimen. *Geochimica et Cosmochimica Acta*, *268*, 73–89.

King, A. J., Russell, S. S., Schofield, P. F., Humphreys-Williams, E. R., Strekopytov, S., Abernethy, F. A. J., Verchovsky, A. B., and Grady, M. M. (2018b). The alteration history of the Jbilet Winselwan CM carbonaceous chondrite: An analog for C-type asteroid sample return. *Meteoritics & Planetary Science*, *54*(3), 521–543.

King, A. J., Schofield, P. F., Howard, K. T., and Russell, S. S. (2015a). Modal mineralogy of CI and CI-like chondrites by X-ray diffraction. *Geochimica et Cosmochimica Acta*, *165*, 148–160.

King, A. J., Schofield, P. F., and Russell, S. S. (2017b). Type 1 aqueous alteration in CM carbonaceous chondrites: Implications for the evolution of water-rich asteroids. *Meteoritics & Planetary Science*, *52*(6), 1197–1215.

King, A. J., Solomon, J. R., Schofield, P. F., and Russell, S. S. (2015b). Characterising the CI and CI-like carbonaceous chondrites using thermogravimetric analysis and infrared spectroscopy. *Earth, Planets and Space*, *67*(198).

Kitazato, K., Milliken, R. E., Iwata, T., Abe, M., Ohtake, M., Matsuura, S., Arai, T., Nakauchi, Y., Nakamura, T., Matsuoka, M., Senshu, H., Hirata, N., Hiroi, T., Pilorget, C., Brunetto, R., Poulet, F., Riu, L., Bibring, J.-P., Takir, D., Domingue, D. L., Vilas, F., Barucci, M. A., Perna, D., Palomba, E., Galiano, A., Tsumura, K., Osawa, T., Komatsu, M., Nakato, A., Arai, T., Takato, N., Matsunaga, T., Takagi, Y., Matsumoto, K., Kouyama, T., Yokota, Y., Tatsumi, E., Sakatani, N., Yamamoto, Y., Okada, T., Sugita, S., Honda, R., Morota, T., Kameda, S., Sawada,

H., Honda, C., Yamada, M., Suzuki, H., Yoshioka, K., Hayakawa, M., Ogawa, K., Cho, Y., Shirai, K., Shimaki, Y., Hirata, N., Yamaguchi, A., Ogawa, N., Terui, F., Yamaguchi, T., Takei, Y., Saiki, T., Nakazawa, S., Tanaka, S., Yoshikawa, M., Watanabe, S., and Tsuda, Y. (2019). The surface composition of asteroid 162173 Ryugu from Hayabusa2 near-infrared spectroscopy. *Science*, *364*(6437), 272–275.

Kley, W., and Nelson, R. (2012). Planet-Disk Interaction and Orbital Evolution. *Annual Review of Astronomy and Astrophysics*, *50*(1), 211–249.

Kobuko, E., and Ida, S. (1998). Oligarchic growth of planetesimals. *Icarus*, *131*, 171–178.

Kobuko, E., and Ida, S. (2000). Formation of protoplanets from planetesimals. *Icarus*, *143*, 15–27.

Konopliv, A. S., Park, R. S., Vaughan, A. T., Bills, B. G., Asmar, S. W., Ermakov, A. I., Rambaux, N., Raymond, C. A., Castillo-Rogez, J. C., Russell, C. T., Smith, D. E., and Zuber, M. T. (2018). The Ceres gravity field, spin pole, rotation period and orbit from the Dawn radiometric tracking and optical data. *Icarus*, *299*, 411–429.

Korotev, R. L. (2005). Lunar geochemistry as told by lunar meteorites. *Chemie der Erde*, *65*(4), 297–346.

Kruijer, T. S., Touboul, M., Fischer-Godde, M., Bermingham, K. R., Walker, R. J., and Kleine, T. (2014). Protracted core formation and rapid accretion of protoplanets. *Science*, *344*(6188), 1150–1153.

Küppers, M., O 'rourke, L., Bockelée-Morvan, D., Zakharov, V., Lee, S., Von Allmen, P., Carry, B., Teyssier, D., Marston, A., Müller, T., Crovisier, J., Barucci, M. A., and Moreno, R. (2014). Localized sources of water vapour on the dwarf planet (1) Ceres. *Nature*, *505*, 525–527.

Kuramoto, K., Kawa-Katsu, Y., Fujimoto, M., Genda, H., Imamura, T., Kameda, S., Matsumoto, K., Miyamoto, H., Morota, T., Na-Gaoka, H., Nakamura, T., Ogawa, K., Otake, H., Ozaki, M., Sasaki, S., Senshu, H., Tachibana, S., Terada, N., Usui, T., Wada, K., and Watanabe, S. (2018). Martian moons exploration (MMX) conceptual study update. In *49th Lunar and Planetary Science Conference*.

Landsman, Z. A., Licandro, J., Campins, H., Ziffer, J., de Prá, M., and Cruikshank, D. P. (2016). The Veritas and Themis asteroid families: 5 to 14 micron spectra with the Spitzer Space Telescope. *Icarus*, *269*, 62–74.

Lane, M. D., and Christensen, P. R. (1997). Thermal infrared emission spectroscopy of anhydrous carbonates. *Journal of Geophysical Research: Planets*, *102*(E11), 25581–25592.

Lane, M. D., Glotch, T. D., Darby Dyar, M., Pieters, C. M., Klima, R., Hiroi, T., Bishop, J. L., and Sunshine, J. (2011). Midinfrared spectroscopy of synthetic olivines: Thermal emission, specular and diffuse reflectance, and attenuated total reflectance studies of forsterite to fayalite. *J. Geophys. Res*, *116*, 8010.

Laplace, P.-S. (1796). *Exposition du Systeme du Monde*. Paris: Courcier.

Larson, H. P., Feierberg, M. A., Fink, U., and Smith, H. A. (1979). Remote spectroscopic identification of carbonaceous chondrite mineralogies: Applications to Ceres and Pallas. *Icarus*, *39*(2), 257–271.

Lauretta, D. S., Balram-Knutson, S. S., Beshore, E., Boynton, W. V., DAubigny, C. D., DellaGiustina, D. N., Enos, H. L., Gholish, D. R., Hergenrother, C. W., Howell, E. S., Johnson, C. A., Morton, E. T., Nolan, M. C., Rizk, B., Roper, H. L., Bartels, A. E., Bos, B. J., Dworkin, J. P., Highsmith, D. E., Lorenz, D. A., Lim, L. F., Mink, R., Moreau, M. C., Nuth, J. A., Reuter, D. C., Simon, A. A., Bierhaus, E. B., Bryan, B. H., Ballouz, R., Barnouin, O. S., Binzel, R. P., Bottke, W. F., Hamilton, V. E., Walsh, K. J., Chesley, S. R., Christensen, P. R., Clark, B. E., Connolly, H. C., Crombie, M. K., Daly, M. G., Emery, J. P., McCoy, T. J., McMahon, J. W., Scheeres, D. J., Messenger, S., Nakamura-Messenger, K., Righter, K., and Sandford, S. A. (2017). OSIRIS-REx: Sample return from asteroid (101955) Bennu. *Space Science Reviews*, *212*, 925 – 984.

Lauretta, D. S., DellaGiustina, D. N., Bennett, C. A., Golish, D. R., Becker, K. J., Balram-Knutson, S. S., Barnouin, O. S., Becker, T. L., Bottke, W. F., Boynton, W. V., Campins, H., Clark, B. E., Connolly, H. C., Drouet d'Aubigny, C. Y., Dworkin, J. P., Emery, J. P., Enos, H. L., Hamilton, V. E., Hergenrother, C. W., Howell, E. S., Izawa, M. R. M., Kaplan, H. H., Nolan, M. C., Rizk, B., Roper, H. L., Scheeres, D. J., Smith, P. H., Walsh, K. J., and Wolner, C. W. V. (2019a). The unexpected surface of asteroid (101955) Bennu. *Nature*, (101955), 1.

Lauretta, D. S., Hergenrother, C. W., Chesley, S. R., Leonard, J. M., Pelgrift, J. Y., Adam, C. D., Asad, M. A., Antreasian, P. G., Ballouz, R. L., Becker, K. J., Bennett, C. A., Bos, B. J., Bottke, W. F., Brozović, M., Campins, H., Connolly, H. C., Daly, M. G., Davis, A. B., de León, J., DellaGiustina, D. N., Drouet d'Aubigny, C. Y., Dworkin, J. P., Emery, J. P., Farnocchia, D., Glavin, D. P., Golish, D. R., Hartzell, C. M., Jacobson, R. A., Jawin, E. R., Jenniskens, P., Kidd, J. N., Lessac-Chenen, E. J., Li, J. Y., Libourel, G., Licandro, J., Liounis, A. J., Maleszewski, C. K., Manzoni, C., May, B., McCarthy, L. K., McMahon, J. W., Michel, P., Molaro, J. L., Moreau, M. C., Nelson, D. S., Owen, W. M., Rizk, B., Roper, H. L., Rozitis, B., Sahr, E. M., Scheeres, D. J., Seabrook, J. A., Selznick, S. H., Takahashi, Y., Thuillet, F., Tricarico, P., Vokrouhlický, D., and Wolner, C. W. (2019b). Episodes of particle ejection from the surface of the active asteroid (101955) Bennu. *Science*, *366*(6470).

Lebofsky, L. A. (1980). Infrared reflectance spectra of asteroids: A search for water of hydration. Tech. Rep. 5.

Lebofsky, L. A., Feierberg, M. A., Tokunaga, A. T., Larson, H. P., and Johnson, J. R. (1981). The 1.7- to 4.2-µm spectrum of asteroid 1 Ceres: Evidence for structural water in clay minerals. *Icarus*, *48*(3), 453–459.

Lecar, M., Podolak, M., Sasselov, D., and Chiang, E. (2006). On the location of the snow line in a protoplanetary disk. *The Astrophysical Journal*, *640*, 1115 – 1118.

Lee, M. R. (1993). The petrography, mineralogy and origins of calcium sulphate within the Cold Bokkeveld CM carbonaceous chondrite. *Meteoritics*, *28*, 53–62.

Lee, M. R., Cohen, B. E., King, A. J., and Greenwood, R. C. (2019). The diversity of CM carbonaceous chondrite parent bodies explored using Lewis Cliff 85311. *Geochimica et Cosmochimica Acta*, *264*, 224–244.

Lee, M. R., Lindgren, P., King, A. J., Greenwood, R. C., Franchi, I. A., and Sparkes, R. (2016). Elephant Moraine 96029, a very mildly aqueously altered and heated CM carbonaceous chondrite: Implications for the drivers of parent body processing. *Geochimica et Cosmochimica Acta*, *187*, 237–259.

Lee, M. R., Sofe, M. R., Lindgren, P., Starkey, N. A., and Franchi, I. A. (2013). The oxygen isotope evolution of parent body aqueous solutions as recorded by multiple carbonate generations in the Lonewolf Nunataks 94101 CM2 carbonaceous chondrite. *Geochimica et Cosmochimica Acta*, *121*, 452–466.

Leinhardt, Z. M., and Stewart, S. T. (2012). Collisions between gravity-dominated bodies I. Outcome regimes and scaling laws. *The Astrophysical Journal*, *745*(27pp), 79.

Levison, H. F. (2016). Lucy: Surveying the diversity of the Trojan asteroids: The fossils of planet formation. In *47th Lunar and Planetary Science Conference*.

Lin, D. N. C., and Papaloizou, J. (1986). On the tidal interation between protoplanets and the protoplanetary disk. III. Orbital migration of protoplanets. Tech. rep.

Lindgren, P., Lee, M. R., Sofe, M., and Burchell, M. J. (2011). Microstructure of calcite in the CM2 carbonaceous chondrite LON 94101: Implications for deformation history during and/or after aqueous alteration. *Earth and Planetary Science Letters*, *306*(3-4), 289–298.

Lindgren, P., Lee, M. R., Sparkes, R., Greenwood, R. C., Hanna, R. D., Franchi, I. A., King, A. J., Floyd, C., Martin, P.-E., Hamilton, V. E., and Haberle, C. (2020). Signatures of the post-hydration heating of highly aqueously altered CM carbonaceous chondrites and implications for interpreting asteroid sample returns. *Geochimica et Cosmochimica Acta*.

Lipschutz, M. E., Zolensky, M. E., and Bell, M. S. (1999). New petrographic and trace element data on thermally metamorphosed carbonaceous chondrites. *Antarctic Meteorite Research*, *12*, 57–80.

Lodders, K. (2003). Solar System Abundances and Condensation Temperatures of the Elements. *The Astrophysical Journal*, *591*, 1220–1247.

Logan, L. M., Hunt, G. R., Salisbury, J. W., and Balsamo, S. R. (1973). Compositional implication of Christiansen frequency maximums for infrared remote sensing applications. *Journal of Geophysical Research*, *78*(23), 430–450.

Lucey, P. G., Honniball, C. I., Gillis Davis, J., Li, S., and Hibbitts, K. (2017). Water Absorption at 6 Microns: A New Tool For Remote Measurements of Lunar Surface Water Abundance and Variation. In *48th Lunar and Planetary Science Conference*.

MacPherson, G. J. (2014). Calcium-aluminium-rich inclusions in chondritic meteorites. In *Treatise on Geochemistry: Second Edition, Volume 1*, (pp. 139–174).

Mahan, B., Moynier, F., Beck, P., Pringle, E. A., and Siebert, J. (2018). A history of violence: Insights into post-accretionary heating in carbonaceous chondrites from volatile element abundances, Zn isotopes and water contents. *Geochimica et Cosmochimica Acta*, *220*, 19–35.

Mamajek, E. E., Meyer, M. R., Hinz, P. M., Hoffmann, W. F., Cohen, M., and Hora, J. L. (2004). Constraining the Lifetime of Circumstellar Disks in the Terrestrial Planet Zone: A Mid-IR Survey of the 30-Myr-old Tucana-Horologium Association. *Astrophysical Journal*, *612*(1), 496 – 510.

Marchis, F., Enriquez, J., Emery, J., Mueller, M., Baek, M., Pollock, J., Assafin, M., Vieira Martins, R., Berthier, J., Vachier, F., Cruikshank, D., Lim, L., Reichart, D., Ivarsen, K., Haislip, J., and LaCluyze, A. (2012). Multiple asteroid systems: Dimensions and thermal properties from Spitzer Space Telescope and ground-based observations. *Icarus*, *221*(2), 1130–1161.

Marley, M. S., Fortney, J. J., Hubickyj, O., Bodenheimer, P., and Lissauer, J. J. (2007). On the luminosity of young Jupiters. *The Astrophysical Journal*, *655*, 541 – 549.

Martin, A., Emery, J., and Lindsay, S. (2019). Mid-IR spectral effects of regolith porosity: Implications for surface mineralogy of Trojan asteroids. In *EPSC-DPS Joint Meeting*.

Marty, B. (2012). The origins and concentrations of water, carbon, nitrogen and noble gases on Earth. *Earth Planet. Sci. Lett*, *313*, 56–66.

Mason, E., King, A. J., Bates, H. C., Schofield, P. F., Donaldson Hanna, K. L., Bowles, N. E., and Russell, S. S. (2018). Tracing the Earliest Stages of Hydrothermal Alteration on Primitive Asteroids. In *49th Lunar and Planetary Science Conference*.

Matsuoka, K., Nakamura, T., Nakamuta, Y., and Takaoka, N. (1996). Yamato-86789: A heated CM-like carbonaceous chondrite. *Proc. NIPR Symp. Antarct. Meteorites*, *9*, 20–26.

McAdam, M. M., Sunshine, J. M., Howard, K. T., and Mccoy, T. M. (2015). Aqueous alteration on asteroids: Linking the mineralogy and spectroscopy of CM and CI chondrites. *Icarus*, *245*, 320–332.

McCord, T. B., and Zambon, F. (2019). The surface composition of Ceres from the Dawn mission. *Icarus*, *318*, 2–13.

McKinnon, W. B. (2012). Where did Ceres accrete? In *Asteroids, Comets, Meteors*.

McSween, H. Y., Binzel, R. P., De Sanctis, M. C., Ammannito, E., Prettyman, T. H., Beck, A. W., Reddy, V., Le Corre, L., Gaffey, M. J., McCord, T. B., Raymond, C. A., and Russell, C. T. (2013). Dawn; the Vesta-HED connection; and the geologic context for eucrites, diogenites, and howardites. *Meteoritics & Planetary Science*, *48*(11), 2090–2104.

McSween, H. Y., Emery, J. P., Rivkin, A. S., Toplis, M. J., C. Castillo-Rogez, J., Prettyman, T. H., De Sanctis, M. C., Pieters, C. M., Raymond, C. A., and Russell, C. T. (2017). Carbonaceous chondrites as analogs for the composition and alteration of Ceres. *Meteoritics & Planetary Science*, *53*, 1793–1804.

Michalski, J. R., Kraft, M. D., Sharp, T. G., Williams, L. B., and Christensen, P. R. (2006). Emission spectroscopy of clay minerals and evidence for poorly crystalline aluminosilicates on Mars from Thermal Emission Spectrometer data. *Journal of Geophysical Research*, *111*(E3), E03004.

Michel, P., Ballouz, R. L., Barnouin, O. S., Jutzi, M., Walsh, K. J., May, B. H., Manzoni, C., Richardson, D. C., Schwartz, S. R., Sugita, S., Watanabe, S., Miyamoto, H., Hirabayashi, M., Bottke, W. F., Connolly, H. C., Yoshikawa, M., and Lauretta, D. S. (2020). Collisional formation of top-shaped asteroids and implications for the origins of Ryugu and Bennu. *Nature Communications*, *11*(1), 1–11.

Milliken, R. E., and Rivkin, A. S. (2009). Brucite and carbonate assemblages from altered olivine-rich materials on Ceres. *Nature Geoscience*, *2*, 258–261.

Minitti, M. E., and Hamilton, V. E. (2010). A search for basaltic-to-intermediate glasses on Mars: Assessing martian crustal mineralogy. *Icarus*, *210*(1), 135–149.

Miyamoto, H., Yano, H., Scheeres, D. J., Abe, S., Barnouin-Jha, O., Cheng, A. F., Demura, H., Gaskell, R. W., Hirata, N., Ishiguro, M., Michikami, T., Nakamura, A. M., Nakamura, R., Saito, J., and Sasaki, S. (2007). Regolith migration and sorting on asteroid Itokawa. *Science*, *316*(5827), 1011–1014.

Miyamoto, M. (1992). Infrared diffuse reflectance spectra of several thermally metamorphosed carbonaceous chondrites. *Proc. NIPR Symp. Antarct. Meteorites*, *5*, 155–164.

Molaro, J. L., Walsh, K. J., Jawin, E. R., Ballouz, R.-l., Bennett, C. A., DellaGiustina, D. N., Golish, D. R., Drouet, C., Rizk, B., Schwartz, S. R., Hanna, R. D., Martel, S. J., Pajola, M., Campins, H., Ryan, A. J., Bottke, W. F., and Lauretta, D. S. (2020). In situ evidence of thermally induced rock breakdown widespread on Bennu's surface. *Nature Communications*, *11*, 2913.

Morbidelli, A., Bottke, W. F., Froeschle, C., and Michel, P. (2002). Origin and evolution of near-Earth objects. In *Asteroids III*, (pp. 409–422).

Morbidelli, A., Chambers, J., Lunine, J. I., Petit, J. M., Robert, F., Valsecchi, G. B., and Cyr, K. E. (2000). Source regions and timescales for the delivery of water to the Earth. *Meteoritics & Planetary Science*, *35*(6), 1309–1320.

Morbidelli, A., Levison, H. F., Tsiganis, K., and Gomes, R. (2005). Chaotic capture of Jupiter's Trojan asteroids in the early Solar System. *Nature*, *435*(7041), 462–465.

Morbidelli, A., Lunine, J., O'Brien, D., Raymond, S., and Walsh, K. (2012). Building Terrestrial Planets. *Annual Review of Earth and Planetary Sciences*, *40*(1), 251–275.

Morbidelli, A., Walsh, K. J., O'Brien, D. P., Minton, D. A., and Bottke, W. F. (2015). The Dynamical Evolution of the Asteroid Belt. In P. Michel, F. E. DeMeo, and B. W. F (Eds.) *Asteroids IV*, (pp. 493–507). The University of Arizona Press.

Mordasini, C., Klahr, H., Alibert, Y., Benz, W., and Dittkrist, K.-M. (2010). Theory of planet formation. In *Circumstellar Disks and Planets: Science Cases for the second generation VLTI instrumentation*, (pp. 1–23).

Moriarty, G. M., Rumble Iii, D., and Friedrich, J. M. (2009). Compositions of four unusual CM or CM-related Antarctic chondrites. *Chemie der Erde - Geochemistry*, *69*, 161–168.

Morlok, A., Bischoff, A., Stephan, T., Floss, C., Zinner, E. K., and Jessberger, E. K. (2006). Brecciation and chemical heterogeneities of CI chondrites. *Geochimica et Cosmochimica Acta*, *70*, 5371–5394.

Morota, T., Sugita, S., Cho, Y., Kanamaru, M., Tatsumi, E., Sakatani, N., Honda, R., Hirata, N., Kikuchi, H., Yamada, M., Yokota, Y., Kameda, S., Matsuoka, M., Sawada, H., Honda, C., Kouyama, T., Ogawa, K., Suzuki, H., Yoshioka, K., Hayakawa, M., Hirabayashi, M., Miyamoto, H., Michikami, T., Hiroi, T., Hemmi, R., Barnouin, O. S., Ernst, C. M., Kitazato, K., Nakamura, T., Riu, L., Senshu, H., Kobayashi, H., Sasaki, S., Komatsu, G., Tanabe, N., Fujii, Y., Irie, T., Suemitsu, M., Takaki, N., Sugimoto, C., Yumoto, K., Ishida, M., Kato, H., and Moroi, K. (2020). Sample collection from asteroid (162173) Ryugu by Hayabusa2: Implications for surface evolution. *Science*, *368*, 654–659.

Moroz, L. V., Schmidt, M., Schade, U., Hiroi, T., and Ivanova, M. A. (2006). Synchrotron-based infrared microspectroscopy as a useful tool to study hydration states of meteorite constituents. *Meteoritics & Planetary Science*, *41*(8), 1219–1230.

Mousis, O., and Alibert, Y. (2005). On the composition of ices incorporated in Ceres. *Monthly Notices of the Royal Astronomical Society*, *358*(1), 188–192.

Mueller, M., Marchis, F., Emery, J. P., Harris, A. W., Mottola, S., Hestroffer, D., Berthier, J., and di Martino, M. (2010). Eclipsing binary Trojan asteroid Patroclus: Thermal inertia from Spitzer observations. *Icarus*, *205*(2), 505–515.

Murchie, S., Thomas, N., Britt, D., Herkenhoff, K., and Bell, J. F. (1999). Mars Pathfinder spectral measurements of Phobos and Deimos: Comparison with previous data. *Journal of Geophysical Research: Planets*, *104*(E4), 9069–9079.

Nakamura, T. (2005). Post-hydration thermal metamorphism of carbonaceous chondrites. *Journal of Mineralogical and Petrological Sciences*, *100*, 260–272.

Nakamura, T. (2006). Yamato 793321 CM chondrite: Dehydrated regolith material of a hydrous asteroid. *Earth and Planetary Science Letters*, *242*(1), 26–38.

Nakamura, T., Noguchi, T., Tanaka, M., Zolensky, M. E., Kimura, M., Tsuchiyama, A., Nakato, A., Ogami, T., Ishida, H., Uesugi, M., Yada, T., Shirai, K., Fujimura, A., Okazaki, R., Sandford, S. A., Ishibashi, Y., Abe, M., Okada, T., Ueno, M., Mukai, T., Yoshikawa, M., and Kawaguchi, J. (2011). Itokawa Dust Particles: A Direct Link Between S-Type Asteroids and Ordinary Chondrites. *Science*, *333*(6046).

Nakato, A., Brearley, A. J., Nakamura, T., Noguchi, T., Ahn, I., Lee, J. I., Matsuoka, M., and Sasaki, S. (2013). PCA 02012: A Unique Thermally Metamorphosed Carbonaceous Chondrite. In *44th Lunar and Planetary Science Conference*.

Nakato, A., Nakamura, T., Kitajima, F., and Noguchi, T. (2008). Evaluation of dehydration mechanism during heating of hydrous asteroids based on mineralogical and chemical analysis of naturally and experimentally heated CM chondrites. *Earth, Planets and Space*, *60*(8), 855–864.

Nakato, A., Nakamura, T., and Noguchi, T. (2009). Mineralogical and chemical variations recorded in dehydrated carbonaceous chondrites. *Meteoritics & Planetary Science*, *44*, A155.

Nesvorný, D., Vokrouhlický, D., Morbidelli, A., and Bottke, W. F. (2009). Asteroidal source of L chondrite meteorites. *Icarus*, *200*(2), 698–701.

Nicodemus, F. E. (1965). Directional Reflectance and Emissivity of an Opaque Surface. *Applied Optics*, *4*(7), 767.

Nolan, M. C., Magri, C., Howell, E. S., Benner, L. A., Giorgini, J. D., Hergenrother, C. W., Hudson, R. S., Lauretta, D. S., Margot, J. L., Ostro, S. J., and Scheeres, D. J. (2013). Shape model and surface properties of the OSIRIS-REx target Asteroid (101955) Bennu from radar and lightcurve observations. *Icarus*, *226*(1), 629–640.

O'Brien, D. P., Walsh, K. J., Morbidelli, A., Raymond, S. N., and Mandell, A. M. (2014). Water delivery and giant impacts in the 'Grand Tack' scenario. *Icarus*, *239*, 74–84.

Ormel, C. W., Dullemond, C. P., and Spaans, M. (2010). A new condition for the transition from runaway to oligarchic growth. *The Astrophysical Journal Letters*, *714*, 103–107.

Ostrowski, D. R., Lacy, C. H., Gietzen, K. M., and Sears, D. W. (2011). IRTF spectra for 17 asteroids from the C and X complexes: A discussion of continuum slopes and their relationships to C chondrites and phyllosilicates. *Icarus*, *212*(2), 682–696.

Pajola, M., Lazzarin, M., Dalle Ore, C. M., Cruikshank, D. P., Roush, T. L., Magrin, S., Bertini, I., La Forgia, F., and Barbieri, C. (2013). Phobos as a D-type captured asteroid, spectral modeling from 0.25 to 4.0 µm. *The Astrophysical Journal*, *777*, 127 – 133.

Palomba, E., Longobardo, A., De Sanctis, M. C., Stein, N. T., Ehlmann, B., Raponi, A., Ciarniello, M., Ammannito, E., Cloutis, E., Galiano, A., Carrozzo, F. G., Capria, M. T., Zambon, F., Tosi, F., Raymond, C. A., and Russell, C. T. (2017). Bright spots on Ceres: Occator, Oxo and the others. In *48th Lunar and Planetary Science Conference*.

Pascucci, I., and Tachibana, S. (2010). The clearing of protoplanetary disks and of the proto-solar nebula. In *Protoplanetary dust: Astrochemical and cosmochemical perspectives*, (pp. 263–28).

Petaev, M. I., and Wood, J. A. (2005). Meteoritic Constraints on Temperatures, Pressures, Cooling Rates, Chemical Compositions, and Modes of Condensation in the Solar Nebula. In *Chondrites and the Protoplanetary Disk: ASP Conference Series*, vol. 341.

Piani, L., Marrocchi, Y., Rigaudier, T., Vacher, L. G., Thomassin, D., and Marty, B. (2020). Earth's water may have been inherited from material similar to enstatite chondrite meteorites. *Science*, *369*(6507), 1110–1113.

Pieters, C. M., Taylor, L. A., Noble, S. K., Keller, L. P., Hapke, B., Morris, R. V., Allen, C. C., McKay, D. S., and Wentworth, S. (2000). Space weathering on airless bodies: Resolving a mystery with lunar samples. *Meteoritics & Planetary Science*, *35*, 1101–1107.

Pitjeva, E. V., and Pitjev, N. P. (2015). Masses of asteroids and total mass of the main asteroid belt. *International Astronomical Union*, (318), 212 – 217.

Pizzarello, S., and Williams, L. B. (2012). Ammonia in the early Solar System: An account from carbonaceous meteorites. *The Astrophysical Journal*, *749*(6pp), 161.

Pommerol, A., Schmitt, B., Beck, P., and Brissaud, O. (2009). Water sorption on martian regolith analogs: Thermodynamics and near-infrared reflectance spectroscopy. *Icarus*, *204*(1), 114–136.

Popescu, M., Vaduvescu, O., de León, J., Gherase, R. M., Licandro, J., Boac, I. L., Ashley, R. P., Močnik, T., Morate, D., Predatu, M., De Prá, M., Fariña, C., Stoev, H., Díaz Alfaro, M., Ordonez-Etxeberria, I., López-Martínez, F., Errmann, R., Galileo Galilei -INAF, F., José Ana Fernández Pérez, R., and Baja, B. (2019). Astronomy Near-Earth asteroids spectroscopic survey at Isaac Newton Telescope.

Poppe, T., Rgen Blum, J. ., and Henning, T. (2000). Experiments on collisional grain charging of micron-sized preplanetary dust. Tech. rep.

Quirico, E., Bonal, L., Beck, P., Alexander, C. M., Yabuta, H., Nakamura, T., Nakato, A., Flandinet, L., Montagnac, G., Schmitt-Kopplin, P., and Herd, C. D. (2018). Prevalence and nature of heating processes in CM and C2-ungrouped chondrites as revealed by insoluble organic matter. *Geochimica et Cosmochimica Acta*, *241*, 17–37.

Raymond, S. N., and Morbidelli, A. (2014). The Grand Tack model: a critical review. In *Proceedings of the International Astronomical Union*, (pp. 194–203).

Rayner, J. T., Toomey, D. W., Onaka, P. M., Denault, A. J., Stahlberger, W. E., Vacca, W. D., Cushing, M. C., and Wang, S. (2003). SpeX: A Medium-Resolution 0.8–5.5 Micron Spectrograph and Imager for the NASA Infrared Telescope Facility. *Publications of the Astronomical Society of the Pacific*, *115*(805), 362–382.

Reddy, V., and Sanchez, J. A. (2016). Reddy Main Belt Asteroid Spectra V1.0.

Reddy, V., Sanchez, J. A., Bottke, W. F., Cloutis, E. A., Izawa, M. R., O'Brien, D. P., Mann, P., Cuddy, M., Le Corre, L., Gaffey, M. J., and Fujihara, G. (2014). Chelyabinsk meteorite explains unusual spectral properties of Baptistina Asteroid Family. *Icarus*, *237*, 116–130.

Reddy, V., Sanchez, J. A., Nathues, A., Moskovitz, N., Li, J. Y., Cloutis, E. A., Archer, K., Tucker, R., Gaffey, M. J., Mann, J. P., Sierks, H., and Schade, U. (2012). Photometric, spectral phase and temperature effects on 4 Vesta and HED meteorites: Implications for the Dawn mission Lunar. *Icarus*, *217*, 153 – 168.

Reuter, D. C., Simon, A. A., Hair, J., Lunsford, A., Manthripragada, S., Bly, V., Bos, B., Brambora, C., Caldwell, E., Casto, G., Dolch, Z., Finneran, P., Jennings, D., Jhabvala, M., Matson, E., McLelland, M., Roher, W., Sullivan, T., Weigle, E., Wen, Y., Wilson, D., and Lauretta, D. S. (2018). The OSIRIS-REx Visible and InfraRed Spectrometer (OVIRS): Spectral maps of the asteroid Bennu. *Space Science Reviews*, *214*(2), 54.

Reynard, B. (1991). Single-Crystal Infrared Refleetivity of Pure Mg2SiO4 Forsterite (Mgo.s6,Feo. 14)2SIO4 Olivine New Data and a Reappraisal. *Phys Chem Minerals*, *8*, 19–25.

Rivkin, A. S. (2002). Hydrated minerals on asteroids: The astronomical record. In *Asteroids III*, (pp. 235–252).

Rivkin, A. S., Binzel, R. P., and Bus, S. J. (2005). Constraining near-Earth object albedos using near-infrared spectroscopy. *Icarus*, *175*(1), 175–180.

Rivkin, A. S., Davies, J. K., Johnson, J. R., Ellison, S. L., Trilling, D. E., Brown, R. H., and Lebofsky, L. a. (2003). Hydrogen Concentrations on C-class Asteroids Derived from Remote Sensing. *Meteoritics & Planetary Science*, *1398*(9), 1383–1398.

Rivkin, A. S., and Emery, J. P. (2010). Detection of ice and organics on an asteroidal surface. *Nature*, *464*, 1322–1323.

Rivkin, A. S., Marchis, F., Stansberry, J. A., Takir, D., Thomas, C., and JWST Asteroids Focus Group, T. (2016). Asteroids and the James Webb Space Telescope. *Publications of the Astronomical Society of the Pacific*, *128*.

Rivkin, A. S., Thomas, C. A., Howell, E. S., and Emery, J. P. (2015). The Ch-class asteroids: Connexting a visible taxonomic class to a 3 µm band shape. *The Astronomical Journal*, *150*, 198–212.

Rochette, P., Gattacceca, J., Bonal, L., Bourot-Denise, M., Chevrier, V., Clerc, J. P., Consolmagno, G., Folco, L., Gounelle, M., Kohout, T., Pesonen, L., Quirico, E., Sagnotti, L., and Skripnik, A. (2008). Magnetic classification of stony meteorites: 2. Non-ordinary chondrites. *Meteoritics & Planetary Science*, *43*(5), 959–980.

Rubin, A. E., Trigo-Rodríguez, J. M., Huber, H., and Wasson, J. T. (2007). Progressive aqueous alteration of CM carbonaceous chondrites. *Geochimica et Cosmochimica Acta*, *71*(9), 2361–2382.

Ruff, S. W., Christensen, P. R., Barbera, P. W., and Anderson, D. L. (1997). Quantitative thermal emission spectroscopy of minerals: A laboratory technique for measurement and calibration. *Journal of Geophysical Research: Solid Earth*, *102*(B7), 14899–14913.

Russell, C. T., and Raymond, C. A. (2011). *The Dawn Mission to Minor Planets 4 Vesta and 1 Ceres*. New York, NY: Springer New York.

Russell, S. S. (2007). The Formation of the Solar System. *Journal of the Geological Society*, *164*, 481–492.

Ruzicka, A., Grossman, J. N., Bouvier, A., Herd, C. D. K., and Agee, C. B. (2015). The Meteoritical Bulletin, No. 101. *Meteoritics & Planetary Science*, *50*(9).

Salisbury, J. W. (1993). Mid-infrared spectroscopy: laboratory data. In *Remote Geochemical Analysis: Elemental and Mineralogical Composition*, (pp. 79–98). Cambridge University Press.

Salisbury, J. W., D'Aria, D. M., and Jarosewich, E. (1991). Midinfrared (2.5-13.5um) reflectance spectra of powdered stony meteorites. *Icarus*, *92*, 280–297.

Salisbury, J. W., and Walter, L. S. (1989). Thermal infrared (2.5–13.5 μm) spectroscopic remote sensing of igneous rock types on particulate planetary surfaces. *Journal of Geophysical Research*, *94*(B7), 9192–9202.

Sanders, I. S. (2017). On Making Chondrules From Molten Planetesimals. In *Chondrules and the Protoplanetary Disk*.

Schilling, G. (1999). From a swirl of dust, a planet is born. *Science*, *286*(54337), 66–68.

Schofield, P. F., Knight, K. S., Covey-Crump, S. J., Cressey, G., and Stretton, I. C. (2002). Accurate quantification of the modal mineralogy of rocks when image analysis is difficult. *Mineralogical Magazine*, *66*(1), 189–200.

Schulze, H., Bischoff, A., Palme, H., Spettel, B., Dreibus, G., and Otto, J. (1994). Mineralogy and chemistry of Rumuruti: The first meteorite fall of the new R chondrite group. *Meteoritics*, *29*(2), 275–286.

Sears, D. W., Kallemeyn, G. W., and Wasson, J. T. (1982). The compositional classification of chondrites: II The enstatite chondrite groups. *Geochimica et Cosmochimica Acta*, *46*(4), 597–608.

Shepard, M. K., Taylor, P. A., Nolan, M. C., Howell, E. S., Springmann, A., Giorgini, J. D., Warner, B. D., Harris, A. W., Stephens, R., Merline, W. J., Rivkin, A., Benner, L. A., Coley, D., Clark, B. E., Ockert-Bell, M., and Magri, C. (2015). A radar survey of M- and X-class asteroids. III. Insights into their composition, hydration state, & structure. *Icarus*, *245*, 38–55.

Shimaki, Y., Senshu, H., Sakatani, N., Okada, T., Fukuhara, T., Tanaka, S., Taguchi, M., Arai, T., Demura, H., Ogawa, Y., Suko, K., Sekiguchi, T., Kouyama, T., Hasegawa, S., Takita, J., Matsunaga, T., Imamura, T., Wada, T., Kitazato, K., Hirata, N., Hirata, N., Noguchi, R., Sugita, S., Kikuchi, S., Yamaguchi, T., Ogawa, N., Ono, G., Mimasu, Y., Yoshikawa, K., Takahashi, T., Takei, Y., Fujii, A., Takeuchi, H., Yamamoto, Y., Yamada, M., Shirai, K., ichi Iijima, Y., Ogawa, K., Nakazawa, S., Terui, F., Saiki, T., Yoshikawa, M., Tsuda, Y., and ichiro Watanabe, S. (2020). Thermophysical properties of the surface of asteroid 162173 Ryugu: Infrared observations and thermal inertia mapping. *Icarus*, *348*, 113835.

Shirley, K. A., and Glotch, T. D. (2019). Particle Size Effects on Mid-Infrared Spectra of Lunar Analog Minerals in a Simulated Lunar Environment. *Journal of Geophysical Research: Planets*, *124*(4), 970–988.

Shu, F. H., Shang, H., Gounelle, M., Glassgold, A. E., and Lee, T. (2001). The Origin of Chondrules and Refractory Inclusions in Chondritic Meteorites. *The Astrophysical Journal*, *548*(2), 1029–1050.

Shu, F. H., Shang, H., and Lee, T. (1996). Toward an astrophysical theory of chondrites. *Science*, *271*(5255), 1545–1552.

Skirius, C., Steele, I. M., and Smith, J. V. (1986). Belgica-7904: A new carbonaceous chondrite from Antarctica; Minorelement chemistry of olivine. *Memoirs of National Institute of Polar Research. Special issue*, *41*, 243–258.

Stansberry, J. A., Cleve, J. V., Reach, W. T., Cruikshank, D. P., Emery, J. P., Fernandez, Y. R., Meadows, V. S., Su, K. Y. L., Misselt, K., Rieke, G. H., Young, E. T., Werner, M. W., Engelbracht, C. W., Gordon, K. D., Hines, D. C., Kelly, D. M., Morrison, J. E., and Muzerolle, J. (2004). Spitzer observations of the dust coma and nucleus of 29P/Schwassmann-Wachmann 1. *The Astrophysical Journal Supplement Series*, *154*, 463–468.

Sugita, S., Honda, R., Morota, T., Kameda, S., Sawada, H., Tatsumi, E., Yamada, M., Honda, C., Yokota, Y., Kouyama, T., Sakatani, N., Ogawa, K., Suzuki, H., Okada, T., Namiki, N., Tanaka, S., Iijima, Y., Yoshioka, K., Hayakawa, M., Cho, Y., Matsuoka, M., Hirata, N., Miyamoto, H., Domingue, D., Hirabayashi, M., Nakamura, T., Hiroi, T., Michikami, T., Michel, P., Ballouz, R.-L., Barnouin, O. S., Ernst, C. M., Schröder, S. E., Kikuchi, H., Hemmi, R., Komatsu, G., Fukuhara, T., Taguchi, M., Arai, T., Senshu, H., Demura, H., Ogawa, Y., Shimaki, Y., Sekiguchi, T., Müller, T. G., Hagermann, A., Mizuno, T., Noda, H., Matsumoto, K., Yamada, R., Ishihara, Y., Ikeda, H., Araki, H., Yamamoto, K., Abe, S., Yoshida, F., Higuchi, A., Sasaki, S., Oshigami, S., Tsuruta, S., Asari, K., Tazawa, S., Shizugami, M., Kimura, J., Otsubo, T., Yabuta, H., Hasegawa, S., Ishiguro, M., Tachibana, S., Palmer, E., Gaskell, R., Le Corre, L., Jaumann, R., Otto, K., Schmitz, N., Abell, P. A., Barucci, M. A., Zolensky, M. E., Vilas, F., Thuillet, F., Sugimoto, C., Takaki, N., Suzuki, Y., Kamiyoshihara, H., Okada, M., Nagata, K., Fujimoto, M., Yoshikawa, M., Yamamoto, Y., Shirai, K., Noguchi, R., Ogawa, N., Terui, F., Kikuchi, S., Yamaguchi, T., Oki, Y., Takao, Y., Takeuchi, H., Ono, G., Mimasu, Y., Yoshikawa, K., Takahashi, T., Takei, Y., Fujii, A., Hirose, C., Nakazawa, S., Hosoda, S., Mori, O., Shimada, T., Soldini, S., Iwata, T., Abe, M., Yano, H., Tsukizaki, R., Ozaki, M., Nishiyama, K., Saiki, T., Watanabe, S., and Tsuda, Y. (2019). The geomorphology, color, and thermal properties of Ryugu: Implications for parent-body processes. *Science*, *364*, 252.

Sunshine, J. M., Bus, S. J., Corrigan, C. M., McCoy, T. J., and Burbine, T. H. (2007). Olivine-dominated asteroids and meteorites: Distinguishing nebular and igneous histories. *Meteoritics & Planetary Science*, *42*(2), 155–170.

Sunshine, J. M., Connolly, H. C., McCoy, T. J., Bus, S. J., and La Croix, L. M. (2008). Ancient asteroids enriched in refractory inclusions. *Science*, *320*(5875), 514–517.

Tachibana, S., Abe, M., Arakawa, M., Fujimoto, M., Iijima, Y., Ishiguro, M., Kitazato, K., Kobayashi, N., Namiki, N., Okada, T., Okazaki, R., Sawada, H., Sugita, S., Takano, Y., Tanaka, S., Watanabe, S., Yoshikawa, M., Kuninaka, H., and Team, T. H. P. (2014). Hayabusa2: Scientific importance of samples returned from C-type near-Earth asteroid (162173) 1999 JU3. *Geochemical Journal*, *48*, 571 – 587.

Takir, D., and Emery, J. P. (2012). Outer main belt asteroids: Identification and distribution of four 3 µm spectral groups. *Icarus*, *219*, 641–654.

Takir, D., Emery, J. P., and Mcsween, H. Y. (2015). Toward an understanding of phyllosilicate mineralogy in the outer main asteroid belt. *Icarus*, *257*, 185–193.

Takir, D., Emery, J. P., Mcsween, H. Y., Hibbitts, C. A., Clark, R. N., Pearson, N., and Wang, A. (2013). Nature and degree of aqueous alteration in CM and CI carbonaceous chondrites. *Meteoritics & Planetary Science*, *48*(9), 1–20.

Takir, D., Kareta, T., Emery, J. P., Hanuš, J., Reddy, V., Howell, E. S., Rivkin, A. S., and Arai, T. (2020). Near-infrared observations of active asteroid (3200) Phaethon reveal no evidence for hydration. *Nature Communications*, *11*(1), 1–7.

Tholen, D. J. (1984). *Asteroid taxonomy from cluster analysis of photometry*. Ph.D. thesis, The University of Arizona.

Thomas, I. R., Bowles, N. E., Greenhagen, B. T., Glotch, T. D., Donaldson Hanna, K. L., Wyatt, M. B., Bandfield, J. L., and Paige, D. A. (2010). Emission measurements of lunar analogues for interpretation of returning data from the Diviner lunar radiometer on NASA's lunar reconnaissance orbiter. In *41st Lunar and Planetary Science Conference*.

Thomas, I. R., Greenhagen, B. T., Bowles, N. E., Donaldson Hanna, K. L., Temple, J., and Calcutt, S. B. (2012). A new experimental setup for making thermal emission measurements in a simulated lunar environment. *Review of Scientific Instruments*, *83*(12).

Thompson, M., Loeffler, M., Morris, R., Keller, L., and Christoffersen, R. (2018). Spectral and chemical effects of simulated space weathering of the Murchison CM2 carbonaceous chondrite. *Icarus*.

Tomeoka, and Kazushige (1990). Mineralogy and petrology of Belgica-7904: A new kind of carbonaceous chondrite from Antarctica. *Proc. NIPR Symp. Antarct. Meteorites*, *3*, 40–54.

Tomeoka, K. (1990). Phyllosilicate veins in a CI meteorite: evidence for aqueous alteration on the parent body. *Nature*, *345*(6271), 138–140.

Tomeoka, K., and Buseck, P. R. (1985). Indicators of aqueous alteration in CM carbonaceous chondrites: Microtextures of a layered mineral containing Fe, S, 0 and Ni. *Geochimica et Cosmochimica Acta*, *49*, 2149–2163.

Tomeoka, K., and Buseck, P. R. (1988). Matrix mineralogy of the Orgueil CI carbonaceous chondrite. *Geochimica et Cosmochimica Acta*, *52*(6), 1627–1640.

Tomeoka, K., Kojima, H., and Yanai, K. (1989a). Yamato-82162: A New Kind of CI Carbonaceous Chondrite Found in Antarctica. *Proc. NIPR Symp. Antarct. Meteorites*, *2*, 36–54.

Tomeoka, K., Kojima, H., and Yanai, K. (1989b). Yamato-86720: A CM carbonaceous chondrite having experienced extensive aqueous alteration and thermal metamorphism. *Proc. NIPR Symp. Antarct. Meteorites*, *2*, 55–74.

Tonui, E. K., Zolensky, M. E., Hiroi, T., Nakamura, T., Lipschutz, M. E., Wang, M.-S., and Okudaira, K. (2014). Petrographic, chemical and spectroscopic evidence for thermal metamorphism in carbonaceous chondrites I: CI and CM chondrites. *Geochimica et Cosmochimica Acta*, *126*, 284–306.

Tonui, E. K., Zolensky, M. E., Hiroi, T., Wang, M.-S., and Lipschutz, M. E. (2001). Petrographic, Chemical and Spectroscopic Data on Thermally Metamorphosed Carbonaceous Chondrites. *Meteoritics & Planetary Science Supplement*, *36*, A207.

Tonui, E. K., Zolensky, M. E., and Lipschutz, M. (2002). Petrography, mineralogy and trace element chemistry of Yamato-86029, Yamato-793321 and Lewis Cliff 85332: Aqueous alteration and heating events. *Antarctic Meteorite Research*, *15*, 38–58.

Tonui, E. K., Zolensky, M. E., Lipschutz, M. E., Wang, M.-S., and Nakamura, T. (2003). Yamato 86029: Aqueously altered and thermally metamorphosed CI-like chondrite with unusual textures. *Meteoritics & Planetary Science*, *38*(2), 269–292.

Tsiganis, K., Gomes, R., Morbidelli, A., and Levison, H. F. (2005). Origin of the orbital architecture of the giant planets of the Solar System. *Nature*, *435*(7041), 459–461.

Tsuda, Y., Saiki, T., Terui, F., Nakazawa, S., Yoshikawa, M., and ichiro Watanabe, S. (2020). Hayabusa2 mission status: Landing, roving and cratering on asteroid Ryugu. *Acta Astronautica*, *171*, 42–54.

Tsuda, Y., Yoshikawa, M., Abe, M., Minamino, H., and Nakazawa, S. (2013). System design of the Hayabusa 2—Asteroid sample return mission to 1999 JU3. *Acta Astronautica*, *91*, 356–362.

Usui, F., Hasegawa, S., Ootsubo, T., and Onaka, T. (2018). AKARI/IRC Near-Infrared Asteroid Spectroscopic Survey: AcuA-spec. *Publ. Astron. Soc. Japan*, (0), 1–42.

Vacher, L., Piralla, M., Gounelle, M., Vacher, L. G., Bizzarro, M., and Marrocchi, Y. (2019). Thermal Evolution of Hydrated Asteroids Inferred from Oxygen Isotopes. *Article in The Astrophysical Journal Letters*.

Van Schmus, W., and Wood, J. (1967). A chemical-petrologic classification for the chondritic meteorites. *Geochimica et Cosmochimica Acta*, *31*(5), 747–765.

Varatharajan, I., Maturilli, A., Helbert, J., Alemanno, G., and Hiesinger, H. (2019). Spectral behavior of sulfides in simulated daytime surface conditions of Mercury: Supporting past (MESSENGER) and future missions (BepiColombo). *Earth and Planetary Science Letters*, *520*, 127–140.

Verdier-Paoletti, M. J., Marrocchi, Y., Vacher, L. G., Gattacceca, J., Gurenko, A., Sonzogni, C., and Gounelle, M. (2019). Testing the genetic relationship between fluid alteration and brecciation in CM chondrites. *Meteoritics and Planetary Science*, *54*(8), 1692–1709.

Vernazza, P., Binzel, R. P., Thomas, C. A., DeMeo, F. E., Bus, S. J., Rivkin, A. S., and Tokunaga, A. T. (2008). Compositional differences between meteorites and near-Earth asteroids. *Nature*, *454*(7206), 858–860.

Vernazza, P., Brunetto, R., Binzel, R. P., Perron, C., Fulvio, D., Strazzulla, G., and Fulchignoni, M. (2009). Plausible parent bodies for enstatite chondrites and mesosiderites: Implications for Lutetia's fly-by. *Icarus*, *202*(2), 477–486.

Vernazza, P., Castillo-Rogez, J., Beck, P., Emery, J., Brunetto, R., Delbo, M., Marsset, M., Marchis, F., Groussin, O., Zanda, B., Lamy, P., Jorda, L., Mousis, O., Delsanti, A., Djouadi, Z., Dionnet, Z., Borondics, F., and Carry, B. (2017). Different origins or different evolutions? Decoding the spectral diversity among C-Type asteroids. *The Astronomical Journal*, *153*(2), 72–82.

Vernazza, P., Delbo, M., King, P., Izawa, M., Olofsson, J., Lamy, P., Cipriani, F., Binzel, R., Marchis, F., Merín, B., and Tamanai, A. (2012). High surface porosity as the origin of emissivity features in asteroid spectra. *Icarus*, *221*(2), 1162–1172.

Vernazza, P., Lamy, P., Groussin, O., Hiroi, T., Jorda, L., King, P. L., Izawa, M. R., Marchis, F., Birlan, M., and Brunetto, R. (2011). Asteroid (21) Lutetia as a remnant of Earth's precursor planetesimals. *Icarus*, *216*(2), 650–659.

Vernazza, P., Marsset, M., Beck, P., Binzel, R. P., Birlan, M., Brunetto, R., Demeo, F. E., Djouadi, Z., Dumas, C., Merouane, S., Mousis, O., and Zanda, B. (2015). Interplanetary Dust Particles As Samples of Icy Asteroids. *Astrophysical Journal*, *806*(2), 204.

Vernazza, P., Marsset, M., Beck, P., Binzel, R. P., Birlan, M., Cloutis, E. A., Demeo, F. E., Dumas, C., and Hiroi, T. (2016). Compositional homogeneity of CM parent bodies. *The Astronomical Journal*, *152*, 54–64.

Vilas, F. (1994). A cheaper, faster, better way to detect water of hydration on solar system bodies. *Icarus*, *111*, 456–467.

Vilas, F., and Gaffey, M. J. (1989). Phyllosilicate absorption features in main-belt and outer-belt asteroid reflectance spectra. *Science*, *246*, 790–792.

Vilas, F., Hatch, E. C., Larson, S. M., Sawyer, S. R., and Gaffey, M. J. (1993). Ferric Iron in Primitive Asteroids: A 0.43-um Absorption Feature. *Icarus*, *102*, 225–231.

Vilas, F., Jarvis, K. S., and Gaffey, M. J. (1994). Iron alteration minerals in the visible and near-infrared spectra of low-albedo asteroids.

Wada, K., Grott, M., Michel, P., Walsh, K. J., Barucci, A. M., Biele, J., Blum, J., Ernst, C. M., Grundmann, J. T., Gundlach, B., Hagermann, A., Hamm, M., Jutzi, M., Kim, M. J., Kührt, E., Le Corre, L., Libourel, G., Lichtenheldt, R., Maturilli, A., Messenger, S. R., Michikami, T., Miyamoto, H., Mottola, S., Müller, T., Nakamura, A. M., Nittler, L. R., Ogawa, K., Okada, T., Palomba, E., Sakatani, N., Schröder, S. E., Senshu, H., Takir, D., and Zolensky, M. E. (2018). Asteroid Ryugu before the Hayabusa2 encounter.

Walsh, K. J. (2018). Rubble Pile Asteroids. *Annual Review of Astronomy and Astrophysics*, *56*, 593–624.

Walsh, K. J., Jawin, E. R., Ballouz, R. L., Barnouin, O. S., Bierhaus, E. B., Connolly Jr., H. C., Molaro, J. L., Mccoy, T. J., Delbo, M., Hartzell, C. M., Pajola, M., Schwartz, S. R., Trang, D., Scheeres, D. J., Susorney, H. C. M., Thuillet, F., Lauretta, D. S., and OSIRIS-REx Team, T. (2019). Craters, boulders and regolith of (101955) Bennu indicative of an old and dynamic surface. *Nature Geoscience*.

Walsh, K. J., Morbidelli, A., Raymond, S. N., O 'brien, D. P., and Mandell, A. M. (2011). A low mass for Mars from Jupiter's early gas-driven migration. *Nature*, *475*(7355), 206–209.

Walsh, K. J., Morbidelli, A., Raymond, S. N., O'Brien, D. P., and Mandell, A. M. (2012). Populating the asteroid belt from two parent source regions due to the migration of giant planets-"The Grand Tack". *Meteoritics & Planetary Science*, *47*(12), 1941–1947.

Wang, M.-S., and Lipschutz, M. E. (1998). Thermally metamorphosed carbonaceous chondrites from data for thermally mobile trace elements. *Meteoritics & Planetary Science*, *33*(6), 1297–1302.

Warner, B. D., Harris, A. W., Vokrouhlický, D., Nesvorný, D., and Bottke, W. F. (2009). Analysis of the Hungaria asteroid population. *Icarus*, *204*(1), 172–182.

Weisberg, M. K., Mccoy, T. J., and Krot, A. N. (2006). Systematics and Evaluation of Meteorite Classification. In *Meteorites and the early solar system II*, vol. 19. University of Arizona Press.

Weisberg, M. K., Prinz, M., Clayton, R. N., Mayeda, T. K., Grady, M. M., Franchi, I., Pillinger, C. T., and Kallemeyn, G. W. (1996). The K (Kakangari) chondrite grouplet. *Geochimica et Cosmochimica Acta*, *60*(21), 4253–4263.

Weisberg, M. K., Prinz, M., Kojima, H., Yanai, K., Clayton, R. N., and Mayeda, T. K. (1991). The Carlisle Lakes-type chondrites: A new grouplet with high Δ17O and evidence for nebular oxidation. *Geochimica et Cosmochimica Acta*, *55*(9), 2657–2669.

Wells, M., Lee, D., Oudenhuysen, A., Hastings, P., Pel, J.-W., and Glasse, A. (2006). The MIRI medium resolution spectrometer for the James Webb Space Telescope. In J. C. Mather, H. A. MacEwen, and M. W. M. de Graauw (Eds.) *Space Telescopes and Instrumentation I: Optical, Infrared, and Millimeter*, vol. 6265, (p. 626514). SPIE.

Xu, S., Binzel, R. P., Burbine, T. H., and Bus, S. J. (1995). Small main-belt asteroid spectroscopic survey: Initial results. Icarus. *Icarus*, *115*, 1–35.

Yang, B., and Jewitt, D. (2007). Spectroscopic Search for Water Ice on Jovian Trojan Asteroids. *The Astronomical Journal*, *134*(1), 223–228.

Yang, B., Lucey, P., and Glotch, T. (2013). Are large Trojan asteroids salty? An observational, theoretical, and experimental study. *Icarus*, *223*, 359–366.

Youdin, A. N., and Shu, F. H. (2002). Planetesimal formation by gravitational instability. *The Astrophysical Journal*, *580*, 494–505.

Young, E. D., and Russell, S. S. (1998). Oxygen Reservoirs in the Early Solar Nebula Inferred from an Allende CAI. *Science*, *282*, 452–455.

Zellner, B., Tholen, D. J., and Tedesco, E. F. (1985). The eight-color asteroid survey: Results for 589 minor planets. *Icarus*, *61*, 355–416.

Ziffer, J., Campins, H., Licandro, J., Walker, M. E., Fernandez, Y., Clark, B. E., Mothe-Diniz, T., Howell, E., and Deshpande, R. (2011). Near-infrared spectroscopy of primitive asteroid families. *Icarus*, *213*(2), 538–546.

Zolensky, M., Barrett, R., Browning, L., Russell, S. S., Cody, G., Brunetto, R., DeMeo, F., Djouadi, Z., Dumas, C., Merouane, S., Mousis, O., and Zanda, B. (1993). Mineralogy and composition of matrix and chondrule rims in carbonaceous chondrites. *Geochimica et Cosmochimica Acta*, *57*(13), 3123–3148.

Zolensky, M., and Frank, D. (2014). Surviving high-temperature components in CI chondrites. In *77th Annual Meeting of the Meteoritical Society*.

Zolensky, M. E., Bourcier, W. L., and Gooding, J. L. (1989). Aqueous alteration on the hydrous asteroids- results of EQ3/6 computer simulations. *Icarus*, *78*(2), 411–425.

Zolensky, M. E., Mittlefehldt, D. W., Lipschutz, M. E., Wang, M.-S., Clayton, R. N., Mayeda, T. K., Grady, M. M., Pillinger, C., and Barber, D. (1997). CM chondrites exhibit the complete petrologic range from type 2 to 1. *Geochimica et Cosmochimica Acta*, *61*(23), 5099–5115.

Appendix A: PSD-XRD beam flux

During a PSD-XRD experimental run I monitored the beam flux from the X-ray source by collecting a pattern from a polished metal block at the beginning and end of each day. Figure A.1 shows three example patterns collected at the beginning, middle and end of an experimental run of approximately two weeks. The variation in beam flux is <1 %.

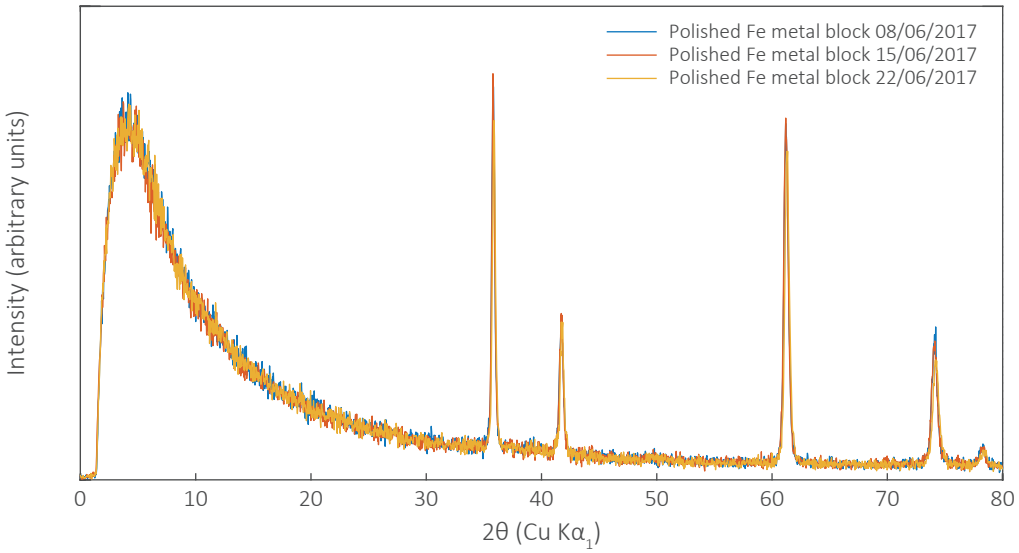


Figure A.1: *Three PSD-XRD patterns of a polished Fe metal block observed over one experimental run. Patterns were taken twice every day, however three are shown here representing the first, middle and final day of measurements to demonstrate the beam flux remains consistent throughout the entire measurement period.*

Appendix B: PSD-XRD standards

Table B.1 shows the chemical formula, British Museum (BM) number and mass absorption coefficients for the standards used in this project.

Mineral	Chemical formula	BM number	Mass absorption coefficient	Notes
Albite	$Na(AlSi_3O_8)$	1962,439	56.3	
Antigorite	$Mg_3(Si_2O_5)(OH)_4$	1922,408	29.7	
Calcite	$CaCO_3$	G1002	74.4	
Cronstedtite	$Fe_2^{2+}Fe^{3+}(SiFe^{3+})O_5(OH)_4$	52294	103.5	
Denmark Clay*		1983,1903	35.1	
Diopside	$CaMgSi_2O_6$	1988,5	58.1	
Dolomite	$CaMg(CO_3)_2$		48.9	Costa Da Vent
Enstatite	$Mg_2Si_2O_6$	1933,1073	36.4	
Fe metal	Fe		304.4	
Gypsum	$CaSO_4.2H_2O$	G1004	46	
Lizardite	$Mg_3(Si_2O_5)(OH)_4$		29.7	E. Rutter
Magnetite	Fe_3O_4	G10093	223.3	
Pentlandite	$(FeNi_9)S_8$	1975,466	146.7	
Pyrrhotite	$Fe_{1-x}S$ (x = 0 to 0.2)	1968,1173	138.1	
Saponite	$Ca_{0.25}(Mg,Fe)_3((Si,Al)_4O_{10})(OH)_2.nH_2O$	1938,1255	52.9	
Troilite	$Fe_{1-x}S$ (x = 0 to 0.2)	1923,21	227.1	
Olivine (Fo100)	Mg_2SiO_4		32.2	
Olivine (Fo90)	$Mg_{1.8}Fe_{0.2}SiO_4$		51.9	
Olivine (Fo80)	$Mg_{1.6}Fe_{0.4}SiO_4$		71.3	
Olivine (Fo70)	$Mg_{1.4}Fe_{0.6}SiO_4$		87.9	
Olivine (Fo60)	$Mg_{1.2}Fe_{0.8}SiO_4$		104.5	

Table B.1: *The chemical formulas, British Museum (BM) numbers and mass absorption coefficients of the standards used in this project.*

Appendix C: Thermogravimetric analysis

C.1 Experimental

Thermogravimetric analysis (TGA) is a useful technique for examining the nature and abundance of hydrated components in meteorites, providing insights into the aqueous and thermal alteration processes they have experienced. TGA can be used to estimate the amount of water in a sample, and in CM chondrites this generally correlates with phyllosilicate abundance and degree of alteration (Garenne et al., 2014). Approximately 10 - 15 mg of the HB1, HB2-1, and HB2-2 powders, which were prepared for XRD analysis, were analysed using a TA Instruments SDT Q600 TGA. The powders were loaded into alumina crucibles and heated from room temperature to 1000 ^{o}C at a rate of 10 ^{o}C min^{-1} while in a N_2 flow of 100 ml min^{-1}. Mass loss was recorded over the whole temperature range with a mass resolution of 0.1 μg, meaning that a 10 % mass loss from a 10 mg sample results in an error of only 0.01 %, and this is even lower for a 15 mg sample. Instead, the main source of uncertainty comes from measuring the mass of the sample, which was done to a precision of 0.01 mg. This gives an error of 0.1 % for samples between 10 and 15 mg. The combined maximum error on the measured mass loss fraction is therefore 0.1 %.

C.2 Results

Garenne et al. (2014) obtained TGA data for a suite of CI, CM and CR carbonaceous chondrites. They proposed that mass loss between 25 - 200 ^{o}C is due to adsorbed terrestrial

water, mass loss between 200 - 400 °C is due to dehydration of Fe-(oxy)hydroxides, mass loss between 400 - 770 °C is due to dehydration of –OH in phyllosilicates, and mass loss above 770 °C is mainly due to the decomposition of carbonates. King et al. (2015b), Mason et al. (2018) went further and showed different phyllosilicate compositions dehydrate at different temperatures: Fe-cronstedtite dehydrates between 300 - 450 °C and Mg-serpentines dehydrate between 450 - 800 °C, and so mass loss in these temperature ranges can give an indication of the abundance of the phyllosilicate chemistry. Included in Table C.1 are the mass losses for all samples in this project over the temperature ranges described by Garenne et al. (2014), Mason et al. (2018). Also included is mass loss between 650 - 750 °C, where calcite has been shown to decompose by King et al. (2015b). I do note that carbonate decomposition depends strongly on grain size of the sample and has been shown to dehydrate at higher temperatures (Garenne et al., 2014), but samples in this project were prepared in a similar manner to the King et al. (2015b) standards. This 650 - 750 °C mass loss was subtracted from the mass loss in the 450 - 800 °C region in all subsequent interpretation.

C.2.1 Aqueously altered CM and CI chondrites

The total mass loss (25 - 900 °C) for the CM1/2 and CM1 chondrites was between 13.0 - 20.8 wt%, (Table C.1), with GRO 95645 and MIL 07689 losing the most mass (18.1 and 20.8 %). All samples show significant mass loss between 300 - 800 °C, consistent with the dehydration and dehydroxylation of Fe-(oxy)hydroxides and abundant serpentine phases present in CM chondrites. The total mass loss in this temperature range can therefore be used to estimate the abundance of H2O in the samples (Garenne et al., 2014), which for the aqueously altered CM and CI samples ranges from 7.3 to 13.8 wt%.

Mass loss events occur at ~225 °C for GRO 95645 and MIL 07689 that are not observed for the other CM1/2 and CM1 chondrites (Fig. C.1). Comparison with the dehydration curves of ferrihydrite, limonite and goethite (King et al., 2015b) suggest that mass loss at

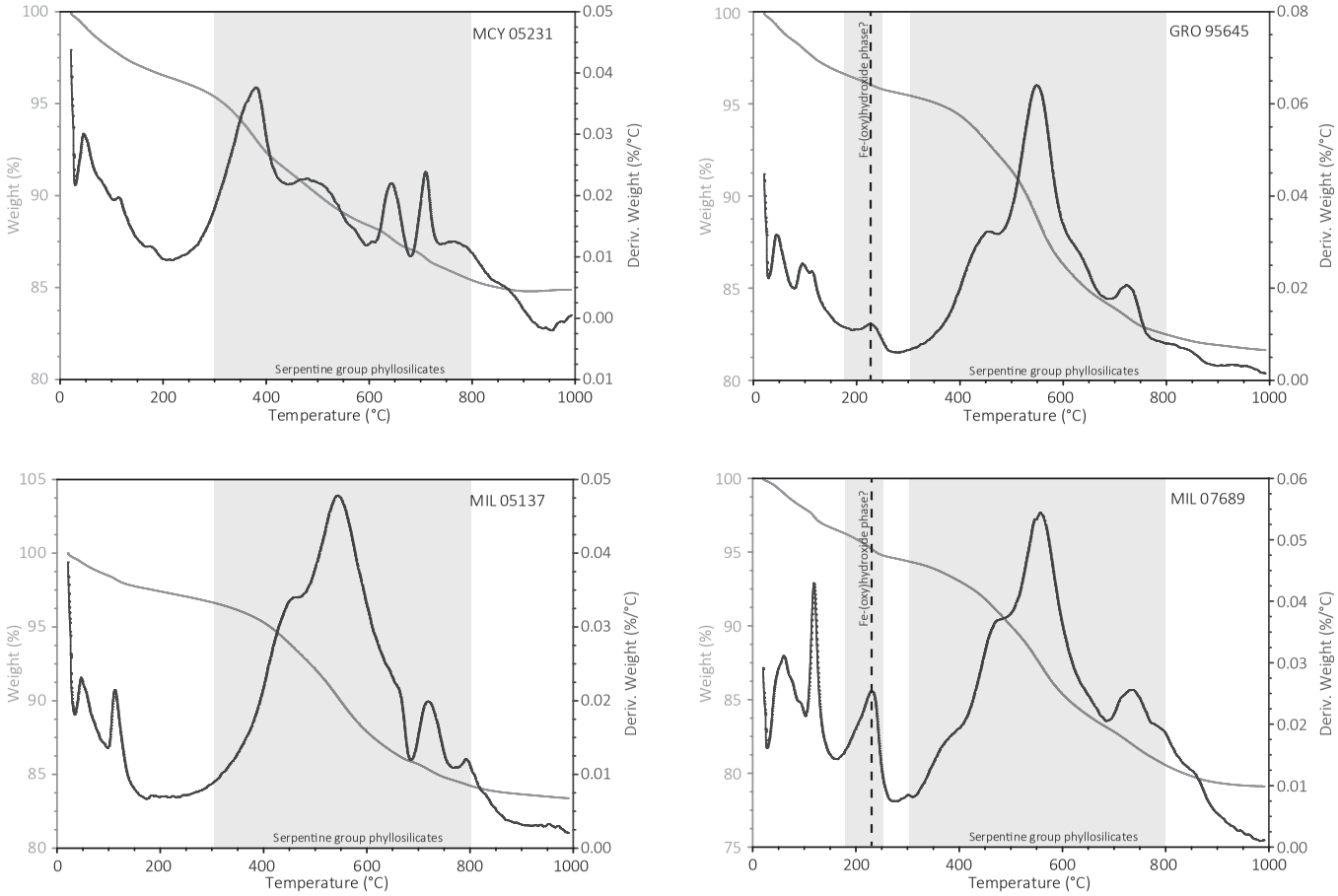


Figure C.1: *Typical mass loss and DTG curves for CM1/2 and CM1 chondrites. The CM1/2 and CM1 chondrites show significant mass loss between 300 – 800 °C due to dehydration of abundant serpentine phyllosilicate minerals. Mass loss under 200 °C is attributed to adsorbed terrestrial water. GRO 95645 and MIL 07689, the most weathered samples investigated, show dehydration of a phase at ~225 °C, which is within the region where Fe-(oxy)hydroxides dehydrate and is likely a terrestrial weathering product.*

			Mass loss (wt%)						
Meteorite	Sample	Classification	25 - 900 °C Total mass loss	25 - 200 °C Molecular water	200 - 400 °C Fe- (oxy) hydroxides	400 - 770 °C Phyllosilicates	300 - 450 °C Fe-rich phyllosilicates	450 - 800 °C Mg-rich phyllosilicates	650 - 750 °C Carbonates
ALH 83100	HB2-1	CM2	18.2	3.1	2.7	11.3	3.2	10.1	2.3
	HB2-2	CM2	18.3	3.0	2.7	11.5	3.3	10.2	2.3
ALH 83102	HB2-1	CM2	17.6	3.0	2.8	10.8	3.3	9.5	2.2
	HB2-2	CM2	18.4	3.2	2.9	11.2	3.5	9.9	2.3
GRO 95645	HB1	CM1	18.1	3.4	2.0	11.6	2.5	10.5	1.9
LAP 02277	HB1	CM1	14.4	2.0	1.6	9.5	2.2	8.7	1.5
LAP 031166	HB1	CM2	17.7	3.4	2.3	9.9	3.4	8.8	2.0
LAP 031214	HB1	CM1/2	18.7	4.8	4.1	9.0	4.5	7.4	1.8
LEW 85311	HB1	CM2	14.1	3.9	3.9	4.9	3.2	4.2	1.0
LEW 90500	HB1	CM2	17.7	4.4	3.2	9.5	3.9	8.3	2.0
LON 94101	HB2-1	CM2	18.4	4.1	3.3	9.9	3.6	8.8	1.9
	HB2-2	CM2	18.9	4.3	2.8	10.7	3.3	9.7	2.0
MCY 05231	HB1	CM1/2	14.9	3.2	4.2	6.6	4.2	5.8	1.5
MIL 05137	HB1	CM1	16.5	2.4	2.1	10.7	2.8	9.6	1.7
MIL 07689	HB1	CM1	20.8	4.0	2.9	11.9	2.6	11.3	2.3
MIL 090288	HB1	CM1/2	17.2	3.0	2.2	10.0	3.1	9.0	1.6
Moapa Valley	HB1	CM1	13.0	1.5	1.1	9.4	1.4	8.9	1.8
NWA 4765	HB1	CM1	15.2	1.5	1.5	11.1	2.5	9.9	2.1
NWA 8534	HB1	CM1/2	14.4	1.6	1.9	9.8	2.7	8.8	1.7
Ivuna	Ivu-1	CI1	28.6	8.8	5.0	13.1	3.2	12.2	3.8
Orgueil	Org-1	CI1	31.1	11.2	5.6	12.6	3.7	11.5	3.1
A 881334	HB1	CM2	14.7	5.8	1.0	6.2	0.9	6.0	1.5
A 881655	HB1	CM2	8.1	3.6	0.6	3.3	0.3	3.3	0.8
B 7904	HB2-1	C2-ung/CY	4.9	1.9	0.0	1.7	-0.3	2.0	0.4
	HB2-2	C2-ung/CY	4.3	1.8	0.1	1.1	0.0	1.4	0.4
Dho 2046	HB1	CM2-an	1.4	1.5	0.3	-1.5	-0.6	-0.6	0.9
DOM 03183	HB1	CM2	14.1	2.3	2.9	7.6	4.0	5.9	1.4
EET 96010	HB1	CM2	1.3	1.0	0.3	0.0	0.0	-0.1	-0.1
EET 96029	HB2-1	CM2	16.2	6.3	1.5	7.0	1.5	6.6	2.0
	HB2-2	CM2	15.2	6.0	1.3	6.5	1.3	6.3	1.8
MIL 07700	HB1	CM2	14.1	5.9	1.8	5.4	1.4	5.3	1.3
PCA 02010	HB2-1	CM2	8.6	3.4	1.4	3.7	0.5	3.4	0.2
	HB2-2	CM2	8.6	3.4	1.4	3.7	0.6	3.3	0.2
PCA 02012	HB2-1	CM2	11.1	4.9	1.6	4.4	0.6	4.1	0.6
	HB2-2	CM2	10.5	4.8	1.5	4.2	0.4	4.0	0.6
PCA 91084	HB1	CM2	19.3	8.5	1.4	7.9	1.1	7.7	1.8
WIS 91600	HB2-1	CM-an	15.7	5.6	1.1	7.3	1.2	7.1	2.1
	HB2-2	CM-an	15.4	5.6	1.3	7.0	1.4	6.8	2.0
Y 793321	HB2-1	CM2	13.3	4.5	1.2	6.4	1.1	6.3	1.7
	HB2-2	CM2	12.5	4.4	1.9	5.1	1.3	5.1	1.6
Y 793595	HB1	CM2	23.0	6.1	3.9	11.3	3.7	10.5	2.3
Y 794080	HB1	CM2	15.2	5.5	1.9	6.4	1.9	5.7	1.2
Y 86029	HB1	CI1/CY	18.4	8.6	2.4	5.6	1.4	5.7	1.1
Y 86720	HB1	C2-ung/CY	2.4	1.7	0.2	0.1	0.0	0.1	-0.1
	HB2-1	C2-ung/CY	5.0	2.3	0.8	1.1	0.4	1.2	0.3
	HB2-2	C2-ung/CY	5.2	2.3	0.9	1.1	0.5	1.2	0.3
Y 86789	HB1	C2-ung/CY	2.0	1.3	-0.1	0.1	-0.2	0.2	0.0
	HB2-1	C2-ung/CY	1.4	1.4	-0.1	-0.1	-0.2	-0.1	-0.1
	HB2-2	C2-ung/CY	1.6	1.4	-0.1	-0.1	-0.3	0.0	0.0
Y 980115	HB2-1	CI1/CY	19.3	9.1	3.1	5.6	2.1	5.4	1.2
	HB2-2	CI1/CY	19.7	9.4	3.2	5.7	1.5	5.5	1.2

Table C.1: *Mass loss of samples from chapters 3 and 4.*

this temperature probably results from the dehydration of rusts formed during the meteorites residence in Antarctica. This is consistent with the high weathering grades previously assigned to GRO 95645 and MIL 07689.

C.2.2 Thermally altered CM, CY and CM-/CY-anomalous chondrites

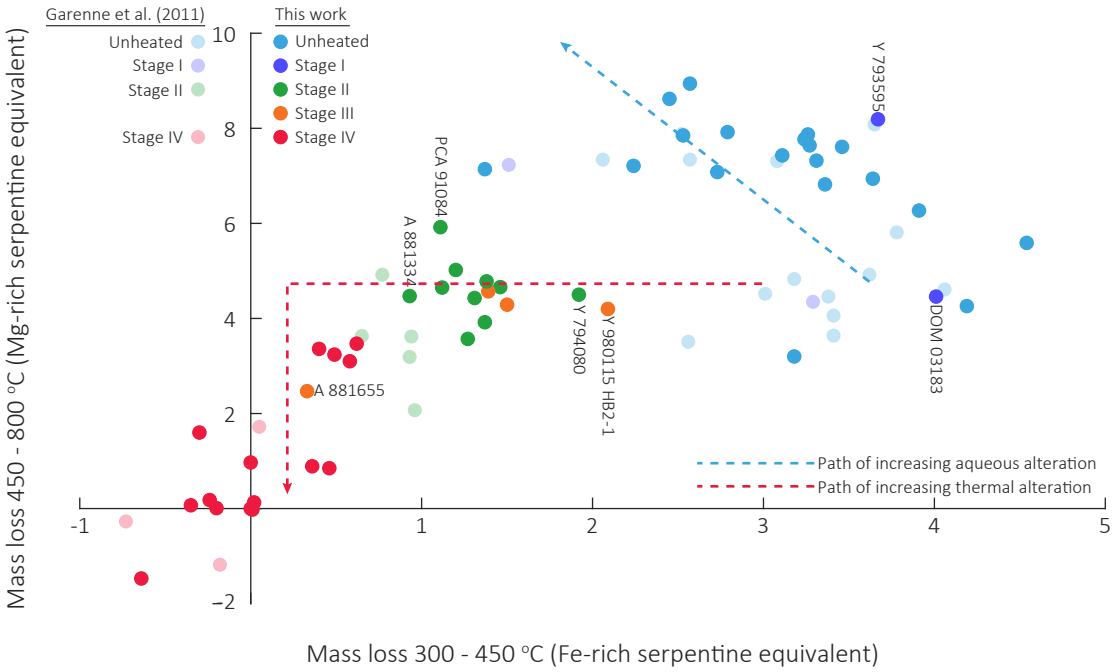


Figure C.2: *Mass loss of samples from chapters 3 and 4 between 450 – 800 °C against mass loss between 300 – 450 °C, showing the effects of aqueous and thermal alteration. Also included are data from Garenne et al. (2014).*

For the thermally altered samples in chapter 4, total mass loss (25 - 900 °C) was between 1.3 - 23.0 wt%. In the Fe-cronstedtite temperature range (300 - 450 °C), mass loss varied from 0 - 4.0 wt%, and in the Mg-serpentine temperature range (450 - 800 °C), mass loss varied from 0 - 10.5 wt%. As Fe-rich serpentines dehydrate at lower temperatures than Mg-rich serpentines (King et al., 2015b, Mason et al., 2018), the relative mass loss in the 300 - 450 °C and 450 - 800 °C temperature ranges should help identify degree of thermal alteration of CM and CY chondrites. This relationship is shown in Figure C.2, along with data from Garenne et al. (2014). Two trends can be identified: the first is with increasing alteration, the mass loss due to Mg-serpentine increases, whilst the mass loss due to Fe-rich serpentine decreases. This is due to an increasing proportion of the phyllosilicates being Mg-rich serpentine as Mg-rich anhydrous phases and Fe-rich phyllosilicates decom-

pose during the later stages of alteration. Dehydration should cause samples to pull off the aqueous alteration trend to the left, as Fe-rich serpentines dehydrate first between 300 - 450 ^{o}C. At high degrees of thermal alteration, Mg-rich serpentines dehydrate, causing a decrease in mass loss between 450 - 800 ^{o}C.

Figure C.3 shows the mass loss curves for the stave IV CM chondrites PCA 02010 and PCA 02012, as well as a representative stage II CM and stage IV CY chondrite sample. They show a mass loss event near 225 ^{o}C, at the same temperature as the mass loss event in the GRO 95625 and MIL 07689 samples, implying PCA 02010 and PCA 02012 may contain some rust phases. This is supported by their larger 3 µm band features compared to the other dehydrated samples.

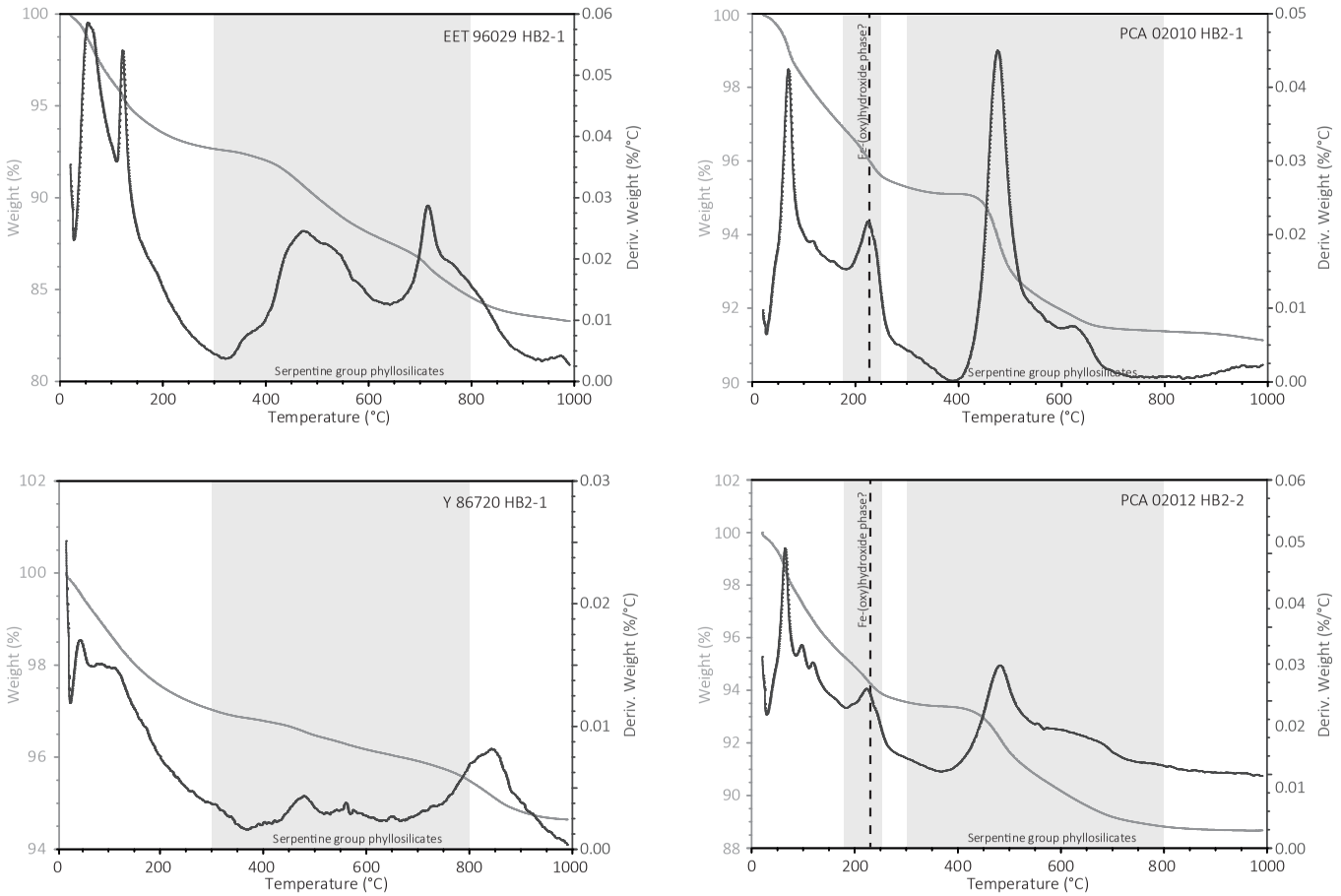


Figure C.3: *Typical mass loss and DTG curves for stage II CM and stage IV CY chondrites. Also included are the mass loss curves for PCA 02010 and PCA 02012, which show dehydration of a phase at ~225 °. This is similar to the mass loss event in GRO 95645 and MIL 07689 and is within the region where Fe-(oxy)hydroxides dehydrate, likely indicating a terrestrial weathering product.*